Doctoral Thesis

Empirical eigenfunctions:
applications in unsteady aerodynamics

Author: Marco Raiola

Supervisors: Andrea Ianiro
Stefano Discetti

Department of Bioengineering and Aerospace Engineering
Universidad Carlos III de Madrid

Leganés, December 2017

Universidad
Carlos III de Madrid
www.uc3m.es

Tesis Doctoral

Empirical eigenfunctions:
applications in unsteady aerodynamics

Autor: Marco Raiola

Directores: Andrea Ianiro
Stefano Discetti

Departamento de Bioingeniería e Ingeniería Aeroespacial
Universidad Carlos III de Madrid

Leganés, Diciembre 2017

Universidad
Carlos III de Madrid
www.uc3m.es

(a entregar en la Oficina de Posgrado, una vez nombrado el Tribunal evaluador, para preparar el documento para la defensa de la tesis)

Tesis Doctoral

Empirical eigenfunctions:

applications in unsteady aerodynamics

Autor: Marco Raiola

Directores: Andrea Ianiro
Stefano Discetti

Firma del Tribunal Calificador:

Firma

Presidente: ______________________________ ______________

Vocal: ______________________________ ______________

Secretario: ______________________________ ______________

Calificación: ______________________________

Leganés, ____ de ______________ de 2017

Abstract

The main aim of modal decompositions is to obtain a set of functions which can describe in a compact way the variability contained in a set of observables/data. While this can be easily obtained by means of the eigenfunctions of the operator from which the observables depends, the *empirical eigenfunctions* allow to obtain a similar result from a set of data, without the knowledge of the problem operator. In Fluid Mechanics and related sciences one of the most prominent techniques to obtain *empirical eigenfunctions* is referred to as Proper Orthogonal Decomposition (POD).

This thesis contains applications of the *empirical eigenfunctions* to (Experimental) Aerodynamics data. The mathematical framework of the POD is introduced following the bi-orthogonal approach by Aubry (1991). The mathematical derivation of the POD is given, wherever possible, in its most general formulation, without bounding it to the decomposition of a specific quantity. This choice of the author depends on the variety of POD applications which are included in this dissertation, ranging from signal processing problems to applications more strictly related with flow physics. The mathematical framework includes also one of the POD extensions, the Extended POD (EPOD), which allows to extract modes linearly correlated to the *empirical eigenfunctions* of a second quantity.

The first two applications of the *empirical eigenfunctions* are strictly connected with the signal treatment in experimental techniques for Fluid Mechanics. In Chapter 3, the *empirical eigenfunctions* are identified as an optimal basis in which perform a "low-pass" spectral filter of experimental fluid data, such as velocity fields measured with Particle Image Velocimetry (PIV). This filtering is extremely beneficial to reduce the random errors contained in the PIV fields and obtain a more accurate estimate of derivative quantities (such as, for instance, vorticity), which are more affected by random errors. In Chapter 4 the POD is exploited for the pre-treatment of a sequence of PIV images. The aim is to remove background and reflections, which are sources of uncertainty in PIV measurements. In this case a "high-pass" spectral filtering is applied to the PIV image ensemble in order to remove the highly-coherent part of the signal corresponding to the background.

In the third and fourth applications, the POD is applied to recover the underlying dynamics of a flow. More specifically, in Chapter 5 the POD is applied to the complex wake of a pair of cylinders in tandem arrangement with the additional perturbation of the wall proximity. Through this technique it is possible to track the changes in the oscillatory behaviour of the wake instabilities ascribed to different geometrical configurations of the cylinders. In Chapter 6 the POD and the EPOD are applied respectively to the flow fields around an airfoil in plunging and pitching motion and to the unsteady aerodynamic forces acting on the airfoil. The decomposition allows to extract a reduced set of modes of the flow field which are related to the force generation mechanism. These modes correspond to well-recognizable phenomena of the flow which can be identified for diverse airfoil kinematics. This flow-field driven force decomposition is analysed on the light of existing force models, enabling their reinterpretation and driving towards possible corrections.

The final application is devoted to overcome the low temporal resolution of typical flow field measurements, such as PIV, by proposing a robust estimation of turbulent flows dynamics. The method employs a modified version of the EPOD to identify the correlation between a non-time-resolved field measurement and a time-resolved point measurement. The estimation of the time-resolved flow fields is obtained exploiting the correlation of the flow fields with the temporal information contained in the point measurements.

Resumen

El objetivo principal de las descomposiciones modales es obtener un conjunto de funciones que sean capaces de describir de una manera compacta la variabilidad contenida en un conjunto de observables/datos. Si bien este objetivo puede ser fácilmente realizado mediante el uso de las autofunciones del operador del cual los observables dependen, las *autofunciones empíricas* permiten obtener un resultado similar partiendo de un conjunto de datos sin la necesidad de conocer el operador del problema. En Mecánica de Fluidos y en ciencias relacionadas con esta disciplina, una de las técnicas más relevantes para obtener *autofunciones empíricas* es la conocida como Descomposición Modal Ortogonal (Proper Orthogonal Decomposition, POD). Esta tesis contiene diversas aplicaciones de las *autofunciones empíricas* en datos de Aerodinámica (Experimental). La base matemática de la POD es introducida siguiendo la aproximación biortogonal realizada por Aubry (1991). La formulación matemática de la POD es expresada siempre que es posible en el marco más general posible, sin condicionarla a la descomposición de una variable en concreto. La elección del autor dependerá de las diferentes aplicaciones de la POD, todas ellas descritas en la presente tesis, las cuales abarcan desde problemas de procesado de señales hasta aplicaciones más estrictamente relacionadas con el análisis de la física del flujo. La formulación matemática incluye también uno de las extensiones de la POD, la POD Extendida (EPOD), la cual permite extraer modos linealmente correlacionados con las *autofunciones empíricas* de una segunda variable. Las dos primeras aplicaciones de las *autofunciones empíricas* están estrictamente relacionadas con el tratamiento de señales en técnicas experimentales de Mecánica de Fluidos. En el Capítulo 3, las *autofunciones empíricas* son identificadas como una base optima, la cual se puede utilizar para realizar un filtro pasa bajos espectral para datos experimentales de flujos, tales como campos de velocidad obtenidos mediante la técnica de Velocimetría por Imágenes de Partículas, (Particle Image Velocimetry, PIV). Este tipo de filtro es muy beneficioso para reducir los errores de carácter aleatorio contenidos en los campos de PIV y por tanto obtener una estimación más precisa en las cantidades que precisan del uso de derivadas (por ejemplo, la vorticidad), ya que están más afectadas por este tipo de errores. En el

Capítulo 4, la POD es utilizada para el pretratamiento de una secuencia de imágenes de PIV. El objetivo es reducir el fondo de la imagen y las reflexiones, ambas fuentes de incertidumbre en las medidas de PIV. En este caso, un filtro pasa altos espectral es aplicado al conjunto de imágenes de PIV para poder quitar la parte mayormente correlacionada de la señal, la cual corresponde con el fondo de la imagen. En la tercera y cuarta aplicación de la POD, está técnica es utilizada para reconstruir las dinámicas fundamentales de un flujo. Concretamente, en el Capítulo 5 la POD es utilizada para analizar la estela compleja que se produce en una pareja de cilindros en tándem con la perturbación adicional de una pared próxima a ellos. A través de esta técnica, es posible poder estudiar los cambios en el comportamiento oscilatorio de las inestabilidades de la estela, las cuales están relacionadas con las diferentes configuraciones geométricas de los cilindros. En el capítulo 6, la POD y la EPOD son aplicadas respectivamente a campos fluidos y fuerzas aerodinámicas producidos por un perfil aerodinámico en movimiento (de rotación y desplazamiento vertical) no estacionario. La técnica de descomposición permite extraer un conjunto reducido de modos del campo fluido que están relacionados con el mecanismo que genera las fuerzas aerodinámicas. Estos modos corresponden con fenómenos característicos del flujo que pueden ser identificados para diferentes cinemáticas de perfiles aerodinámicos. Estas dinámicas del flujo que están conectadas con las fuerzas aerodinámicas son analizadas teniendo en cuenta los modelos ya existentes en la literatura que describen las fuerzas aerodinámicas, permitiendo su reinterpretación e incluso pudiendo añadir posibles correcciones. La última aplicación propuesta está destinada a subsanar la baja resolución temporal típica de las medidas de campo fluido, como en aquellas realizadas utilizando PIV, mediante una estimación robusta de las dinámicas del flujo turbulento. El método propuesto emplea una versión modificada de la EPOD para identificar para correlación entre un campo fluido medido que no está resuelto en el tiempo y una medida puntual que sí que está resulta en el tiempo. La estimación del campo fluido resuelto en el tiempo es obtenida mediante la correlación de los campos de flujo con la información temporal contenida en la medida puntual.

Acknowledgements

Despite this section is supposed to be included in the very first pages of this manuscript, I have to admit that I deliberately procrastinated writing it 'till the very last moment. Honestly, I was not even entirely sure that at some point I would have written something in this section: the topic to be treated here seemed too tough for an emotionally-flat-lined person like me. I felt that, despite all my efforts, the "Acknowledgements" section was doomed to be mediocre and impersonal. Which, actually, seemed a good reason to quit this task. Yet, in some moment, I considered that, in some way, this manuscript is the result of all the people I ran into during the last years. And that they would deserve to be acknowledged. Or, most likely, blamed.

Perhaps, I must acknowledge first my two advisors, Andrea and Stefano, without whom I wouldn't have written this thesis and, probably, I wouldn't even have started my PhD. Which means that, without them, I would have preserved much more of my mental health -I should blame especially Andrea and his "ehmm" for this. Joking aside, I am grateful to you guys for your guidance and support during these years and for all the hilarious moments inside and outside the lab.

All my thoughts and prayers are with Carlos for sharing with me the misfortune of having the two mentioned above as thesis advisors. May this manuscript be for you the proof that sooner or later all this pain will come to an end. The same equally applies to Güemes, even if he seems not yet aware of his miserable fate.

I wish to thank the group of PhD students in room H03: for all the confusion, the good jokes and the bad ones (you all know who I'm referring about here) and for all the time you made me waste. Without you I would have probably worked much more than I actually did, but indeed all the time (too much time) I spent in the university would have been much less fun. I should also say something nice about the guys in room H05, but I feel a chill down my spine every time I think about the "Church of Plasma" (I'm sorry, there was nothing I could have done to save you!).

I wish to acknowledge our lab technician Carlos for his help in setting up the experiments. Thanks to Pablo Fajardo, for his invaluable help in many occasions (especially during this last semester which has been tougher than I expected). And thanks to Javi Rodriguez, for all the discussions, the jokes and for always borrowing me equipment for the experiments. Finally thanks also to the people of TU Delft for welcoming me in their group during my short stay: I will never forget the stress of those few months (even if in the end it was kind of fun).

I wish to thank also my flatmates, the present and the old ones for the very good moments we spent together. Without you that house wouldn't have been as warm as I felt during these years (no, I'm not referring to the heating system, even if it helped). Whatever be the future, I hope we will keep in touch.

Finally, I wish to acknowledge my family. Thanks to my parents and to my sister for supporting me during these years. You never let me felt away from home, despite I was in a foreign country. All your unconditioned love and especially your complains always found a way to reach me. And thanks also to all my cousins: we perhaps took different paths, scattered around the globe, but each time we meet everything seems unchanged even if all changed.

This work has been partially supported by the Grant TRA2013-41103-P of the Spanish Ministry of Economy and Competitiveness, which includes FEDER funding, and by the Grant DPI2016-79401-R, funded by the Spanish State Research Agency (SRA) and European Regional Development Fund (ERDF).

Table of contents

List of figures xv

List of tables xxi

Nomenclature xxiii

I Modal decomposition for unsteady flows 1

1 Introduction 3

1.1 Why modal decomposition? 3

1.2 A short summary on modal decomposition techniques 5

1.3 POD and data mining 8

1.4 Empirical eigenfunctions in Fluid Mechanics 9

1.5 Motivation and outline of the work 13

2 Mathematical framework 17

2.1 Proper Orthogonal Decomposition 17

2.1.1 Discrete Proper Orthogonal Decomposition 19

2.1.2 Low-rank approximation 21

2.2 POD and random noise 23

2.2.1 Optimal low-rank approximation of noise-perturbed datasets 24

2.3 POD and modelling of non-time-resolved flow field measurements 26

2.4 Extended Proper Orthogonal Decomposition 28

2.4.1 Properties of the EPOD 29

2.4.2 Connection with Linear Stochastic Estimation 31

II Applications to signal treatment 33

3 Optimal flow-feature oriented filtering for field measurements 35
3.1 The uncertainty in Particle Image Velocimetry 36
3.2 POD as a de-noising tool in PIV measurements 37
3.3 Optimal low-rank approximation of PIV data 38
3.4 Validation 41
3.4.1 Numerical validation on synthetic images 41
3.4.2 Validation of the criterion for modes selection 47
3.4.3 Comparison with spatial filtering 51
3.4.4 Experimental validation 52
3.5 Conclusion 55

4 Eigenbackground removal for PIV images 59
4.1 State of the art in pre-processing methods for PIV images 60
4.2 Reduced-order modelling of PIV image sequences 62
4.2.1 Eigenbackground removal algorithm and error estimation 63
4.3 Validation 65
4.3.1 Statistical convergence of an ideal PIV sequence 65
4.3.2 Background removal in a synthetic test case 67
4.3.3 Background removal in an experimental test case 74
4.4 Conclusions 76

III Flow modelling: POD for data exploration 79

5 Wake of cylinders in tandem configuration near a wall 81
5.1 Tandem cylinders in cross flow 81
5.2 Experimental setup 84
5.3 Results 86
5.3.1 Average fields and turbulence statistics 86
5.3.2 POD modes organization and mutual relation 95
5.4 Discussion and conclusions 102

6 Unsteady force and flow structures over flapping airfoil 107
6.1 Introduction 107
6.1.1 Potential flow models for force generation in flapping airfoils . . 109
6.1.2 Force generation and flow organization 113

6.1.3 Bridging the gap between flow topology and reduced-order models 115
6.2 Experimental setup 116
6.2.1 Wing kinematics and motion system 117
6.2.2 Aerodynamic forces measurements 121
6.2.3 Flow field measurements 122
6.3 Data Processing 122
6.3.1 Change of reference frame 122
6.3.2 Estimation of the extended POD modes 124
6.4 Flow topology and forces 126
6.4.1 Phase-averaged flow fields and forces 126
6.4.2 Time average flow fields and forces in the wing-fixed reference frame 130
6.5 Modal decomposition 133
6.5.1 Spectral distribution of extended POD modes 133
6.5.2 Low-order reconstruction of the force 135
6.5.3 Description of the 1st and 2nd extended POD modes 137
6.5.4 Description of higher order extended POD modes 142
6.6 Low-order model of the flow field features and their contribution to the force 145
6.6.1 Low-order reconstruction of flow features 145
6.6.2 Reduced-order model of the force 148
6.7 Conclusions 153

IV Other applications 157

7 Estimation of time-resolved turbulent fields 159
7.1 Dynamic estimation of turbulent flow fields 160
7.2 Mathematical foundations 164
7.2.1 An extended POD approach for turbulent fields estimation . . . 164
7.2.2 Truncation of the time coefficients correlation matrix 166
7.3 Method validation 168
7.3.1 DNS test case 168
7.3.2 Experimental test case 175
7.4 Conclusions 181

V Final remarks

8 Conclusions **185**

8.1 Summary . . . 185

8.2 Future work . . . 188

9 Conclusiones **191**

9.1 Síntesis . . . 191

9.2 Perspectivas futuras . . . 194

References **197**

Papers and author contributions **215**

List of figures

1.1 Number of monthly searches for the word "Big Data" in the period 01 January 2007 - 01 January 2017. 5

2.1 POD spectrum and another non-optimal basis spectrum for a dissipative system. 22

3.1 Sub-domains extracted from the Channel Flow DNS spatial domain for the synthetic PIV experiment. 41
3.2 DNS test case: δ_{RT}, δ_{RM} and F versus the number of modes used in the reconstruction. 43
3.3 DNS test case: POD eigenvalues of the 4000 most energetic modes. . . 43
3.4 DNS test case: instantaneous fluctuating vorticity field. 45
3.5 DNS test case: transverse velocity and vorticity spectra in stream-wise direction 46
3.6 Test case with 6000 images: δ_{RT}, δ_{RM}, F and traverse velocity spectra. 47
3.7 Test case with 4000 images: δ_{RT}, δ_{RM}, F and traverse velocity spectra. 48
3.8 Test case with $\varsigma_e = 0.11$: δ_{RT}, δ_{RM}, F and traverse velocity spectra. . . 49
3.9 Test case with $\varsigma_e = 0.27$: δ_{RT}, δ_{RM}, F and traverse velocity spectra. . . 49
3.10 Test case with lower spatial resolution: δ_{RT}, δ_{RM}, F and traverse velocity spectra. 50
3.11 Spatial filter comparison: traverse velocity and vorticity spectra. 51
3.12 Spatial filter comparison: instantaneous fluctuating vorticity field. . . . 52
3.13 δ_{RT}, δ_{RM} and F versus the number of modes used in the reconstruction. 54
3.14 Cylinder test case: transverse velocity spectra in stream-wise direction. 54
3.15 Cylinder test case: comparison of fluctuating velocity fields. 56

4.1 Example snapshot of the background source and corresponding PIV synthetic image. 66

4.2 Analysis of statistical convergence on synthetic PIV images with source density $N_S = 0.02$ and $N_S = 0.9$. 67
4.3 Singular value spectra of the synthetic image sequence, of the background, and of the ideal PIV pattern sequences, compared to the theoretical spectrum of the ideal particle images. 69
4.4 Synthetic test case: scalar products of corresponding temporal eigenvectors with the first temporal eigenvector of the ideal PIV images 69
4.5 Synthetic test case:: comparison of the first temporal eigenvectors for the image sequence and the background sequence. 70
4.6 Synthetic test case: examples showing the result of image pre-processing using historical minimum removal, high-pass filtering, CLAHE recontrasting, min/max adjusting and the proposed POD filtering method. . 71
4.7 Synthetic test case: error plots in the average velocity magnitude for the original image sequence, historical minimum removal , high-pass filter, CLAHE recontrasting, min/max adjusting, and the proposed POD filtering. 73
4.8 Computational cost of several pre-processing methods as a function of the number of images having resolution of 1Mpixels. 74
4.9 Sketch of the 2D flapping wing experiment. 75
4.10 Example of snapshot for the PIV investigation of the flow over a flapping wing. 76
4.11 Flapping wing experiment: image crops and cross-correlation maps for the original sequence and for the results of the ensemble minimum removal and POD filter. 77
4.12 Flapping wing experiment: singular value spectra of the experimental image sequence and scalar product of the corresponding temporal eigenvectors with the first temporal eigenvector. 78

5.1 Flow behaviors for cylinders in tandem configurations. 82
5.2 Schematic of the experimental setup. 85
5.3 Velocity deficit profiles for varying L/D and G/D. 87
5.4 Contour maps of the average stream-wise velocity component for all the longitudinal pitch ratios (L/D) and wall gap ratios (G/D) object of the study. 88
5.5 Contour maps of the Turbulent Kinetic Energy for all the longitudinal pitch ratios (L/D) and wall gap ratios (G/D) object of the study. . . . 89

5.6 Comparison of wake width and maximum velocity deficit for several L/D and $G/D = 3$. 90
5.7 Wake width comparisons for several G/D. 92
5.8 Maximum velocity deficit comparisons for several G/D. 93
5.9 Energy content of the first 20 modes expressed in percentage of the total in-plane turbulent kinetic energy. 96
5.10 Contour maps of non-dimensional vorticity of the 1st POD mode. . . . 98
5.11 Scatter plot of time coefficients of the 2nd POD mode with respect to the time coefficients of the 1st mode. 99
5.12 Contour maps of non-dimensional vorticity of POD modes. 102
5.13 Scatter plot of time coefficients of POD modes with respect to the time coefficients of the 1st mode. 103

6.1 Sketch of the experimental setup. 117
6.2 Pitching/plunging airfoil motion and forces. 117
6.3 Four-bar mechanical linkage. 119
6.4 Parametric space spanned by the motion system. 119
6.5 Effective angle of attack history for all the cases. 120
6.6 Phase-averaged flow field and force components evolution during the flapping cycle: case A, B and C. 128
6.7 Phase-averaged flow field and force components evolution during the flapping cycle: case D, E and F. 129
6.8 Average flow field in wing-fixed reference frame for all the cases. 131
6.9 Cumulative spectral density of the Extended POD modes. 133
6.10 Low-order reconstruction of the chord-normal force component with extended POD modes. 136
6.11 Low-order reconstruction of chord-wise force component with extended POD modes. 136
6.12 Compact overview of the 1st POD modes of velocity and extended POD modes of vorticity and force for all the cases. 138
6.13 Compact overview of the 2nd POD modes of velocity and extended POD modes of vorticity and force for all the cases. 139
6.14 Compact overview of the 3rd, 4th, 5th and 6th POD modes of velocity and extended POD modes of vorticity and force for case B. 143
6.15 Compact overview of the 3rd, 4th, 5th and 6th POD modes of velocity and extended POD modes of vorticity and force for case E. 144

6.16 Case B. Snapshot of the flow field: fluctuating flow field; LOR with 1st and 2nd modes; LOR with 3rd to 6th modes. 146
6.17 Case E. Snapshot of the flow field: fluctuating flow field; LOR with 1st and 2nd modes; LOR with 3rd and 4th modes. 147
6.18 Chord-normal component of the fluctuating force: comparison of LOR and theoretical force models. 149
6.19 Chord-wise component of the fluctuating force: comparison of LOR and theoretical force models. 150

7.1 Energy spectrum and cumulative energy contribution of the flow field modes of the channel simulation. 168
7.2 North-West corner of the time coefficients correlation matrix $\underline{\underline{\Xi}}$ for a probe acquisition time of 1 convective time h/U_b: 3 probes and 11 probes. 169
7.3 Temporal evolution of the time coefficients of the first mode estimated with three probes, using a sampling length of one convective time. No truncation is performed on the time-coefficients correlation matrix. . . 170
7.4 Squared correlation coefficient of the reconstructed time coefficient series with the ground truth solution for the case of sampling length equal to h/U_b and for different number of probes. 170
7.5 Temporal evolution of the time coefficients of the first 6 modes obtained with sampling time equal to h/U_b for different number of probes. 171
7.6 Contour plot of fluctuating stream-wise velocity component with superimposed (down-sampled) vector arrows. Top: comparison of the dynamic reconstruction of the flow field (a) against the exact flow field (c) and the exact low-order reconstruction with the same mode truncation (200 modes) as the dynamically estimated flow field (b). Bottom: reconstruction error distributions in percentage with respect to the LOR (e) and to the original field (e). 172
7.7 Squared correlation coefficient of the reconstructed time coefficient series with the ground truth solution for the case with 11 probes and different probes sampling time equal to 0.75, 1 and 1.25 $\mathrm{h/U_b}$. 174
7.8 Sketch of the PIV experimental setup. 177
7.9 Energy spectrum and cumulative energy contribution of the flow field modes of the experimental test case. 177
7.10 Contour plot of the stream-wise velocity component of the first 6 flow fields modes with superimposed (down-sampled) vector arrows. 178

7.11 Squared correlation coefficient between dynamically estimated time coefficient and original time coefficients of the PIV sequence. The squared correlation coefficient is calculated in the time instants of the used PIV samples. 178
7.12 Time coefficients of the true measured signal, of the dynamic estimation and of the subsampled PIV sequence. 179
7.13 Contour plot of stream-wise velocity component with superimposed (down-sampled) vector arrows. Top: comparison of the dynamic reconstruction of the flow field (a) against the exact flow field (c) and the exact low-order reconstruction with the same mode truncation (20 modes) as the dynamically estimated flow field (b). Bottom: reconstruction error distributions in percentage with respect to the LOR (e) and to the original field (e). 180

List of tables

6.1 Lengths of the bars of the linkage mechanism. 117
6.2 Summary of the wing kinematics parameters. 120
6.3 Summary of time-averaged force coefficients for all the cases analysed. . 131
6.4 Coefficient of determination R^2 of the force LOR. 137

Nomenclature

Roman Symbols

$\underline{\mathscr{A}}$	generic vector field
$\underline{\mathscr{a}}$	fluctuating part of a generic vector field
$\underline{\underline{A}}$	generic dataset matrix
$\underline{a}^{(i)}$	i^{th} realization vector
$\underline{\underline{A}}_n$	approximation of rank n of the matrix $\underline{\underline{A}}$
$b^{(i)}$	i^{th} temporal coefficient
c	airfoil chord
C_D	drag coefficient
C_d	drag coefficient of the airfoil
$C_{F_{x'}}$	chord-wise force coefficient
$C_{F_{y'}}$	chord-normal force coefficient
C_L	lift coefficient
C_l	lift coefficient of the airfoil
C_p	particle density
$C(\cdot)$	Theodorsen's function
$\mathscr{D}$	drag force
D	cylinders diameter

d_p	particle diameter
$\boldsymbol{e}$	spatially-averaged turbulent kinetic energy
$\underline{\underline{E}}$	random error matrix
E_F	particle pattern's reconstruction error
Err_V	velocity magnitude error
F	relative decrease rate of δ_{RM}
f	frequency
f_k	temporal evolution of the kth background feature
$F_{x'}$	force along the chord-wise direction
$F_{y'}$	force along the chord-normal direction
G	cylinder-wall gap height
g_k	spatial structure of the kth background feature
h	channel height
$h(t)$	plunging motion
h_0	plunging amplitude
$H_n^{(2)}(\cdot)$	Hankel function on the second kind of order n
$\underline{\underline{I}}_n$	identity matrix of rank n
$\mathscr{I}_L$	intensity of the laser sheet
$\underline{\underline{\mathrm{Im}}}^{(i)}$	i^{th} image intensity map
$\mathscr{I}_P$	intensity distribution of the particle
$\underline{\underline{J}}$	Jacobian matrix
$\underline{\underline{K}}$	inner product matrix
k	reduced frequency
ℓ	wavelength

$\mathscr{L}$	lift force
L	cylinders longitudinal pitch
$\underline{\underline{M}}$	rotation matrix
m	number of probes
n_m	number of modes
N_p	number of particles
n_p	number of point measurements
n_{pr}	number of probe samples
N_s	source density
n_t	number of temporal realizations
n_{tt}	number of virtual probes
nvv	percentage of invalid vectors
n_x	x-axis snapshot size
n_y	y-axis snapshot size
p_f	pixel fill factor
q	dynamic pressure
R	recovery ratio
r	matrix rank
R^2	coefficient of determination / squared correlation coefficient
r_b	rank of the background features matrix
$\underline{\underline{R}}$	residual matrix
Re	Reynolds number
Re_c	Reynolds number based on the centerline velocity
Re_τ	Reynolds number based on the friction velocity

RF	theoretical noise reduction factor
R_s	two-point spatial correlation tensor
R_t	two-point temporal correlation tensor
S	wing surface
s	probe supersampling factor
St	Strouhal number
T	observation time
t	time
$\widehat{T}$	non-dimensional vortex formation time
TKE	local turbulent kinetic energy
$\underline{\underline{U}}$	snapshot matrix of the velocity component in the x-axis direction
u	velocity component in the x-axis
u_1	wake deficit of momentum
$u_{1,max}$	maximum deficit of momentum
U_b	bulk velocity
u_{max}	local velocity maximum
$\underline{\underline{V}}$	snapshot matrix of the velocity component in the y-axis direction
V_{eff}	effective velocity relative to the airfoil
V_∞	free-stream velocity
$V_{x'}$	relative velocity along the chord-wise direction
$V_{y'}$	relative velocity along the chord-normal direction
w	wake width
$W(\cdot)$	Wagner's indicial function
$\underline{x}$	position vector

$\underline{x}'$	position vector in the wing-fixed reference frame
$y_{1,max}$	vertical position of the maximum deficit of momentum
y_{wake}	vertical position of the wake boundaries

Greek Symbols

$\alpha(t)$	pitching motion
α_0	pitching amplitude
$\alpha_{eff}(t)$	effective angle of attack history
α_m	mean pitch angle
δ_{BL}	boundary-layer thickness
δ_{RM}	reconstruction error with respect to the measured field
δ_{RT}	reconstruction error with respect to the objective function
Γ	circulation
γ	vorticity distribution along the chord-wise direction
ι	imaginary unit
$\underline{\lambda}^{(i)}$	i^{th} squared singular value
$\underline{\underline{\Lambda}}$	squared singular values diagonal matrix
μ_p	spatial average of the particle pattern's intensity
ν	fluid kinematic viscosity
Ω	spatial domain
ω_z	local out-of-plane vorticity
$\underline{\phi}^{(i)}$	i^{th} discrete *topos*/right eigenvector
$\underline{\underline{\Phi}}$	right eigenvectors matrix / spatial basis
$\underline{\upphi}^{(i)}$	i^{th} *topos*/spatial POD eigenfunction
$\underline{\underline{\Phi}}_n$	rank n truncation of the spatial basis $\underline{\underline{\Phi}}$

φ	phase delay
$\underline{\psi}^{(i)}$	i^{th} discrete *chronos*/left eigenvector
$\underline{\underline{\Psi}}$	left eigenvectors matrix / temporal basis
$\uppsi^{(i)}$	i^{th} *chronos*/temporal POD eigenfunction
$\underline{\underline{\Psi}}_n$	rank n truncation of the temporal basis $\underline{\underline{\Psi}}$
ρ	fluid density
$\sigma^{(i)}$	i^{th} discrete singular value
$\underline{\underline{\Sigma}}$	diagonal matrix of singular values
$\upsigma^{(i)}$	i^{th} singular value
$\underline{\underline{\Sigma}}_n$	rank n truncation of the singular values matrix $\underline{\underline{\Sigma}}$
ς_e	standard deviation of the normally distributed error
ς_p	spatial standard deviation of the particle pattern's intensity
τ	period
ϑ	period phase
$\underline{\underline{\Xi}}$	correlation matrix between temporal modes
ξ	non-dimensional chord-wise coordinate
ξ_p	non-dimensional position of the pivot point
$\zeta(\cdot)$	Euler-Riemann zeta function

Operators

$\lvert \cdot \rvert$	absolute value
$\langle \cdot \rangle$	ensemble average
$\lVert \cdot \rVert_F$	Frobenius norm
$\delta_{i,j}$	Kronecker delta symbol
$\lVert \cdot \rVert^2$	L^2 norm in space

$\mathrm{rank}(\cdot)$	rank of a matrix
$(\cdot,\cdot)$	scalar product
$\dot{a}$	time derivative of a
$\mathrm{Tr}(\cdot)$	trace of the matrix
$\underline{\underline{A}}^T$	transpose of the matrix $\underline{\underline{A}}$

Superscripts

δ	referred to the effective minimum of δ_{RT}
F	referred to the point satisfying the relation $F = 0.999$
(i)	referred to the ith element
$\hat{\ }$	non-dimensional quantity
$\star$	referred to the theoretical minimum of δ_{RT}
$\tilde{\ }$	quantity referred to the objective function / noise-free quantity
$+$	relative to a generic out-of-sample time instant
$'$	quantity referred to the wing-fixed reference frame

Subscripts

A	referred to the quantity A
a	relative to the added-mass contribution
B	referred to the quantity B
b	referred to the background features
c	circulatory contribution
DYN	estimated in the out-of-sample time instants
e	relative to the EPOD modes
F_x/F_y	quantity referred to the chord-wise/chord-normal force component
f	friction contribution

$inst$	instantaneous
nc	non-circulatory contribution
ω	quantity referred to the vorticity
p	referred to the particle pattern
pr	relative to the probe
rot	circulatory contribution induced by rotation
s	suction contribution
$trans$	circulatory contribution induced by translation
$true$	relative to the ground truth
u/v	quantity referred to the chord-wise/chord-normal velocity component
wc	wake-capture contribution

Acronyms / Abbreviations

BPOD	Balanced Proper Orthogonal Decomposition
DMD	Dynamic Mode Decomposition
DNS	Direct Numerical Simulation
EPOD	Extended Proper Orthogonal Decomposition
ERA	Eigensystem Realization Algorithm
IR	Infra-Red
K-L	Karhunen-Loéve
LES	Large Eddy Simulation
LOR	Low Order Reconstruction
LSE	Linear Stochastic Estimation
PCA	Principal Components Analysis
PIV	Particle Image Velocimetry

POD	Proper Orthogonal Decomposition
ROM	Reduced-Order Model
SVD	Singular Value Decomposition
VIC	Vortex In Cell

Part I

Modal decomposition for unsteady flows

Chapter 1

Introduction

1.1 Why modal decomposition?

In the 60's Richard Feynman wrote that "turbulence is the most important unsolved problem of classical physics" (Feynman et al., 1964), addressing with these words the great scientific challenge offered by turbulent flows. Along the last century, turbulent flows have been one of the most explored topics in Fluid Mechanics research. The first use of the word 'turbulence' in the context of Fluid Mechanics is associated to the experimental observations of eddies decay by Leonardo da Vinci in 1500 (Da Vinci, 1500). The onset of modern turbulence studies, however, should be set at the end of the 19th century with the works of Boussinesq (1877) and Reynolds (1894) who tailored the problem with a statistical approach. Several other seminal works, mainly empirical and semi-empirical, followed in the beginning of the 20th century, among them the works by Taylor (1915), Prandtl (1925) and von Kármán (1935). The theoretical formalization of turbulence was mainly due to Kolmogoroff (1933), who developed a rigorous axiomatic foundation of probability theory including a strict definition of stochastic function of any number of variables. Based on this mathematical framework, Kolmogoroff (1941a,b) introduced the well known theory of turbulence named after him. Landau and Lifshitz (1959) and Hopf (1948), independently, developed a theory on the transition to turbulence.

Similarly to what happened in most of the natural and mathematical sciences, the second half of the 20th century represented a turning point for Fluid Mechanics with the introduction of computational science, which, after empirical and theoretical studies, became the third paradigm in turbulence studies. After the introduction of Direct Numerical Simulations (DNS, Orszag and Patterson, 1972) and Large Eddy Simulations (LES, Deardorff, 1970), computational studies were mainly carried out between Stanford University and NASA Ames Research Laboratory (Reynolds, 1976), before becoming a common approach worldwide.

Due to its intrinsic random nature, turbulence is notoriously difficult to be described in compact form, thus requiring large datasets for its description. The progress of numerical simulations and experimental techniques have made available an increasing amount of data, which needs to be processed and analysed. It has become clear that a fourth paradigm should be added, the data-intensive science (Hey et al., 2009), which resumes the idea of scientific discovery driven by data-intensive processes. This approach in the field of turbulence can be dated back to the early works by Lumley (1967), becoming more and more common with the recent availability of computational power and recorded data.

The technological advances in the fields of electronics and informatics have led to an exponential growth over the past 20 years of the collected/produced data to be processed, which is transversally permeating all aspects of the modern human activities. The abundance of information led to the creation of a whole new branch of data science, focused on the opportunities and the problems related to handling such a large quantity of data. The use of a buzzword like "Big Data", which resumes both issues and advantages of data-intensive applications, can be considered as a good marker of this phenomenon. Fig. 1.1 shows the exponential growth of the interest in this topic during the last 10 years. Usually scientific data are less problematic than what is commonly referred to as "Big Data" since they are generally well structured. Nevertheless, the quantity of data to handle often requires some sort of data reduction in order to be analysed.

On the other hand, there is no doubt that the availability of large datasets has the potential to drive toward a deeper knowledge about complex flow phenomena. Modern Aerodynamics (and Fluid Mechanics in general) is focused on problems whose solution cannot depend simply on average quantities, i.e. flows in which the assumption of *steadiness* cannot be retained. Turbulence modelling, aerodynamic noise production, turbulent convective heat transfer, transport of contaminants and generation of unsteady aerodynamic forces form just a short and incomplete list of problems which require a proper understanding of the flow evolution both in space and time. The behaviour of these flows might result too complex to model due to the non-linearity of the governing equations (i.e. the Navier-Stokes equations) and requires proper mathematical tools to be analysed.

The term *modal decomposition* indicates a family of mathematical tools which offer a solution for problem-adaptive data reduction. The scope of the modal decomposition

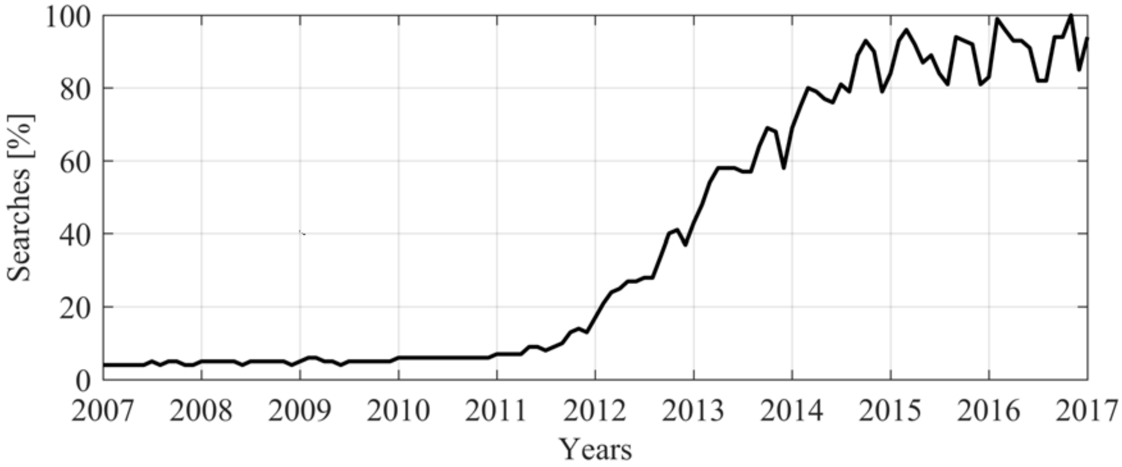

Fig. 1.1 Number of monthly searches for the word "Big Data" in the period 01 January 2007 - 01 January 2017. Results are normalized with respect to the maximum number of monthly searches. Source: Google Trends.

is to reduce the dimensionality of a problem, dividing the phenomena under study into simpler components and, thus, reducing the available dataset to a more compact and accessible set of information. From this perspective, modal decomposition can be included among the *data mining* techniques. Due to the transversal interest in these techniques, it should be not surprising that modal decomposition has been widely exploited in many different fields and for the most varied scopes, among them the study of turbulence. In the following, some of the modal decomposition techniques more commonly employed in Fluid Mechanics will be shortly introduced in the context of decomposition of flow fields. The discussion will focus on the Proper Orthogonal Decomposition. The reason of this choice is twofold: thanks to its relative simplicity (both in terms of implementation and of requirements) this technique will be largely employed (for different scopes) in this work; on top of that, POD is to be considered a "fundamental" data-driven decomposition technique, being included in different forms in other more advanced decomposition techniques.

1.2 A short summary on modal decomposition techniques

Decomposing a varying feature (in time, space or any other dimension) to reduce its complexity is a common procedure in almost any branch of physics and mathematics.

Some notable examples are the Taylor and Fourier series expansions or the wavelet decomposition. In these cases the varying quantity is projected onto a set of functions which are assumed to form a basis of the observation space and have been fixed *a priori*. In Fluid Mechanics, and especially in turbulence, such decompositions have been widely explored. A notable example is the Fourier spectrum of turbulence, with the celebrated $-5/3$ decay rate in the inertial sub-range (Kolmogoroff, 1941a,b).

In the most recent approaches, the modal decomposition of flow fields aims to identify a set of modes, acting as decomposition components, which effectively describe the most relevant flow features (thus driven by the data or the equations describing the problem). Each mode is associated to a spatial description of the flow features, to their temporal description and their magnitude. Two different kind of approaches are possible to perform the modal decomposition (Taira et al., 2017). In the *operator-based* approaches, the analysis is performed directly on an operator, i.e. a set of equations which govern the problem (the Navier-Stokes equations for Fluid Mechanics problems). The *data-based* approaches provide a pathway to extract modes from a set of observations, thus performing an *a posteriori* modal analysis of the flow. This second kind of approaches is intimately connected to data mining techniques, which allow to extract reduced-order informations from a dataset without requiring an *a priori* knowledge of the problem operator.

A prominent example of operator-based modal decomposition in Fluid Mechanics is the flow stability analysis. Earlier theories on flow stability were based on the *local linear stability analysis*, which extracts the flow instabilities around a base-flow (i.e. an exact steady solution of the problem) after linearising the problem operator in one direction (time or space). More recently it has been introduced the *global linear stability analysis* (see Theofilis, 2011, for a review). Global stability analysis differs from the local stability analysis since it considers a base-flow depending on all the problem directions. Introducing a modal formulation for the perturbation (i.e. assuming linear dynamics of the perturbation) the original Navier-Stokes equations can be restated as an eigenvalue problem. The complex eigenvalues represent the oscillation frequency and the decay rate of the perturbation. The eigenvectors represent the spatial structure of the perturbation.

The *Koopman analysis* (recently reviewed by Mezić, 2013) provides a decomposition on a basis which is associated to the dynamical evolution of the flow field. The Koopman -or composition- operator describes a transformation of the state space in which the problem to study is linear, thus extending the range of linear approximation of the system. The eigenvalues of the Koopman operator are the complex-valued exponents of the exponential function describing the linearised temporal evolution of the system. The Koopman modes are defined as the projections of a flow field quantity (such as the velocity field) on the eigenfunctions of the Koopman operator.

While the Koopman analysis is formally an operator-based technique, it is possible to approximate Koopman modes from an experimental/numerical dataset through the Dynamic Mode Decomposition (DMD, Schmid, 2010, Tu et al., 2014). The DMD allows to calculate a set of modes from an ordered set of observables of the flow fields. The DMD modes may be considered as the finite-rank approximation of the Koopman modes for non-linear dynamical systems (Rowley et al., 2009). Being a data-based technique, the advantage of DMD lies in that it does not require the *a priori* knowledge of the operator underlying the flow dynamics. On the other hand, the DMD does not provide a univocal ranking of the modes. Recognising the most relevant modes may be a hard task, although some efforts in that direction have been performed by Jovanović et al. (2014). Additionally, DMD requires datasets with high spatial/temporal resolution (depending on the coordinate along which the decomposition is carried out), that significantly reduces the range of applicability of this technique. For example, optical measurement techniques (such as PIV) suffer hardware limitations (for instance, repetition rate of light sources and frame rate of the camera), which bound spatio-time resolved techniques to relatively low Reynolds number flows.

The first data-based modal decomposition technique introduced in Fluid Mechanics is the Proper Orthogonal Decomposition (POD, Lumley, 1967). Depending on the context, this technique has been also known as Principal Component Analysis (PCA) or Karhunen–Loève (K-L) expansion. POD modes are usually referred also as *empirical eigenfunctions* (Berkooz et al., 1993) to highlight the difference with respect to the modes obtained through stability analysis. POD modes are calculated under the constraint of modes orthogonality and minimizing the residual error (according to the L^2 norm) of the truncated reconstruction. The empirical eigenfunctions calculated through the POD form an exact decomposition basis which allows for an exact reconstruction of the dataset without introducing any residual error. Moreover, POD modes are ranked according to their contribution to the variance in the dataset. The ranking and modal orthogonality properties are at the basis of the success of the POD for the generation of reduced-order models of experimental/numerical datasets. With respect to other modal decomposition techniques, POD relies on the statistical properties of the dataset, thus it does not require temporal resolution of the data.

POD is, perhaps, the most widespread between all the modal decomposition techniques listed above. Under several names, POD found large application in a huge number of different topics, also, and perhaps mostly, outside the context of Fluid Mechanics and turbulence. The next paragraph will specifically focus on the wide attention that the POD received in fields different from Fluid Mechanics, giving few examples of them. A short historical perspective on the applications of POD in the context of Fluid Mechanics will be addressed in §1.4. The mathematical details of the POD will be discussed in Chapter 2.

1.3 POD and data mining

The Proper Orthogonal Decomposition has been first introduced by Pearson (1901) and Hotelling (1933) under the name of Principal Component Analysis (PCA) in statistical analysis. PCA rapidly spread (even if under several different names) to a wide variety of branches of natural and social sciences thanks to its capability to easily recognize underlying patterns in large datasets, independently of the source (and the nature) of the data. In the following, the terms Principal Component Analysis (PCA), Proper Orthogonal Decomposition (POD), Singular Values Decomposition (SVD) and Karhunen–Loève (K-L) expansion will be freely interchanged as they represent (in their matrix formulation) the solution to the same problem (Liang et al., 2002). The different nomenclature is mostly ascribed to historical reasons, owing to the different fields of application.

The ability of K-L expansion to reduce the dimensionality of large datasets rendered it an important tool for data compression (Andrews et al., 1967). The use of this compression technique especially spread for medical signals such as electrocardiographic data (Jalaleddine et al., 1990, Olmos et al., 1996). Apart from signal compression, K-L expansion has been successfully applied to signal de-noising, thanks to its capability of spectrally separating the noise content (Algazi and Sakrison, 1969). Such property has been used to retrieve multichannel signals measured by a sensor array (such as a radar in Wax and Kailath, 1985). This same property is exploited in Chapter 3 for a signal de-noising method for Particle Image Velocimetry (PIV) applications developed by the author of this dissertation (Raiola et al., 2015).

In its very first applications, the PCA has been applied to the analysis of random variables (see, e.g. Papoulis, 1965), becoming in modern days a standard tool for multivariate analysis of stochastic processes (Jolliffe, 2002). One of the main advantages of PCA is that it does not require an *a priori* probability model of the variable under study (Tipping and Bishop, 1999), thus it is of straightforward application without requiring further efforts on the user side (apart from the interpretation of the results, of course).

PCA revealed to be very effective in the analysis of video images. This technique has been largely employed for the decomposition of human faces features (Kirby and Sirovich, 1990), and it is commonly applied to face recognition problems in computer vision (Turk and Pentland, 1991). PCA of video images is employed also for video element segmentation, for example to extract a fixed background and moving objects (see e.g. Li et al., 2004). Based on these results, a method to remove the background from PIV images has been developed (Mendez et al., 2017). Chapter 4 reports the theoretical model of the PIV video sequence decomposition, on which the method is based, and shows the significant particle image quality improvement obtained with the method.

With the recent advances of data technology and the availability of both large datasets and computational power, the presence of PCA has become even more ubiquitous. Its use is now widespread in a number of different data mining tasks (Berry et al., 1995, Korn et al., 1998, Kleinberg, 1999). Azar et al. (2001) reports several uses of SVD in *Latent Semantic Indexing* (for retrieval of information from documents) and in *Collaborative Filtering* (i.e. automatic research suggestions based on other users experience). The use of this technique as a spectral filter is attested also in sensitive fields (such as the privacy preserving data mining) to recover information covered with random noise (on purpose, for privacy preservation) (Kargupta et al., 2003, Guo et al., 2006).

The above list of PCA applications is not meant to be in any way exhaustive. Nonetheless the variety of applications reported here is indicative of the flexibility and robustness of this tool.

1.4 Empirical eigenfunctions in Fluid Mechanics

POD has been first introduced in fluid flows investigation by Lumley (1967) as a mathematical technique which objectively defines coherent structures in turbulent flows without relying on event-based definitions. According to the decomposition proposed by Lumley, the *empirical eigenfunctions* were obtained as the eigenfunctions of the two-point spatial correlation matrix of the velocity field. It must be pointed out that each entry of the two-point spatial correlation matrix was obtained by means of a synchronous two-point hotwire measurement. Consequently, different entries were temporally uncorrelated. The large scale coherent structures in the flow can be detected as the most energetic spatial modes, i.e. the ones which mostly contribute in terms of variance to the ensemble. In this sense, the POD spectrum is "optimum", i.e. the variance in the POD-defined space decays faster than in any other vectorial space.

Initially Lumley's work was received sceptically by the turbulence community. The main concern was that *empirical eigenfunctions* were simply second-order statistics, thus phase information was lost in the decomposition (even though it can be recovered in certain conditions, as it will be shown in Chapter 5). Most of the earlier work on the topic was therefore carried out by Lumley himself and by his students (Bakewell and Lumley, 1967, Payne and Lumley, 1967). Nearly 20 years after the first Lumley's publication on the topic, the POD started to attract the interest of the turbulence community. Moin and Moser (1989) applied POD for the decomposition of one-, two- and three-dimensional flow in a turbulent channel. Differently from previous works, the two-point spatial correlation tensor was obtained from DNS data. POD was used to extract the characteristic eddies, while a shot-noise expansion (Lumley, 1981) was used in order to determine their phase.

Sirovich (1987) introduced a computationally efficient method for the POD modes calculation based on a set of *snapshots* of the flow field, i.e. multi-point simultaneous measurements of the flow field. POD modes are calculated as the projection of the flow field on the eigenfuctions of the temporal two-point correlation matrix. The method, defined *snapshot method*, is especially suited for field measurements, such as those from Particle Image Velocimetry (PIV) and numerical simulation results, both providing snapshots of the flow field on an eulerian grid for a limited number of frames. In case the number of grid points is larger than the number of snapshots, the snapshot method is more computationally efficient than the classic method from Lumley (1967), since the temporal correlation matrix is significantly smaller than the spatial correlation matrix.

Aubry et al. (1991) pointed out that the POD, in a bi-orthogonal decomposition approach, recovers two sets of modes which are orthogonal both in space and time. The two set of modes (named *chronoi* and *topoi* after the Greek words for time and space) have a one-to-one correspondence between them, i.e. each POD mode in space is connected to a temporal evolution defined by the temporal mode. The eigenvalues associated to the spatio-temporal couples of modes are representative of the spatio-temporal kinetic energy contained in the modes. The work from Aubry et al. (1991) allowed to use the POD as a tool to study the spatio-temporal non-linear dynamics of turbulent flows and extract both linear and non-linear instabilities. The bi-orthogonal approach is different from the approach by Sirovich or Lumley in the sense that a single realization of the flow field, varying both in space and time, is used in the decomposition. This advance was indeed connected to the increased availability of simultaneous data at different locations (e.g. obtained by means of PIV, by means of rakes of hotwires or by means of high-fidelity simulations).

An interesting application of the POD is its use as filtering technique. While most of the previous studies focused on the POD eigenfunction as a means to describe the characteristic eddies in the flow, Liu et al. (2001) applied the POD to project the flow field in a energy-aligned basis. This technique has been applied to PIV measurements of a turbulent channel flow. A low-pass filtered version of the flow field is obtained by retaining only the most energetic modes in the reconstruction, i.e. the first POD modes. Owing to the energy spectral distribution of turbulent flows, this low-order reconstruction process retains prevalently the large scale features in the flow, which carry the bulk of the energy. Wu and Christensen (2010) applied a similar approach to study the effect of irregular roughness in a turbulent boundary layer. The POD was applied on a PIV measurements ensemble as a spectral filter in order to separate the content due to large scale structures from the content due to small scale structures. Similarly to Liu et al. (2001), the selection of the threshold for the low-order reconstruction is based on a turbulent kinetic energy criterion. The comparison of the POD filtered fields in the smooth wall case and in the rough wall case was used to prove that large scales are affected spatially by the roughness, while small scales are relatively insensitive to it.

Owing to its capabilities to deal with both linear and non-linear instability, the POD has been also largely applied on free shear flows. Particularly rewarding is its use in case of spectrally-sparse instabilities. Some examples are the wake behind bluff bodies which shed von Kármán vortices (see e.g. Deane et al., 1991, for the wake of a circular cylinder) or turbulent jets developing ring vortices (see e.g. Glauser et al., 1989). The presence of a distinct signature of a certain frequency in the energy spectrum allows to extract phase information also from non-time-resolved measurements. An example is given in Perrin et al. (2007), which reconstructed the phase-average of the vortex shedding from a circular cylinder. Feng et al. (2011) applied the POD to 2D-PIV measurements in the wake of a circular cylinder with synthetic jet control located in the rear stagnation point. The decomposition allowed the identification of the shedding from the cylinder and its modification in terms of frequency and spatio-temporal organization for different jet actuations. For the first time on 3D experimental data Ceglia et al. (2014) applied phase-extraction techniques from POD to obtain a low-order model of the helical vortex instabilities in a turbulent swirling jet.

The POD has been also widely exploited to reduce the dimensionality of fluid problems, both to simplify the results interpretation and to reduce computational cost. In this approach the original differential equation governing the problem can be projected by means of the Galerkin method onto a truncated POD basis. The solution of the projected problem relies only on the resolved modes (which are included in the truncation) while higher order modes (which have been discarded in the truncation) are considered irrelevant for the solution of the flow dynamics. Rodriguez and Sirovich (1990) applied this approach for the solution of the Ginzburg-Landau equation. Chambers et al. (1988) applied POD for the solution of the Burgers' equation in turbulence problems. Rowley et al. (2004) extended this approach to compressible flows. The advantage of the Galerkin projection is indeed that the solution of the problem can be found in a lower dimensional space than the original problem. The number of modes to retain, however, is a parameter that strongly depends on the problem and on the user experience. For (spectrally) complex problems, the required number of modes can be large, thus reducing the computational advantage with respect to a complete simulation. In order to increase the computational advantage of this approach, the Galerkin projection method can be modified in order to include a specific model for the modes which are not included in the truncation. The solution to the problem would therefore still indirectly account for the excluded modes (through the model) while only the modes included in the truncation are effectively solved numerically. This approach has the advantage of not requiring a large number of modes to correctly solve the dynamics, thus can be more effective in reducing its dimensionality than a pure Galerkin projection. Some examples can be found in Aubry et al. (1988) for large scale structures in a turbulent boundary layer or in Glauser et al. (1989) for large scales in a jet mixing layer.

Several modifications of the POD have been proposed to extend its capabilities. Here some relevant examples are reported, namely the Extended POD, the Balanced POD and the Spectral POD. Maurel et al. (2001) first introduced the Extended POD (EPOD) to analyse the correlation between local and global events in a locally-significant POD basis. Borée (2003) formalized the EPOD as an extension of the Linear Stochastic Estimation (LSE) in the POD spectral basis. As noticed by Borée (2003), in a previous work by Picard and Delville (2000) the EPOD was implicitly applied to extrapolate a set of velocity modes which were statistically correlated to the POD modes of the pressure field. In their work, Picard and Delville (2000) showed that there is a physical correspondence between the pressure modes and the estimated velocity modes. The estimated velocity modes have been employed to solve the Lighthill's equation, obtaining interesting results for the far-field noise. Rowley (2005) proposed the Balanced POD (BPOD) algorithm which incorporates elements of control theory (i.e. the balanced truncation) in the POD. The BPOD modes represent the most controllable/observable directions of the dynamic system under analysis. The dataset used for this method is generally quite more specific than for POD as it is composed of the linear response of the system to impulsive inputs and of the impulsive responses of an adjoint system. Due to the requirement of an adjoint system, BPOD is generally not suited for experimental measurements. In this case the Eigensystem Realization Algorithm (ERA) represents an alternative and equivalent decomposition with respect to the BPOD (see e.g. Brunton et al., 2013, for experimental measurements on a flapping wing). Sieber et al. (2016) introduced the Spectral POD to bridge the gap between Fourier decomposition and POD. The Spectral POD is based on the consideration that the eigenfunctions of the covariance matrix coincide with a Fourier expansion when the covariance is calculated in an homogeneous direction. In case of homogeneous direction, the covariance matrix is constant in its main diagonal direction. Sieber et al. (2016) proposed to filter the matrix in this direction before applying the POD algorithm: the filtering parameters constitute therefore a tuning knob to pass from the standard POD (no filtering on the covariance matrix) to the Fourier decomposition (covariance matrix constant along the diagonal). The Spectral POD by Sieber et al. (2016) should not be confused with the POD performed in the frequency domain as described in the early works by Lumley (1967, 1970), and recently linked to DMD by Towne et al. (2017).

1.5 Motivation and outline of the work

As discussed in the previous paragraphs, the POD is now widely accepted to model the complex behaviour of unsteady flows. Even more recent techniques which are gaining popularity in the Fluid Mechanics community can be considered as extensions of the POD (such as the BPOD and the Spectral POD) or make extensive use of the POD (see e.g. the DMD algorithm, Schmid, 2010). The ease in its implementation, its robustness to errors and its (relatively) low technical requirements makes the POD a very valuable technique to be used in many contexts.

In this work, the use of the POD both as a tool for signal processing and as tool to model flow dynamics will be discussed. After a brief introduction to the mathematical properties of the POD contained in Part I, the discussion is organized in three other parts.

Part II focuses on novel contributions of the author to (mainly, but not restricted to) Particle Image Velocimetry measurement technology. As discussed above, in signal processing, the POD is exploited to spectrally separate a spatially/temporally coherent component of the signal from a random component. Two different applications to PIV are discussed. In the first one, POD is applied to an ensemble of velocity fields measured with PIV to remove the random component of the measurement noise. An optimal threshold is identified to provide the best estimation of the signal. In the second application, POD is applied to raw PIV images in order to identify the time-varying background and reflections and separate them from the particles. The removal of the background from the raw PIV images allows to enhance the correlation between the particles and thus significantly reduce the measurement uncertainty. While these applications are specifically developed for PIV, their extension to different signal sources is straightforward. Noise-filtering via POD can be used, for instance, to improve the quality of IR temperature measurements for convective heat transfer measurements (Raiola et al., 2017). Eigenbackground removal can find extensive application in imaging-based techniques (Pressure-Sensitive Paint, Temperature-Sensitive Paint, schlieren, etc.).

In Part III, POD is exploited to extract flow features from unsteady flow fields and to model the flow dynamics in compact form. The first application of POD as a flow analysis tool is the turbulent wake of two circular cylinders in tandem configuration in cross flow near a wall. The instabilities which arise in this flow are extremely sensitive to the geometrical arrangement of the cylinders, i.e. cylinder spacing and gap between the cylinders and the wall. Depending on the selected geometrical parameters, it is possible to pass from the typical von Kármán vortex shedding of bluff-body wakes to more spectrally rich flow instabilities. The second case is the flow around a flapping airfoil in forward flight. This flow is mainly dominated by concentrated vortices over the wing which arise due to the flapping motion. These vortices largely contribute to the generation of the aerodynamic forces applied to the wing. The aim of this study is to model both the flow behaviour and the aerodynamic forces. In order to achieve this result, a more elaborated decomposition approach is employed. Both flow fields and forces are expressed in a body-fixed reference frame, which represents a more natural choice for the evolution of the vortices on the wing. The relation between the modal decomposition of the flow and the aerodynamic forces is accounted for through the Extended POD (Borée, 2003). Through this decomposition it is finally possible to analyse the force generation on the wing and modify accordingly the existing force models already present in the literature.

Finally, in Part IV it is described an application of POD and EPOD for the dynamic estimation of time-resolved turbulent flow fields from non-time-resolved flow field measurements and time-resolved point measurements. The method relies on the correlation between field measurements and point measurements which can be evaluated through a modified EPOD approach. The correlation can be then extended to the estimate of the time-resolved flow fields thanks to the temporal information contained in the point measurements. The EPOD employed for this method requires a statistical truncation which allows to exclude the errors due to uncorrelated signals and thus obtain a more robust estimation.

Chapter 2

Mathematical framework

The term *modal decomposition* refers to a set of mathematical techniques which aims to give a description in terms of *modes* of a varying phenomenon; in the specific field of Fluid Mechanics, these modes aim to describe a flow-related quantity, varying dynamically both in time and space. This chapter will focus on the Proper Orthogonal Decomposition (POD), introduced with a historical perspective in the previous chapter. The general mathematical framework of POD will be described, following the bi-orthogonal approach by Aubry (1991), which is perhaps the most common approach employed nowadays. The main properties of this decomposition will be formally derived. Moreover, one of the extensions of this technique, the Extended POD (Borée, 2003), will be introduced along with its main properties. The mathematical foundations of the POD, introduced in this chapter, are necessary to build up a framework for the applications included in the remainder of the thesis.

2.1 Proper Orthogonal Decomposition

The Proper Orthogonal Decomposition is a mathematical procedure which aims to identify a set of orthonormal functions which best correlate on average with a set of observations. Each observation can be either an experimental measurement or a numerical solution of a scalar or vector field (such as velocity, vorticity, temperature etc.) at different time instants (or different physical parameters). For continuous problems, the functions are estimated as the solution of the Fredholm equation, which is an integral eigenvalue problem (for a more rigorous formulation see Berkooz et al., 1993).

In the following, the bi-orthogonal decomposition by Aubry et al. (1991) will be adopted, i.e. it will be considered a single realization of the dynamical system varying both in space and time. This approach fits very well with the applications presented in this thesis, in which a set of spatially-resolved realizations (either of velocity vector fields or raw images) is sampled in time. Suppose that a vector field $\underline{\mathcal{A}}(\underline{x}, t)$ is approximated by:

$$\underline{\mathcal{A}}(\underline{x}, t) = \langle \underline{\mathcal{A}}(\underline{x}, t) \rangle + \underline{a}(\underline{x}, t) \approx \langle \underline{\mathcal{A}}(\underline{x}, t) \rangle + \sum_{i=1}^{n_m} \psi^{(i)}(t) \sigma^{(i)} \underline{\phi}^{(i)}(\underline{x}) \tag{2.1}$$

Without any loss of generality, let $\underline{x}$ and t be the space and time coordinates, respectively. The symbols $\langle \underline{\mathcal{A}}(\underline{x}, t) \rangle$ and $\underline{a}(\underline{x}, t)$ indicate the ensemble average and the fluctuating part of the vector field $\underline{\mathcal{A}}(\underline{x}, t)$, respectively; the set of functions $\underline{\phi}^{(i)}(\underline{x})$ constitutes the spatial decomposition basis of the fluctuating velocity field; the functions $\psi^{(i)}(t)$ constitute the temporal basis; $\sigma^{(i)}$ is the norm associated to each spatio-temporal mode; the symbol n_m indicates the number of modes. The relation in Eq. 2.1 becomes an equality for $n_m \to \infty$.

The solution for the decomposition in Eq. 2.1 is not unique, as it depends on the chosen set of basis functions. In the classic implementation by Lumley (1967), the POD aims to maximize the correlation between the vector field and a space domain function $\underline{\phi}^{(i)}(\underline{x})$, i.e. it aims to maximize the projection of $\underline{a}(\underline{x}, t)$ on the function $\underline{\phi}^{(i)}(\underline{x})$:

$$\left\langle \int_\Omega \left(\underline{a}(\underline{x}, t), \underline{\phi}^{(i)}(\underline{x}) \right) d\underline{x} \right\rangle = \max_{\|\underline{f}(\underline{x})\|^2=1} \left\langle \int_\Omega \left(\underline{a}(\underline{x}, t), \underline{f}(\underline{x}) \right) d\underline{x} \right\rangle \tag{2.2}$$

with $(\cdot, \cdot)$ being the scalar product and $\| \cdot \|^2 = \int_\Omega (\cdot, \cdot) d\underline{x}$ being the L^2 norm in space. The integral in Eq. 2.2 is extended to the entire observation domain Ω. The choice of the functions $\underline{\phi}^{(i)}(\underline{x})$ is limited to functions with unitary norm. Moreover, the functions $\underline{\phi}^{(i)}(\underline{x})$ are subjected to an orthogonality constraint:

$$\left\langle \int_\Omega \left(\underline{\phi}^{(i)}(\underline{x}), \underline{\phi}^{(j)}(\underline{x}) \right) d\underline{x} \right\rangle = \delta_{i,j} \tag{2.3}$$

where $\delta_{i,j}$ is the Kronecker delta symbol. It can be shown that this problem is equivalent to find the solution of the Fredholm equation:

$$\int_\Omega R_s(\underline{x}, \underline{x}') \underline{\phi}^{(i)}(\underline{x}')\, d\underline{x}' = |\sigma^{(i)}|^2 \underline{\phi}^{(i)}(\underline{x}) \tag{2.4}$$

with $R_s(\underline{x}, \underline{x}')$ being the two-point spatial correlation tensor:

$$R_s(\underline{x}, \underline{x}') = \langle (\underline{a}(\underline{x}, t), \underline{a}(\underline{x}', t)) \rangle \tag{2.5}$$

An alternative implementation (especially popular in the field of Fluid Mechanics for both PIV measurements and DNS) is the *snapshot method* (Sirovich, 1987) as discussed in §1.4. The basis chosen in this implementation is the one maximizing the projection of $\underline{a}(\underline{x}, t)$ on the time domain function $\psi^{(i)}(t)$:

$$\left\langle \|\underline{a}(\underline{x}, t)\psi^{(i)}(t)\|^2 \right\rangle = \max_{\langle |f(t)|^2 \rangle = 1} \left\langle \|\underline{a}(\underline{x}, t) f(t)\|^2 \right\rangle \tag{2.6}$$

The choice of the set of function $\psi^{(i)}(t)$ is limited to functions with unitary norm and respecting the orthogonality constraint:

$$\left\langle \psi^{(i)}(t)\psi^{(j)}(t) \right\rangle = \delta_{i,j} \tag{2.7}$$

The Fredholm equation for this problem is given by:

$$\int_T R_t(t, t')\psi^{(i)}(t')dt' = |\sigma^{(i)}|^2 \psi^{(i)}(t) \tag{2.8}$$

with $R_t(t, t')$ being the two-point temporal correlation tensor:

$$R_t(t, t') = \frac{\displaystyle\int_\Omega \left(\underline{a}(\underline{x}, t), \underline{a}(\underline{x}, t')\right) d\underline{x}}{\displaystyle\int_\Omega d\underline{x}} \tag{2.9}$$

The integral in Eq. 2.8 is extended to the entire observation time T.

From Eq. 2.8, the temporal basis is composed by the eigenfunctions of the spatially averaged temporal correlation operator. From Eq. 2.4, the spatial basis is composed by the temporally averaged spatial correlation operator. Due their intrinsic temporal and spatial nature, the elements of the temporal basis are also known as *chronoi*, while the elements of the spatial basis are known as *topoi* (Aubry et al., 1991). The bi-orthogonal approach by Aubry et al. (1991) discloses the possibility to extract a spatio-temporal modal decomposition, which is optimal according to the L^2 norm. It should be remarked that no assumption on the statistical property of the signal, such as ergodicity or statistical stationarity, is required in the implementation by Aubry et al. (1991) In the work by Lumley (1967) additional hypothesis on the flow were required since the two-point correlation matrix was built from uncorrelated measurements.

2.1.1 Discrete Proper Orthogonal Decomposition

The datasets produced by experiments or simulations are most often in discrete form, i.e. on a spatial grid and over a set of instantaneous realizations. For this reason, a discrete formulation of the POD is needed. The discrete formulation of the POD can be straightforwardly rewritten using matrix notation. Let the dataset be composed of n_t temporal realizations, each one containing n_p point measurements. Following the bi-orthogonal approach (Aubry et al., 1991), the dataset may be composed of the values assumed by a scalar field at n_t different times in n_p different spatial points. Without accounting for the relative position of the spatial points, each realization can be reshaped in a row vector $\underline{a}^{(j)} \in \mathbb{R}^{1\times n_p}$. The dataset can be organized in a rectangular matrix $\underline{\underline{A}} \in \mathbb{R}^{n_t\times n_p}$ with rank $r \leq \min(n_t, n_p)$:

$$\underline{\underline{A}} = \begin{bmatrix} \underline{a}^{(1)} \\ \underline{a}^{(2)} \\ \vdots \\ \underline{a}^{(n_t)} \end{bmatrix} \in \mathbb{R}^{n_t\times n_p} \tag{2.10}$$

In the classical implementation of the discrete POD problem, the Fredholm equation is equivalent to the eigenvalue problem of the two-point spatial correlation matrix of $\underline{\underline{A}}$ (obtained through the inner product matrix $\underline{\underline{A}}^T\,\underline{\underline{A}} \in \mathbb{R}^{n_p\times n_p}$):

$$\underline{\underline{A}}^T\,\underline{\underline{A}}\,\underline{\underline{\Phi}} = \underline{\underline{\Phi}}\,\underline{\underline{\Lambda}} \tag{2.11}$$

with $\underline{\underline{\Lambda}} = diag(\lambda^{(1)}, \dots, \lambda^{(r)}) \in \mathbb{R}^{r\times r}$ containing the set of eigenvalues and $\underline{\underline{\Phi}} = \left[\underline{\phi}^{(1)}, \dots, \underline{\phi}^{(r)}\right] \in \mathbb{R}^{n_p\times r}$ containing the set of eigenvectors of $\underline{\underline{A}}^T\,\underline{\underline{A}}$.

In the *snapshots* implementation of the discrete POD problem, the Fredholm equation is equivalent to the eigenvalue problem of the two-point temporal correlation matrix (obtained through the outer product matrix $\underline{\underline{A}}\,\underline{\underline{A}}^T \in \mathbb{R}^{n_t\times n_t}$):

$$\underline{\underline{A}}\,\underline{\underline{A}}^T\underline{\underline{\Psi}} = \underline{\underline{\Psi}}\,\underline{\underline{\Lambda}} \tag{2.12}$$

with $\underline{\underline{\Psi}} = \left[\underline{\psi}^{(1)}, \dots, \underline{\psi}^{(r)}\right] \in \mathbb{R}^{n_t\times r}$ containing the set of eigenvectors of $\underline{\underline{A}}^T\,\underline{\underline{A}}$.

Since both $\underline{\underline{A}}^T\,\underline{\underline{A}}$ and $\underline{\underline{A}}\,\underline{\underline{A}}^T$ are non-negative Hermitian matrices, they have a complete set of non-negative eigenvalues equal to their rank r. The solution of both Eq. 2.11 and Eq. 2.12 is given by:

$$\underline{\underline{A}} = \underline{\underline{\Psi}}\,\underline{\underline{\Sigma}}\,\underline{\underline{\Phi}}^T = \sum_{i=1}^{r} \underline{\psi}^{(i)}\sigma^{(i)}\underline{\phi}^{(i)\,T} \tag{2.13}$$

with $\underline{\underline{\Phi}}$ being the orthonormal basis for the rows of $\underline{\underline{A}}$, $\underline{\underline{\Psi}}$ the orthonormal basis for the columns of $\underline{\underline{A}}$, and $\underline{\underline{\Sigma}} = diag\left(\sigma^{(1)}, \dots, \sigma^{(r)}\right) \in \mathbb{R}^{r\times r}$ the diagonal matrix containing the norm of each contribution. The orthogonality condition imposed to the components of the columns and rows basis leads to $\underline{\psi}^{(i)\,T}\underline{\psi}^{(j)} = \delta_{i,j}$ and $\underline{\phi}^{(i)\,T}\underline{\phi}^{(j)} = \delta_{i,j}$ and thus to:

$$\begin{aligned} \underline{\underline{\Psi}}^T \underline{\underline{\Psi}} &= \underline{\underline{I}}_r \\ \underline{\underline{\Phi}}^T \underline{\underline{\Phi}} &= \underline{\underline{I}}_r \end{aligned} \tag{2.14}$$

with $\underline{\underline{I}}_r$ being the identity matrix with rank r.

The different arrangements of the discrete Fredholm equation expressed in Eq. 2.11 and 2.12 demonstrate that the classical implementation of the POD (Lumley, 1970) is preferable when $n_p < n_t$ (which is the typical case for hotwire measurements) while the *snapshot* POD implementation (Sirovich, 1987) is preferable when $n_t < n_p$ (which is the most common case in velocity fields obtained by means of PIV measurements or numerical simulations).

When decomposing a discrete scalar field, the columns of $\underline{\underline{\Psi}}$ are the temporal modes (or *chronoi*) $\psi^{(i)}(t)$ and the rows of $\underline{\underline{\Phi}}$ are the spatial modes (or *topoi*) $\phi^{(i)}(\underline{x})$. The set of singular values $\underline{\underline{\Sigma}}$ is equal to the square root of the eigenvalues $\underline{\underline{\Lambda}}$ from Eq. 2.11 and Eq. 2.12, as shown by:

$$\begin{aligned} \underline{\underline{A}}^T\,\underline{\underline{A}} &= \left(\underline{\underline{\Phi}}\,\underline{\underline{\Sigma}}\,\underline{\underline{\Psi}}^T\right)\left(\underline{\underline{\Psi}}\,\underline{\underline{\Sigma}}\,\underline{\underline{\Phi}}^T\right) = \underline{\underline{\Phi}}\,\underline{\underline{\Lambda}}\,\underline{\underline{\Phi}}^T \\ \underline{\underline{A}}\,\underline{\underline{A}}^T &= \left(\underline{\underline{\Psi}}\,\underline{\underline{\Sigma}}\,\underline{\underline{\Phi}}\right)\left(\underline{\underline{\Phi}}^T\,\underline{\underline{\Sigma}}\,\underline{\underline{\Psi}}^T\right) = \underline{\underline{\Psi}}\,\underline{\underline{\Lambda}}\,\underline{\underline{\Psi}}^T \end{aligned} \tag{2.15}$$

It is worth noting that the discrete POD as described above is formally equivalent to the reduced Singular Value Decomposition (SVD) of the matrix $\underline{\underline{A}}$ (Fahl, 2000), with $\sigma^{(i)}$, $\underline{\psi}^{(i)}$ and $\underline{\phi}^{(i)}$ being respectively the singular values (sorted in decreasing order), the left singular vectors and the right singular vectors.

2.1.2 Low-rank approximation

The scope of low dimensional modelling (or low-rank approximation) of a matrix $\underline{\underline{A}}$ is to find the approximation $\underline{\underline{A}}_{n_m} \in \mathbb{R}^{n_t \times n_p}$ of rank $n_m < r = \mathrm{rank}(\underline{\underline{A}})$ minimizing the Frobenius norm ($\|\cdot\|_F$) of the error matrix:

$$\|\underline{\underline{A}} - \underline{\underline{A}}_{n_m}\|_F = \min_{\mathrm{rank}(\underline{\underline{X}})=n_m} \left(\|\underline{\underline{A}} - \underline{\underline{X}}\|_F\right) . \tag{2.16}$$

The solution to this minimization problem, given by the Eckart-Young theorem (Eckart and Young, 1936), is the n_m-truncated SVD of the original matrix:

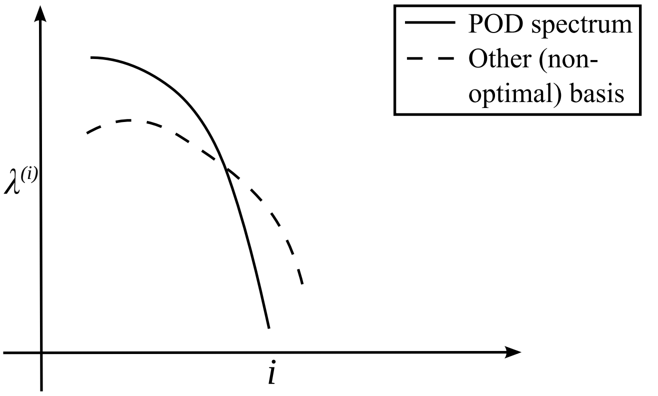

Fig. 2.1 POD spectrum and another non-optimal basis spectrum for a dissipative system. Adapted from Berkooz et al. (1993).

$$\underline{\underline{A}}_{n_m} = \underline{\underline{\Psi}}_{n_m} \underline{\underline{\Sigma}}_{n_m} \underline{\underline{\Phi}}^T_{n_m} = \sum_{i=1}^{n_m} \underline{\psi}^{(i)} \sigma^{(i)} \underline{\phi}^{(i)\,T} \tag{2.17}$$

with $\underline{\underline{\Phi}}_{n_m} = \left[\underline{\phi}^{(1)}, \dots, \underline{\phi}^{(n_m)}\right] \in \mathbb{R}^{n_p \times n_m}$ being the orthonormal basis for the columns of $\underline{\underline{A}}$, $\underline{\underline{\Psi}}_{n_m} = \left[\underline{\psi}^{(1)}, \dots, \underline{\psi}^{(n_m)}\right] \in \mathbb{R}^{n_t \times n_m}$ being the orthonormal basis for the rows of $\underline{\underline{A}}$, and $\underline{\underline{\Sigma}}_{n_m} = diag(\sigma^{(1)}, \dots, \sigma^{(n_m)}) \in \mathbb{R}^{n_m \times n_m}$ being the diagonal matrix containing the norm of each contribution. The orthonormality of these bases ensures that the error in Eq. 2.16 is minimal and that the decomposition is exact ($\|A - A_{n_m}\|_F = 0$) for $n_m = r$. Each of the modal contributions $\underline{\psi}^{(i)} \sigma^{(i)} \underline{\phi}^{(i)\,T}$ is a rank one *component* of the original matrix, having optimal and sorted norm $\sigma^{(i)} > \sigma^{(i+1)}\, \forall i \in [1, r-1]$.

Alternatively, the truncated reconstruction of rank n_m can be expressed as:

$$\underline{\underline{A}}_{n_m} = \underline{\underline{\Psi}} \begin{pmatrix} \underline{\underline{I}}_{n_m} & 0 \\ 0 & 0 \end{pmatrix} \underline{\underline{\Sigma}}\, \underline{\underline{\Phi}}^T \tag{2.18}$$

with $\underline{\underline{I}}_{n_m}$ being a rank n_m identity matrix with $n_m < r$.

Observing that $\underline{\underline{A}}\, \underline{\underline{\Phi}}_{n_m} = \underline{\underline{\Psi}}_{n_m} \underline{\underline{\Sigma}}_{n_m}$, Eq. 2.17 can be also written as:

$$\underline{\underline{A}}_{n_m} = \underline{\underline{A}}\, \underline{\underline{\Phi}}_{n_m} \underline{\underline{\Phi}}^T_{n_m} \tag{2.19}$$

This form of the equation, with no emphasis on the temporal evolution of the modes, describes the decomposition as the projection of the data set (of rank r) into a lower dimensional space (of rank $n_m < r$) spanned by the orthonormal basis $\underline{\underline{\Phi}}_{n_m} = \left[\underline{\phi}^{(1)}, \dots, \underline{\phi}^{(n_m)}\right]$. This formulation is common in Principal Component Analysis (Pearson, 1901, Hotelling, 1933, Jolliffe, 2002) where it is introduced in the framework of variance maximization or minimal error of the approximation matrix $\underline{\underline{A}}_{n_m}$ (Noy-Meir, 1973, Bishop, 2006, Miranda et al., 2008).

The minimization problem exposed in Eq. 2.16 sets the basis of the optimality property of the Proper Orthogonal Decomposition. According to this property the truncated POD of rank n_m is the best possible representation of rank n_m of the original matrix according to the Frobenius norm, meaning that it will achieve the minimum reconstruction error amongst all the possible representations. Due to this property the spectral representation of the original dataset obtained from the POD basis will always decay faster or at least with the same rate of the spectrum in another non-optimal basis, such as, for instance, the Fourier spectrum. This concept is well represented in Fig. 2.1, adapted from Berkooz et al. (1993).

2.2 POD and random noise

Measurements are usually corrupted by noise, which may pose a limit to most of the analysis techniques to extract meaningful information. The POD, thanks to its spectral optimality, can be generally considered quite robust with respect to random errors. In the following, the effect of random noise on the POD will be analysed. The fluctuating part of the measured data ensemble $\underline{\underline{A}}$ can be decomposed into the sum of a random error part $\underline{\underline{E}}$ and an objective function $\underline{\underline{\tilde{A}}}$. From now on, symbols unsigned refer to measured quantities, while symbols signed with a tilde refer to objective function quantities. The objective function $\underline{\underline{\tilde{A}}}$ is not necessarily the unperturbed measurement dataset, as it may be affected by bias errors. The measured dataset is:

$$\underline{\underline{A}} = \underline{\underline{\tilde{A}}} + \underline{\underline{E}} \tag{2.20}$$

Therefore, the sample covariance matrix obtained from the outer product is:

$$\underline{\underline{A}}\,\underline{\underline{A}}^T = \underline{\underline{\tilde{A}}}\;\underline{\underline{\tilde{A}}}^T + \underline{\underline{\tilde{A}}}\,\underline{\underline{E}}^T + \underline{\underline{E}}\;\underline{\underline{\tilde{A}}}^T + \underline{\underline{E}}\,\underline{\underline{E}}^T \tag{2.21}$$

Eq. 2.21 can be simplified under the assumption that random errors are uncorrelated with the objective field (even though this might not always be the case). Considering a normally-distributed error with standard deviation ς_e, and provided that the number of vectors is sufficiently large, according to Huang et al. (2005), the sample covariance matrix is approximately equal to:

$$\underline{\underline{A}}\,\underline{\underline{A}}^T \approx \underline{\underline{\tilde{A}}}\,\underline{\underline{\tilde{A}}}^T + n_p \varsigma_e^2 \,\underline{\underline{I}}_{n_t} \tag{2.22}$$

For a non-Gaussian (but still independent and identically distributed) error the approximation is still valid when the matrix $\underline{\underline{A}}$ is rectangular, so that all the eigenvalues of $\underline{\underline{E}}\,\underline{\underline{E}}^T$ are with high probability in a neighborhood of ς_e (Marchenko and Pastur, 1967). This is formally equal to assume a spectrally-white distribution of the random error part in the eigenvalues of the covariance matrix.

Recalling that the POD solves the eigenproblem for the sample covariance matrix in both perturbed and unperturbed cases:

$$\begin{cases} (\underline{\underline{\widetilde{A}}}\,\underline{\underline{\widetilde{A}}}^T + n_p\varsigma_e^2\,\underline{\underline{I}}_{n_t} - \lambda^{(j)}\,\underline{\underline{I}}_{n_t})\underline{\psi}^{(j)} = 0 \\ (\underline{\underline{\widetilde{A}}}\,\underline{\underline{\widetilde{A}}}^T - \widetilde{\lambda}^{(j)}\,\underline{\underline{I}}_{n_t})\underline{\widetilde{\psi}}^{(j)} = 0 \end{cases} \tag{2.23}$$

It is possible to conclude that:

$$\begin{cases} \lambda^{(j)} \approx \widetilde{\lambda}^{(j)} + n_p\varsigma_e^2 \\ \underline{\psi}^{(j)} \approx \underline{\widetilde{\psi}}^{(j)} \end{cases} \Rightarrow \begin{cases} \underline{\underline{\Lambda}} \approx \underline{\underline{\widetilde{\Lambda}}} + n_p\varsigma_e^2\,\underline{\underline{I}}_{n_t} \\ \underline{\underline{\Psi}} \approx \underline{\underline{\widetilde{\Psi}}} \end{cases} \tag{2.24}$$

These relationships can be more accurately derived from matrix perturbation theory, along with their bounds, and are a common assumption in perturbed Principal Component Analysis (PCA) applications (Kargupta et al., 2003, Huang et al., 2005). This approximation is correct if the random errors are small with respect to the distance between two successive eigenvalues of $\underline{\underline{\widetilde{A}}}\,\underline{\underline{\widetilde{A}}}^T$ (Stewart, 2001, Kargupta et al., 2003, Venturi, 2006). The perturbation of the eigenvectors increases as $\widetilde{\lambda}$ approaches the value of ς_e.

2.2.1 Optimal low-rank approximation of noise-perturbed datasets

If we indicate with $\underline{\underline{A}}_{n_m}$ the reconstruction of the measured flow fields with the first n_m components, considering Eq. 2.18 and Eq. 2.20, the difference between the objective field and $\underline{\underline{A}}_{n_m}$ modes is:

$$\begin{aligned} \underline{\underline{\widetilde{A}}} - \underline{\underline{A}}_{n_m} &= \underline{\underline{\Psi}}\,\underline{\underline{I}}_{n_t}\,\underline{\underline{\Psi}}^T\,\underline{\underline{\widetilde{A}}} - \underline{\underline{\Psi}}\begin{pmatrix} \underline{\underline{I}}_{n_m} & \underline{\underline{0}} \\ \underline{\underline{0}} & \underline{\underline{0}} \end{pmatrix}\underline{\underline{\Psi}}^T(\underline{\underline{\widetilde{A}}} + \underline{\underline{E}}) \\ &= \underline{\underline{\Psi}}\begin{pmatrix} \underline{\underline{0}} & \underline{\underline{0}} \\ \underline{\underline{0}} & \underline{\underline{I}}_{n_t-n_m} \end{pmatrix}\underline{\underline{\Psi}}^T\,\underline{\underline{\widetilde{A}}} - \underline{\underline{\Psi}}\begin{pmatrix} \underline{\underline{I}}_{n_m} & \underline{\underline{0}} \\ \underline{\underline{0}} & \underline{\underline{0}} \end{pmatrix}\underline{\underline{\Psi}}^T\,\underline{\underline{E}} \end{aligned} \tag{2.25}$$

and considering Eq. 2.24 (again, assuming statistical independence between $\underline{\underline{\widetilde{A}}}$ and $\underline{\underline{E}}$):

$$\begin{aligned}
&(\underline{\underline{\widetilde{A}}} - \underline{\underline{A}}_{n_m})(\underline{\underline{\widetilde{A}}} - \underline{\underline{A}}_{n_m})^T \\
&\quad = \underline{\underline{\Psi}} \begin{pmatrix} \underline{\underline{0}} & \underline{\underline{0}} \\ \underline{\underline{0}} & \underline{\underline{I}}_{n_t - n_m} \end{pmatrix} \underline{\underline{\Psi}}^T \, \underline{\underline{\widetilde{A}}} \, \underline{\underline{\widetilde{A}}}^T \, \underline{\underline{\Psi}}^T \begin{pmatrix} \underline{\underline{0}} & \underline{\underline{0}} \\ \underline{\underline{0}} & \underline{\underline{I}}_{n_t - n_m} \end{pmatrix} \underline{\underline{\Psi}} \\
&\quad + \underline{\underline{\Psi}} \begin{pmatrix} \underline{\underline{I}}_{n_m} & \underline{\underline{0}} \\ \underline{\underline{0}} & \underline{\underline{0}} \end{pmatrix} \underline{\underline{\Psi}}^T \, \underline{\underline{E}} \, \underline{\underline{E}}^T \, \underline{\underline{\Psi}}^T \begin{pmatrix} \underline{\underline{I}}_{n_m} & \underline{\underline{0}} \\ \underline{\underline{0}} & \underline{\underline{0}} \end{pmatrix} \underline{\underline{\Psi}} \\
&\quad = \underline{\underline{\widetilde{\Psi}}} \begin{pmatrix} \underline{\underline{0}} & \underline{\underline{0}} \\ \underline{\underline{0}} & \underline{\underline{I}}_{n_t - n_m} \end{pmatrix} \underline{\underline{\widetilde{\Lambda}}} \, \underline{\underline{\widetilde{\Psi}}}^T + \underline{\underline{\widetilde{\Psi}}} \begin{pmatrix} \underline{\underline{I}}_{n_m} & \underline{\underline{0}} \\ \underline{\underline{0}} & \underline{\underline{0}} \end{pmatrix} n_p \varsigma_e^2 \, \underline{\underline{\widetilde{\Psi}}}^T
\end{aligned} \tag{2.26}$$

Exploiting the linearity and rotation invariance of the trace of a tensor:

$$\begin{aligned}
&\mathrm{Tr}\Big((\underline{\underline{\widetilde{A}}} - \underline{\underline{A}}_{n_m})(\underline{\underline{\widetilde{A}}} - \underline{\underline{A}}_{n_m})^T \Big) \\
&\quad = \mathrm{Tr}\left(\begin{pmatrix} \underline{\underline{0}} & \underline{\underline{0}} \\ \underline{\underline{0}} & \underline{\underline{I}}_{n_t - n_m} \end{pmatrix} \underline{\underline{\widetilde{\Lambda}}} \right) + \mathrm{Tr}\left(\begin{pmatrix} \underline{\underline{I}}_{n_m} & \underline{\underline{0}} \\ \underline{\underline{0}} & \underline{\underline{0}} \end{pmatrix} n_p \varsigma_e^2 \right) \\
&\quad = \sum_{i=n_m+1}^{n_t} \widetilde{\lambda}^{(i)} + \sum_{i=1}^{n_m} n_p \varsigma_e^2 = \sum_{i=n_m+1}^{n_t} \widetilde{\lambda}^{(i)} + n_m n_p \varsigma_e^2
\end{aligned} \tag{2.27}$$

Using the Frobenius norm, we define the reconstruction error δ_{RT} with respect to the objective function as:

$$\begin{aligned}
\delta_{RT}(n_m) &= \left(\frac{1}{n_t n_p} \right)^{\frac{1}{2}} \left\| \underline{\underline{\widetilde{A}}} - \underline{\underline{A}}_{n_m} \right\|_F \\
&= \left(\frac{1}{n_t n_p} \mathrm{Tr}\left((\underline{\underline{\widetilde{A}}} - \underline{\underline{A}}_{n_m})(\underline{\underline{\widetilde{A}}} - \underline{\underline{A}}_{n_m})^T \right) \right)^{\frac{1}{2}}
\end{aligned} \tag{2.28}$$

Substituting Eq. 2.27 into the error expression:

$$\delta_{RT}(n_m) = \left(\frac{1}{n_t n_p} \right)^{\frac{1}{2}} \left(\sum_{i=n_m+1}^{n_t} \widetilde{\lambda}^{(i)} + n_m n_p \varsigma_e^2 \right)^{\frac{1}{2}} \tag{2.29}$$

Due to the optimality property of the POD, the eigenspectrum $\widetilde{\lambda}^{(i)}$ decays faster than any other spectral representation of the data ensemble. This assures that if a spectral representation other than a white spectrum exists for the objective dataset, its eigenspectrum will be a strictly decreasing function of i with faster decay rate than in any other basis. Therefore a minimum of the reconstruction error δ_{RT} exists according to Eq. 2.29, meaning that there would exist an optimal value $n_m^\star$ for which $\underline{\underline{A}}_{n_m}(n_m^\star)$

is the best approximation of $\underline{\underline{\widetilde{A}}}$. This concept can be straightforwardly applied to filter out the noise content from a database, in the same fashion of a low-pass filter. Further insight will be given in Chapter 3, where optimal flow-feature-oriented filtering will be applied to velocity field measurements obtained by means of PIV.

2.3 POD and modelling of non-time-resolved flow field measurements

When dealing with experimental or numerical data, most often the POD is applied to fluctuating velocity vector fields. In this case, according to the L^2 norm defined in §2.1, the squares of the singular values $\lambda^{(i)} = \sigma^{(i)\,2}$ measure the space-averaged contributions to the turbulent kinetic energy of each mode. It must be remarked that $\lambda^{(i)}$ is strictly the turbulent kinetic energy content of each mode only if a regularly spaced grid is considered for the flow field, otherwise a weight matrix should be added to Eq. 2.12. The optimality property of POD ensures that the most energetically relevant turbulent features are contained in the first modes and that the energy content of the modes rapidly decays as the number of modes increases. This last property is at the basis of an energy-optimal low-order reconstruction (LOR) of the velocity field snapshot matrix $\underline{\underline{A}}$ from the low-rank approximation derived from the POD (see §2.1.2).

In case of phenomenologies characterized by dominant periodic features (such as the wake shedding of a bluff body) the POD generally shows a quite clear spectral separation between first modes accounting for the dominant features and the small-scale turbulence. This spectral separation can be exploited to effectively extract periodic flow features (see e.g. Perrin et al., 2007). In case of temporal homogeneity of the features it is safe to assume that the first POD modes, apart from being orthogonal, might also align to a Fourier decomposition of the field and show a strong harmonic relation. Following Holmes et al. (1997), in case of temporal homogeneity of the flow, the two-point correlation matrix is a function of solely the temporal separation between two points, i.e. $R_t(t, t') = R_t(t - t')$. The eigenfunctions of this matrix coincide with the Fourier modes, i.e. $\psi^{(i)} = e^{\iota 2\pi f t}$ with ι being the imaginary unit. This can be verified by substituting the eigenfunction in the Fredholm eigenvalue problem in Eq. 2.8:

$$\begin{aligned}\int_\Omega R_t(t-t')\psi^{(i)}(t')dt' = \int_\Omega R_t(t-t')e^{\iota 2\pi f t'}dt' = \int_\Omega R_t(\Delta t)e^{\iota 2\pi f(t-\Delta t)}d\Delta t \\ = \left(\int_\Omega R_t(\Delta t)e^{-\iota 2\pi f \Delta t}d\Delta t\right)e^{\iota 2\pi f t} = |\sigma^{(i)}|^2 e^{\iota 2\pi f t}\end{aligned} \tag{2.30}$$

Hence $e^{\iota 2\pi f t}$ is an eigenfunction of $R_t(t-t')$ with eigenvalue $|\sigma^{(i)}|^2$ given by the Fourier transform of the spatially averaged covariance matrix.

Therefore, POD can be used to obtain phase information from non-time-resolved data and to extract a low-order model of the phenomenon. It is particularly relevant the case of convected flow features, such as the Kármán vortices shed in the wake of a bluff body or ring vortex developed due to shear-layer instabilities in submerged jets. In these cases the travelling instability is accounted by two high-energy modes (generally the first two modes). Both modes share the same periodicity, i.e. the shedding period τ, thus, according to the orthogonality of the POD *chronoi*, it is possible to assume that the POD would coincide with the following decomposition (Ben Chiekh et al., 2004, Ceglia et al., 2014):

$$\begin{aligned}\underline{\mathscr{A}}(\underline{x},t) = & \langle\underline{\mathscr{A}}(\underline{x})\rangle + b^{(1)}(\vartheta)\underline{\phi}^{(1)}(\underline{x}) \\ & + b^{(2)}(\vartheta)\underline{\phi}^{(2)}(\underline{x}) + \sum_{i=3}^{N_m} b^{(i)}(\vartheta)\underline{\phi}^{(i)}(\underline{x}).\end{aligned} \tag{2.31}$$

$$b^{(1)} = \sqrt{2\lambda^{(1)}}\sin(\vartheta), \quad b^{(2)} = \sqrt{2\lambda^{(2)}}\cos(\vartheta) \tag{2.32}$$

with $\vartheta = 2\pi t/\tau$ being the period phase. In order to verify that the first two modes represent the coherent harmonics related to the vortex shedding, the scatter plot of the coefficients normalized with their respective eigenvalues $b^{(1)}/\sqrt{2\lambda^{(1)}}$ and $b^{(2)}/\sqrt{2\lambda^{(2)}}$ should be observed in search of Lissajous figures. If the points distribute in the neighbourhood of a goniometric circle, the Eq. 2.31 is respected (Ben Chiekh et al., 2004, Ceglia et al., 2014).

In general, the scatter plot of the time coefficients might unlock information on the phase and frequency relation between higher order modes, thus shedding light on the interconnection between the different flow features highlighted by the modal analysis. Assuming that the higher-order POD modes are harmonically related and phase-shifted with respect to the 1st mode:

$$b^{(i)} = \sqrt{2\lambda^{(i)}}\sin(m^{(i)}\vartheta + \varphi^{(i)}) \tag{2.33}$$

where $m^{(i)}$ is a positive integer and $\varphi^{(i)}$ is the phase shift of the ith mode with respect to the first mode. The procedure to identify the harmonic relation and the phase shift for higher order modes relies on the simplifying assumption that the first 2 modes are at the same frequency with $\pi/2$ phase shift (as in Eq. 2.32). It is possible to extract the period phase from the time coefficient of the first two modes:

$$\tan(\vartheta) = \sqrt{\frac{\lambda^{(2)}}{\lambda^{(1)}}} \frac{b^{(1)}}{b^{(2)}} \tag{2.34}$$

Subsequently, the positive integer $m^{(i)}$ and the phase shift $\varphi^{(i)}$, that characterize the harmonic relation, can be extracted from the minimization problem in Eq. 2.35:

$$\min\left(\frac{b^{(i)}}{2\sqrt{\lambda^{(i)}}} - \sin(m^{(i)}\vartheta + \varphi^{(i)})\right) \tag{2.35}$$

in which $m^{(i)}$ and $\varphi^{(i)}$ are the free parameters to set.

An example of this procedure is given in Chapter 5, where it is applied to analyse the wake instabilities produced by different geometrical configuration of two tandem cylinders in cross-flow nearby a wall.

2.4 Extended Proper Orthogonal Decomposition

It has been mentioned above that the discrete POD in the snapshot method implementation solves the eigenvalue problem for the two-point temporal correlation matrix (Eq. 2.12). The eigenvectors $\underline{\underline{\Psi}}_A$ constitute the *chronoi* of the snapshot matrix $\underline{\underline{A}}$. According to the bi-orthogonal decomposition, the corresponding *topoi* $\underline{\underline{\Phi}}_A$ can be found by re-arranging Eq. 2.13 :

$$\underline{\underline{\Sigma}}_A \underline{\underline{\Phi}}_A^T = \underline{\underline{\Psi}}_A^T \underline{\underline{A}} \tag{2.36}$$

Eq. 2.36 expresses the POD *topoi* as the projection of the snapshot ensemble onto the *chronoi*. Apart being an easy implementation for the calculation of the *topoi* in the snapshot method, Eq. 2.36 can be used to extend the POD to other fluid quantities. This approach is generally named Extended POD (Borée, 2003).

The aim of the Extended POD is to draw a correlation between the flow features extracted from a given dataset $\underline{\underline{A}}$ and the flow features contained in a second dataset $\underline{\underline{B}}$. The only constraint imposed is that the datasets have to be captured/generated in the same time reference frame. The nature of the data contained and/or the spatial domain they span may instead be different. In general the two datasets will have different sizes, for example $\underline{\underline{A}} \in \mathbb{R}^{n_A \times n_t}$ and $\underline{\underline{B}} \in \mathbb{R}^{n_B \times n_t}$.

Following Eq. 2.36, the temporal basis $\underline{\underline{\Psi}}_A$ is used to project the dataset $\underline{\underline{B}}$:

$$\underline{\underline{\Sigma}}_B \underline{\underline{\Phi}}_B^T = \underline{\underline{\Psi}}_A^T \underline{\underline{B}} \tag{2.37}$$

where $\underline{\underline{\Sigma}}_B$ is a diagonal matrix containing the norm $\sigma_B^{(i)}$ of the projection of the dataset $\underline{\underline{B}}$ on each *chronos* of the dataset $\underline{\underline{A}}$, and each column of $\underline{\underline{\Phi}}_{B,n_m}$ is the ith *topos* $\underline{\phi}_B^{(i)}$ (with unitary norm) of the projection of $\underline{\underline{B}}$. The ith *topos* $\underline{\phi}_B^{(i)}$ is analogous to the ith extended POD mode (Maurel et al., 2001, Borée, 2003). Notice that the EPOD *topos* $\underline{\phi}_B^{(i)}$ here defined formally differ from the EPOD mode defined in Borée (2003), which is instead equivalent to $\underline{\phi}_B^{(i)} \sigma_B^{(i)} \sigma_A^{(i)\,-1}$.

2.4.1 Properties of the EPOD

Following both Eq. 2.17 and Eq. 2.37 it is possible to define also a truncated EPOD:

$$\underline{\underline{B}}_{n_m} = \underline{\underline{\Psi}}_{A,n_m} \underline{\underline{\Sigma}}_{B,n_m} \underline{\underline{\Phi}}_{B,n_m}^T = \underline{\underline{\Psi}}_A \begin{pmatrix} \underline{\underline{I}}_{n_m} & 0 \\ 0 & 0 \end{pmatrix} \underline{\underline{\Sigma}}_B \underline{\underline{\Phi}}_B^T \tag{2.38}$$

which represents the part of $\underline{\underline{B}}$ correlated with $\underline{\underline{A}}_{n_m}$. Therefore, the resulting decomposition of the dataset $\underline{\underline{B}}$ is given by:

$$\underline{\underline{B}} = \underline{\underline{\Psi}}_{A,n_m} \underline{\underline{\Sigma}}_{B,n_m} \underline{\underline{\Phi}}_{B,n_m}^T + \underline{\underline{R}} = \underline{\underline{B}}_{n_m} + \underline{\underline{R}} \tag{2.39}$$

where $\underline{\underline{R}}$ is the residual of the decomposition. It must be highlighted that the residual $\underline{\underline{R}}$ is necessarily equal to zero for $n_m = r$, since $\underline{\underline{\Psi}}_A$ is an orthonormal basis and $\underline{\underline{\Sigma}}_{B,n_m} \underline{\underline{\Phi}}_{B,n_m}^T$ would represent the matrix $\underline{\underline{B}}_{n_m}$ rotated in the new basis.

The following propositions, adapted from Borée (2003), are proven in the following for illustration purpose.

Proposition 1. *$\underline{\underline{B}}_{n_m}$ is the only part of $\underline{\underline{B}}$ which correlates with $\underline{\underline{A}}_{n_m}$.*

Proof. The cross-correlation tensor between the two datasets, according to Eq. 2.13 and to Eq. 2.37, can be written as:

$$\begin{aligned} \underline{\underline{A}}_{n_m}^T \underline{\underline{B}} &= \underline{\underline{\Phi}}_{A,n_m} \underline{\underline{\Sigma}}_{A,n_m}^{-1} \left(\underline{\underline{\Psi}}_{A,n_m}^T \underline{\underline{B}} \right) \\ &= \left(\underline{\underline{\Phi}}_{A,n_m} \underline{\underline{\Sigma}}_{A,n_m}^{-1} \right) \left(\underline{\underline{\Sigma}}_{B,n_m} \underline{\underline{\Phi}}_{B,n_m}^T \right) \end{aligned} \tag{2.40}$$

The cross-correlation between $\underline{\underline{A}}_{n_m}$ and $\underline{\underline{B}}_{n_m}$, according to Eq. 2.39 and to Eq. 2.14, is given by:

$$\begin{aligned} \underline{\underline{A}}^T_{n_m}\underline{\underline{B}}_{n_m} &= \left(\underline{\underline{\Phi}}_{A,n_m}\underline{\underline{\Sigma}}^{-1}_{A,n_m}\underline{\underline{\Psi}}^T_{A,n_m}\right)\left(\underline{\underline{\Psi}}_{A,n_m}\underline{\underline{\Sigma}}_{B,n_m}\underline{\underline{\Phi}}^T_{B,n_m}\right)\\ &= \left(\underline{\underline{\Phi}}_{A,n_m}\underline{\underline{\Sigma}}^{-1}_{A,n_m}\right)\left(\underline{\underline{\Sigma}}_{B,n_m}\underline{\underline{\Phi}}^T_{B,n_m}\right) \end{aligned} \tag{2.41}$$

Due to the linearity of the matrix product, it must hold that:

$$\underline{\underline{A}}^T_{n_m}\underline{\underline{B}} = \underline{\underline{A}}^T_{n_m}\underline{\underline{B}}_{n_m} + \underline{\underline{A}}^T_{n_m}\underline{\underline{R}} \tag{2.42}$$

and therefore, introducing Eq. 2.40 and Eq. 2.41, it must be:

$$\underline{\underline{A}}^T_{n_m}\underline{\underline{R}} = \underline{\underline{0}} \tag{2.43}$$

which proves the proposition. □

Proposition 2. *$\underline{\psi}^{(i)}_A\,\sigma^{(i)}_B\,\underline{\phi}^{(i)\,T}_B$ is the only component of $\underline{\underline{B}}_c$ to be correlated with the contribution of the ith POD mode to $\underline{\underline{A}}$.*

Proof. The ith POD contribution to $\underline{\underline{A}}$ is given by $\underline{\psi}^{(i)}_A\,\sigma^{(i)}_A\,\underline{\phi}^{(i)\,T}_A$. The cross-correlation matrix between this component and $\underline{\underline{B}}_c$ can be rewritten as:

$$\begin{aligned} \underline{\phi}^{(i)}_A\,\sigma^{(i)}_A\,\underline{\psi}^{(i)\,T}_A\,\underline{\underline{B}}_{n_m} &= \underline{\phi}^{(i)}_A\,\sigma^{(i)}_A\,\underline{\psi}^{(i)\,T}_A\,\underline{\underline{\Psi}}_{A,n_m}\underline{\underline{\Sigma}}_{B,n_m}\underline{\underline{\Phi}}^T_{B,n_m}\\ &= \sum_j \underline{\phi}^{(i)}_A\,\sigma^{(i)}_A\,\underline{\psi}^{(i)\,T}_A\,\underline{\psi}^{(j)}_A\,\sigma^{(j)}_B\,\underline{\phi}^{(j)\,T}_B \end{aligned} \tag{2.44}$$

According to the orthogonality property of the POD basis, $\underline{\psi}^{(i)\,T}_A\,\underline{\psi}^{(j)}_A = \delta_{ij}$. Therefore the only contribution to the cross-correlation is given by:

$$\underline{\phi}^{(i)\,T}_A\,\sigma^{(i)}_A\,\underline{\psi}^{(i)\,T}_A\,\underline{\underline{B}}_{n_m} = \underline{\phi}^{(i)\,T}_A\,\sigma^{(i)}_A\,\underline{\psi}^{(i)\,T}_A\,\underline{\psi}^{(i)}_A\,\sigma^{(i)}_B\,\underline{\phi}^{(i)}_B \tag{2.45}$$

which proves the proposition. □

Proposition 3. *The matrix $\underline{\underline{B}}_{n_m}$ does not account entirely for the variance content of $\underline{\underline{B}}$.*

Proof. Following the POD, the energy content of the ensemble $\underline{\underline{B}}$ is given by the norm of the two-point correlation matrix. According to Eq. 2.39, it can be rewritten as:

$$\begin{aligned}\underline{\underline{B}}^T\underline{\underline{B}} &= \left(\underline{\underline{B}}_{n_m} + \underline{\underline{R}}\right)^T \left(\underline{\underline{B}}_{n_m} + \underline{\underline{R}}\right) \\ &= \underline{\underline{B}}^T_{n_m}\underline{\underline{B}}_{n_m} + \underline{\underline{B}}^T_{n_m}\underline{\underline{R}} + \underline{\underline{R}}^T\underline{\underline{B}}_{n_m} + \underline{\underline{R}}^T\underline{\underline{R}}\end{aligned} \tag{2.46}$$

Since $\underline{\underline{B}}_{n_m}$ components results in a linear combination of the components of $\underline{\underline{A}}_{n_m}$, the cross-products $\underline{\underline{B}}^T_{n_m}\underline{\underline{R}} = \underline{\underline{R}}^T\underline{\underline{B}}_{n_m} = \underline{\underline{0}}$. Therefore:

$$\underline{\underline{B}}^T\underline{\underline{B}} = \underline{\underline{B}}^T_{n_m}\underline{\underline{B}}_{n_m} + \underline{\underline{R}}^T\underline{\underline{R}} = \underline{\underline{\Phi}}_{B,n_m}\underline{\underline{\Sigma}}^2_{B,n_m}\underline{\underline{\Phi}}^T_{B,n_m} + \underline{\underline{R}}^T\underline{\underline{R}} \tag{2.47}$$

which proves the proposition. Proposition 3 expresses the fact that the EPOD, differently from the POD, is not an exact decomposition. If $n_m = r$ in Eq. 2.39, $\underline{\underline{\Psi}}_{A,n_m}$ is an orthonormal matrix and thus $\underline{\underline{R}}^T\underline{\underline{R}} = 0$. □

2.4.2 Connection with Linear Stochastic Estimation

The Linear Stochastic Estimation (LSE, Adrian, 1977) is a technique that is typically employed to estimate an unknown quantity given a quantity that is known. As the name suggests, this technique attempts to statistically draw a linear relation between the known quantity and the quantity which has to be estimated. A strong connection between the LSE and EPOD exists: the EPOD can be considered as the LSE of the *topoi* $\underline{\phi}_B^{(i)}$ given the *topoi* $\underline{\phi}_A^{(i)}$.

Some attempts to determinate the velocity modes correlated to the POD modes of a multi-channel pressure signal through Linear Stochastic Estimation (LSE) have been performed by Picard and Delville (2000) for an axisymmetric jet and Taylor and Glauser (2004) for a backward facing step.

The method employed by Taylor and Glauser (2004) attempts to find a linear stochastic estimation of the *chronoi* corresponding to a decomposition of the velocity field starting from the knowledge of an array of pressure measurements. The LSE results in a linear overdetermined system:

$$\underline{\underline{\Psi}}_{B,n_m} \approx \underline{\underline{A}}_{n_m}\underline{\underline{C}} \tag{2.48}$$

with $\underline{\underline{A}}$ corresponding to the pressure ensemble matrix and $\underline{\underline{B}}$ to the velocity ensemble matrix.

The solution $\underline{\underline{C}}$ to this system is found by solving the equation:

$$\left(\underline{\underline{A}}^T_{n_m}\underline{\underline{A}}_{n_m}\right)\underline{\underline{C}} = \left(\underline{\underline{A}}^T_{n_m}\underline{\underline{\Psi}}_{A,n_m}\right) \tag{2.49}$$

It is possible to observe that:

$$\begin{aligned}\underline{\underline{C}} &= \left(\underline{\underline{A}}_{n_m}^T \underline{\underline{A}}_{n_m}\right)^{-1} \left(\underline{\underline{A}}_{n_m}^T \underline{\underline{\Psi}}_{A,n_m}\right) \\ &= \left(\underline{\underline{\Phi}}_{A,n_m} \underline{\underline{\Sigma}}_{A,n_m}^2 \underline{\underline{\Phi}}_{A,n_m}^T\right)^{-1} \left(\underline{\underline{\Phi}}_{A,n_m} \underline{\underline{\Sigma}}_{A,n_m} \underline{\underline{\Psi}}_{A,n_m}^T \underline{\underline{\Psi}}_{A,n_m}\right) \\ &= \underline{\underline{\Phi}}_{A,n_m} \underline{\underline{\Sigma}}_{A,n_m}^{-2} \underline{\underline{\Phi}}_{A,n_m}^T \underline{\underline{\Phi}}_{A,n_m} \underline{\underline{\Sigma}}_{A,n_m} = \underline{\underline{\Phi}}_{A,n_m} \underline{\underline{\Sigma}}_{A,n_m}^{-1}\end{aligned} \tag{2.50}$$

Introducing the previous solution in Eq. 2.48, results in:

$$\underline{\underline{\Psi}}_{B,n_m} \approx \underline{\underline{A}}_{n_m} \underline{\underline{\Phi}}_{A,n_m} \underline{\underline{\Sigma}}_{A,n_m}^{-1} = \underline{\underline{\Psi}}_{A,n_m} \tag{2.51}$$

Following the approach by Picard and Delville (2000), it is possible to show that the ith contribution to the velocity field $\underline{\psi}_A^{(i)} \, \sigma_B^{(i)} \underline{\phi}_B^{(i)\,T}$ is strictly identical to the LSE of the velocity field from the ith POD mode of the pressure.

The LSE of $\underline{\underline{B}}_{n_m}$ from $\underline{\underline{A}}_{n_m}$ is given by the overdetermined linear system:

$$\underline{\underline{B}}_{n_m} \approx \underline{\underline{A}}_{n_m} \underline{\underline{C}} \tag{2.52}$$

The matrix $\underline{\underline{C}}$ is found as the solution to the equation system:

$$\left(\underline{\underline{A}}_{n_m}^T \underline{\underline{A}}_{n_m}\right) \underline{\underline{C}} = \left(\underline{\underline{A}}_{n_m}^T \underline{\underline{B}}_{n_m}\right) \tag{2.53}$$

It can be observed that:

$$\begin{aligned}\underline{\underline{C}} &= \left(\underline{\underline{A}}_{n_m}^T \underline{\underline{A}}_{n_m}\right)^{-1} \left(\underline{\underline{A}}_{n_m}^T \underline{\underline{B}}_{n_m}\right) \\ &= \left(\underline{\underline{\Phi}}_{A,n_m} \underline{\underline{\Sigma}}_{A,n_m}^2 \underline{\underline{\Phi}}_{A,n_m}^T\right)^{-1} \left(\underline{\underline{\Phi}}_{A,n_m} \underline{\underline{\Sigma}}_{A,n_m} \underline{\underline{\Psi}}_{A,n_m}^T \underline{\underline{B}}_{n_m}\right) \\ &= \underline{\underline{\Phi}}_{A,n_m} \underline{\underline{\Sigma}}_{A,n_m}^{-1} \underline{\underline{\Psi}}_{A,n_m}^T \underline{\underline{B}}_{n_m}\end{aligned} \tag{2.54}$$

The solution to Eq. 2.52 is therefore implicitly found by means of the pseudo-inverse matrix of $\underline{\underline{A}}_{n_m}$, i.e. through the SVD. Eq. 2.52 can be rewritten as:

$$\underline{\underline{B}}_{n_m} \approx \underline{\underline{A}}_{n_m} \underline{\underline{\Phi}}_{A,n_m} \underline{\underline{\Sigma}}_{A,n_m}^{-1} \underline{\underline{\Psi}}_{A,n_m}^T \underline{\underline{B}}_{n_m} = \underline{\underline{\Psi}}_{A,n_m} \underline{\underline{\Sigma}}_{B,n_m} \underline{\underline{\Phi}}_{B,n_m}^T \tag{2.55}$$

from which the equivalence between the LSE of the $\underline{\underline{B}}$ modes and the EPOD of $\underline{\underline{B}}$ is found. All the properties of the LSE can be therefore extended to the EPOD. In particular, it must be noted that, while the relation between velocity fields and other quantities may be formally non-linear, the LSE may still prove to be adequate due to the small-magnitude of second-order terms (as shown by Adrian et al., 1989, for the case of homogeneous turbulence).

Part II

Applications to signal treatment

Chapter 3

Optimal flow-feature oriented filtering for field measurements

Random noise removal from experimental data in turbulent flows is of paramount importance, especially for the computation of derivative quantities and spectra. Data filtering is a critical step, in which most often part of the signal has to be traded for filtering effectiveness. Thanks to its capability to align with the most energetically relevant flow features, the POD can be used to enforce the separation between signal and noise content. Results achieved through this approach can easily perform better than traditional spectral filtering in the Fourier basis due to the POD spectral optimality, as discussed in Chapter 2. The POD allows a better separation between low-energy features, associated to small fluctuations which are dominated by random noise, and high-energy features, associated to larger fluctuations and therefore less affected by noise contamination.

In this chapter, a filtering method based on truncated POD is described. The advantage of a POD-based filtering criterion stands in that it is flow-feature oriented, i.e. it is driven by the data and not by a generic impulse response. The flow-feature oriented filter described in this chapter has been published by Raiola et al. (2015), where the method is applied on Particle Image Velocimetry data. The method consists in the determination of an optimal threshold on the number of modes to consider for the low-order reconstruction of the flow field. Modes which are ranked above this threshold (i.e. with higher energy content) are retained, modes ranked below the threshold (i.e. with lower energy content) are discarded.

While a theoretical demonstration of the existence of an optimum is given, its *a priori* determination is impossible without the knowledge of the spectral content of the noise-free dataset. Therefore, an *a posteriori* criterion, inspired by the scree plot test

(Cattell, 1966), is provided. The robustness of the criterion is demonstrated on both synthetic and experimental datasets. A significant reduction of the measurement error is achieved, thus resulting in an enhancement of the dynamic velocity range (i.e. the ratio between the largest and the smallest measurable velocity, Adrian, 1997). Considering the improvement observed in the measurement of turbulent spectra and derivative quantities, the proposed POD-based filter can potentially extend the capability of PIV to large Reynolds number flows, where high dynamic spatial and velocity ranges are required. In this chapter the focus is on velocity field measurements; nonetheless, the proposed filter, can be straightforwardly extended to other applications, such as temperature surface measurements using infrared thermography as discussed in the work by Raiola et al. (2017).

3.1 The uncertainty in Particle Image Velocimetry

The key of the success of Particle Image Velocimetry (PIV) lies in its ability to measure the instantaneous velocity simultaneously at several points thus enabling the computation of derivative quantities, such as vorticity and rate of strain (Westerweel et al., 2013). Unfortunately experimental noise and spuriously detected vectors (commonly referred as outliers) pose great challenges to the reliability of the measurement of gradient-based quantities. For instance, for tomographic PIV measurements, the standard deviation of the divergence computed on raw data of an incompressible flow can be assumed as an estimation of the accuracy of measurement of the velocity spatial derivatives and it is typically found to be around 7% (Ceglia et al., 2014) of the maximum vorticity in the measured flow field (locally the error can be much higher). Even using advanced PIV algorithms and temporal filtering of data, a typical figure of 3% error in the vorticity measurements is reported (see, e.g. Violato et al. 2012).

PIV measurement uncertainty is traditionally classified in bias and random errors. The bias errors typically appear in the form of peak-locking, i.e. bias towards integer displacement due to the pixel discretization (Westerweel, 1997), or as a modulation due to finite spatial resolution effects (Scarano, 2003). Even though the bias error received a more significant attention from the community of PIV developers, the random error is often the dominant component of the measurement uncertainty. According to Adrian (1991), the root mean square (rms) of the random error is proportional to the particle image diameter (and hence to the correlation peak width). Other sources of random errors are the change of relative intensity between two exposures of particle images due to out-of-plane motion, fluctuating background intensity and camera noise introduced during the recording process. Westerweel (2000) reported a typical figure of 0.05 pixels for the rms of the random error. The random error is highly sensitive to the interrogation procedure: the use of window weighting functions and of advanced interpolators is shown to affect its amplitude (Astarita, 2006, 2007). Moreover, false correlation peaks detection mostly occurs when the correlating windows produce an insufficient number of particle image pairs, resulting in the occurrence of spurious vectors (Huang et al., 1997). Recognizing and eliminating such incorrect vectors is a mandatory step to obtain undistorted velocity statistics. This procedure is referred to as data validation (Westerweel, 1994, Westerweel and Scarano, 2005).

One path to reduce the instantaneous measurement uncertainty due to random error consists in exploiting temporal coherence to improve measurement quality. Nowadays the availability of high speed hardware has multiplied the number of attempts in this direction (see e.g. Sciacchitano et al. 2012, Cierpka et al. 2013). In three-dimensional flow field measurements physical criteria can be exploited to reduce the measurement uncertainty (see, for instance, the solenoidal filtering approach by Schiavazzi et al. 2014). This is generally not possible in planar PIV experiments. In case of non time-resolved data, the options to reduce the measurement uncertainty are very limited and often rely simply on spatial filtering which provides a smoother field but, on the downside, implies a loss of spatial dynamic range.

3.2 POD as a de-noising tool in PIV measurements

In this chapter an approach based on the extraction of a statistical filter from Proper Orthogonal Decomposition of velocity data ensembles is explored. POD allows for the identification of the flow field principal components. In §2.1.2 it has been shown that it is possible to extract the instantaneous flow field topology by taking into account a subset of modes containing the bulk of the energy. A low-order reconstruction acts as a filter on the data while, at the same time, redistributes information from the entire ensemble into the single snapshots, even if they are statistically uncorrelated. The POD, similarly to discrete orthogonal transforms (such as Fourier, Chebyshev or Legendre transforms), projects the dataset onto a set of orthogonal functions, i.e. the empirical eigenfunctions. While in orthogonal transforms the orthogonal functions are fixed *a priori* (for instance sinusoidal functions, Chebyshev or Legendre polynomials) the empirical eigenfunctions are selected accordingly to a spectral optimality principle. Therefore, assuming empirical eigenfunctions being properly converged (and thus that

POD has been performed on a large enough dataset) the POD-based filter is expected to perform better than other filters based on orthogonal transforms.

The reconstruction of the flow field with a limited set of POD modes is already a quite assessed instrument for PIV data handling, both for the identification of turbulent coherent structures (Berkooz et al., 1993, Adrian et al., 2000) and for spurious vectors replacement (Venturi and Karniadakis, 2004, Raben et al., 2012). In the latter case one can set up criteria based on data smoothness to assess the optimal number of modes (Everson and Sirovich, 1995, Raben et al., 2012). On the other hand, for data reconstruction, the trade-off between reconstructed signal and noise contamination is still left to empirical judgement. A common criterion is based on the heuristic consideration that the energy content of the POD-based LOR should be a significative percentage of the energy of the field (Fahl, 2000, Ravindran, 2000, Bergmann et al., 2005). For instance, Liu et al. (2001) in a channel-flow PIV measurement set a 48% of the turbulent kinetic energy threshold to define the most representative large-scale coherent structures. However, in general, no consideration on the amount of contamination of noise in the reconstructed field is provided, neither the number of modes selected is shown to be optimal.

The choice of the number of modes to obtain an optimal low-order reconstruction of noise-corrupted data has been long debated. The filtering capacities of a LOR have been widely investigated in the branches of computers science and data mining (see, e.g. Kargupta et al. 2003, Huang et al. 2005, Guo et al. 2006). On PIV measurements of turbulent flows, instead, the efforts have been focused on the definition and identification of non-corrupted modes more than on the identification of an optimality criterion for the reconstruction of the measured flow field (Venturi, 2006).

3.3 Optimal low-rank approximation of PIV data

In §2.2.1 it has been shown that POD can be used to define an optimal low-rank approximation of a noise-perturbed dataset which best approximates the noise-free content of the dataset. In this paragraph this concept is further extended and applied to PIV data with the aim of removing the spurious noise content. In the following it will be supposed that the POD is performed on the correlation matrix of the fluctuating velocity field. In this scenario, it is possible to hypothesize that the POD's eigenvalues decay rate can be approximated with that of a turbulent spectrum in the Fourier space. This hypothesis is rather conservative as the eigenspectrum of the POD has a faster decay rate due to the spectral optimality property (see §2.1.2). Therefore, for turbulent velocity fields it is possible to consider a decay rate in the inertial sub-range given by the Kolmogorov law:

$$\widetilde{\lambda}^{(i)} = C i^{-\frac{5}{3}} \tag{3.1}$$

where C is a proportionality constant. To evaluate it, one can consider that the sum of the $\widetilde{\lambda}^{(i)}$ is equal to the total kinetic energy in the ensemble:

$$\sum_{i=1}^{n_t} \widetilde{\lambda}^{(i)} = \sum_{i=1}^{n_t} C i^{-\frac{5}{3}} = n_t n_p \mathscr{e} \Rightarrow C \approx \frac{n_t n_p \mathscr{e}}{\zeta(5/3)} \tag{3.2}$$

where $\mathscr{e}$ is the turbulent kinetic energy averaged over all the spatio-temporal data ensemble, n_t and n_p are the size of the data ensemble respectively in time and space and $\zeta(s)$ is the Euler-Riemann zeta function. In the mid equality of Eq. 3.2 it has been assumed for simplicity that the data are produced on a structured grid, which is commonly the case for PIV. Substituting Eq. 3.1 and Eq. 3.2 into Eq. 2.29, discrete deriving the reconstruction error δ_{RT} with respect to the number of reconstructed modes n_m and equating to zero:

$$\begin{gathered} \frac{\Delta \delta_{RT}(n_m^\star)}{\Delta n_m} = 0 \\ \Downarrow \\ \sum_{i=n_m^\star+1}^{n_t} \widetilde{\lambda}_i - \sum_{i=n_m^\star}^{n_t} \widetilde{\lambda}_i + n_p \varsigma_e^2 = -\frac{n_t n_p \mathscr{e}}{\zeta(5/3)} {n_m^\star}^{-\frac{5}{3}} + n_p \varsigma_e^2 = 0 \end{gathered} \tag{3.3}$$

where ς_e is the standard deviation of the random error and $n_m^\star$ indicates a critical point for the function δ_{RT}. It is easy to notice that $n_m^\star$ is a minimum point as $\frac{\Delta^2}{\Delta n_m^2} \delta_{RT} > 0$. The optimum number of modes to reconstruct the field, i.e. the one that minimizes the reconstruction error, is:

$$n_m^\star = \left(\frac{n_t \mathscr{e}}{\varsigma_e^2 \zeta(5/3)} \right)^{\frac{3}{5}} \tag{3.4}$$

In general the effective $n_m^\star$ corresponds to a lower number of modes than indicated in Eq. 3.4 due to POD optimality with respect to the L^2 norm. It should also be noted that, in principle, in experimental applications the standard deviation of the random error is not known a priori; furthermore the Eq. 3.4 is a direct consequence of assuming the POD eigenvalues decaying as in the inertial sub-range of a high Reynolds number turbulent flow, which is a conservative assumption (as discussed above) and it cannot be extrapolated directly to the full spectral range. Consequently, Eq. 3.4 has a limited practical applicability; nonetheless, it is useful to demonstrate the existence of an optimum number of modes for the LOR when the flow-field reference spectrum is not white. Additionally, the relation provides a useful description of the $n_m^\star$ dependencies: it increases both with the ratio of the turbulent kinetic energy and the random error energy and with the number of samples in the ensemble.

Even if Eq. 3.4 cannot be used to choose $n_m^\star$, it can be used to safely estimate the number of samples required for the convergence of the proposed method. Suppose that the objective is a noise reduction by a factor RF (i.e. the residual error energy in the reconstructed fields is $(1-\mathrm{RF})\varsigma_e^2$). Since the noise spectral distribution is white, the relation $n_t \approx (1-\mathrm{RF})^{-1} n_m^\star$ is a reasonable approximation. Then, from Eq. 3.4:

$$n_t \approx (1-\mathrm{RF})^{-\frac{5}{2}} \left(\frac{\boldsymbol{\mathscr{e}}}{\varsigma_e^2 \zeta({}^5\!/_3)} \right)^{\frac{3}{2}} \tag{3.5}$$

The required number of samples can be assessed via a prior approximate estimate of $\boldsymbol{\mathscr{e}}$ and of the expected measurement random error.

In order to find an operative criterion for the choice of the optimal number of modes to be retained, the reconstruction error with respect to the measured field can be considered:

$$\begin{aligned} \delta_{RM}(n_m) &= \left(\frac{1}{n_t n_p}\right)^{\frac{1}{2}} \left\| \underline{\underline{A}} - \underline{\underline{A}}_{n_m} \right\|_F \\ &= \left(\frac{1}{n_t n_p}\right)^{\frac{1}{2}} \left(\sum_{i=n_m}^{n_t} \lambda_i + (n_t - n_m) n_p \varsigma_e^2 \right)^{\frac{1}{2}} \end{aligned} \tag{3.6}$$

Consider the relative decrease rate of the reconstruction error δ_{RM}, here called $F(n_m)$, defined as the ratio between forward and backward discrete derivative of $\delta_{RM}^2(n_m)$:

$$F(n_m) = \frac{\delta_{RM}^2(n_m+1) - \delta_{RM}^2(n_m)}{\delta_{RM}^2(n_m) - \delta_{RM}^2(n_m-1)} = \frac{\widetilde{\lambda}_{n_m} + n_p \varsigma_e^2}{\widetilde{\lambda}_{n_m-1} + n_p \varsigma_e^2} = \frac{\lambda_{n_m}}{\lambda_{n_m-1}} \tag{3.7}$$

in which the last equality derives Eq. 2.24. The quantity in Eq. 3.7 may reach asymptotically 1, for n_m sufficiently large. In the next section it will be shown that a reasonable threshold for the number of modes to retain can be set at $F(n_m^\star) = 0.999$. This is formally equivalent to look for an elbow in δ_{RM}^2, and can be considered a restatement of the classic *scree test plot* (Cattell, 1966) used in PCA to determine the number of components to retain in a low-order reconstruction. It is important to remark that even though the theoretical estimates of Eq. 3.4 and Eq. 3.5 are limited to

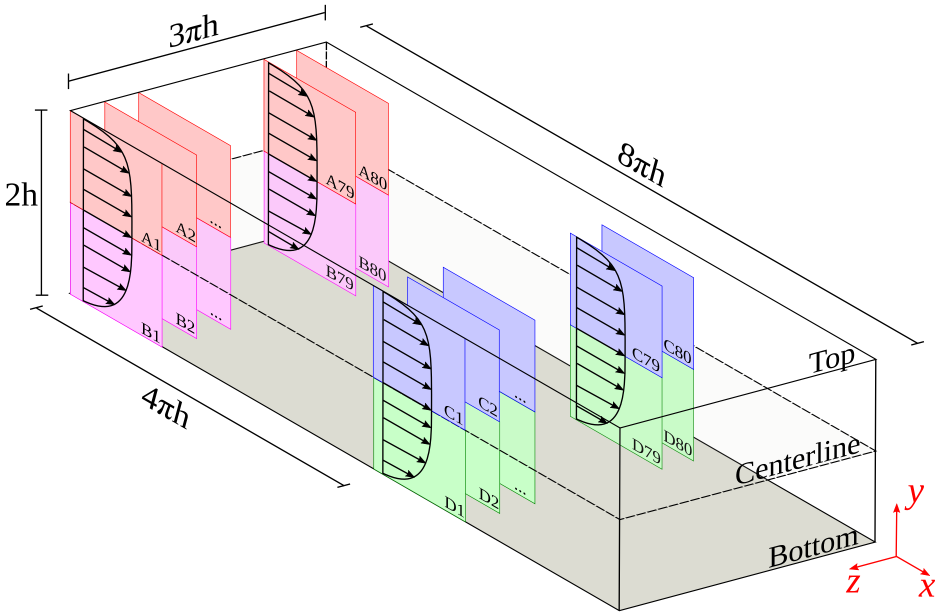

Fig. 3.1 Sub-domains extracted from the Channel Flow DNS spatial domain for the synthetic PIV experiment. Different positions in the $x - y$ plane are accounted with different letter (A, B, C and D).

turbulent flows, the thresholding of Eq. 3.7 is of general application, including laminar flows.

3.4 Validation

3.4.1 Numerical validation on synthetic images

A set of synthetic PIV images is generated from the Channel Flow DNS database from the John Hopkins Turbulence Databases (`http://turbulence.pha.jhu.edu/`, Li et al., 2008, Yu et al., 2012a, Graham et al., 2013). The Channel Flow DNS database includes a complete channel flow velocity field with bulk velocity U_b equal to 1 over a domain of 2 half-channel-heights h from wall to wall, 3π channel half heights in the span-wise direction and 8π channel half heights in the stream-wise direction. The DNS sequence duration is of one channel flow-through time $8\pi h/U_b$ with data stored each $\delta t = 0.0065 h/U_b$ (with U_b being the bulk velocity in the channel). The simulation results in a friction Reynolds number $Re_\tau \approx 1000$ and a centerline Reynolds number $Re_c \approx 20000$. The data are stored in a $2048 \times 512 \times 1536$ points grid. For the purpose of simulating a planar PIV synthetic experiment, the velocity field is extracted over bi-dimensional square $h \times h$ sub-domains (going from the wall to the centerline) in the $x-y$ planes to simulate a set of PIV snapshots. In order to reduce the temporal correlation between different snapshots, the velocity field is extracted over a total of 25 different temporal positions spanning the entire DNS temporal sequence. Since a set of 25 snapshots is not enough to reach statistical convergence, at each temporal position 4 sequences of spatially-separated snapshots are extracted exploiting problem symmetry, spatial homogeneity and statistical stationary state. Each spatially-separated sequence comprises 80 slices equally spacing the channel width (along the z direction) at a fixed $x-y$ position. The spatially-separated sequences are obtained at 4 different $x-y$ positions, in particular at the beginning and at half channel steam-wise position and both at the bottom side and at the upper side of the channel. A sketch of the slices extracted from the DNS domain is given if Fig. 3.1. A maximum of 8000 flow-field sub-domains are extracted from the DNS simulation for this synthetic experiment.

The sub-domains extracted are used to generate synthetic images with dimensions 1024×1024 pixels (resulting in a resolution of 4 pixels/grid DNS points). The displacements are multiplied by a scaling factor in order to achieve a mean displacement on the channel centerline equal to 15 pixels.

Gaussian particles (mean diameter 3 pixels, standard deviation 0.5 pixels, 300 counts peak intensity) are randomly generated with a particle image density of 0.01 particles per pixel. The laser intensity is simulated to be Gaussian (with half power width equal to 4 pixels along the thickness of the light sheet) in order to take into account the effect of correlation degradation due to the out-of-plane motion. Noise with uniform distribution (maximum intensity 50 counts, standard deviation 14.4 counts) is added on the images.

The interrogation strategy is an iterative multi-step image deformation algorithm, with final interrogation windows of 32×32 pixels, 75% overlap. A Blackman weighting window is used to improve the stability and the spatial resolution (Astarita, 2007). Vector validation is carried out with a universal median test (Westerweel and Scarano, 2005) on a 3×3 vectors kernel and threshold equal to 2 is used to identify invalid vectors. Discarded vectors are replaced with a distance-weighted average of neighbour valid vectors. The spatial resolution achieved in this simulated experiment is realistic and consistent with that of recent PIV experiments (see, e.g. Hong et al. 2012 achieving a resolution of about 125×60 vectors in a $2h \times h$ domain). The standard deviation of the random error ς_e is estimated by interrogating images with zero-imposed displacement and same background noise feature, and it is found to be equal to 0.18 pixels. The mean turbulent kinetic energy $\mathcal{e}$ in the ensemble is of about 1.29 square pixels.

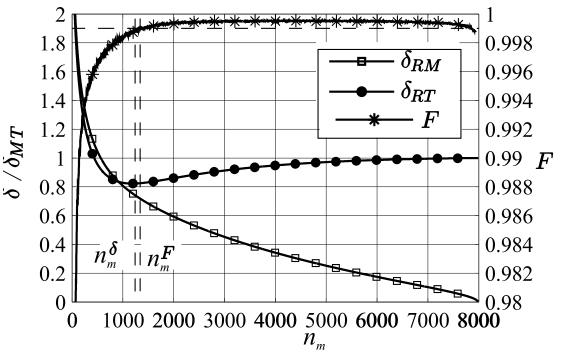

Fig. 3.2 δ_{RT}, δ_{RM} (left axis) and F (right axis) versus the number of modes used in the reconstruction. Errors are presented in non-dimensional form using δ_{MT}.

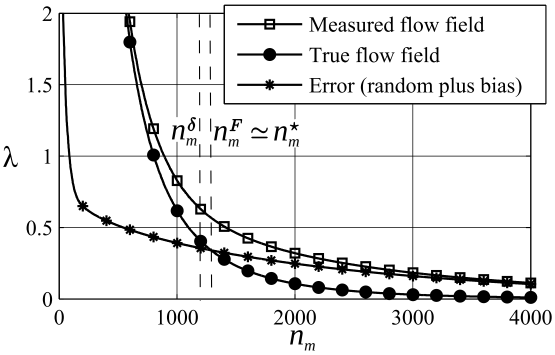

Fig. 3.3 POD eigenvalues of the 4000 most energetic modes for the true field, the measured field and the error field. Note that error includes both bias and random part.

According to Eq. 3.5, in order to aim to a target of random error reduction of about 84%, 8000 synthetic images are generated to form the ensemble. With the same values, the expected optimal number of modes $n_m^\star$ (Eq. 3.4) is of about 1300 modes. The 8000 images are obtained by using flow fields with a time separation equal to 250 DNS timesteps (corresponding to a displacement of 250 pixels on the channel centerline) and with a space separation along the z direction equal to $0.23h$ (235 pixels). The flow fields are taken at two stream-wise positions, i.e. $x = 0$ and $x = 4\pi h$. The number of images is doubled by flipping data from the other half of the channel.

In Fig. 3.2 the values of $\delta_{RT}(n_m)$ and $\delta_{RM}(n_m)$ as defined by Eq. 2.28 and Eq. 3.6 are plotted; data are presented in non-dimensional form dividing by δ_{MT}, i.e. the error of the measured field with respect to the true one, that in this test is equal to 0.32 pixels. It has to be outlined here that this value is higher than the random noise since it includes also signal modulation and other bias errors. The minimum δ_{RT} is reached when the first 1200 modes are used for the reconstruction (corresponding to 96.6% of the fluctuating energy of the measured field). The effective number of modes which minimizes the reconstruction error will be indicated with n_m^δ. It has to be remarked that a quite extended plateau of about 500 modes width is present, thus the exact choice of the number of modes to be retained is not critical, provided that one can identify a reasonable estimate of the range in which the optimum should be. In this plateau the error is of about 0.82 δ_{MT} (corresponding to a 0.06 pixels total error reduction). Beyond 1200 modes δ_{RM} has approximately a linear trend with n_m. Indeed, as noise has a white spectral distribution, it is reasonable to expect that for large n_m

the contribution of each mode is approximately constant. The relative decrease rate of the reconstruction error $F(n_m)$ defined in Eq. 3.7 is also plotted; its values are low-pass filtered (windowed linear-phase FIR digital filter with 25 points span and normalized cutoff frequency 0.0313). The relative decrease rate of the reconstruction error approaches 1 beyond 1200 modes, apart from the very last coefficients in which the linearity of the contribution of noise is lost. A reasonable threshold is $F(n_m) = 0.999$, corresponding to $n_m \approx 1300$ and to a δ_{RT} nearby the minimum. The number of modes satisfying the relation $F(k) = 0.999$ will be referred from now on with the symbol n_m^F.

In Fig. 3.3 the POD eigenvalues of the measured and true flow fields and of the error are illustrated. The latter is defined as the difference between measured and true flow fields, thus it includes both bias and random errors. The eigenvalues of both measured and true fields follow approximately a power law, at least for the first half of the set of POD modes. The eigenvalues of the error present a slower decay rate. Even if this may seem in contrast with the hypothesis introduced in §2.2.1, i.e. white random error distribution, it should be remarked that, in the plot, the error includes also a bias component, which is not necessarily "spectrally white". It is worth to highlight that true eigenvalues and error eigenvalues cross over in the region that contains the values $n_m^\star$, n_m^δ and n_m^F. Beyond the cross-over point, the measured spectrum approaches the error eigenvalues. This means that, from this point on, each additional mode included in the reconstruction would introduce a contribution in which noise is predominant on the signal.

In Fig. 3.4 a true snapshot is compared to the raw snapshots obtained with PIV interrogation and with POD-based low-order reconstruction. Maps of the out-of-plane vorticity component are reported to stress differences. The measured field (Fig. 3.4c) is affected by spurious vortical features that are not present in the original field. As an example, the negative vorticity peak marked as A in the figure is much weaker in the original field, while in the measured field has intensity comparable to that of the vortex marked as B, that is an original field feature. The optimal reconstruction with 1300 modes (Fig. 3.4d) provides a remarkable improvement of the data quality with respect to the measured field. This reconstruction smears out the negative vorticity peak in A, while retaining vortex B. Such a result could not be achieved by a conventional spatial filter as it will be shown in 3.4.3. Even though the residual error $\delta_{RT}(n_m^\delta)$ from Fig. 3.2 might still appear relatively large, it has to be reminded that in this simulated experiment the measurement error is dominated by bias due to finite spatial resolution effects. If the number of modes used for the low-order reconstruction is significantly

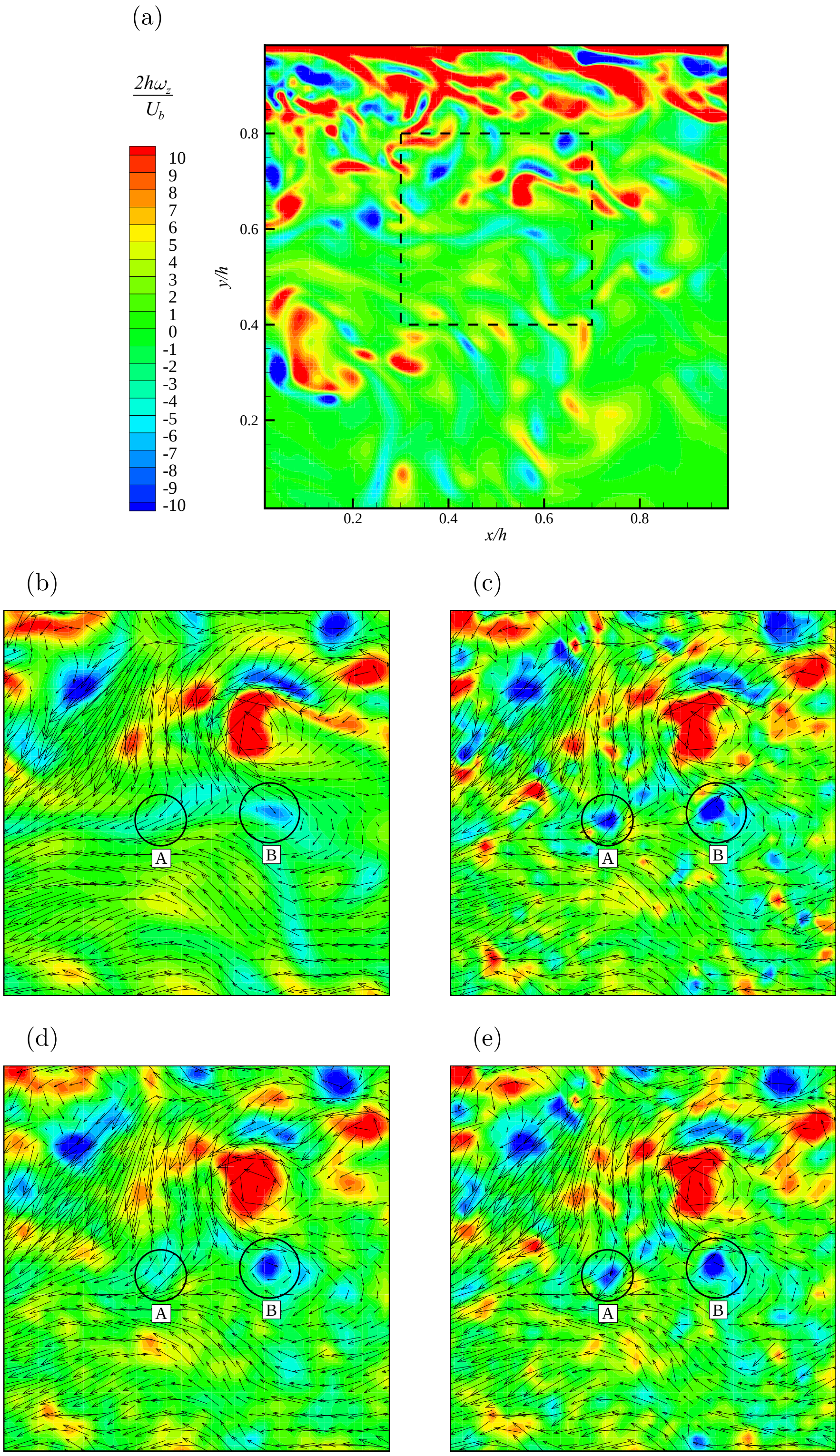

Fig. 3.4 Instantaneous fluctuating vorticity (ω_z) field. a) The DNS field used for this benchmark. Magnified view of the: b) DNS field, c) measured field, d) field reconstructed with 1300 modes, e) field reconstructed with 3000 modes.

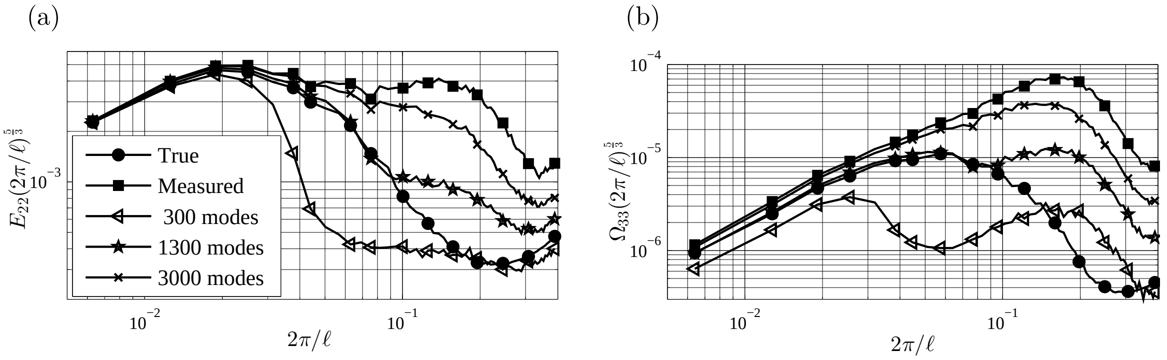

Fig. 3.5 a) Compensated transverse velocity spectra E_{22} in stream-wise direction versus wavenumber $2\pi/\ell$; b) transverse vorticity spectra Ω_{33} in stream-wise direction versus wavenumber $2\pi/\ell$.

increased (e.g. 3000 modes in Fig. 3.4e) the noise contamination is stronger, and, for instance, the vortex A is still present.

In Fig. 3.5 the spatial power spectra (E_{22} for the traverse velocity spectrum and Ω_{33} for the traverse vorticity spectrum) of the true, the measured and the reconstructed fields are reported. Spectra are computed at a fixed tunnel height and ensemble averaged. In both Fig. 3.5a and 3.5b the wavelengths ℓ are expressed in pixels. Data are proposed in Fig. 3.5a in the form of the compensated spectrum (multiplied by the wavenumber to the 5/3) in order to magnify the effects at the smallest scales. It has to be remarked that, even in the case of the original DNS data, the spectrum at the small scales is contaminated by aliasing effects due to the finite length of the domain. The reconstruction with 1300 modes closely follows the DNS spectral behaviour to a larger extent with respect to reconstructions with a larger number of modes. The growth of the error with respect to the true spectrum for smaller wavelengths can be associated mostly to the residual noise. For the sake of completeness, the spectrum obtained by a reconstruction with a lower number of modes is also reported. The reconstruction with 300 modes (which corresponds to 95% of the fluctuating energy) causes a significant underestimation of the spectral energy of a wide range of large scales, thus highlighting that the information obtained from these modes is still insufficient to achieve a proper description of the flow field. The vorticity spectra reported in Fig. 3.5b further stress the improvement achieved using the optimal POD filter. The spectrum obtained using 1300 modes for the reconstruction follows with high fidelity the true one up to a wavelength of 70 pixels. The spectrum obtained from the PIV measured data largely overestimate the vorticity power spectrum already at very large scales (e.g. 35% at 512 pixels and 100% at 128 pixels) due to the measurement noise. The LOR with only

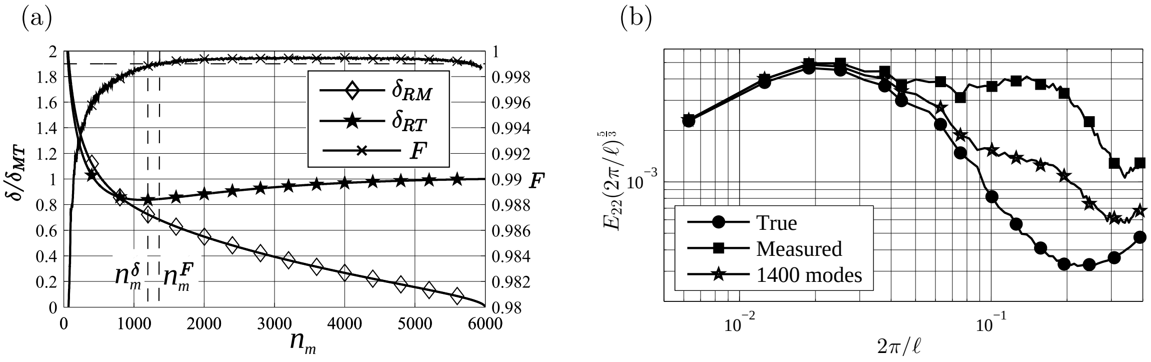

Fig. 3.6 Test case with 6000 images: a) δ_{RT}, δ_{RM} (left axis) and F (right axis) versus the number of modes used in the reconstruction; b) Compensated transverse velocity spectra E_{22} in stream-wise direction versus wavenumber $2\pi/\ell$ reconstructed with n_m^F number of modes.

300 modes provides a completely distorted view of the vorticity distribution over the turbulent scales (even if taking into account 95% of the energy content).

3.4.2 Validation of the criterion for modes selection

In the §3.4.1 the relative decrease rate of the reconstruction error $F(n_m)$ was shown to be a possible parameter to be used for the choice of the optimal number of modes n_m to be included in the LOR, being $F(n_m) = 0.999$ a suitable threshold value. This criterion is here assessed on synthetic images for several conditions, by changing the parameters affecting $n_m^\star$ as given by Eq. 3.4 (i.e. the number of snapshots used in the POD n_t and the standard deviation of the random noise ς_e). A study to evaluate the effects of a change of resolution on the selection criterion is also performed. It will be shown in the following that the spatial resolution is not an independent parameter, since it affects both q, ς_e and also the maximum number of images to be used in the POD.

The effect of a lower number of images (6000 images in Fig. 3.6 and 4000 in Fig. 3.7) is tested under the same noise level and resolution of the test case in §3.4.1. Figs. 3.6a-3.7a show that the number of modes that minimize the error n_m^δ decreases with decreasing n_t, in agreement with the trend predicted by Eq. 3.4. The weaker reduction of n_m^δ with respect to the theoretical prediction of Eq. 3.4 can be associated to the hypothesis of POD spectrum equal to the inertial sub-range spectrum introduced for simplification in §3.3. The flatness of the curve δ_{RT} is also affected by a smaller number of snapshots: the maximum achievable error reduction decreases (82% of δ_{MT}

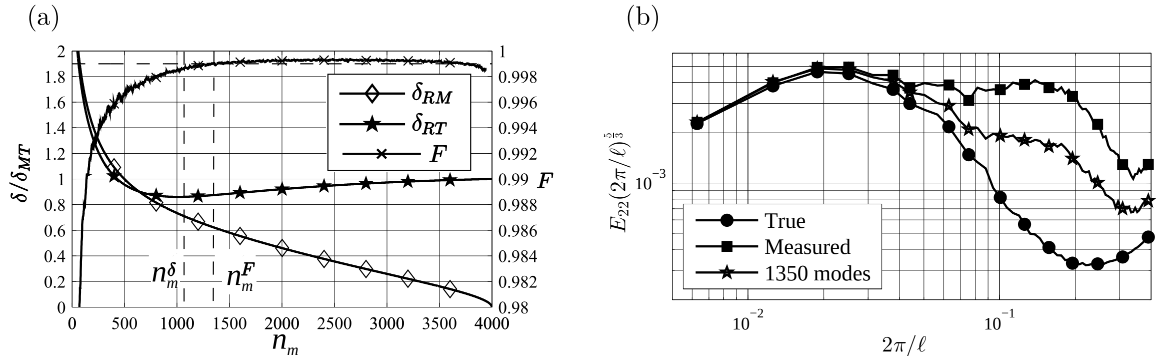

Fig. 3.7 Test case with 4000 images: a) δ_{RT}, δ_{RM} (left axis) and F (right axis) versus the number of modes used in the reconstruction; b) Compensated transverse velocity spectra E_{22} in stream-wise direction versus wavenumber $2\pi/\ell$ reconstructed with n_m^F number of modes.

for 8000 images, 84% of δ_{MT} for 6000 images and 86% of δ_{MT} for 4000 images), while the plateau centered in n_m^δ increases in size. This behavior is consistent with a lower degree of separation between true field and noise modes, that produces a stronger contamination of the measured field modes. The values of n_m^F track the n_m^δ value in a conservative way (with respect to preserving the signal content), always predicting a number of modes slightly larger than n_m^δ. The difference between n_m^F and n_m^δ increases as the ensemble decreases in size. This is mainly due to an increase in the extension of the optimal plateau and affects only marginally the reconstruction: the value n_m^F estimated with the $F(n_m) = 0.999$ criterion always identifies a δ_{RT} inside the optimal plateau, i.e. a low-order reconstruction with an error nearly equal to the optimal one. The effect of a smaller ensemble size on velocity spectra is shown in Fig. 3.6b and 3.7b, respectively for $n_t = 6000$ and $n_t = 4000$ snapshots. The low-order reconstruction obtained with the $F = 0.999$ criterion is less effective in predicting the true spectrum as the ensemble size decreases, but it still achieves remarkable results (reduction of about 75% and 40% of the original error for a 64 pixels wavelength, respectively for $n_t = 6000$ and $n_t = 4000$).

Fig. 3.8 and 3.9 show the effect of a change in the level of background noise. The intensity of the uniformly distributed noise is set to 25 and 75 counts (the original case was generated with 50 counts noise), leading respectively to $\varsigma_e = 0.11$ and $\varsigma_e = 0.27$ pixels (estimated with the zero-displacement test) on the calculated velocity fields. Resolution and number of images are set as in the test case of §3.4.1. A lower level of noise (Fig. 3.8a) shifts the n_m^δ value towards a higher number of modes, meaning that it is possible to achieve a higher order reconstruction without introducing strongly

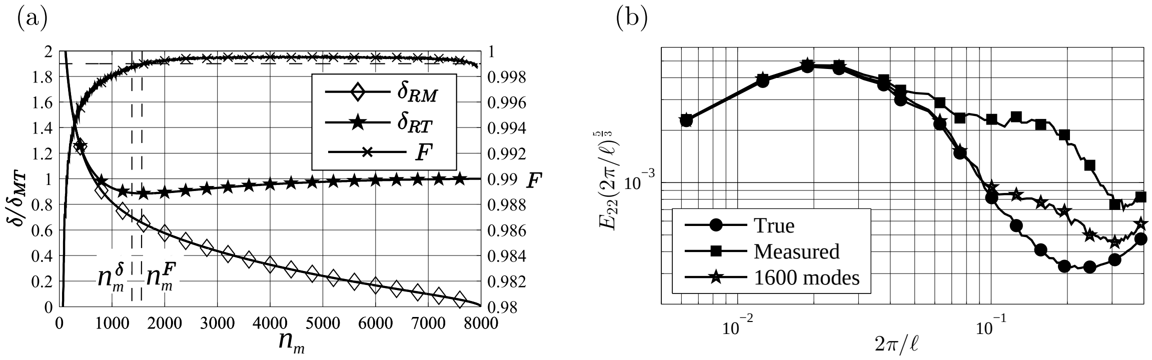

Fig. 3.8 Test case with $\varsigma_e = 0.11$: a) δ_{RT}, δ_{RM} (left axis) and F (right axis) versus the number of modes used in the reconstruction; b) Compensated transverse velocity spectra E_{22} in stream-wise direction versus wavenumber $2\pi/\ell$ reconstructed with n_m^F number of modes.

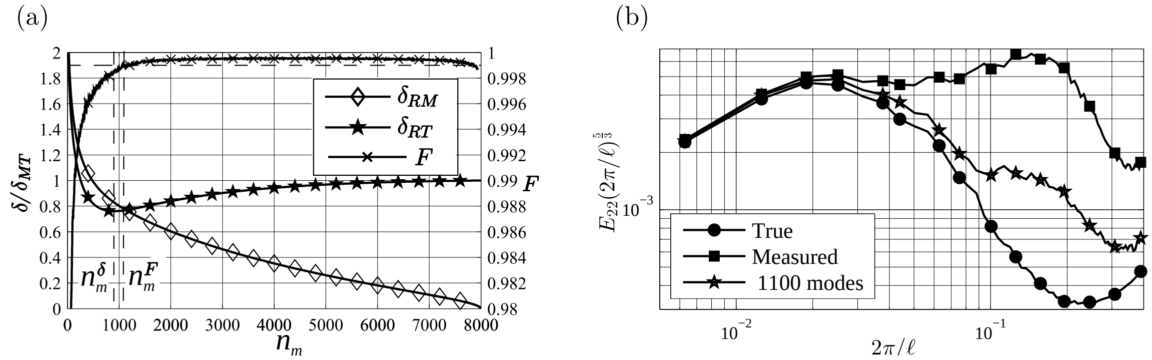

Fig. 3.9 Test case with $\varsigma_e = 0.27$: a) δ_{RT}, δ_{RM} (left axis) and F (right axis) versus the number of modes used in the reconstruction; b) Compensated transverse velocity spectra E_{22} in stream-wise direction versus wavenumber $2\pi/\ell$ reconstructed with n_m^F number of modes.

corrupted modes. Conversely, a higher noise level (Fig. 3.9a) shifts n_m^δ towards a lower number of modes, meaning that noise is contaminating a larger spectrum of modes. As in the previous case, the variation of n_m^δ follows the trend predicted by Eq. 3.4. It should be highlighted that the δ_{RT} curve shape is strongly affected by the noise level: the maximum relative noise reduction increases when the noise level increases, while the optimal plateau extension decreases. The $F(n_m^F) = 0.999$ criterion allows a reasonable prediction of the n_m^δ position with a conservative weak overestimation, still achieving a value of δ_{RT} inside the optimal plateau. For lower noise levels the LOR obtained with the $F(n_m^F) = 0.999$ criterion achieves a lower relative noise reduction with a larger n_m^F. The effect of this behaviour on velocity spectra is shown in Fig. 3.8b: a lower

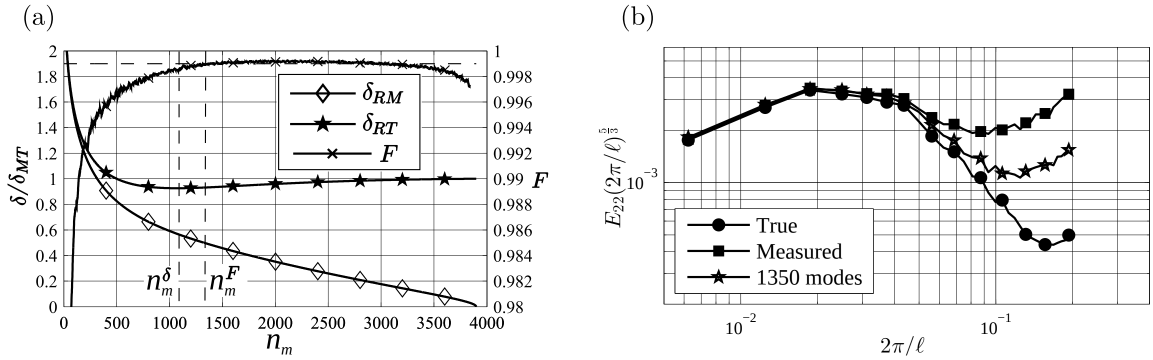

Fig. 3.10 Test case with lower spatial resolution: a) δ_{RT}, δ_{RM} (left axis) and F (right axis) versus the number of modes used in the reconstruction; b) Compensated transverse velocity spectra E_{22} in stream-wise direction versus wavenumber $2\pi/\ell$ reconstructed with n_m^F number of modes.

fraction of energy is discarded, while the higher order reconstruction leads to a more precise computation of the spectra (predicted spectrum is accurate up to a 64 pixels wavelength). In Fig. 3.9b the effect of a more intense noise contention on velocity spectrum is shown. Less favourable cases allow to discard a higher percentage of noise-related fluctuation energy, at the cost of a poorer, but still satisfying description of the spectrum (reduction of the 85% of the original error for a 64 pixels wavelength).

As previously reported in §2.1.1, the maximum number of modes of the POD is given by the rank of the snapshots matrix $\underline{\underline{A}}$, meaning that the maximum number of images n_t that can be used in the POD snapshot method is limited by the velocity field grid points n_p, i.e. by the PIV algorithm final resolution. This means that it is not possible to change the spatial resolution without modifying also the number of images used for POD and the noise level. A test is performed on the PIV images used for the basic test case, reducing the overlap to 50% (Fig. 3.10). For this test case a $q = 1.32$ square pixels and a $\varsigma_e = 0.17$ pixels are estimated, while the number of images used for the POD has been reduced to 3900. It is difficult in this case to extract information that a change in resolution produces on the estimate of n_m^δ, since the effects of a change of both noise level and number of snapshots should be taken into account. As in the previous cases, also for this case the $F(n_m^F) = 0.999$ criterion predicts an overestimation of n_m^δ, even though with $\delta_{RT}(n_m^F)$ value well within the optimal plateau. The main effect that can be distinguished is a smaller maximum error reduction with respect to the case with 4000 images (Fig. 3.7a) that seems to be at least partially justified by a reduction of the noise level and an increment of average turbulent kinetic energy. The velocity spectrum reconstructed with n_m^F number of

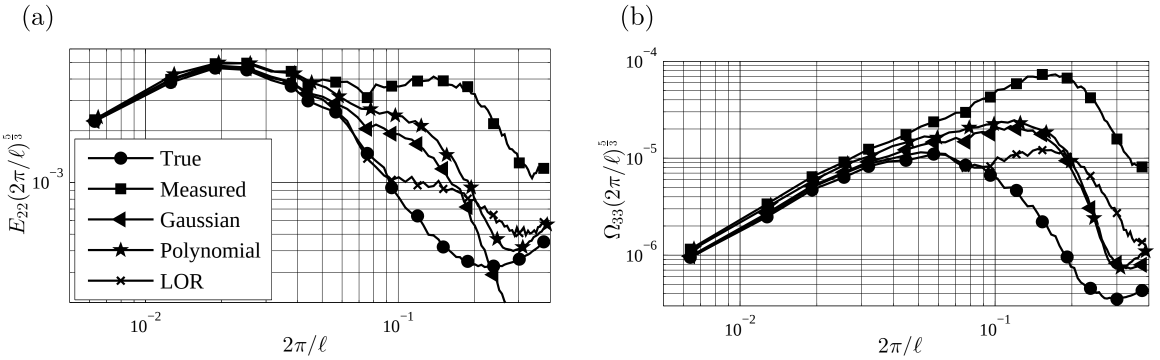

Fig. 3.11 Spatial filter comparison: a) Compensated transverse velocity spectra E_{22} in stream-wise direction versus wavelength ℓ; b) transverse vorticity spectra Ω_{33} in stream-wise direction versus wavenumber $2\pi/\ell$.

modes (Fig. 3.10b) still gives outstanding results (the error reduction for a 64 pixels wavelength is higher than 60% of the original error).

3.4.3 Comparison with spatial filtering

In this subsection the performances of the proposed optimal low-order reconstruction are compared with those of standard spatial filtering techniques. The test case is the same of §3.4.1. In Fig. 3.11 the velocity and vorticity spectra of the LOR with 1300 modes are compared with those of two of the most commonly adopted spatial filtering techniques found in PIV literature: Gaussian filter (kernel size 5×5 grid points, corresponding to ± 3 standard deviations) and second order polynomial filter (kernel size 5×5 grid points). The low-order reconstruction (LOR) outperforms the standard spatial filtering techniques, achieving a precise description of both velocity and vorticity spectra up to a 70 pixel wavelength. For the velocity spectrum at the same wavelength the Gaussian filter and the polynomial filter provide respectively an error reduction of 65% and 40% with respect to the original error. A similar behaviour is observed for the vorticity spectra.

A direct comparison of the instantaneous vorticity fields (Fig. 3.12) clarifies the outstanding performance of the optimal POD-based LOR with respect to conventional spatial filters. As anticipated in §3.4.1, the optimal LOR (Fig. 3.12b) is capable of retaining true field vortical features (such as the vortex labelled as B) and of discarding spurious vortical features (such as the vortex labelled as A) even if the intensities of these features are quite similar. Conversely, in the same context, both Gaussian

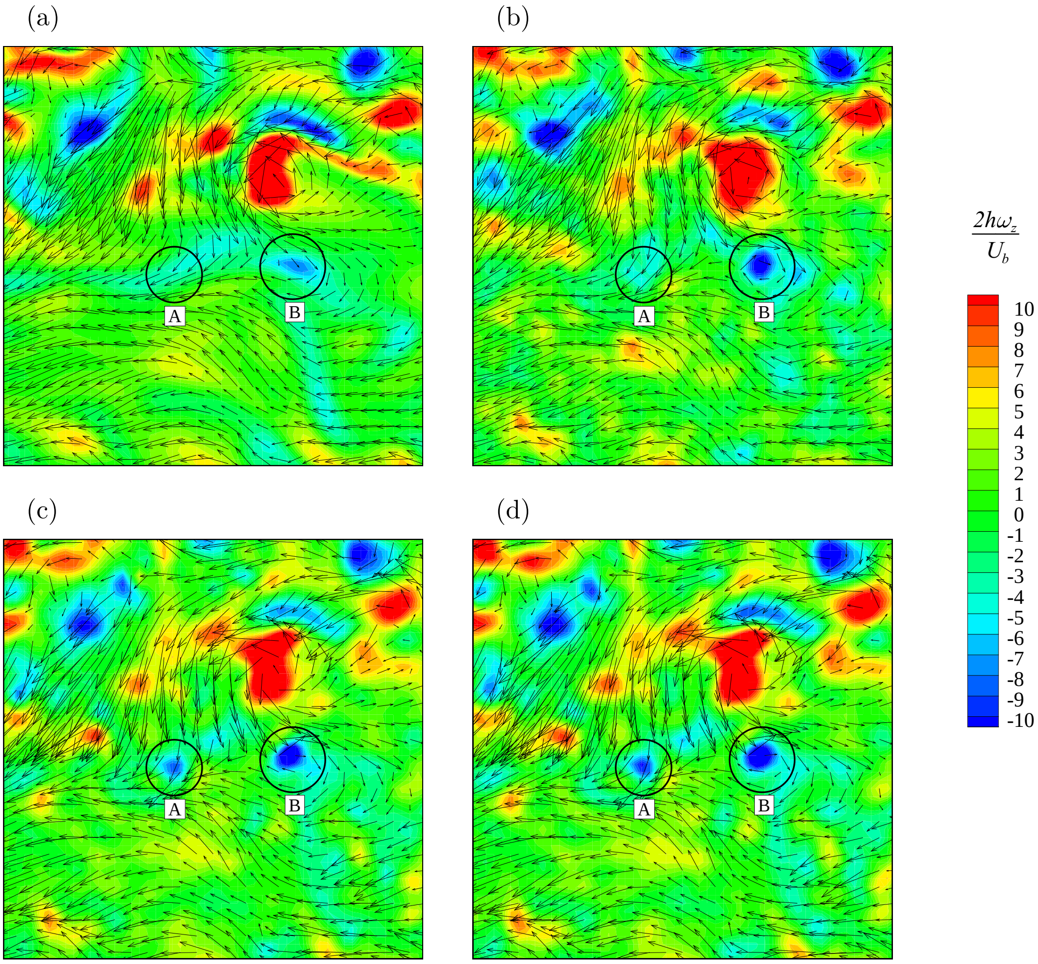

Fig. 3.12 Instantaneous fluctuating vorticity (ω_z) field. Magnified view of the: a) DNS field, b) field reconstructed with 1300 modes, c) field filtered with Gaussian filter, d) field filtered with polynomial filter.

filter and polynomial filter (respectively Figs. 3.12c-3.12d) retain both true field and spurious vortical features.

3.4.4 Experimental validation

The POD-based filter is validated on an experimental PIV dataset. The flow field under investigation is the turbulent wake of a 2D circular cylinder.

The experiment is performed in the closed loop wind tunnel of the Aerospace Engineering Group at *Universidad Carlos III of Madrid*. This wind tunnel has a square test section of 0.4 m × 0.4 m with a length of 1.5 m. The ceiling and the lateral walls of the tunnel are made in methacrylate in order to enable optical access. Free-stream turbulence intensity is estimated to be lower than 1% by means of PIV measurements in the empty tunnel. A circular cylinder, with diameter $D = 10\,\mathrm{mm}$, is mounted at the tunnel's half height, spanning the entire test section width. The blockage ratio is equal to 0.025. The free-stream velocity U_∞ at the end of the contraction is about 6.2 m/s which gives a Reynolds number based on the cylinder diameter of about 3900.

The flow is seeded with Di-Ethyl-Hexyl-Sebacate droplets with diameter of approximately 1 µm. The light source is a Big Sky Laser CFR400 ND:Yag (230 mJ/pulse). The acquisition is performed with two Andor Zyla 5.5MP sCMOS cameras (2560×2160 pixels^2 resolution, 16.6×14.0 mm^2 sensor size). The cameras are synchronized in order to acquire images simultaneously. The first camera is equipped with a 25 mm focal length objective. The resolution of the images acquired with the first camera is equal approximately to 55 pix/D (5.5 pix/mm). The second camera is equipped with a 60 mm focal length objective. The resolution of the images acquired with the second camera is equal approximately to 110 pix/D (11 pix/mm). The time delay between laser pulses is chosen to be 200 µs, in order to give a displacement of about 14 pixels in the higher resolution images and of about 7 pixels in the lower resolution images. The higher resolution camera has then a lower relative error, since the measured displacement is larger while the expected absolute error is the same (the typical figure of merit of 0.1 pixels, Adrian and Westerweel 2011). The velocity fields acquired from the higher resolution camera are considered to be the reference fields due to their intrinsically lower noise content (as in the work by Neal et al., 2015), while the corresponding velocity fields from the lower resolution camera are used to test the POD-based filtering. The cameras are placed side by side in order to have an overlap region between their respective field of view of about 14 cylinder diameters. An optical calibration is performed on both the cameras as described in Heikkila (2000). Using the calibration parameters, dewarping is applied to the two cameras images in order to match the overlap region, as in Giordano et al. (2012). The overlap regions of both images are dewarped on the same grid (size 1548×443 pixels^2) with resolution equal to 110 pix/D (11 pix/mm). The PIV interrogation strategy is an iterative multistep image deformation algorithm with final interrogation window of 32×32 pixels^2 and 75% overlap. The Blackman weighting window is used in the cross-correlation step (Astarita, 2007). The vector validation (universal median test, 5×5 kernel, threshold 2) is implemented similarly to the synthetic test case. The processed images result in 190×52 velocity vectors fields. The POD-based filter is applied on an ensemble of 9000 velocity fields acquired from the lower resolution camera.

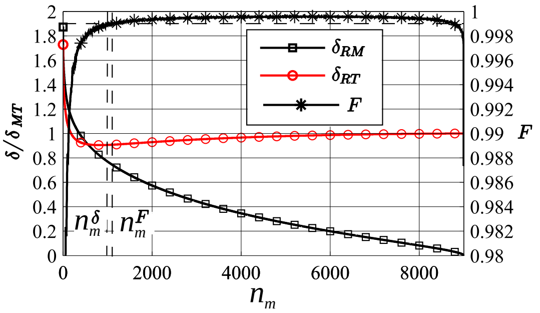

Fig. 3.13 δ_{RT}, δ_{RM} (left axis) and F (right axis) versus the number of modes used in the reconstruction. Errors are normalized with δ_{MT}.

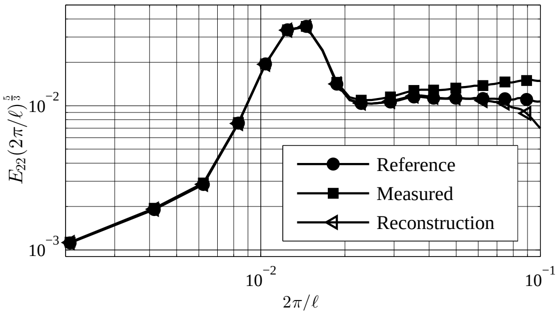

Fig. 3.14 Compensated transverse velocity spectra E_{22} in stream-wise direction versus wavenumber $2\pi/\ell$.

The values of $\delta_{RM}(n_m)$, $\delta_{RT}(n_m)$ and of the function $F(n_m)$ (low-pass filtered by windowed linear-phase FIR digital filter with 25 points span and normalized cutoff frequency 0.0313) are plotted in Fig. 3.13. The reconstruction errors $\delta_{RM}(n_m)$ and $\delta_{RT}(n_m)$ are presented in non-dimensional form, normalized by the error of the measured field over the true field δ_{MT}, that for this test has been estimated to be 1.29 pixels from the high resolution measurements. Compared with the previous synthetic benchmarks, a similar shape in the error both with respect to the measured flow field $\delta_{RM}(n_m)$ and with respect to the true flow field $\delta_{RT}(n_m)$ is found. The minimum δ_{RT} is reached for $n_m^\delta \approx 1000$ (corresponding to 84.7% of the fluctuating energy of the measured field). As in the synthetic benchmark, in this test an extended plateau is present around the value n_m^δ, in which the function δ_{RT} has a nearly constant value of about 0.9 δ_{MT}. By taking as a criterion a value of $F(n_m^F) = 0.999$, an optimum number of modes $n_m^F \approx 1100$ is found. For a number of modes higher than n_m^F, the error δ_{RM} has a nearly linear trend that indicates a dominant contribution of random noise to the reconstruction.

In Fig. 3.14 the power spectra of the true, the measured and the reconstructed velocity fields are reported. Data are plotted in the form of compensated spectrum (multiplied by the wavenumber to the 5/3) in order to magnify the effects at the smallest scales; wavelengths are expressed in pixels. Wavelengths smaller than 64 pixels are not considered in the comparison. This limit is posed to account for the filtering behaviour of the PIV algorithm itself, that degrades spectral information at scales comparable to the interrogation window size. The reconstruction with 1100 modes closely follows the reference field spectral behaviour nearly up to the limit considered in the comparison, slightly underestimating the spectral power (4% error at 90 pixels).

The spectrum obtained from non-filtered data, instead, considerably overestimates the reference spectrum even at large scales (14% at 160 pixels and 25% at 90 pixels) due to its noise content.

The direct comparison of raw, filtered and reference fluctuating velocity fields (Fig. 3.15) gives a better insight on the noise removal obtained using the POD-based filter. The raw measured flow field (Fig. 3.15c) is degraded by measurement noise if compared to the reference field (Fig. 3.15a). A number of spurious vectors are present in the measured field, and even some large-scale flow structures appear to be distorted and hard to recognize. The POD-filtered velocity field (Fig. 3.15b) is smoother and more regular than both measured field (Fig. 3.15c) and reference field (Fig. 3.15a). This result has a twofold explanation: indeed one should consider that the reference field itself is a measurement, meaning that it contains some measurement uncertainty and thus noise. Moreover the POD-filter is able to recover coherent structures in the field and save them from being smeared out in the filtering process. While this certainly happens for large structures that are well discretized, this is not likely to happen to poorly discretized structures due to the nature of the proposed method, that looks for a trade-off between flow field description and noise removal. This behaviour can be better appreciated in the velocity spectrum (Fig. 3.14), where the POD reconstruction appears to overfilter the smaller scales.

3.5 Conclusion

In this chapter it has been introduced a feature-oriented filter for applications in flow field measurements (and specifically for PIV measurements) based on the property of the POD to achieve a good spectral separation between correlated features and uncorrelated random noise. The reduction of the random error attained through this method is extremely beneficial in the computation of derivative quantities of the flow field, which are more prone to be affected by noise amplification. The feature-oriented filter relies on the truncated low-order reconstruction obtained from the POD of the velocity fields. The existence of an optimal number of POD modes to achieve random error minimization in low-order reconstruction of randomly perturbed flow fields (such as PIV data) has been demonstrated mathematically assuming a reference spectrum to model the flow features (i.e. the Kolmogorov spectrum in the inertial range). While the existence of a minimum-error reconstruction can be easily extended to any other flow spectral behaviour different from the white one, the theory developed in this chapter

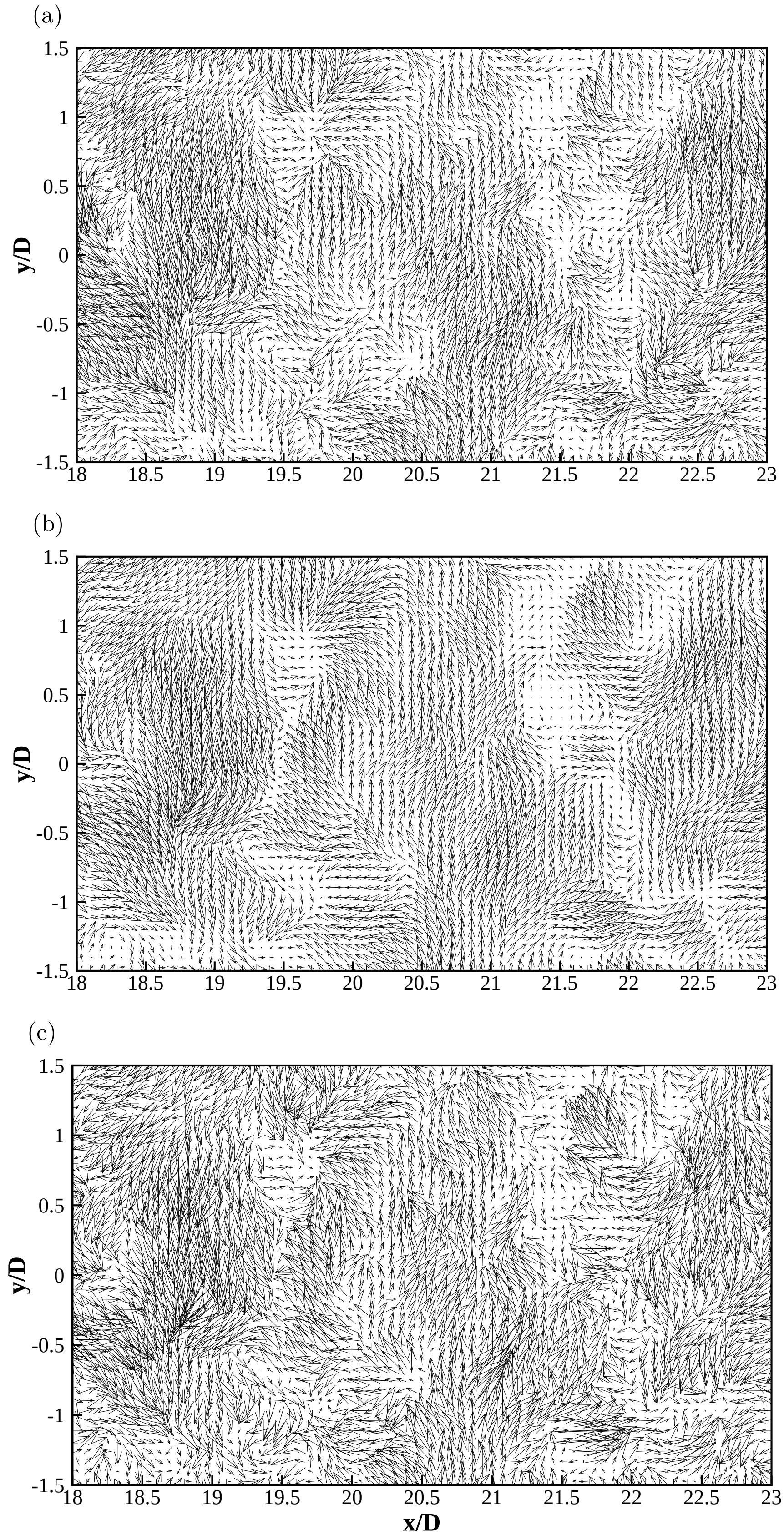

Fig. 3.15 Magnified view of fluctuating velocity fields: a) reference velocity field, b) velocity field reconstructed with 1100 POD modes, c) measured velocity field.

cannot be employed to obtain the optimal number of POD modes without the direct knowledge of the noise-free field spectral behaviour.

An empirical criterion for the choice of the optimal number of modes has been therefore indicated and validated. The optimal number of modes can be obtained by simply observing the variation of the difference between the reconstructed fields and the original ones, without adding any hypothesis on the features of the flow field itself, thus making the method robust and flexible. Following the *scree plot* method, the optimal number of modes can be identified with a threshold on the second derivative of the reconstruction error. The robustness of the optimum identification is guaranteed by the relatively low sensitivity of random error to the number of modes.

The method has been validated on synthetic images ensembles generated from a channel-flow DNS dataset and on real PIV measurements in the wake of a circular cylinder. In the first test case the error is dominated by modulation effects, which cannot be recovered by the POD-based low-order reconstruction. Nevertheless, a total error reduction of about 18% is achieved, corresponding to a value that is about the 33% of the noise estimated with a zero-displacement benchmark test, while retaining most of the spectral information of the original field. The vorticity distributions highlight that the method is able to suppress spurious vorticity blobs without removing original vortical structures with comparable size and intensity. The spectra of the data closely follow those of the DNS for a wider portion of the wavelengths with respect to reconstruction with a larger number of modes. The cutoff wavelength is slightly larger than twice the interrogation window size. In the experimental test case a total error reduction of about 10% with respect to the reference field is achieved. The velocity spectrum of the low-order reconstruction reveals that noise reduction preserves small scale structures down to scales comparable with the interrogation window size. Furthermore, the low-order reconstruction is very effective in removing clusters of spurious vectors, which generally pose a challenge to the standard validation methods. An extensive parametric validation with synthetic test cases is performed, proving the robustness of the method and of the criterion used for the identification of the optimal low-order reconstruction.

As expected, the improvement is more evident on derivative quantities (see, for instance, the vorticity spectra). Comparison with common spatial filtering techniques provides a clear idea of the advantages that this technique could introduce, especially for measurement of turbulence statistics.

The method described here is expected to contribute in enhancing the reliability of PIV as it allows for uncertainty reduction and robustness improvement. The spatial resolution might also indirectly benefit from it. Indeed, generally the choice of the processing algorithm (window size, interrogation method, etc.) arises from a trade-off between desired spatial resolution and measurement noise amplification. The optimal low-order reconstruction allows for the use of advanced high-resolution interrogation algorithms since the random noise can be consistently reduced in the post-processing phase. As turbulent flows investigation is demanding in terms of dynamic spatial range requirements, this advancement would be beneficial.

As a final note, while the method has been here described specifically for PIV applications, it can be easily extended to other measurements. As an example, in Raiola et al. (2017) an application to temperature maps measured with infrared thermography is described. In this case, the random error reduction is extremely beneficial to obtain a better estimate of small temperature fluctuations, paving the way to time-resolved heat transfer measurements.

Chapter 4

Eigenbackground removal for PIV images

PIV image quality is often affected by time-dependent light reflections and strongly non-uniform background, which are challenging to be removed by image pre-processing. It is clear that the image quality strongly affects the final results; consequently, the benefits of proper image conditioning are expected to flow along the processing chain and to reduce the measurement uncertainty. In this chapter, modal analysis will be exploited in a quite different scenario than in the previous and in the following chapters, with the aim of enhancing the PIV image quality. The method presented here is based on the concept of *eigenbackground*, and it has been published in the work by Mendez et al. (2017). Eigenbackgrounds are closely related to the Proper Orthogonal Decomposition as they represents the *topoi* obtained by the modal decomposition of an image sequence. Exploiting the different spatial and temporal coherence of background and particles images, it is possible to isolate the former from the latter in the POD spectrum. A reduced-order model (ROM) can be extracted, retaining the PIV particle pattern, while excluding the highly coherent background included in the low-rank modes. Therefore, this methodology may be intended as a "high-pass" filter in the POD spectrum, and represents the specular approach of the filter proposed in Chapter 3. It should be noted that in this scenario the separation between coherent and non-coherent scales is much stronger than in the scenario reported in the previous chapter due to the rank-deficiency of the background features, as shown by Mendez et al. (2017).

The enhancement of the image quality obtained by filtering out the background features allows to significantly reduce the uncertainty of the PIV measurements, especially near walls and in conditions in which good imaging is difficult to be achieved. It is shown that the improvement of the image quality obtained through this method is independent of the image sequence temporal resolution, background features sharpness or brightness. After introducing the theoretical framework, the method is tested on synthetic and experimental images. Finally the method is compared with widely used pre-processing techniques in terms of image quality enhancement, improvements in the PIV interrogation and computational cost to assess its performances. An open-source version of the pre-processing tool presented in this chapter is available at `http://seis.bris.ac.uk/~aexrt/PIVPODPreprocessing/`.

4.1 State of the art in pre-processing methods for PIV images

Particle Image Velocimetry infers velocity fields from the analysis of image pairs/sequences, either with statistical operators (cross-correlation, least-square matching) or with individual particle tracking, or with a combination of them. Regardless of the method employed to identify the particle displacement, the final accuracy of the velocity measurement strongly relies on the quality of the images which are fed to the PIV algorithm. An ideal PIV image consists of bright particles (with a typical diameter of 2-3 pixels, Westerweel, 2000) over a perfectly dark background (Fincham and Spedding, 1997, Okamoto et al., 2000). For a set of ideal PIV images, the identification of the cross-correlation peak position can be obtained with a sub-pixel accuracy of the order of 0.01 pixels (Fincham and Delerce, 2000). In real PIV images, however, several undesired background features usually pollute the cross-correlation map and lower the accuracy of the measurement. Some examples are uneven gray level offsets produced by multiple laser light reflections due to variations in the refractive index within the experimental setup, or random noise produced by camera dark noise and multiple light scattering between particles. These background features typically reduce the signal-to-noise ratio of the particle displacement cross-correlation peak by both reducing the particle contrast and introducing spurious peaks in the cross-correlation map.

The image quality can be improved during the imaging phase by physically reducing the laser light reflected towards the camera. For instance, for PIV measurements over opaque objects, a proper material selection or an adequate surface treatment can reduce the omnidirectional light scattering (Paterna et al., 2013) while a suitable camera observation angle can reduce the reflected light gathered by the image sensor (Lin, 1998). These solutions, however, strongly depend on the actual experimental setup and often can not be implemented due to restrictions in the model materials and/or on the optical access. Therefore, the PIV image quality is generally enhanced in the post-recording stage. Two common approaches to improve the image quality are *levelization* and *normalization*. In the *levelization* approach a reference intensity map, representative of the background, is subtracted from each PIV image. The reference intensity map can be obtained from low-pass filtered versions of the images (Willert, 1997) or by considering each PIV frame as the reference intensity of the following (Honkanem and Nobach, 2005, Mejia-Alvarez and Christensen, 2013). Alternatively, when the image set is sufficiently large, the reference images can be obtained on a statistical ground by considering the ensemble minimum intensity (Gui et al., 1997), the ensemble average (Werely and Gui, 2002) or the intensity probability density distribution (Stitou and Riethmuller, 2001). In the *normalization* approach the original image intensity is rescaled using the entire dynamic range available in order to maximize the contrast between particles and background. This rescaling can be accomplished via either linear or non-linear transformations (Dellenback et al., 2000). The rescaling can be performed globally on the full image or locally on small portions of the image (Zuiderveld, 1994, Hart, 1996, Roth and Katz, 2001). The intensity capping method proposed by Shavit et al. (2007) represents an alternative to the full rescaling of the intensity levels. In this method, the relative intensity of bright objects with respect to particle intensities is limited by setting an upper limit for the gray scale values of the images. The min/max filtering technique proposed by Westerweel (1993) and Meyer and Westerweel (2000) combines both the levelization and the normalization approaches: the original intensity levels of the image are normalized with respect to the minimum and maximum intensities, determined on the $m \times n$ neighbour pixels.

All the pre-processing methods reported above do not perform satisfactorily when reflections are either very bright, largely time-varying, or sharp. To remove similar reflections from the image it is necessary to combine multiple techniques in complex schemes (e.g. Deen et al., 2010, Theunissen et al., 2008) or, in case of time-resolved high-repetition-rate PIV experiments, to employ temporal high-pass filtering (Sciacchitano and Scarano, 2014). The final image quality mostly depends on the experience of the user (Kähler et al., 2016).

In the following, a background removal method based on the Proper Orthogonal Decomposition will be discussed. The mathematical foundations of the method, based of the decomposition of a typical PIV image sequence, are briefly introduced. Finally the method is applied on both a synthetic and an experimental test case to assess the quality improvement achieved by this method.

4.2 Reduced-order modelling of PIV image sequences

In §2.2 it has been shown that the Proper Orthogonal Decomposition can be used to identify a projection basis in which the valuable signal content of a dataset and the spurious random noise can be separated. In this basis, in fact, it is possible to apply a "low-pass" POD-based filter (i.e. a filter cutting out high order modes) to remove the noise content (as shown in Chapter 3). In the following it will be shown that a "high-pass" POD-based filter can instead be applied to a PIV image sequence to retain the particle images and remove the background image.

The strategy for the background features removal described in this chapter relies on the reduced-order modelling of a generic PIV image sequence. The reduced-order modeling of image sequences was first proposed by Oliver et al. (2000) to detect moving objects for automatic video analysis by means of the PCA. A large number of ROM methods has been later applied for pattern recognition and video processing applications (Bouwmans et al., 2016). These methods decompose the original image sequence matrix in the sum of a low-rank component, representative of static and large objects, and a sparse one, representative of small and moving objects. In the following, the reduced-order modelling of a PIV image sequence is introduced accordingly with Mendez et al. (2017).

A PIV image sequence can be considered as the sum of an ideal PIV image sequence $\underline{\underline{A}}_p$ (i.e. bright particle images superimposed onto a black background) and a background image sequence $\underline{\underline{A}}_b$, which can be expressed via the singular value decomposition as:

$$\underline{\underline{A}} = \underline{\underline{\Psi}}\,\underline{\underline{\Sigma}}\,\underline{\underline{\Phi}}^T = \underline{\underline{A}}_p + \underline{\underline{A}}_b = \underline{\underline{\Psi}}_p\,\underline{\underline{\Sigma}}_p\,\underline{\underline{\Phi}}_p^T + \underline{\underline{\Psi}}_b\,\underline{\underline{\Sigma}}_b\,\underline{\underline{\Phi}}_b^T \tag{4.1}$$

with $\underline{\underline{\Phi}}_p$ and $\underline{\underline{\Phi}}_b$ being the set of spatial modes (or *eigenbackgrounds*) respectively of $\underline{\underline{A}}_p$ and $\underline{\underline{A}}_b$. Typically, the background of a PIV image sequence strongly auto-correlates both spatially and temporally. Due to the similarity in the rows and in the columns of the background image sequence, $\underline{\underline{A}}_b$ is close to be rank-deficient ($r_b = \mathrm{rank}(\underline{\underline{A}}_b) \ll n_t$) and only few of its modes are required to approximate it, i.e.:

$$\begin{aligned} &\underline{\underline{A}}_b \approx \underline{\underline{\Psi}}_b \begin{pmatrix} \underline{\underline{I}}_{r_b} & \underline{\underline{0}} \\ \underline{\underline{0}} & \underline{\underline{0}} \end{pmatrix} \underline{\underline{\Sigma}}_b\,\underline{\underline{\Phi}}_b^T \\ &\sigma_b^{(i)} \approx 0 \quad ,\forall i > r_b \end{aligned} \tag{4.2}$$

with $\underline{\underline{I}}_{r_b}$ being the rank r_b identity matrix.

For an ideal PIV sequence, it is possible to consider each image as a realization of a random variable. If statistical convergence is reached such that the spatial average μ_p and the spatial standard deviation ς_p are valid for the entire sequence, the inner product of the ideal PIV sequence reads:

$$\underline{\underline{K}}_p = \underline{\underline{A}}_p \underline{\underline{A}}_p^T \approx n_p \left(\mu_p^2 \underline{\underline{1}} + \varsigma_p^2 \underline{\underline{I}}_{n_t} \right) \tag{4.3}$$

where $\underline{\underline{1}} \in \mathbb{R}^{n_t \times n_t}$ is a square matrix of ones and $\underline{\underline{I}}_{n_t}$ the rank n_t identity matrix.

For a statistically-converged PIV image sequence, it is possible to assume the following:

Assumption 1. *For $i > r_b$, the contribution of the ideal PIV image sequence $\underline{\underline{A}}_p$ is equally distributed, such that $\sigma_p^{(i)} \approx \sigma_p^{(i+1)}\,, \forall i \in [r_b, n_t - 1]$. In particular, for $i > 1$: (i) the singular values of the ideal PIV sequence are equal to $\sqrt{n_p}\varsigma_p$; (ii) the eigenvector of the ideal PIV image sequence $\underline{\underline{A}}$ are orthonormal to the constant vector $\underline{1}$, such that $\left(\underline{\psi}^{(i)}, \underline{1}\right) = 0\,, \forall i \in [2, n_t]$.*

Assumption 2. *For $i > r_b$, the decomposition of the image sequence $\underline{\underline{A}}$ is aligned with that of the ideal PIV sequence $\underline{\underline{A}}_p$, such that $\sigma^{(i)} \approx \sigma_p^{(i)}\,, \forall i \in [r_b, n_t]$.*

For a theoretical proof of these assumptions, the reader is referred to the original journal paper (Mendez et al., 2017). The complete theoretical derivation of the properties of the PIV image set decomposition is not included in this dissertation since its development is mostly a contribution of the first author of the paper, i.e. Miguel Alfonso Mendez.

4.2.1 Eigenbackground removal algorithm and error estimation

Since the background sequence is rank-deficient ($r_b \ll n_t$) and according to *Assumption 1* ($\sigma_p^{(i)} \approx \sigma_p^{(i+1)}\, \forall i \in [r_b, n_t - 1]$), an estimate of the ideal PIV image sequence $\underline{\underline{A}}_p$ underlying the image sequence $\underline{\underline{A}}$ (Eq. 4.1) can be obtained by filtering out its first r_b POD modes:

$$\underline{\underline{A}}_p = \sum_{i=1}^{n_t} \underline{\psi}_p^{(i)} \sigma_p^{(i)} \underline{\phi}_p^{(i)\,T} \approx \underline{\underline{A}}_{p,r_b} = \sum_{i=r_b+1}^{n_t} \underline{\psi}_p^{(i)} \sigma_p^{(i)} \underline{\phi}_p^{(i)\,T} \tag{4.4}$$

Moreover, according to *Assumption 2* ($\sigma^{(i)} \approx \sigma_p^{(i)}\, \forall i \in [r_b, n_t]$), it is reasonable to expect the eigenfunctions of $\underline{\underline{A}}$ to be aligned with those of $\underline{\underline{A}}_p$ for $i > r_b$, thus:

$$\begin{cases} \underline{\phi}^{(i)} \approx \underline{\phi}_p^{(i)} \\ \underline{\psi}^{(i)} \approx \underline{\psi}_p^{(i)} \end{cases} , \forall i \in [r_b + 1, n_t] \tag{4.5}$$

Using Eq. 2.19, the background-free estimation of the image sequence reads:

$$\underline{\underline{A}}_{p,r_b} \approx \underline{\underline{A}}_{r_b} = \sum_{i=r_b+1}^{n_t} \underline{\psi}^{(i)} \sigma^{(i)} \underline{\phi}^{(i)\,T} = \underline{\underline{A}}_p \, \underline{\underline{\Phi}}_{r_b} \, \underline{\underline{\Phi}}_{r_b}^T \tag{4.6}$$

where $\underline{\underline{\Phi}}_{r_b} = \left[\underline{\phi}^{(r_b+1)}, \ldots, \underline{\phi}^{(n_t)}\right]$ is the basis for the reduced-order model of $\underline{\underline{A}}$.

The combination of *Assumption 1* and *Assumption 2* gives the condition $\sigma^{(i)} \approx \sigma^{(i+1)}\, \forall i \in [r_b, n_t - 1]$. In addition to the equality of the singular values, the temporal modes $\underline{\psi}^{(i)}$ approximating the ideal PIV sequence are required to be orthonormal to $\underline{\psi}_p^{(1)} = \underline{1}/\sqrt{n_t}$, i.e. $\left(\underline{\psi}^{(i)}, \underline{1}\right) = 0$, according to *Assumption 1(ii).* The occurrence of these two conditions identifies the interval $[r_b + 1, n_t]$ of the POD modes that approximate the PIV pattern and, thus, that have to be retained in the reconstruction. Once the reconstruction interval is defined according to the criteria given above, the reduced basis restricted to this interval can be built and used as projection basis for the set of images. To minimize the number of background modes in case of significant difference in the illumination of two consecutive camera exposures, the algorithm should be applied independently on the two sequences containing the first and second PIV exposures. This is also beneficial to limit the memory requirements of the algorithm.

The pseudo-code of the eigenbackground removal method is reported in *Algorithm* 1, where the tolerances in line 6 are set as $\varepsilon_1 = 0.01\sigma_p^{(i)} = 0.01\sqrt{n_p}\varsigma_p$ and $\varepsilon_2 = 0.01$.

```
1: Reshape 2D Images $\underline{\underline{Im}}^{(i)} \in \mathbb{R}^{n_x \times n_y}$ in $\underline{a}^{(i)} \in \mathbb{R}^{1 \times n_p}$
2: Assemble Snapshots Matrix $\underline{\underline{A}} \in \mathbb{R}^{n_t \times n_p}$
3: Compute $\underline{\underline{K}} = \underline{\underline{A}}\,\underline{\underline{A}}^T$
4: Diagonalize $\underline{\underline{K}} = \underline{\underline{\Psi}}\ \underline{\underline{\Sigma}}^2\ \underline{\underline{\Psi}}^T$
5: Compute $\underline{\underline{\Phi}} = \underline{\underline{A}}\ \underline{\underline{\Psi}}^T\ \underline{\underline{\Sigma}}^{-1}$
6: Find $r_b :\ \sigma^{(i+1)} - \sigma^{(i)} < \varepsilon_1$ & $\left(\underline{1}/\sqrt{n_t}, \underline{\psi}_p^{(i)}\right) < \varepsilon_2\ \ \forall i > r_b$
7: Construct $\underline{\underline{\Phi}}_{r_b}^T = \left[\underline{\phi}^{(r_b+1)\,T}, \ldots, \underline{\phi}^{(n_t)\,T}\right]$
8: Compute $\underline{\underline{A}}_{r_b} = \underline{\underline{A}}\,\underline{\underline{\Phi}}_{r_b}^T\,\underline{\underline{\Phi}}_{r_b}$ with $\underline{\underline{A}}_{r_b} = \left[\underline{a}_{r_b}^{(1)}, \ldots, \underline{a}_{r_b}^{(n_t)}\right]$
9: Reshape $\underline{a}_{r_b}^{(i)} \in \mathbb{R}^{1 \times n_p}$ back to $\underline{\underline{Im}}_{r_b}^{(i)} \in \mathbb{R}^{n_x \times n_y}$
```

Algorithm 1 POD Filter for PIV Image pre-processing.

A measure of the particle pattern's intensity retained in the reconstructed image sequence $\underline{\underline{A}}_{r_b}$ is given by the recovery ratio R, defined using the Frobenius norm as:

$$R = \frac{\left\|\underline{\underline{A}}_{p,r_b}\right\|_F}{\left\|\underline{\underline{A}}_{p}\right\|_F} \approx \frac{\left\|\underline{\underline{A}}_{r_b}\right\|_F}{\left\|\underline{\underline{A}}_{p}\right\|_F} = \sqrt{\frac{\sum_{r_b+1}^{n_t} \sigma_p^{(i)\,2}}{\sum_1^{n_t} \sigma_p^{(i)\,2}}} \tag{4.7}$$

where the last two equalities are a result of Eq. 4.6 and of *Assumption* 2.

It is possible to demonstrate (see Mendez et al., 2017, for further details) that the recovery ratio of the POD-filtered image sequence is equal to:

$$R = \sqrt{\frac{(n_t - r_b)\varsigma_p^2}{\mu_p^2 n_t + n_t \varsigma_p^2}}\ . \tag{4.8}$$

Eq. 4.8 can be used to estimate the error introduced by the approximations in Eq. 4.4 and Eq. 4.6 and thus the impact of the algorithm on the PIV particle pattern. Observing that ideal PIV images are characterized by an exponential probability density distribution (Westerweel, 2000), it is possible to assume that $\varsigma_p^2 \gg \mu_p^2$, and thus estimate the recovery ratio as $R \approx \sqrt{1 - r_b/n_t}$. Finally, it is interesting to observe that upon the assumption of statistical convergence (i.e. that the image set is large enough to obtain a good estimate for μ_p and ς_p), the recovery ratio does not depend on the image resolution n_p.

4.3 Validation

4.3.1 Statistical convergence of an ideal PIV sequence

The hypothesis of statistical convergence in ideal PIV images is tested on sequences of synthetic PIV images characterized by different sizes $n_p = n_x \times n_y$, number of images n_t and image particle concentration C_p. Random particle positions (i_p, j_p, k_p) (expressed in pixels) are extracted from a volume such that $i_p \in [1, n_x]$, $j_p \in [1, n_y]$ and $k_p \in [-0.5, 0.5]$. Particle images are superposed onto a perfectly dark background. The intensity map $\mathrm{Im}_p(i,j)$ of each image is defined as:

$$\mathrm{Im}_p(i,j) = \sum_{p=1}^{N_P} \mathscr{I}_L(k_p)\mathscr{I}_P(i - i_p, j - j_p, d_p, p_f)\ , \tag{4.9}$$

where N_P is the number of particles per image ($N_P = C_p n_p$) and $\mathscr{I}_L$ is the intensity of the laser sheet. $\mathscr{I}_P$ refers to the 2D Gaussian intensity distribution produced by a particle of d_p pixels diameter, centered in (i_p, j_p) and integrated over the sensitive

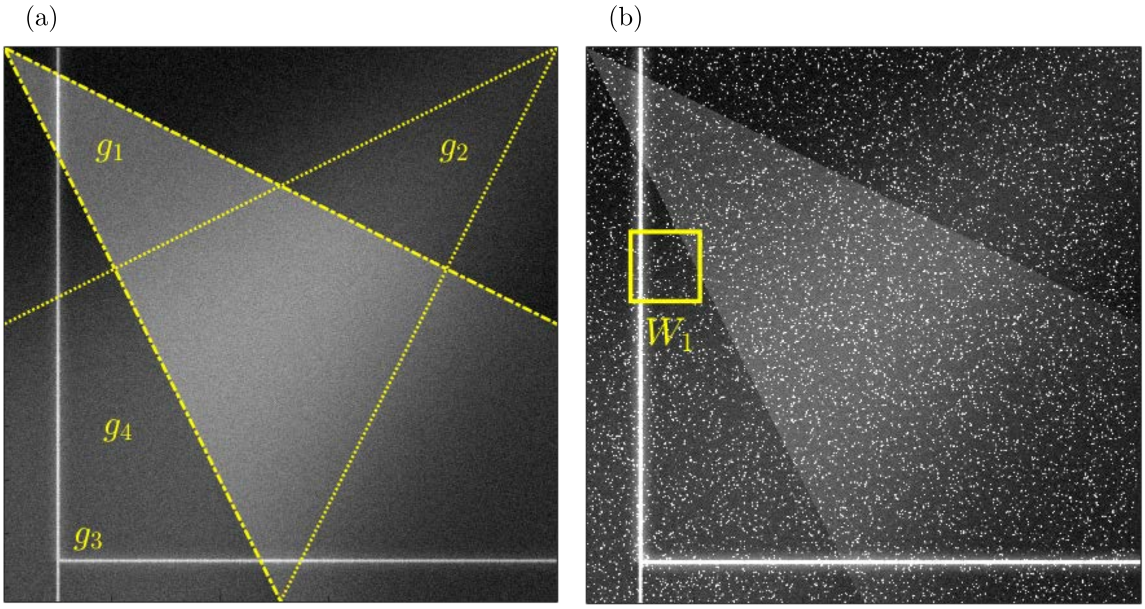

Fig. 4.1 Example snapshot of the background source $\underline{a}_b^{(i)}$ (a) and corresponding PIV synthetic image $\underline{a}^{(i)} = \underline{a}_b^{(i)} + \underline{a}_p^{(i)}$ (b). The insert W_1 is illustrated in Fig. 4.6.

part of a pixel having fill factor p_f. The laser profile $\mathcal{I}_L$ is assumed to be Gaussian (Raffel et al., 2007) and the particle intensity $\mathcal{I}_P$ is expressed in terms of error function (Lecordier and Westerweel, 2004) assuming aberration-free optics. The pixel fill factor is set to 0.7 and particle diameters are selected from a normal distribution with a mean of 2 pixels and standard deviation of 0.5 pixels. The camera's dynamic range is set to $0 - 255$ (8 bits). The test is performed for two particle densities representing extreme conditions for practical PIV experiments: $C_p = 0.0064$ and $C_p = 0.287$ particles per pixel (*ppp*), corresponding to source densities of $N_s = 0.02$ and $N_s = 0.9$, where the source density N_s (Adrian and Westerweel, 2011) can be computed as C_p times the particle area. A representative image is shown in Fig. 4.1 for each source density. For each synthetic PIV image sequence the actual inner product matrix $\underline{\underline{K}}_p$ is compared to the theoretical prediction given in Eq. 4.3. The Frobenius norm is selected to quantify the deviation from the hypothesis of statistical convergence over the entire singular value spectrum. The error for varying image size $n_p = n_x \times n_y$ and number of images n_t is given by:

$$E_F = \frac{\left\| \underline{\underline{K}}_p - n_p \left(\mu_p^2 \underline{\underline{1}} + \varsigma_p^2 \, \underline{\underline{I}}_{n_t} \right) \right\|_F}{\left\| \underline{\underline{K}}_p \right\|_F} \tag{4.10}$$

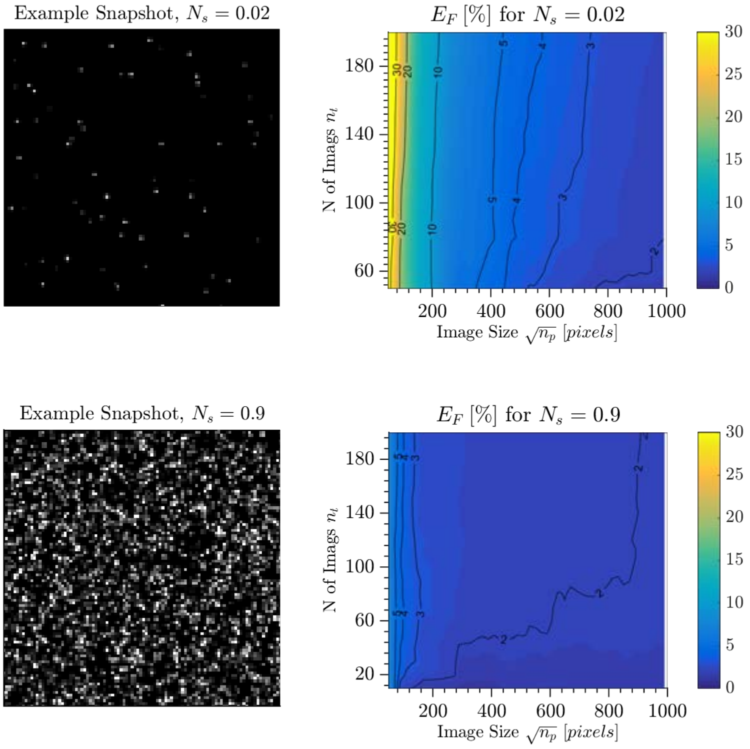

Fig. 4.2 Analysis of statistical convergence on synthetic PIV images with source density $N_S = 0.02$ (example in *top-left*) and $N_S = 0.9$ (example in *bottom-left*). In *top-right* and *bottom-right* are compared the corresponding error maps, defined in term of Frobenius norm in Eq. 4.10, as a function of image size and number of images.

Fig. 4.2 shows the resulting error maps for several sequences of square images. The source density N_s and the image size n_p strongly affect the error map, with lower source densities and smaller image sizes deviating more significantly from the statistical convergence hypothesis. The number of images n_t has a minor influence on the validity of the hypothesis. For a set of images of realistic size, ($\sqrt{n_p} > 600$), the error E_F is within 2%, even at very low particle concentrations, confirming the validity of the hypothesis.

4.3.2 Background removal in a synthetic test case

The assumptions given in §4.2 are tested on a synthetic PIV image sequence. Additionally, the background removal performances of the proposed image-quality enhancement algorithm (§4.2.1) are compared to those of common PIV pre-processing techniques.

The image sequence is composed of a set of synthetic image pairs. A total of $n_t = 200$ statistically independent image pairs with resolution of $n_p = 1024 \times 1024$

pixels is used. Each image is constructed as the sum of an ideal PIV sequence $\underline{\underline{A}}_p$ and a background sequence $\underline{\underline{A}}_b$ as assumed in Eq. 4.1. The displacement of the particles contained in the ideal PIV sequence $\underline{\underline{A}}_p$ is extracted from the DNS of a channel flow included in the John Hopkins Turbulence Database (Li et al., 2008, Yu et al., 2012a, Graham et al., 2013). The velocity fields used for the generation of the synthetic PIV images are extracted from the database as described in Chapter 3. For the image database used in this chapter, the particles are randomly distributed in space with a concentration of 0.01 ppp and with diameters randomly assigned according to a normal distribution with a mean of 3 pixels and standard deviation of 0.5 pixels. The laser intensity is modelled with a Gaussian profile with half power width equal to 4 pixels along the laser sheet thickness direction, in order to take into account the effect of correlation degradation due to the out-of-plane motion.

The intensity maps Im_b forming the background sequence $\underline{\underline{A}}_b$ are constructed as the sum of four sources each having a spatial structure $g_k(i,j)$ and temporal evolution $f_k(n)$:

$$\mathrm{Im}_b(i,j,n) = \sum_{k=1}^{4} f_k(n)\, g_k(i,j) \tag{4.11}$$

Since this background sequence would be characterized by time-resolved background features, the images are randomly reordered inside the sequence. The first two background sources introduce in the image brighter triangular areas bounded by lines connecting the top corners with the mid-points on the opposite side (g_1, g_2 in Fig.4.1). Within these regions, the gray intensity levels have a Gaussian form:

$$g_{1,2} = \exp\left(\frac{-(i-i_{01,2})^2-(j-j_{01,2})^2}{2\varsigma_{g1,2}^2}\right) \tag{4.12}$$

centered in the top corners $(i_{01}, j_{01}) = (1,1)$ and $(i_{02}, j_{02}) = (1, n_x)$. These Gaussians have standard deviations of respectively $\varsigma_{g1} = 800$ pixels and $\varsigma_{g2} = 1600$ pixels. The resulting gray level distributions are further blurred with a square Gaussian kernel of 150 pixels, leading to different levels of intensity and sharpness. The temporal evolution of these two noise sources is simulated with squared sinusoids of the form:

$$f_{1,2}(n) = \mathcal{J}_{1,2} \sin^2\left(\frac{2\pi}{T_{1,2}} n - \theta_{1,2} + f_{m1,2}\right) \tag{4.13}$$

where the periods, in terms of number of images n, are chosen as $T_1 = 15n$ and $T_2 = 33n$; the phase delays are $\theta_1 = 0$, $\theta_2 = \pi/2$; both amplitudes are $\mathcal{J}_{1,2} = 100$ counts and the average intensity is $f_{m1,2} = 40$ counts. The third source g_3 accounts for

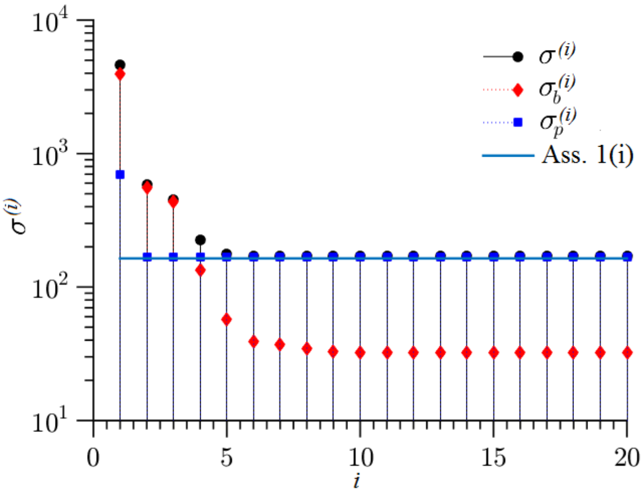

Fig. 4.3 Singular value spectra of the synthetic image sequence $\sigma^{(i)}$, of the background $\sigma_b^{(i)}$, and of the ideal PIV pattern $\sigma_p^{(i)}$ sequences, compared to the theoretical spectrum of the ideal particle images $\sqrt{n_p}\varsigma_p$. To improve the figure readability, the plots are limited to $i \leq 20$.

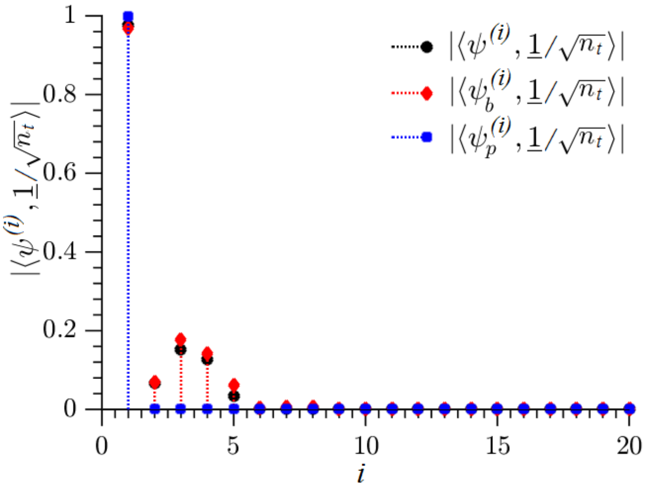

Fig. 4.4 Normalized scalar products of corresponding temporal eigenvectors $\underline{\psi}^{(i)}$, $\underline{\psi}_b^{(i)}$ and $\underline{\psi}_p^{(i)}$ with the constant vector $\underline{1}/\sqrt{n_t}$. To improve the figure readability, the plots are limited to $i \leq 20$.

omnidirectional laser light scattering caused by surface roughness, including flare, over a vertical and a horizontal line. In order to simulate realistic light reflection and flare, for each pixel along the defined horizontal and vertical lines, two Gaussian intensities are superimposed in the normal directions t:

$$g_3(t,i,j) = \mathcal{I}_r \exp\left(\frac{-t^2}{2\varsigma_r^2(i,j)}\right) + \mathcal{I}_f \exp\left(\frac{-t^2}{2\varsigma_f^2(i,j)}\right) \tag{4.14}$$

The reflection intensity amplitude $\mathcal{I}_r$ is set equal to the maximum possible grayscale (255). Prior to spatial smoothing, the widths of the intensity distributions ς_r were drawn from a normal probability with a mean of 2 pixels and standard deviation of 0.5 pixels. Flare is modelled imposing a constant standard deviation ς_f of 10 pixels with a maximum intensity $\mathcal{I}_f$ of 20% of the maximum image intensity, followed by the spatial convolution with a Gaussian of 3 pixels in standard deviation. The resulting intensities

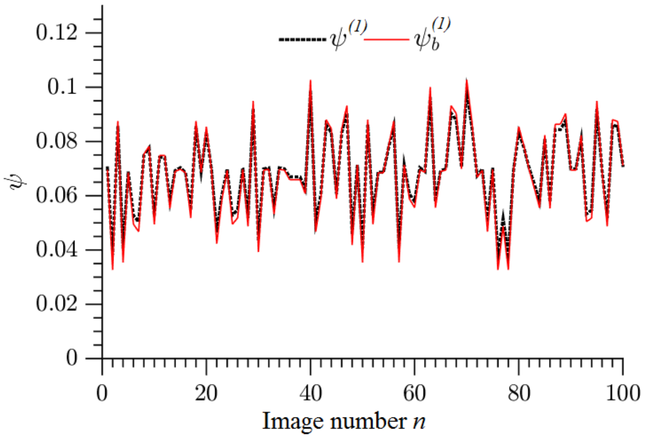

Fig. 4.5 Comparison of the first temporal eigenvectors for the image sequence ($\psi^{(1)}$) and the background sequence ($\psi_b^{(1)}$).

are capped to 255 gray levels before imposing a sinusoidal temporal variation of f_3 with a period $T_3 = 5n$ and an amplitude of $\mathcal{I}_3 = 125$ counts, producing periodical pixel saturation.

Finally, the fourth background source $f_4 g_4$ mimics the thermal camera noise, modelled as a random distribution in both time and space with a mean value of 20 counts and standard deviation of 8 counts.

The singular values of the image sequence $\sigma^{(i)}$, of the background sequence $\sigma_b^{(i)}$ and of the ideal PIV sequence $\sigma_p^{(i)}$ are reported in Fig. 4.3. The theoretical values of the ideal PIV sequence given in *Assumption 1(i)*, i.e. $\sigma_p^{(i)} = \sqrt{n_p}\varsigma_p$, are reported for comparison. For $i > 5$, the singular values of the ideal PIV sequence $\sigma_p^{(i)}$ show a constant value, in agreement with *Assumption 1*, while the singular values of the image sequence become $\sigma^{(i)} \approx \sigma_p^{(i)}$, in agreement with *Assumption 2*. For $i > 5$ the singular values of the background drop to the constant value $\sigma_b^{(i)} \approx 31 \ll \sigma_p^{(i)}$. This value is strictly connected to the random noise component $g_4 f_4$ of the background, having standard deviation of $\varsigma_b = 8/256 \approx 0.031$. As this noise source is randomly distributed both in time and space, the related singular values are such that $\sigma_b^{(i)} \approx \sqrt{n_p}\varsigma_b\,, \forall i \in [r_b + 1, n_t]$, similarly to the ideal PIV sequence. For $i > 5$ the temporal eigenvectors of both the complete image sequence, of the background image sequence and of the particles image sequence result orthogonal to the constant vector $\underline{1}/\sqrt{n_t}$ (see Fig. 4.4) accordingly to *Assumption 1(ii)*. The assumptions in §4.2 are therefore valid also in presence of moderate uncorrelated background, typical of camera sensor noise, as long $\sigma_b^{(i)} \ll \sigma_p^{(i)}$.

Fig. 4.5 compares the first temporal eigenvector of the image sequence with that of the background sequence. Indeed, regardless of the loss of temporal resolution produced by the sequence reordering, the removed POD modes are well representative of the background, as expected from Eq. 4.6.

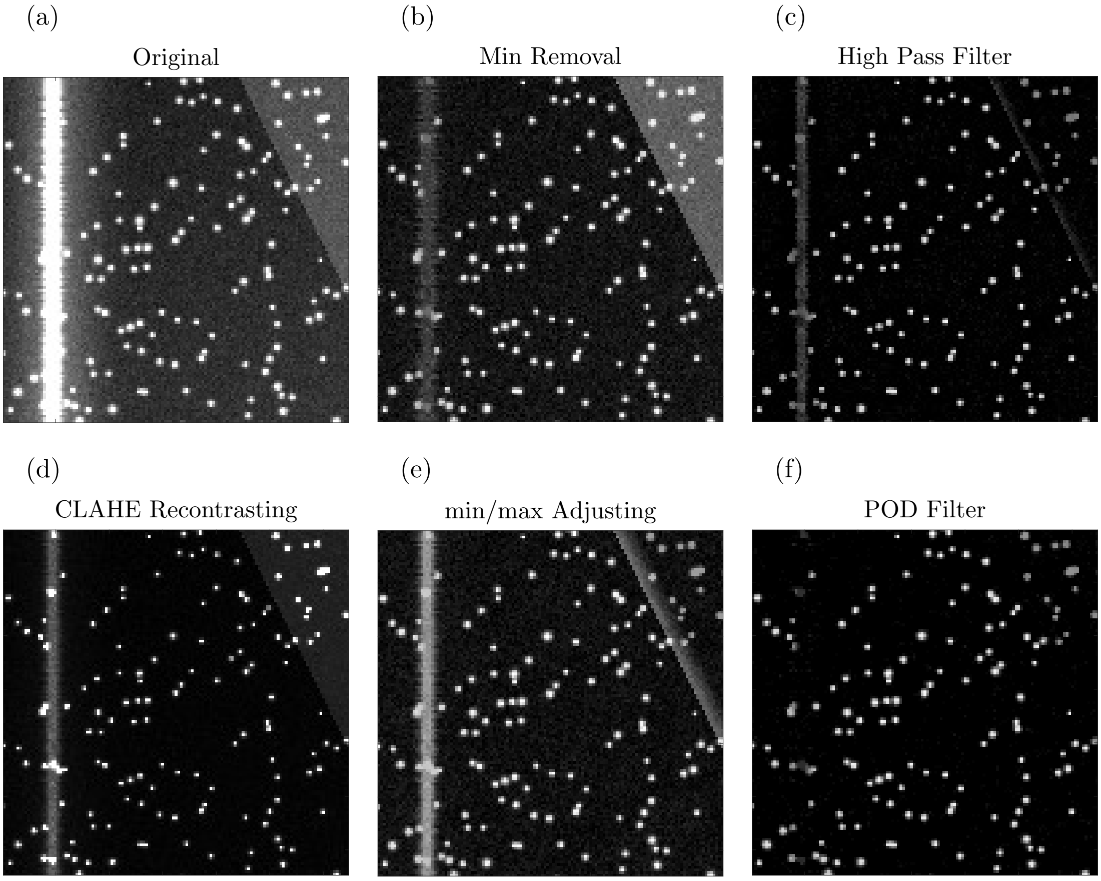

Fig. 4.6 Examples 128×128 image crop in the window W_1 in Fig. 4.1, showing the result of image pre-processing using historical minimum removal, high-pass filtering, CLAHE recontrasting, min/max adjusting and the proposed POD filtering method. While levelization methods such as b) and c) performs poorly for time varying and sharp reflections, normalization methods encounter difficulties for background features brighter than the particle images. The proposed POD filter is insensitive to both issues.

According to the criteria given in §4.2.1, the ideal PIV sequence can be estimated with the last $i \in [6, n_t]$ POD modes of the image sequence (Eq. 4.6). To prove the efficiency of the eigenbackground removal method, its results are compared to that of four popular image pre-processing techniques: the minimum intensity background subtraction (Gui et al., 1997), the high-pass filtering (Willert, 1997), the contrast-limited adaptive histogram equalization (CLAHE) (Shavit et al., 2007, Thielicke and Stamhuis, 2014) and the min/max recontrasting (Westerweel, 1993). For the 128×128 window W_1 shown in Fig. 4.1b, the images pre-processed with each technique are compared to the original one in Fig. 4.6.

The minimum removal method is applied separately on the two series of camera exposure ‘a’ and ‘b’. The high-pass filter is constructed by removing a blurred version of the images using a convolution with a squared Gaussian kernel of size 10 and standard deviation 4. The CLAHE histogram equalization is performed using the Matlab function ‘*adapthisteq*’ with 8×8 *tiles* (i.e. image sub-regions) and exponential histogram distribution with $\alpha = 5$, to reproduce the exponential distribution typical of PIV images (Westerweel, 2000). The min/max method is applied using the *Matlab* function listed in Adrian and Westerweel (2011), using a kernel size of 8×8 pixels^2 and a level of 230 counts. From the comparison, the worst performing method is the minimum removal method (Fig. 4.6b), due to the temporal evolution of the background features in the images. The high-pass filter (Fig. 4.6c) performs well in removing both the blurred background feature g_2 and the random noise source pedestal g_4, but it is challenged by the high gradient regions of the background features g_1 and g_4. An increase of the spatial cutoff frequency may result beneficial to reduce the residuals of the background features g_1 and g_4, but at the cost of chopping the particle images in the smooth areas, and thus increasing the risk of peak locking (Westerweel, 1997). Both CLAHE (Fig. 4.6d) and min/max (Fig. 4.6e) show poor performances in removing the brightest portions of the background exceeding the particle intensities. The proposed POD filter (Fig. 4.6f), instead, is insensitive to reflection intensity, gradient and temporal variations. The reconstructed sequence $\underline{\underline{A}}_{r_b}$ approximates the particles pattern with a recovery ratio $R \approx 96\%$ (Eq. 4.8), being able to recover several particles lying on high-intensity background areas. The eigenbackground removal method has a limited impact on the particles, while background features are almost completely removed.

The impact of the different image pre-processing methods on the estimation of the velocity fields has been analysed using the same PIV interrogation strategy. An iterative multi-step image deformation algorithm (Scarano, 2001), with final interrogation windows of 8×8 pixels^2, 75% overlap has been applied to the pre-processed images. Vector validation is carried out with a universal median test (Westerweel and Scarano, 2005) on a 3×3 vectors kernel and threshold equal to 2. Discarded vectors are replaced with a distance-weighted average of neighbour valid vectors. The interrogation strategy has been implemented by means of a custom-made PIV software, developed at University of Naples Federico II (Astarita and Cardone, 2005, Astarita, 2006, 2007). The results of the PIV algorithm on the window W_1 reported in Fig. 4.6 are shown in Fig. 4.7 for the different pre-processing methods. The contour plots report the velocity magnitude error, defined as the error of the estimated velocity field (u, v) with respect

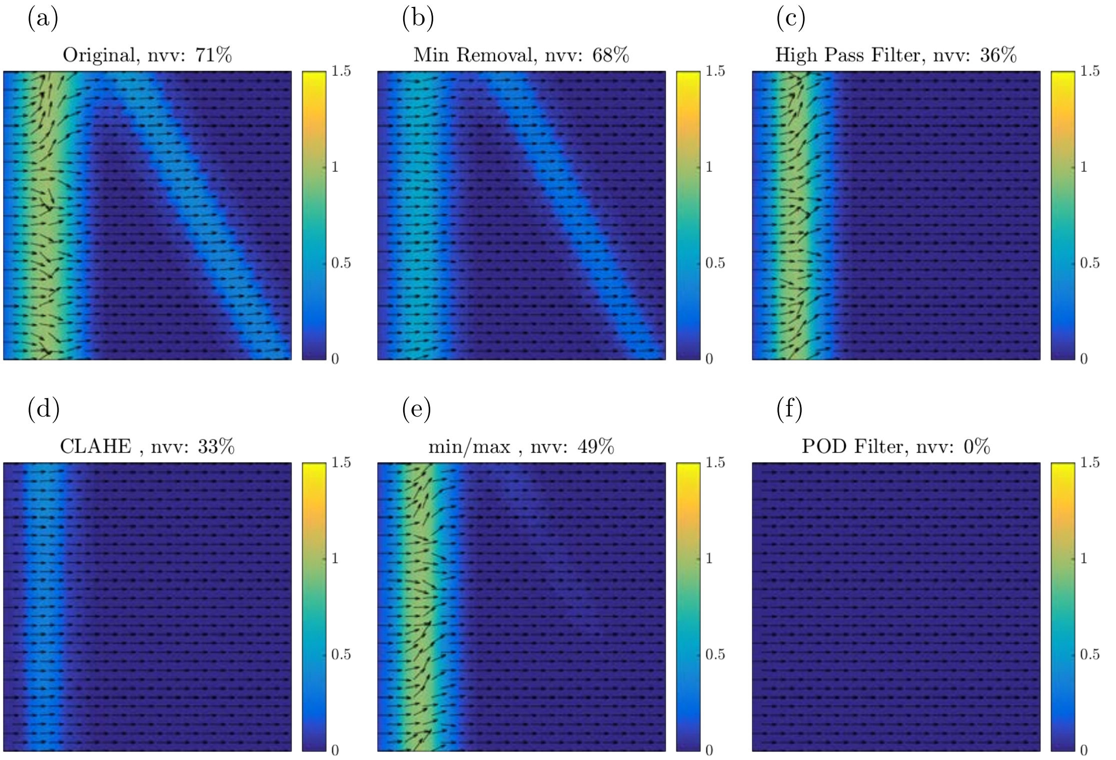

Fig. 4.7 Error plots in the average velocity magnitude within the 128 × 128 example window W_1 in Fig. 4.1, for the original image sequence, historical minimum removal, high-pass filter, CLAHE recontrasting, min/max adjusting, and the proposed POD filtering. The velocity error is defined in Eq. 4.15 and the sub-title reports the percentage of vectors, within the window, for which $Err_V > 0.01$ (nvv).

to the velocity fields evaluated from the ideal PIV sequence $\underline{\underline{A}}_p$ (considered as the reference flow field (u_{ref}, v_{ref})) according to:

$$Err_V = \frac{(u - u_{ref})^2 + (v - v_{ref})^2}{(u_{ref})^2 + (v_{ref})^2} \tag{4.15}$$

The figure sub-titles report the percentage nnv of invalid vectors in the window, which has been calculated in post-processing as the vectors for which $Err_V > 0.01$.

The error on the flow field evaluated from the original images (cf. Fig. 4.7a) is quite large in correspondence of the sharp and time varying edges of the background features g_1 and g_3 (c.f Fig. 4.1). The vector validation introduced in the PIV algorithm results ineffective in reducing this error. The PIV algorithm applied on the original images yields up to 71% of invalid vectors vectors. All the standard pre-processing methods tested (Fig. 4.7b to Fig. 4.7e) suffer from errors produced by the poor background removal performances, which can not be compensated by the outliers interpolation.

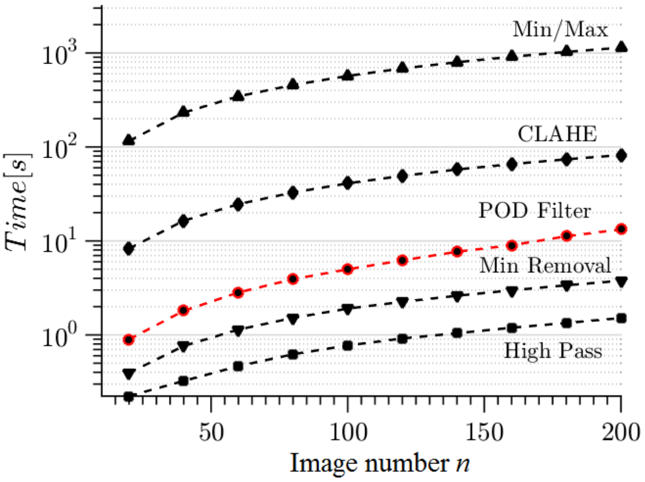

Fig. 4.8 Computational cost of several pre-processing methods as a function of the number of images n_t having resolution of 1Mpixels: min/max adjusting (▲) ; CLAHE recontrasing (◆); proposed POD filter (●); ensemble minimum removal (▼); high-pass filtering (■).

The best results, achieved by the CLAHE re-contrasting, yields 33% of invalid vectors. The proposed POD-based filter (Fig. 4.7f) shows remarkably higher performances with no invalid vectors, resulting in an estimated flow field which matches almost perfectly the ideal one and no invalid vectors.

The computational cost of the tested pre-processing techniques is assessed on a PIV sequence of 1000 × 1000 pixels for different numbers of images n_t in Fig. 4.8. All the methods are implemented on *Matlab 2015* running on an *Intel(TM) i7-3770* processor. While the high-pass filter remains the computationally cheapest method, the computational cost of the proposed POD filter is two orders of magnitude lower than that of the min/max filtering method.

4.3.3 Background removal in an experimental test case

The background removal capabilities of the proposed algorithm have been assessed on an experimental test case featuring unsteady reflections. The selected test case is a PIV investigation of the flow around a 2D flapping wing, sketched in Fig. 4.9.

The flapping motion of the wing consists of a plunging translation along the y-axis and a pitching rotation around the z-axis. The wing section is a NACA 0012 airfoil with a chord of $c = 30\,\mathrm{mm}$ and a span of 490 mm. Plunging and pitching motions are produced by a four-bar linkage, driven by linear actuators in periodic oscillation with an amplitude equal to the wing chord for the heaving and to 10° for the pitching. A detailed description of the experimental setup is given in §6.2.

The experiment is performed in the water tunnel at *Universidad Carlos III de Madrid*, which has a rectangular cross-section of $500 \times 550\,\mathrm{mm}^2$. The free-stream velocity is set to $V_\infty = 0.1\,\mathrm{m/s}$, corresponding to a Reynolds number $Re = V_\infty c/\nu = 3 \cdot 10^3$,

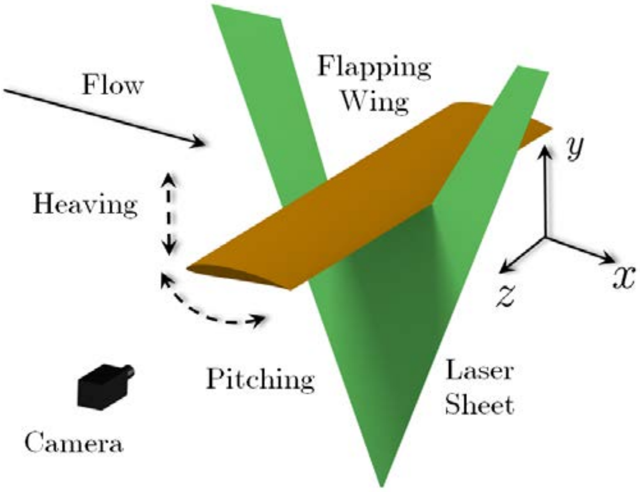

Fig. 4.9 Sketch of the 2D flapping wing experiment. The flow field is illuminated from the bottom, and the wing motion results in time-varying laser light reflection.

and the flapping frequency is set to $f = 0.5\,\mathrm{Hz}$, resulting in a Strouhal number equal to $St = 2cf/V_\infty = 0.3$. The flow is seeded with neutrally-buoyant polyamide particles, with 56 µm diameter. The illumination is provided by a dual cavity Nd:Yag Quantel Evergreen laser (200 mJ/pulse at 15 Hz), reshaped in a sheet with 1 mm thickness, illuminating the flow from the wing lower side. A 5.5 Mpixels Andor sCMOS camera is used to grab $n_t = 400$ image pairs in phase-locked mode, with a resolution of about 12 pix/mm.

A PIV snapshot extracted from the experimental test case is shown in Fig. 4.10 for reference. Fig. 4.10 also includes the intensity difference of two consecutive exposures for a 96×96 image window W located in the trailing edge area. The intensity difference highlights the presence, close to the wing surface, of both particles pairs (with relatively low density) and of a strong reflection which displaces with the wing. Thanks to the low particle density the average particle displacement can be evaluated in about 7 pixels in the x-axis and 10 pixels in the y-axis through a visual inspection. The wing displacement can be evaluated from the reflection in about 1 pixel in the x-axis and 12 pixels in the y-axis. Fig. 4.11d reports the cross-correlation map in the window W for the original image pair. The correlation map is dominated by the correlation peak corresponding to the wing displacement, due both to the high intensity of the reflection and to the low particle density.

The experimental conditions are particularly challenging due to the presence of time-varying reflection caused by laser flickering. Even restricting the image-pre-processing to a phase-locked sub-sample of the image set, random variations in the background intensity map are present, preventing an effective image correction by means of the historical minimum removal method. Fig. 4.11b shows the result on the image crop W

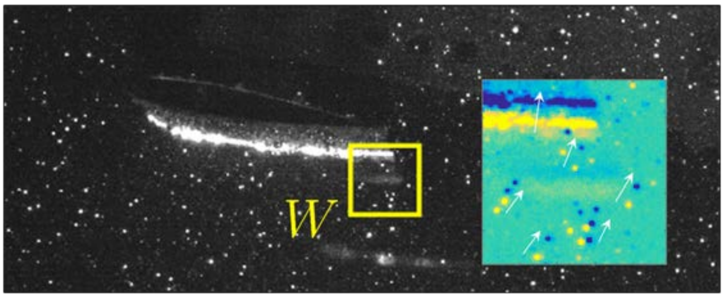

Fig. 4.10 Example of snapshot for the PIV investigation of the flow over a flapping wing. In a 96 × 96 window W located close to the wing trailing edge, the image difference between two exposures is shown (inset). Particles and wing motion are evident, with the yellow referring to the first exposure, the blue referring to the second.

of the minimum removal method (applied separately to the two sequences of image exposures 'a' and 'b'). The persistence of the reflection after the image correction does not allow to identify the particle displacement correlation peak (see Fig. 4.11e), which is covered by the wing motion correlation peak as observed for the raw images.

The eigenbackground removal method is applied separately on both the exposures image sets 'a' and 'b'. The singular-value spectrum for the image set 'a' is reported in Fig. 4.12a; the scalar product of the temporal eigenvectors with the constant vector $\underline{1}/\sqrt{n_t} \in \mathbb{R}^{n_t \times 1}$ is reported in Fig. 4.12b. The eigenbackground removal algorithm (§4.2.1) is applied with $\epsilon_1 = 0.0001\sigma_1$ and $\epsilon_2 = 0.001$. The threshold selected corresponds to the removal of the first $r = 40$ modes from the image sequence a and of the first $r = 35$ modes from the image sequence b. The recovery ratio (cf. Eq. 4.8) is $R \approx 95\%$ from both the image sets.

The results of the eigenbackground removal method on the image crop W are shown in Fig. 4.11c. The intensity of the reflection on the wing is drastically reduced, while particle intensity is not altered appreciably. This results in a cross-correlation map (Fig. 4.11f) from which the wing displacement peak is below the noise-to-signal threshold and a sharp peak for the particle displacement is recovered.

4.4 Conclusions

In this chapter an image pre-processing method for Particle Image Velocimetry (PIV) based on the Proper Orthogonal Decomposition has been described. The eigenbackground removal method relies on the identification of the background source by means of a reduced set of eigenbackgrounds (i.e. the spatial POD modes of an image sequence). Different portions of the singular value spectrum (and thus a different subset of the

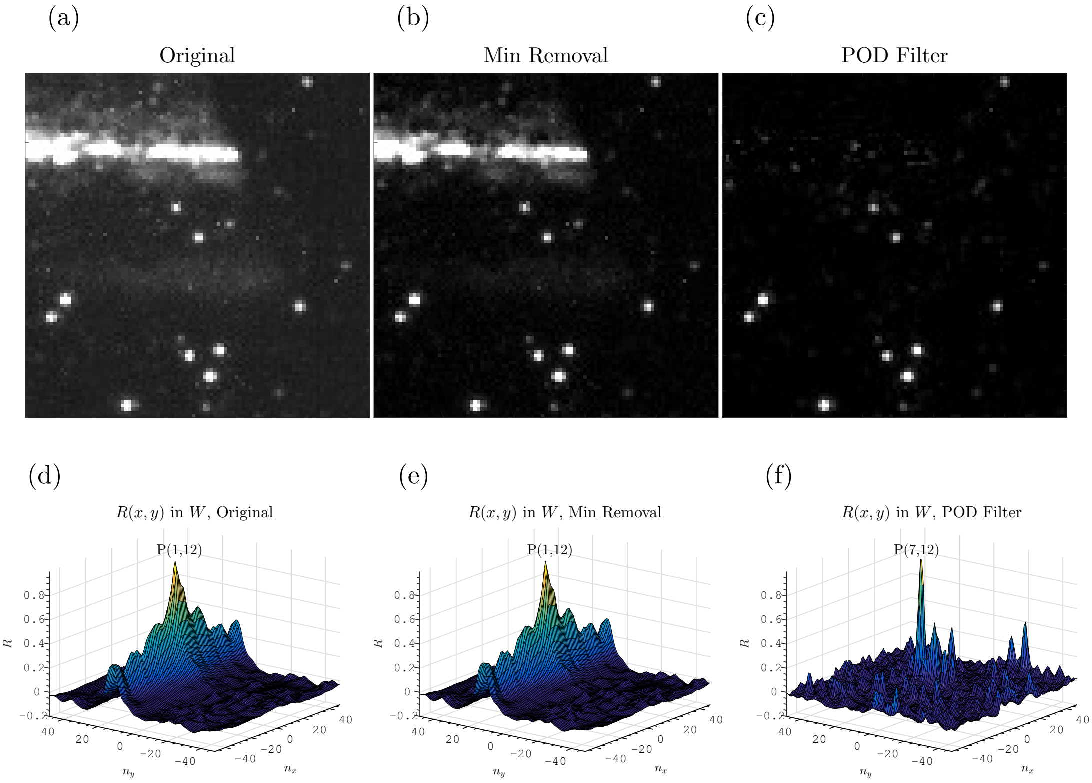

Fig. 4.11 Top: image crop from Fig. 4.10 for the original sequence (a) and the results of the ensemble minimum removal (b) and POD filter (c). Bottom: plots of the corresponding cross-correlation maps. Contrary to the ensemble minimum removal (e), the proposed POD filter (f) is insensitive to the reflection variation produced by the laser flickering and the cross-correlation map recovers the particle displacement.

eigenbackgrounds) of an image sequence can be used to construct either the background features or the particle images. Particles images and background are distinguished according to the higher degree of correlation of the background features compared to that of the particle pattern. In particular, highly-correlated background features are well approximated by a subset formed by the first few eigenbackgrounds. The spectral content of the uncorrelated particle patterns, instead, is equally distributed along the entire spectrum, behaving similarly to white noise. The method identifies the minimal number of modes representing the background features, excluding them from the particle pattern reconstruction. The eigenbackground removal method described in this chapter, therefore, can be considered as a "high-pass" POD-based filter, whereas the filter described in Chapter 3 can be considered as a "low-pass" POD-based filter. A robust criterion to select the threshold on the number of modes is given by Mendez

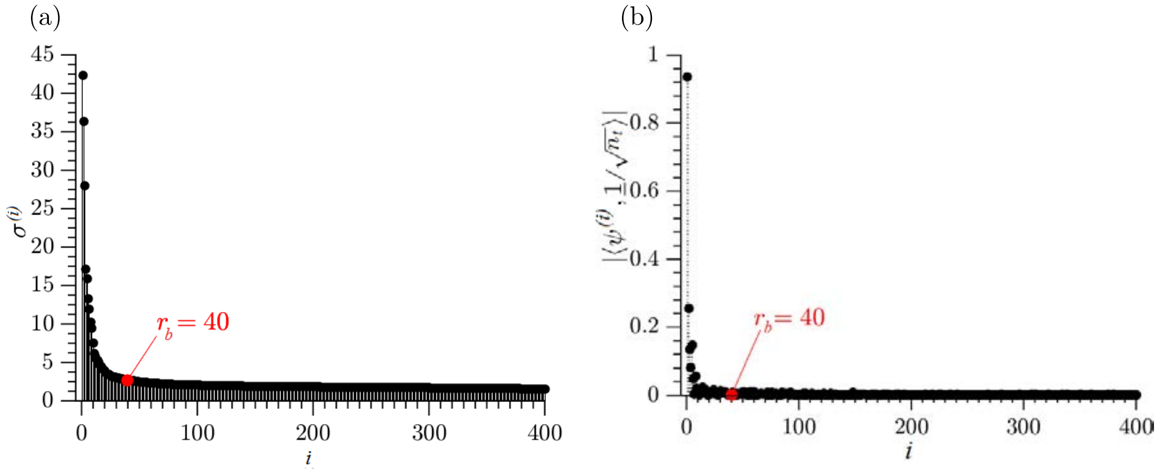

Fig. 4.12 a) Singular value spectra of the experimental image sequence for the flapping wing experiment ; b) scalar product of the corresponding temporal eigenvectors $\psi^{(i)}$ constant vector $\underline{1}/\sqrt{n_t}$. For $r > 40$, the singular values become constant and the eigenvectors orthonormal to $\underline{1}/\sqrt{n_t}$, indicating that no significant background contribution remains.

et al. (2017) exploiting the different spectral properties of the background features and of the particle patterns.

The method performances have been assessed using a synthetic test case featuring a turbulent channel flow. The eigenbackground removal method performances have been compared to those of existing image pre-processing methods. Differently from other existing methods, the eigenbackground removal is insensitive to background features size, intensity, gradient, and temporal oscillations. The intensity reduction of the background features operated by the eigenbackground removal method drastically reduces the uncertainty in the velocity field estimated from cross-correlation PIV algorithms. The computational cost of the proposed method is comparable to that of already existing techniques.

The eigenbackground removal method has been tested on an experimental test case, featuring a wing in flapping motion. The test case is characterized by sharp, large, bright, and moving reflections which pollute the cross-correlation map and bias the measurement towards the wing velocity. Despite the complexity of the experimental setup, the eigenbackground removal method drastically reduced the reflection intensity without significantly alter the particle intensities. The image quality enhancement resulted in the recovery of the particle displacement peak from an otherwise corrupted cross-correlation map. An open-source version of the POD pre-processing toolbox is available at `http://seis.bris.ac.uk/~aexrt/PIVPODPreprocessing/`.

Part III

Flow modelling: POD for data exploration

Chapter 5

Wake of cylinders in tandem configuration near a wall

This chapter reports an experimental investigation on the near wake of two circular cylinders in tandem configuration with the additional interference of the ground. Such a flow is characterized by more complex flow features with respect to the classical von Kármán wake shed by a bluff body, including multiple phenomena occurring at different scales. The study of such a flow is limited by the difficulties in performing time-resolved measurements over the entire flow field at sufficiently large Reynolds number. Nevertheless, the knowledge of the flow dynamics is fundamental to understand, for instance, the periodic force generation on the cylinders. Modal analysis is here exploited to extract information on the dynamics of the coherent structures in the wake. The temporal evolution of the most energetic features is obtained through observation of the Lissajous figures obtained from the *chronoi* of the decomposition. The modal analysis presented in this chapter is enriched by an exhaustive study of the time-averaged flow field, which gives a better physical picture of the different flow dynamics observed by varying the geometrical parameters of the problem. The results reported in this chapter have been published in the work by Raiola et al. (2016).

5.1 Tandem cylinders in cross flow

The periodic flow behaviour generated by a cylinder, or by a bluff body in general, immersed in a cross flow is a widely explored topic (Williamson, 1996). The periodic shedding of counter rotating vortices, known as von Kármán vortices, gives rise to fluctuating forces and noise. The shedding occurs at a Strouhal number based on the cylinder diameter ($St = fD/V_\infty$ where f is the shedding frequency, D is the cylinder

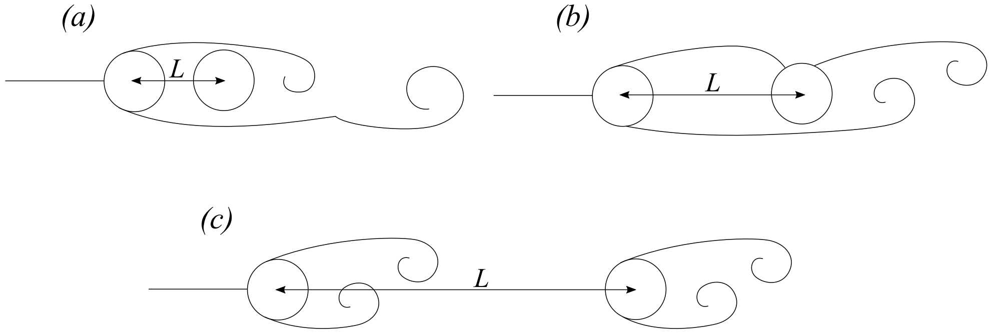

Fig. 5.1 Flow behaviors for cylinders in tandem configurations: (a) bluff-body regime, (b) reattachment regime, (c) co-shedding regime.

diameter and V_∞ is the free-stream velocity) equal to about 0.2 in a range of Reynolds number $1300 < Re < 5000$ (Fey et al., 1998). In this Reynolds number range the shedding generally starts with separation of a laminar boundary layer, while transition to turbulent wake occurs further downstream with respect to the separation points.

The flow around arrays of cylinders immersed in a cross flow is a typical engineering problem that can be found in several applications. Cylinder-like structures are typical elements, for example, of heat exchangers, cooling systems for nuclear power plants, offshore structures, buildings, chimneys, powerlines, struts, grids, screens, and cables. Often these structures work in close proximity, thus introducing strong interaction effects between their respective wakes, with effects on both amplitude and frequency of the periodic flow oscillations. Similarly, ground-structure interaction can effectively modify the behaviour of the flow surrounding these objects such as in the case of underwater pipelines or arrays of bluff-bodies in ground effect. The wake of bluff-body arrays in ground effect is especially relevant for solar energy production. Solar plants (either photovoltaic or thermal) feature arrays of elements (e.g. solar panels or parabolic trough collectors) which behaves like bluff bodies. Often these elements are loaded with unsteady aerodynamic forces arising from the wake of upwind elements. This may lead to structural damage, which increments the maintenance costs of solar plants and, thus, the final cost of solar energy. Understanding the behaviour of canonical bluff bodies, such as cylinders, in tandem arrangement and in ground effect is of paramount importance to predict unsteady loads and design structures immersed in complex wakes.

The flow around two cylinders in tandem configuration in cross flow has been widely studied by Igarashi (1981) and Zdravkovich (1987). A review of the subject is given by Sumner (2010). Depending on the Reynolds number and on the the center-to-center longitudinal pitch (expressed in non dimensional form as L/D, abbreviated hereafter as the longitudinal pitch ratio) three main flow behaviours can be identified. At small longitudinal pitch ratios (approximately $1 < L/D < 1.2 - 1.8$ according to Zdravkovich, 1987, or $1 < L/D < 2$ according to Zhou and Yiu, 2006, depending on the Re range) the Kármán vortex shedding for the upstream cylinder is completely suppressed and the two cylinders act as a single bluff body. Meneghini et al. (2001) observed that vortex roll-up occurs closer to the downstream cylinder with respect to the single cylinder case. This flow regime has been often defined as *extended-body* or *single bluff-body regime* as sketched in Fig. 5.1a. At intermediate longitudinal pitch ratios (approximately $1.2 - 1.8 < L/D < 3.4 - 3.8$ according to Zdravkovich, 1987 or $2 < L/D < 5$ according to Zhou and Yiu, 2006, depending on the range of Re) a complex flow behaviour appears in the space between the cylinders. Even if in this regime the flow can show different behaviours, it can be mostly characterized by the reattachment of the separated free shear layers from the upstream cylinder on the surface of the downstream cylinder. This regime is referred to as *reattachment regime* as sketched in Fig. 5.1b. At larger longitudinal pitch ratios (approximately $L/D > 3.4 - 3.8$ according to Zdravkovich, 1987 or $L/D > 5$ according to Zhou and Yiu, 2006, depending on the range of Re) both the cylinders develop a wake with the typical features of a von Kármán street. This regime, sketched in Fig. 5.1c, is referred to as *co-shedding regime*. In the co-shedding regime, both the cylinders shed vortices at the same frequency, with the upstream cylinder shedding triggering the downstream one (see Alam and Zhou, 2007). The vortices shed from the downstream cylinder are larger in size but weaker in intensity than in the previous regimes (Zhou and Yiu, 2006).

The different regimes for various L/D are characterized also by the variation of the shedding frequency of the von Kármán vortices in the cylinder wake; in particular Xu and Zhou (2004) characterized the variation of the corresponding Strouhal number spanning through the tandem-cylinders regimes in the range $Re \in [800, 42000]$. For small longitudinal pitch-to-diameter ratios the Strouhal number is higher than 0.2 (shedding occurs at a higher frequency than for an isolated cylinder). For higher longitudinal pitch ratios, the Strouhal number decreases, reaching values lower than 0.2 in the reattachment regime. A discontinuous jump occurs when the flow behaviour passes from the *reattachment* to the *co-shedding regime*. For higher longitudinal pitch ratios the Strouhal number slowly approaches 0.2.

The effect of the ground proximity has been investigated for both circular (e.g. Lei et al., 1999, Price et al., 2002, Wang et al., 2013) and square (see Martinuzzi et al., 2003, Wang and Tan, 2008, Mahir, 2009, Shi et al., 2010) single cylinders. The ground affects the pressure distributions on the cylinder surface, as well as the flow-induced vibration modes. The interaction of the cylinder with the wall has been also demonstrated to be a useful mean to control the flow in more complex arrangements (e.g. Michelis and Kotsonis, 2015). The flow behavior is controlled by the ratio between the cylinder-to-wall gap height and the cylinder diameter (G/D, abbreviated hereafter as the wall gap ratio). According to Zovatto and Pedrizzetti (2001) for a critical wall gap ratio between 0.3 and 0.5 the von Kármán vortex shedding is suppressed as the impermiability of the wall poses an irrotational constraint on the cylinder wake. According to Price et al. (2002), however, periodical release of vorticity is still present and its frequency depends on the Reynolds number for $Re < 2000$. Lin et al. (2009) found evidence of the presence of a wall-jet flowing from the wall gap for wall gap ratios lower than 0.3, showing that this jet presents a self-similar velocity profile.

Little attention has been paid to the effect of the wall proximity in the case of two cylinders in tandem configuration. Bhattacharyya and Dhinakaran (2008) investigated with 2D simulations the flow around two near-wall tandem square cylinders ($G/D = 0.5$, $L/D = 1.5 - 6$, $Re = 100 - 200$) with a shear velocity profile imposed upstream of them, and found that the cylinders wake resulted in a non-symmetric flow behaviour: both non-uniformity of the flow and wall-induced vorticity weakens the lower separated shear layer with respect to the upper one. Harichandan and Roy (2012) simulated the flow around two near-wall tandem circular cylinders ($G/D = 0.5 - 1$, $L/D = 2 - 5$, $Re = 100 - 200$) immersed in a zero-pressure-gradient flat-plate boundary layer: for $L/D = 5$ the shedding frequencies of both upstream and downstream cylinders are found to be equal. Moreover, the wake of tandem cylinders is less effective than the wake of a single cylinder in destabilizing the downstream wall boundary layer and causing separation. Wang et al. (2014) measured with PIV the flow field around two square cylinders at $Re = 6300$ spanning a wide parametric space in both longitudinal pitch ratio ($L/D = 1.5 - 7$) and wall gap ratio ($G/D = 0.25 - 2$). Similarly to the case of the single cylinder for wall gap ratios below 0.5 the shedding is found to be suppressed. The interaction with the wall boundary layer is found to be relevant up to $G/D = 1$.

5.2 Experimental setup

An experimental campaign has been carried out to study the near wake mechanisms downstream of two circular cylinders in tandem arrangement and its perturbation due to the proximity of a plane wall. The experimental study has been carried out in the

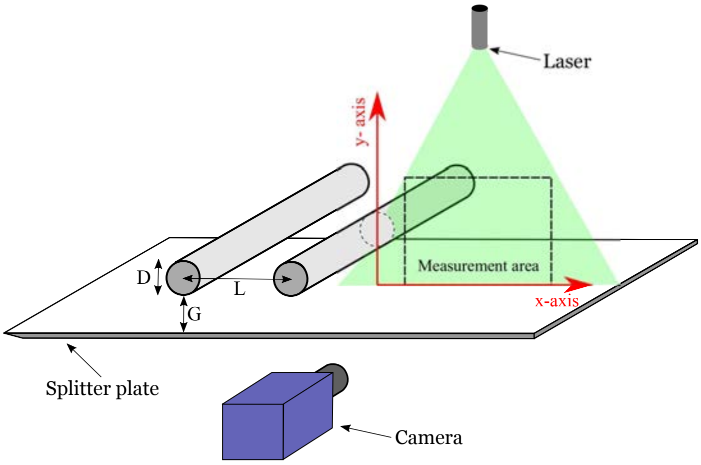

Fig. 5.2 Schematic of the experimental setup.

closed loop wind tunnel of the Aerospace Engineering Group at the *Universidad Carlos III de Madrid*. Details about this facility are given in §3.4.4 (as well as in the works by Raiola et al., 2015, 2016). The tunnel is equipped with a plane splitter plate (750 mm length, 2 mm thickness) with a sharp leading edge. The splitter plate is used as ground (instead of a tunnel wall) in the attempt of obtaining a ground effect on the cylinders along with a relatively thin boundary layer. The boundary layer thickness on the plate without cylinders has been measured with PIV and resulted being smaller than 7 mm at the position of the downstream cylinder and smaller than 11 mm at the trailing edge of the splitter plate. Two PVC cylinders, with diameter $D = 32$ mm and length 400 mm (blockage ratio 0.08), are used as test models spanning the wind tunnel test section from side to side. Figure 5.2 shows a schematic of the experimental setup. The stream-wise position of the downstream cylinder is kept fixed with respect to the plate trailing edge for all the experiments, at a distance of $10D$. The stream-wise position of the upstream cylinder is changed in order to vary the longitudinal pitch ratio L/D. The minimum distance of the first cylinder to the leading edge of the splitter plate (i.e. for the case $L/D = 6$) is slightly less than $7.5D$. The vertical position of the plate with respect to the tandem cylinders is changed to vary the wall gap G/D. Experiments are carried out for L/D spanning from 1.5 to 6 and G/D in the range 0.3-3. The wind tunnel velocity is monitored before each test with a Pitot tube in order to keep it constant and equal to 2.3 m/s for all the experiments. The Reynolds number based on the cylinder diameter is equal to 4.9×10^3.

Velocity field measurements are performed with digital Particle Image Velocimetry. The flow is seeded with Di-Ethyl-Hexyl-Sebacate droplets with diameter of approximately 1 µm. The light source is a Big Sky Laser CFR400 ND:Yag (230 mJ/pulse, pulse duration 3 ns). The acquisition is performed with a *TSI PowerView^{TM} Plus* 2MP

Camera (1600 × 1200 pixel array, 7.4 µm × 7.4 µm sensor size) with a spatial resolution of about 7.2 pixels/mm. The sampling frequency of the PIV measurements is 10 Hz. An ensemble of 2000 image couples is acquired for each experiment.

The image quality is improved by removing laser reflections and illumination background by means of the eigenbackground removal technique (Mendez et al., 2017) illustrated in Chapter 4, allowing unbiased measurements near the wall.

The same custom-made software of the University of Naples used in §4.3.2 is adopted here for the velocity fields extraction from the PIV images. The final interrogation windows of the multi-step image deformation process is set to 16 × 16 pixels, 50% overlap (final vector spacing 8 pixels, corresponding to $0.035D$). The vector validation is carried out with a universal median test (Westerweel and Scarano, 2005) on a 3 × 3 vectors kernel and a threshold equal to 2 is used to identify invalid vectors. Discarded vectors are replaced with a distance-weighted average of neighbour valid vectors.

5.3 Results

5.3.1 Average fields and turbulence statistics

The velocity fields are processed to extract the distributions of the first and second order statistics. Analysing the profiles of the wake deficit of momentum $u_1(x, y) = \langle u(x, y)\rangle - u_{max}(x)$, where $u_{max}(x)$, reported in Fig. 5.3, is the local velocity maximum along the wall normal direction, the maximum deficit $u_{1,max}(x)$ and its position $y_{1,max}(x)$ are identified (the reference frame is indicated in Fig. 5.2). The maximum deficit is of paramount importance in order to properly scale the velocity profiles in the wake (Schlichting and Gersten, 2003). Following the literature about turbulent wakes (Sarkar and Sarkar, 2010), the wake boundaries $y_{wake}(x)$ are defined as the locations in which $u_1(x, y_{wake})/u_{1,max}(x) = 0.5$. The wake width $w(x)$ is defined as the y-distance between the wake boundaries.

The velocity deficit profiles at various x-distances from the downstream cylinder for the case $L/D = 3$, $G/D = 3$ are illustrated in Fig. 5.3d. After rescaling the y-coordinate with the wake width w and the velocity deficit with $u_{1,max}$, the velocity deficit profiles tend to collapse on a single curve. Despite self-similarity cannot be assured at the tested short stream-wise distance, velocity deficit profiles compare quite well with the theoretical asymptotic result given by Schlichting and Gersten (2003):

$$u_1 = u_{1,max}\left(1 - \left(\frac{y}{w}\right)^{\frac{3}{2}}\right)^2 \tag{5.1}$$

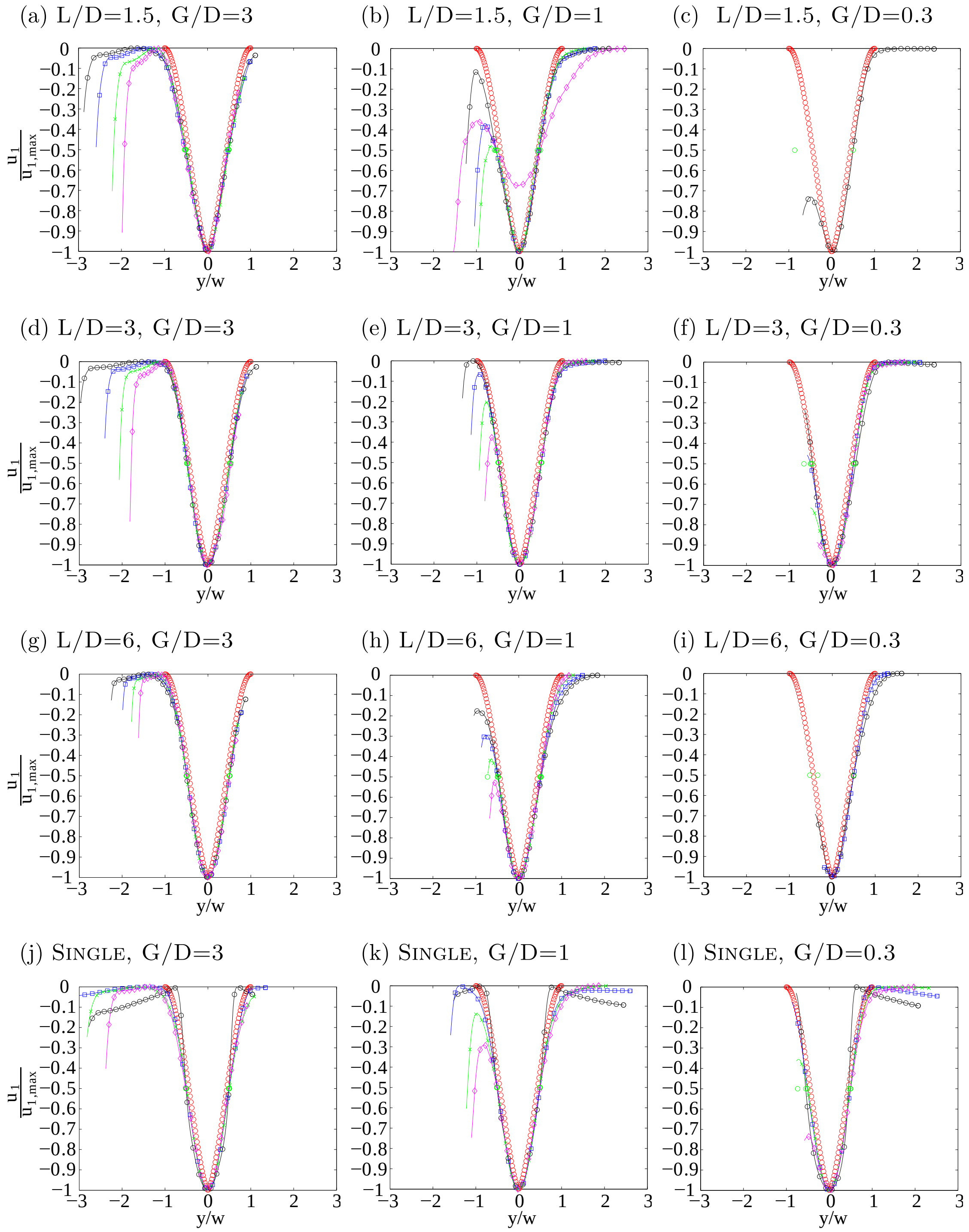
(a) L/D=1.5, G/D=3 (b) L/D=1.5, G/D=1 (c) L/D=1.5, G/D=0.3

(d) L/D=3, G/D=3 (e) L/D=3, G/D=1 (f) L/D=3, G/D=0.3

(g) L/D=6, G/D=3 (h) L/D=6, G/D=1 (i) L/D=6, G/D=0.3

(j) Single, G/D=3 (k) Single, G/D=1 (l) Single, G/D=0.3

Fig. 5.3 Velocity deficit profiles for varying L/D and G/D. Self-similar solution by Schlichting and Gersten (2003) (○). Measured profiles at different stream-wise stations: $X/D = 2.0$ (—○—); $X/D = 3.0$ (—□—); $X/D = 4.0$ (—×—); $X/D = 5.0$ (—◇—).

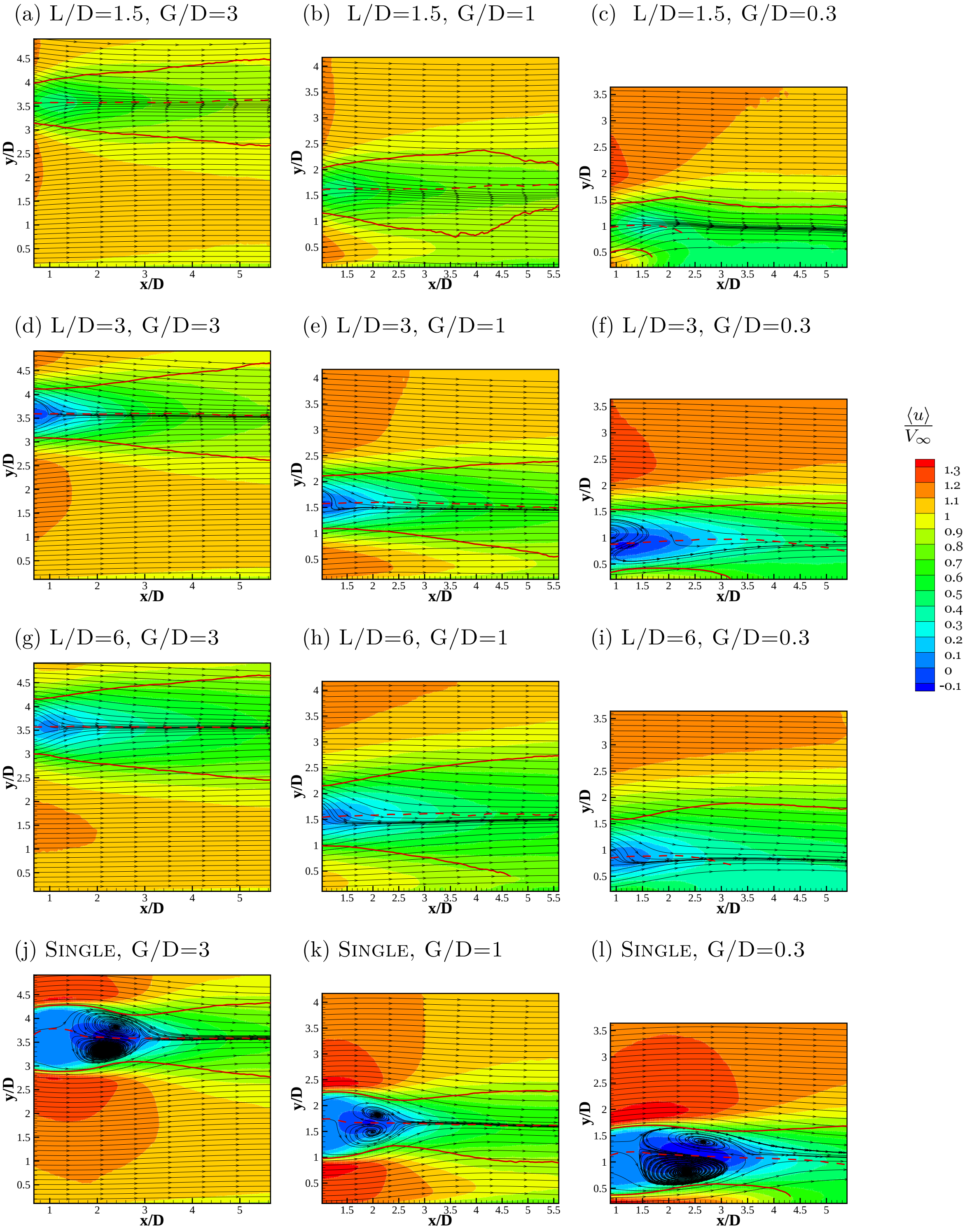

(a) L/D=1.5, G/D=3 (b) L/D=1.5, G/D=1 (c) L/D=1.5, G/D=0.3

(d) L/D=3, G/D=3 (e) L/D=3, G/D=1 (f) L/D=3, G/D=0.3

(g) L/D=6, G/D=3 (h) L/D=6, G/D=1 (i) L/D=6, G/D=0.3

(j) SINGLE, G/D=3 (k) SINGLE, G/D=1 (l) SINGLE, G/D=0.3

Fig. 5.4 Contour maps of the average stream-wise velocity component for all the longitudinal pitch ratios (L/D) and wall gap ratios (G/D) object of the study. The stream-wise distance is measured from the downstream cylinder center; the vertical distance is measured from the splitter plate. The red dashed curve represents the position of $u_{1,max}(x)$. The red continuous curves represent the wake boundaries for which the condition $u_1(x, y_{wake})/u_{1,max}(x) = 0.5$ is satisfied. The streamlines depict the average field behavior.

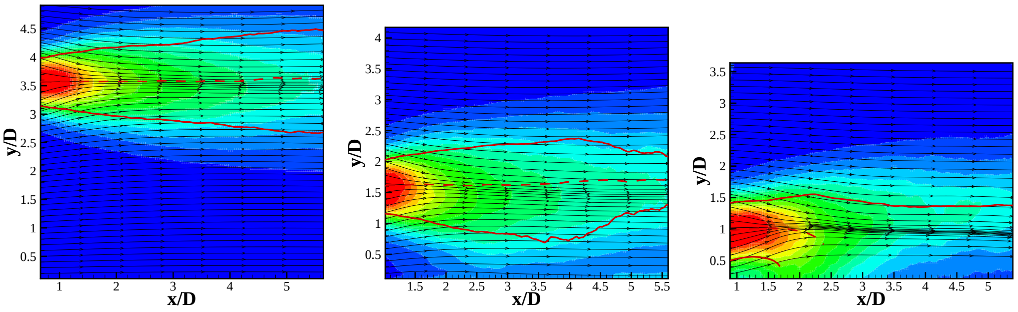

(a) L/D=1.5, G/D=3 (b) L/D=1.5, G/D=1 (c) L/D=1.5, G/D=0.3

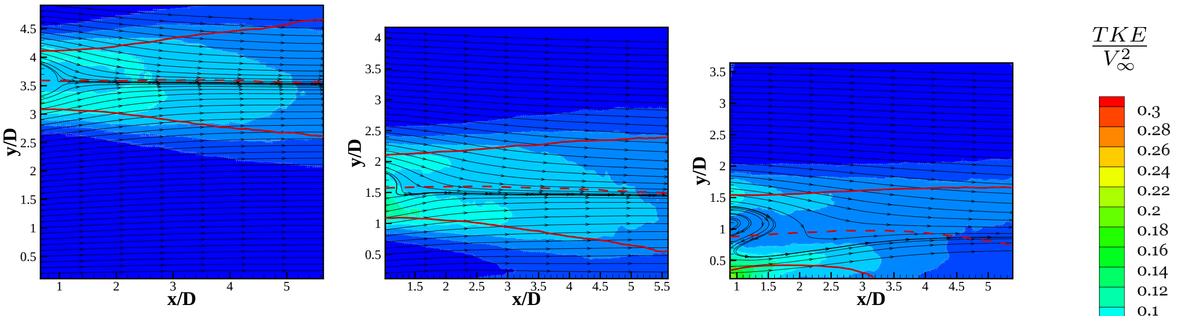

(d) L/D=3, G/D=3 (e) L/D=3, G/D=1 (f) L/D=3, G/D=0.3

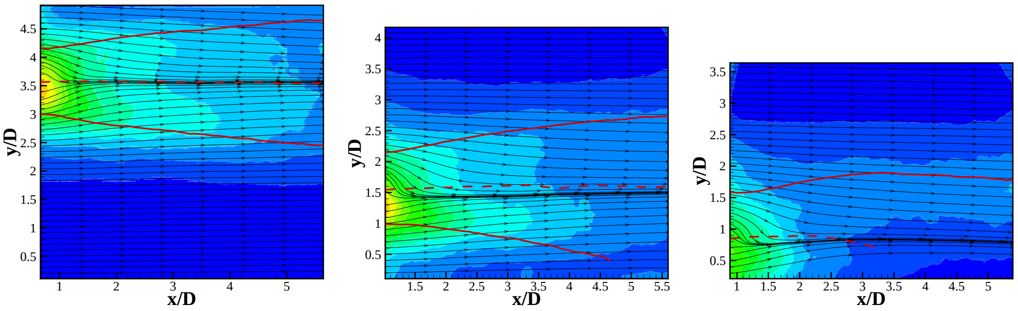

(g) L/D=6, G/D=3 (h) L/D=6, G/D=1 (i) L/D=6, G/D=0.3

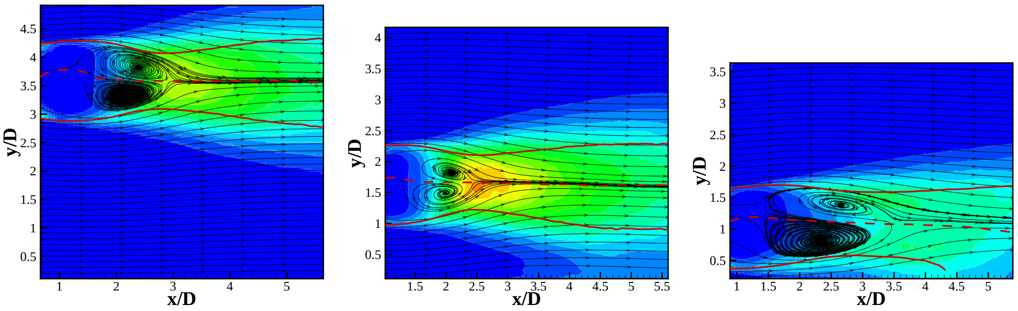

(j) Single, G/D=3 (k) Single, G/D=1 (l) Single, G/D=0.3

Fig. 5.5 Contour maps of the turbulent kinetic energy (TKE) for all the longitudinal pitch ratios (L/D) and wall gap ratios (G/D) object of the study. The stream-wise distance is measured from the downstream cylinder center; the vertical distance is measured from the splitter plate. The red dashed curve represents the position of $u_{1,max}(x)$. The red continuous curves represent the wake boundaries for which the condition $u_1(x, y_{wake})/u_{1,max}(x) = 0.5$ is satisfied. The streamlines depict the average field behavior.

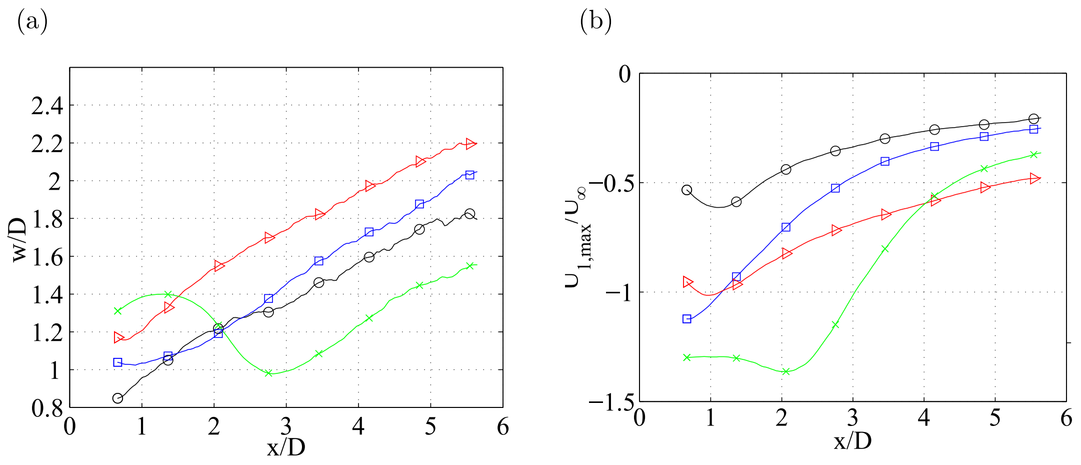

Fig. 5.6 Comparison of a) wake width and b) maximum velocity deficit for $G/D = 3$ and varying L/D: $L/D = 1.5$ (—○—); $L/D = 3.0$ (—□—); $L/D = 6.0$ (—▷—) ; single cylinder (—×—).

Similar results have been found for almost all cases at $G/D = 3$ (Fig. 5.3a,d,g,j). This assures that the blockage effects on the presented results is minimal. Moreover, the absence of symmetry alteration in the profiles for $-1 < y/w < 1$ suggests that for all the cases with $G/D = 3$ the effect of the wall is negligible along the whole stream-wise extension of the measured domain. This is also consistent with the symmetry of the distributions of average stream-wise velocity (see Fig. 5.4a,d,g,j) and turbulent kinetic energy (see Fig. 5.5a,d,g,j) and by the absence of rotation in the wake (in both figures red dashed and solid lines depict respectively the maximum deficit location and the wake boundaries). The turbulent kinetic energy (TKE) is computed as $\mathrm{TKE} = 3/4(\langle u'u' \rangle + \langle v'v' \rangle)$. As the cylinders approach the wall (see Fig. 5.3e,f) the symmetry in the velocity deficit profiles is disrupted, departing from the Schlichting profile in the wake portion on the wall side. In this region the Schlichting profile is substituted by a jet-like behaviour that can be associated to the wall-jet described by Lin et al. (2009). Differently from the work by Lin et al. (2009), a proper scaling for this jet has not been found for the present experiment, suggesting that the presence of multiple bluff-bodies may significantly change the characteristics of this jet. The wall-jet profile and the wake profile coexist until the jet maximum position approaches the lower wake boundary; from this point on the given wake width definition does not appear as a proper scaling for the velocity deficit profile (Fig. 5.3b).

In Fig. 5.6 the wake width and the maximum velocity deficit evolution along the x-axis are shown for the cases at $G/D = 3$. Fig. 5.6a depicts clearly the effect of different L/D on the wake: while the growth rate appears to be quite similar for all the cases past $x/D = 3$, the near wake ($x/D < 2$) shows the most remarkable differences. The single cylinder case presents a protracted region (about 3 diameters long) in which the wake expands before contracting again and finally spreading with higher growth rate similar to the tandem cylinders cases. This region can be associated with the distance required by the Kármán vortices to roll up and with the presence of an elongated recirculation bubble (refer to Williamson, 1996 for further details). In this region the maximum velocity deficit (see Fig. 5.6b) is nearly constant.

For $L/D = 1.5$ a relatively thin wake forms in close proximity of the downstream cylinder (20% smaller than the cylinder diameter, see Fig. 5.6a). The absence of the recirculation bubble is consistent with the picture of a *bluff-body regime* (Zdravkovich, 1987). It can be conjectured that the shear layers are rolling up closer to the downstream cylinder with respect to the single cylinder case (thus outside of the measurement region). For $L/D = 3$ the wake width in proximity of the downstream cylinder is larger, being almost equal to one cylinder diameter. In contrast with the previous case, the wake width has a plateau for $x/D < 1.5$, and then starts growing, with slope similar to the other cases. This different wake behaviour can be ascribed to the occurrence of a *reattachment regime* (Zdravkovich, 1987), with the wake of the upstream cylinder reattaching on the downstream one. Differently from the *bluff-body regime*, in the *reattachment regime* the shear layer detaches directly from the surface of the downstream cylinder, thus showing some similarity to the case of the single cylinder. The velocity deficit is stronger with respect to the case falling in the *bluff-body regime*, especially in the near wake ($x/D < 2$). The combined analysis of wake growth and maximum velocity deficit reveals a stronger drag being produced in this configuration, as found in literature for similar longitudinal pitch ratios (Alam et al., 2003). For the case at $L/D = 6$ the wake is thicker than both the previous cases at $L/D = 1.5$ and $L/D = 3$, while the growth rate is similar to the one falling in the *bluff-body regime*. The maximum velocity deficit remarkably increases with respect to both the other tandem cylinder cases throughout almost all the measurement domain. The effect of both increasing wake width and maximum velocity deficit suggests a dramatic increase of the drag for the case with $L/D = 6$, depicting the scenario of a *co-shedding regime* (Alam et al., 2003).

The effect of reducing the wall gap ratio is more diversified (see Fig. 5.7) and seems to affect significantly the flow field regime. In most of the cases the wake width is relatively unaffected by the wall interference. For the case of the single cylinder the growth rate downstream of the recirculation bubble is unchanged when passing from $G/D = 3$ to $G/D = 1$, while the only appreciable effect seems to be a change of

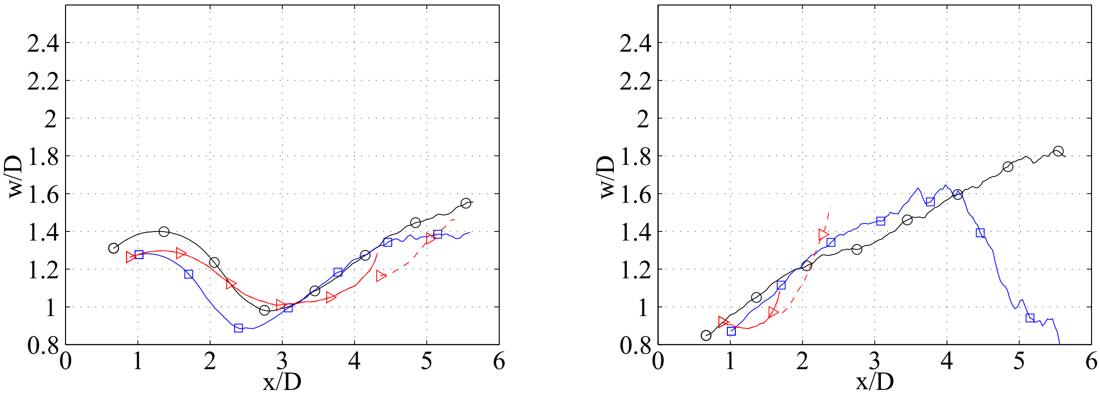
(a) Single cylinder (b) L/D=1.5

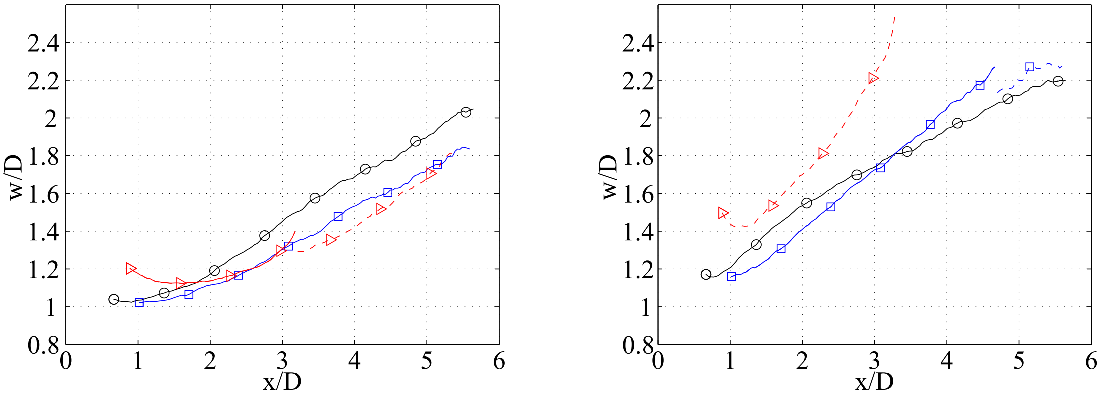
(c) L/D=3 (d) L/D=6

Fig. 5.7 Wake width comparisons for varying G/D: $G/D = 3.0$ (—○—); $G/D = 1.0$ (—□—); $G/D = 0.3$ (—▷—). Solid lines represent $w(x) = y_{wake,up}(x) - y_{wake,low}(x)$. Dashed lines represent $w_{up}(x) = 2(y_{wake,up}(x) - y_{1,max}(x))$.

the bubble extension. For $G/D = 0.3$ the general characteristics of the wake width evolution along the stream-wise coordinate are preserved approximately up to a point in which the cylinder wake on the wall side and the wall boundary layer merge (at about $x/D = 4$ as can also be appreciated in Fig. 5.4l). A similar behaviour of the wake width evolution can be observed for almost all the cases. A very exemplifying case is represented by $L/D = 1.5$, $G/D = 1$: the wake growth rate is nearly unaltered with respect to the $G/D = 3$ case up to $x/D = 4$, while at this value it starts decreasing due to the merging of the wake with the boundary layer (see Fig. 5.4b). Starting from $x/D > 4$ the wake width w cannot be used as a suitable scaling parameter (see e.g. Fig. 5.3b). The effect on the maximum velocity deficit (see Fig. 5.8) clearly indicates that, as the cylinders approach the wall, the momentum deficit tends to increase, possibly

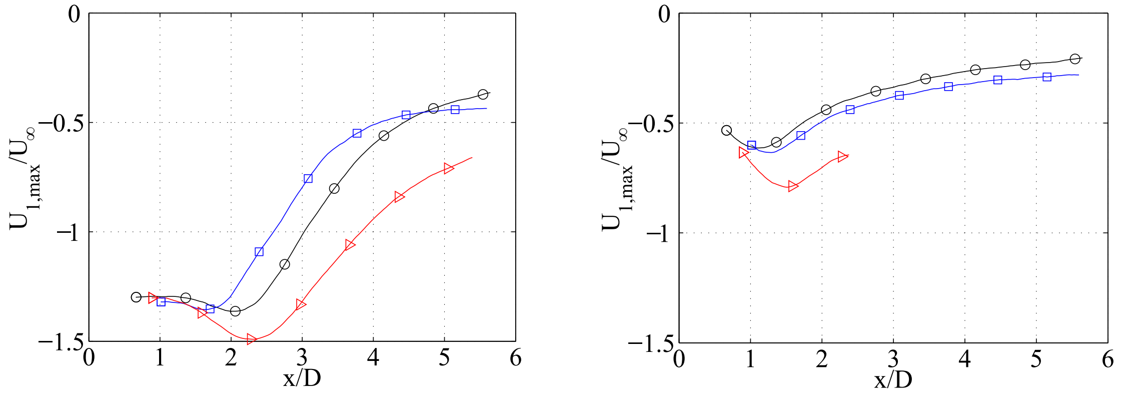
(a) Single cylinder (b) L/D=1.5

(c) L/D=3 (d) L/D=6

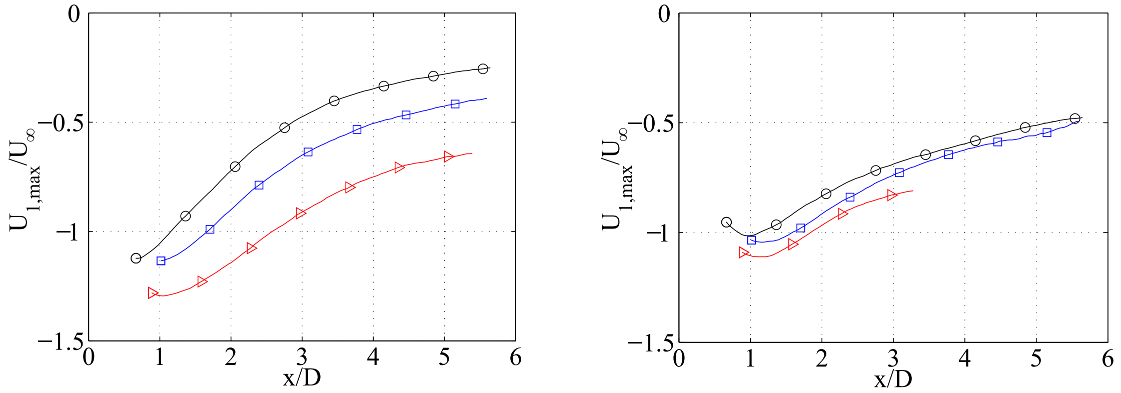

Fig. 5.8 Maximum velocity deficit comparisons for varying G/D: $G/D = 3.0$ (—○—); $G/D = 1.0$ (—□—); $G/D = 0.3$ (—▷—).

due to the addition of the mass flow deficit of the wall boundary layer to the wake mass flow deficit.

A better insight on the effect of the wall on the wake evolution is given by Fig. 5.4, that shows the contour plots of the average stream-wise component of the velocity, along with the curves depicting the positions of the wake boundaries and the line of maximum velocity deficit. With respect to the symmetric cases (exemplified by wall gap ratio $G/D = 3$), all the cases at $G/D = 1$ (Fig. 5.4b,e,h,k) and $G/D = 0.3$ (Fig. 5.4c,f,i,l) present a wake bending, showing a concavity towards the wall, as highlighted by the maximum deficit position and by the wake boundaries. The maximum velocity deficit line (red dashed line in the figures) is slightly rotated upwards for the closer-to-the-cylinder portion of the wake. This behavior has been already observed for the single cylinder in Lin et al. (2009), showing that the recirculation region rotates far from the wall following the wall jet. The farther-from-the-cylinder portion of the wake, instead, appears to rotate towards the wall, suggesting the formation of a low pressure region on the wall that could draw the wake toward the ground.

This rotation effect can be addressed as a weak interaction between the cylinders wake and the wall. As the wake lower boundary and the wall boundary layer (whose edge corresponds to the point of maximum velocity in the wall jet) merge, a strong interaction occurs: the upper wake boundary -that represent the only well-recognizable feature of the former wake- no longer spreads, remaining nearly parallel to the wall or shrinking. In this case no more distinction can be performed between wake and wall boundary layer: they completely merge in a single low speed region attached to the wall. It can be expected that this structure may eventually develop in a boundary layer, being the cylinders considered as an overtripping (e.g. see Marusic et al., 2015). The geometrical configuration of the cylinders appears to be a major player in determining the position at which the two structures merge, controlling both wake characteristics -such as wake width and maximum velocity deficit- and wall jet/boundary layer characteristics.

The contour maps of turbulent kinetic energy (TKE) are reported in Fig. 5.5. For all the cases at $G/D = 3$ the TKE presents a symmetric pattern with respect to the wake centerline, in agreement with the previously reported results on first-order moments and wake behaviour. Significant differences between the different configurations can be appreciated for varying L/D. For $L/D = 1.5$ (*bluff-body regime*) the wake is characterized by a strong TKE production, especially localized on the wake centerline and close to the downstream cylinder. This TKE distribution resembles closely the one observed for the single cylinder, even if the TKE values are consistently higher. Differently from the single cylinder case, the low turbulence intensity region associated with the recirculation bubble is not present, in agreement with the previously outlined results. For $L/D = 3$ (*reattachment regime*) the TKE in the wake is characterized by the presence of two elongated production regions, with some analogy with the shear layer development observed for the single cylinder case. This is again consistent with the view of a *reattachment regime*. For $L/D = 6$ (*co-shedding regime*) the TKE values are slightly stronger and diffused than in the previous case, with peaks along the wake boundaries. This behaviour appears to be consistent with the release of Kármán vortices from the upstream cylinder, as observed by (Zdravkovich, 1987): the downstream cylinder is invested by a pulsating flow that convects the wake of the downstream cylinder; this determines a more intense spatial spreading of the TKE and an increase of the fluctuations in the most external part of the wake.

As the wall gap ratio is reduced to $G/D = 1$ (see Fig. 5.5b,e,h), the TKE distribution becomes asymmetric, increasing in intensity in the wall-facing portion of the wake. For low wall gap ratios ($G/D = 0.3$ in Fig. 5.5c,f,i) and for $L/D = 1.5$, $G/D = 1$ (Fig. 5.5b) a remarkable change in the spatial distribution of the TKE is present: in the most downstream portion of the wake the energy tends to redistribute from the centerline to the upper wake boundary as soon as the lower wake boundary and the wall boundary layer merge. This determines the formation of a low TKE region nearby the wall and the displacement of the maximum TKE region farther from the wall with respect to the wake centerline. Close to the downstream cylinder a strong asymmetry in the TKE distribution is still present, generally with an increase of TKE close to the wall and flowing out from the cylinder-wall gap. More than to turbulence production, this strong intensity of the fluctuating field can be addressed to a periodical mean flow, suggesting the presence of a pulsating-jet-like flow in the gap between the downstream cylinder and the wall.

5.3.2 POD modes organization and mutual relation

The turbulent kinetic energy content of the first 20 POD modes is reported in Fig. 5.9 for the nine tandem cylinders configurations that have been tested (along rows, variable wall gap ratio; along columns, variable longitudinal pitch ratio). The case of a single cylinder is included for comparison in the last row. Similarly to the case of the single cylinder, at $G/D = 3$ the first two modes account for most of the turbulent kinetic energy in both the *bluff-body regime* (about 70% of the total energy) and *reattachment regime* (about 55% of the total energy). These modes, as it will be clarified later in this section, are related to the first harmonic of the von Kármán vortex shedding. A strong drop in the energy content of the first two modes occurs for the *co-shedding regime* (about 20% of the total energy), while energy redistributes over higher order modes, unveiling a more complex behaviour. The effect of small wall gap ratios is evident for the case of the single cylinder: due to ground effect, the energy content of the first two modes strongly drops (passing from nearly 60% at $G/D = 3$ to about 35% at $G/D = 0.3$). This behaviour is compatible with a flow not dominated anymore by the shedding. Similarly, for cylinders in tandem configuration, a more or less intense drop can be observed for all the cases when wall gap ratio decreases. Energy tends to redistribute from the first modes (strongly dominant at $G/D = 3$) over higher order modes that may be uncorrelated with the typical von Kármán shedding behaviour.

The most energetic POD mode is reported in Fig. 5.10 for all the cases under study. The case of a single cylinder in cross flow is also included for reference. Data

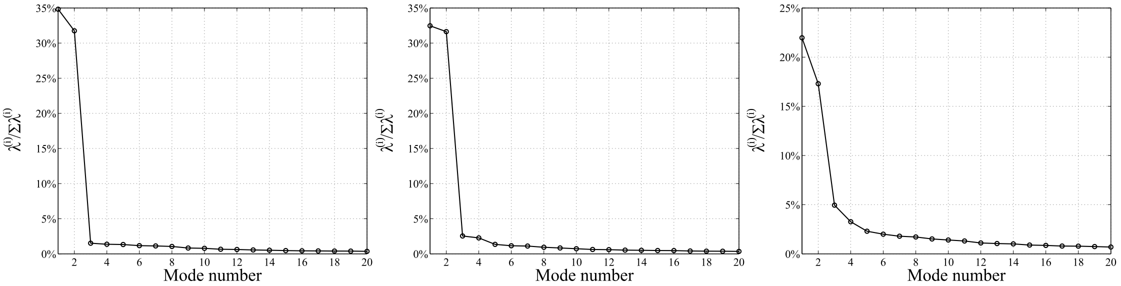

(a) L/D=1.5, G/D=3 (b) L/D=1.5, G/D=1 (c) L/D=1.5, G/D=0.3

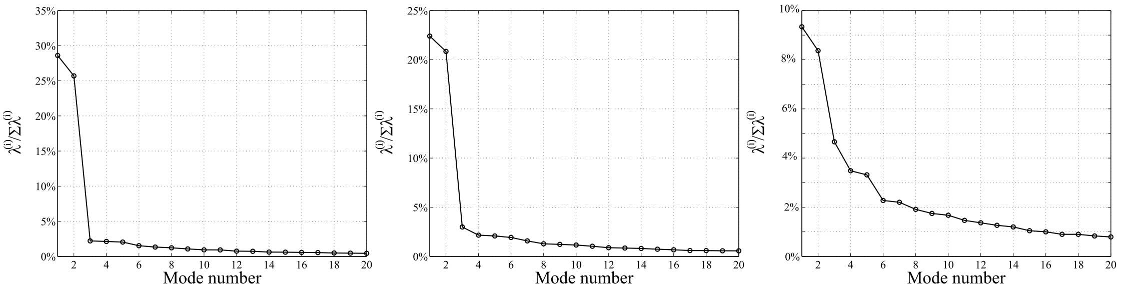

(d) L/D=3, G/D=3 (e) L/D=3, G/D=1 (f) L/D=3, G/D=0.3

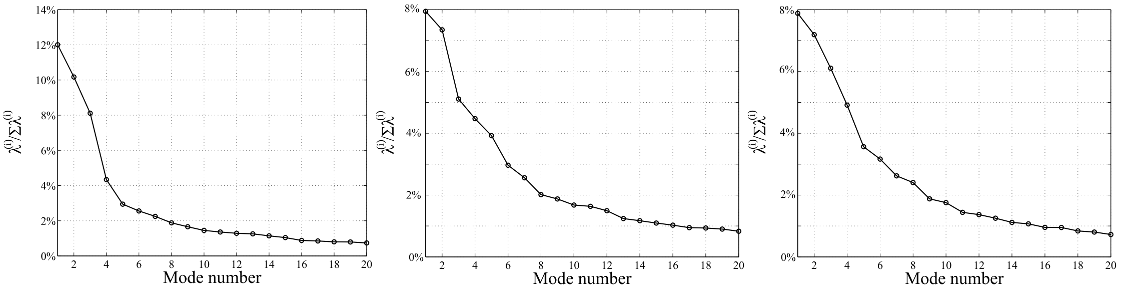

(g) L/D=6, G/D=3 (h) L/D=6, G/D=1 (i) L/D=6, G/D=0.3

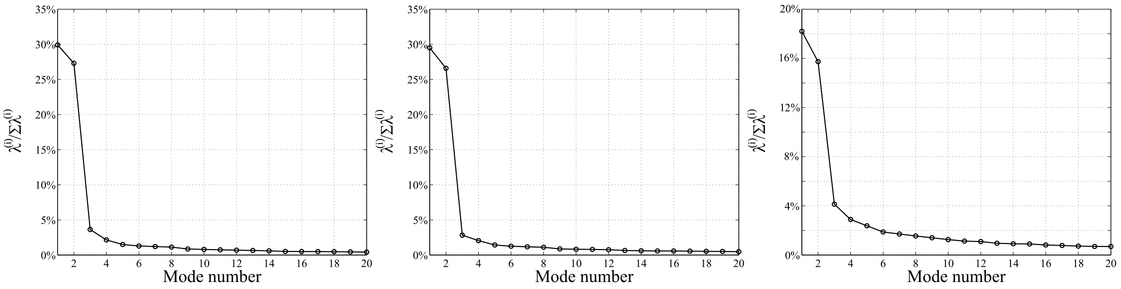

(j) Single Cylinder, G/D=3 (k) Single Cylinder, G/D=1 (l) Single Cylinder, G/D=0.3

Fig. 5.9 Energy content of the first 20 modes expressed in percentage of the total in-plane turbulent kinetic energy.

are presented in terms of out-of-plane non-dimensional vorticity component maps to spotlight the vortical features. In all the cases the vorticity maps are dominated by the intermittent release of vorticity, coherently with the scenario of a shedding wake. This picture was expectable, and it is confirmed by the analogous vorticity distributions in the second mode (not included for brevity). The dominance of a shedding is also confirmed by the scatter plot of the time coefficients of the first two POD modes (Fig. 5.11), normalized with twice the square root of the corresponding eigenvalue. The Lissajous curve obtained from low-order modelling of the scatter plot is indicated in red in Fig. 5.11. The analytical form of the Lissajous curve is:

$$b^{(1)} = \sqrt{2\lambda^{(1)}} sin(2\pi f^{(1)} t), \quad b^{(2)} = \sqrt{2\lambda^{(2)}} sin(2\pi f^{(1)} t \pm \pi/2) \tag{5.2}$$

with $f^{(1)}$ the frequency of the first oscillatory mode.

In most of the cases under examination, the normalized time coefficients of the first two POD modes distribute with quite good fidelity on a circle with unitary radius. Notice that the agreement is more evident for the case of the *single-body regime* at the largest wall gap ratio. This is due to the different nature of the shedding. For the case of the *single-body regime* ($L/D = 1.5$, $G/D = 3$, see Fig. 5.10a), a regular shedding similar to that of a single cylinder (see Fig. 5.10j) is released, with concentrated blobs of vorticity on the centerline. It must be highlighted that the vorticity blobs in the single cylinder case present a double tail, corresponding to the shear layers released from the cylinder in the vortex formation region. This shows a strong statistical correlation between the shear layers oscillations and the vortex shedding. A similar behaviour cannot be observed for the *bluff-body regime*, as the vortices roll-up very close to the downstream cylinder. This difference is reflected also by the scatter plots: while in the *single-body regime* there is a very weak scattering of the time coefficients from the Lissajous curve (see Fig. 5.11a), in the single cylinder case (see Fig. 5.11j) a stronger scattering appears, revealing a lower harmonic coherence due to the presence of the shear layers in the first two POD modes. For the case of the *reattachment regime* ($L/D = 3$, $G/D = 3$, see Fig. 5.10d) the vorticity blobs appear more stretched along the stream-wise direction and mix up with the shear layer of the wake of the first cylinder. The two phenomena are statistically correlated but might be characterized by different characteristic frequencies, thus reducing the clearness of the scatter plot of the normalized time coefficients (Fig. 5.11d). In the *co-shedding regime* ($L/D = 6$, $G/D = 3$, see Fig. 5.10g) this process is further stressed, leading to the appearance of pairs of vortices with similar vorticity value released in the wake for the case of the

(a) L/D=1.5, G/D=3 (b) L/D=1.5, G/D=1 (c) L/D=1.5, G/D=0.3

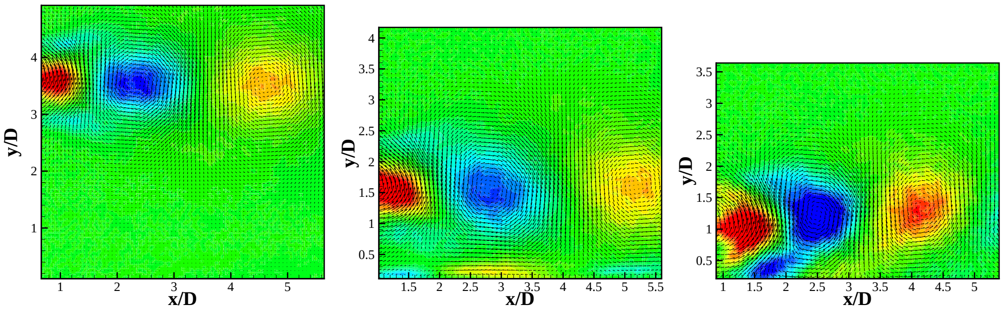

(d) L/D=3, G/D=3 (e) L/D=3, G/D=1 (f) L/D=3, G/D=0.3

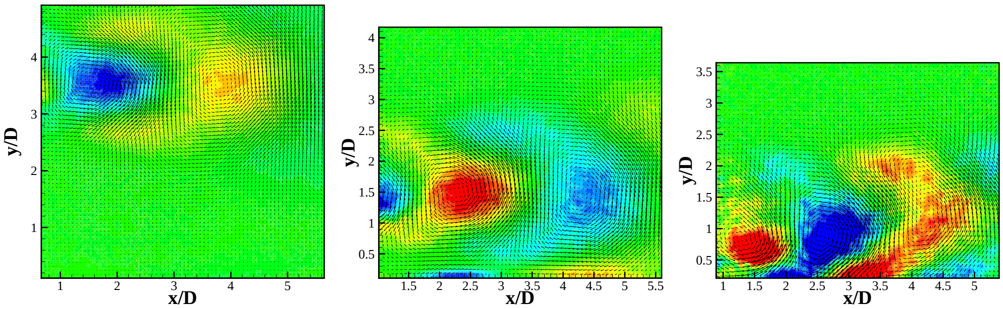

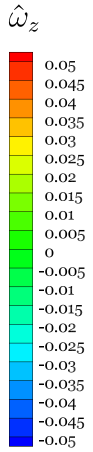

(g) L/D=6, G/D=3 (h) L/D=6, G/D=1 (i) L/D=6, G/D=0.3

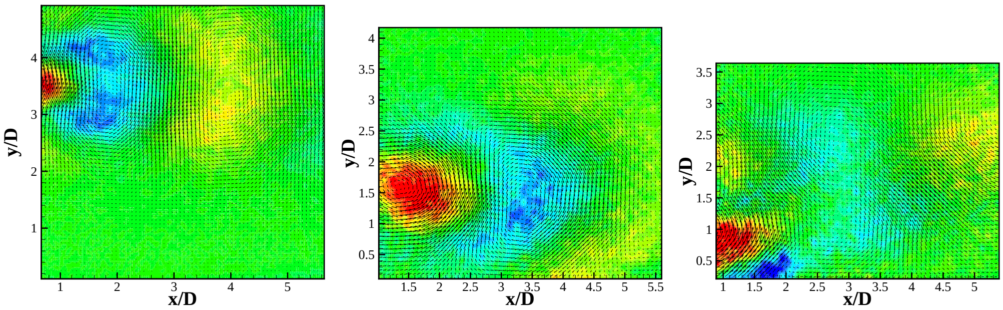

(j) Single Cylinder, G/D=3 (k) Single Cylinder, G/D=1 (l) Single Cylinder, G/D=0.3

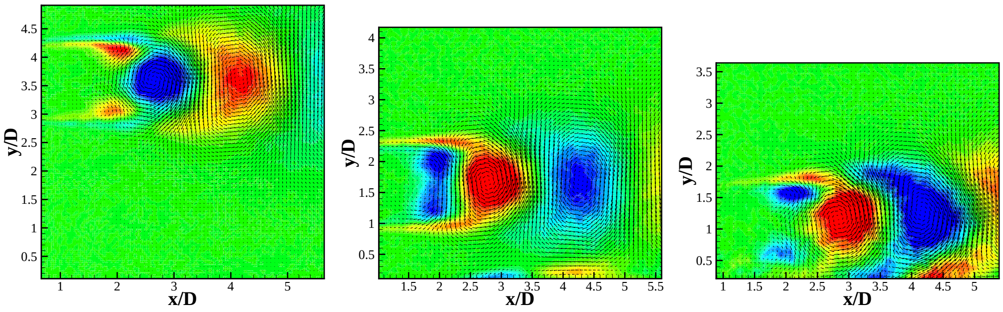

Fig. 5.10 Contour maps of non-dimensional vorticity $\hat{\omega}_z = D\left(\frac{\partial \phi_y}{\partial x} - \frac{\partial \phi_x}{\partial y}\right)$ of the 1st POD mode.

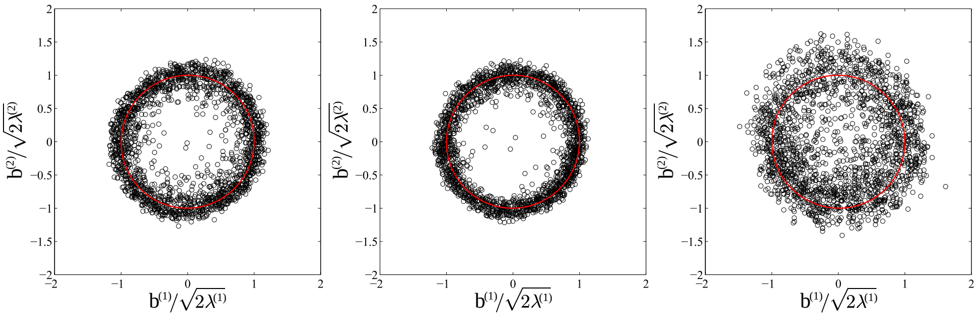

(a) L/D=1.5, G/D=3 (b) L/D=1.5, G/D=1 (c) L/D=1.5, G/D=0.3

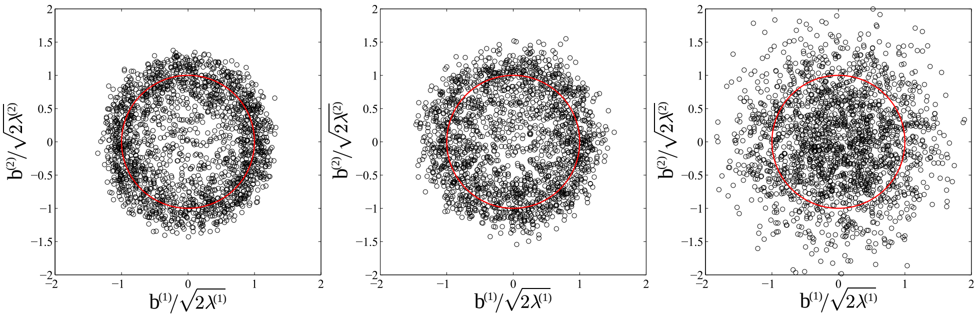

(d) L/D=3, G/D=3 (e) L/D=3, G/D=1 (f) L/D=3, G/D=0.3

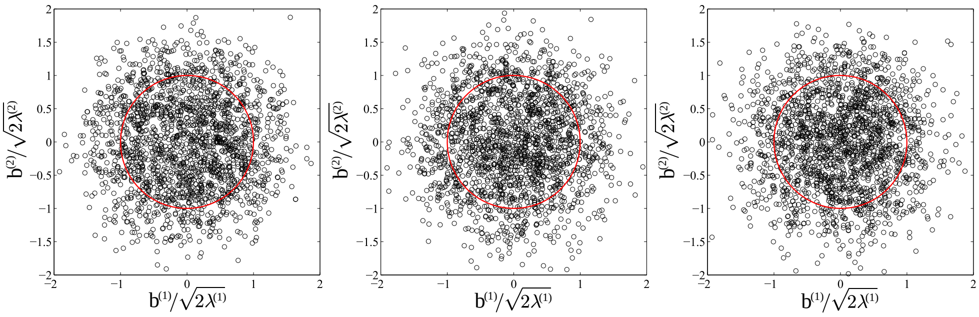

(g) L/D=6, G/D=3 (h) L/D=6, G/D=1 (i) L/D=6, G/D=0.3

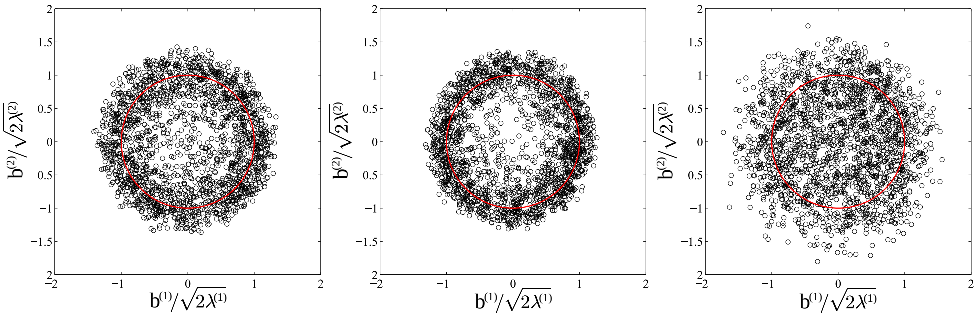

(j) Single Cylinder, G/D=3 (k) Single Cylinder, G/D=1 (l) Single Cylinder, G/D=0.3

Fig. 5.11 Scatter plot of time coefficients of the 2nd POD mode with respect to the time coefficients of the 1st mode. The red line indicate the Lissajous curve with analytical form $b^{(1)} = \sqrt{2\lambda^{(1)}} sin(2\pi f^{(1)} t)$; $b^{(2)} = \sqrt{2\lambda^{(2)}} sin(2\pi f^{(1)} t \pm \pi/2)$.

largest distance from the wall. This is symptomatic of a phase-locked shedding of the two cylinders.

As the two cylinders approach the wall, intermittent release of vorticity is still clearly observed in all cases, revealing an underlying shedding behaviour also for $G/D = 0.3$. At $G/D = 0.3$ (see Fig. 5.10c,f,i,l) the spatial frequency of the shedding strongly increases with respect to the case of $G/D = 3$. The shedding behaviour is confirmed also by the circular pattern in the scatter plots of the time coefficients (see, in particular, Fig. 5.11c and 5.11f). The not perfect agreement of the harmonic relation with time coefficients suggests a more chaotic behaviour than in the far-from-the-wall cases, possibly characterized by the contamination of multiple frequencies. It must be also pointed out that the energy content of the first two modes (Fig 5.9c and 5.9f) strongly drops for the close-to-the-wall cases, revealing that the shedding loses its dominance. For $L/D = 3$, $G/D = 0.3$, due to the energy drop, the shedding mode may be nearly completely covered by other oscillations in the wake. Similar shedding modes are present also for the single cylinder case at $G/D = 0.3$ (Fig. 5.10l). Despite most of the literature agrees with the observation that von Kármán shedding from a cylinder should disappear at wall gap ratios equal to $G/D = 0.3$ (see, e.g. Lei et al. (1999)), the presence of similar vortical structures in the wake has been already evidenced by Price et al. (2002) and Michelis and Kotsonis (2015). For a single cylinder, the frequency at which this vorticity is released has been observed to be strongly dependent on the Reynolds number (Price et al., 2002). It must be highlighted that the shedding spatial frequencies observed for $L/D = 1.5$, $G/D = 0.3$ (Fig. 5.10c) and for $L/D = 3$, $G/D = 0.3$ (Fig. 5.10f) are similar to those observed for the single cylinder. This suggests that the mechanism that promotes this shedding should be similar for both single and tandem cylinders. A possible explanation is that these oscillations are synchronized with the instabilities in the wall jet flow released from the wall gap: oscillations may then depend on the effective wall gap passage area -i.e. the equivalent passage area once the boundary layer mass deficit has been subtracted. This justifies the different behaviour for $L/D = 6$.

The picture of a strong interaction of the wall boundary layer with the shedding in the wake is further enforced by the asymmetry of the POD modes for low wall gap ratio cases. A prominent feature of these cases is the production on the wall of intermittent vorticity patches synchronized with the shedding (see Fig. 5.10b, 5.10e and 5.10h) that, for the lowest wall gap ratio, tend to merge with the vorticity shed by the downstream cylinder (see Fig. 5.10c, 5.10f and 5.10g), thus introducing stronger asymmetry in the modes.

The case of $L/D = 6$, i.e. within the *co-shedding regime* for $G/D = 3$, is significantly different. While for the far-from-the-wall case a dual shedding wake has been observed, at $G/D = 1$ the wake assumes features which are more similar to those of the case of $L/D = 3$, i.e. to the *reattachment regime*. This would suggest that the effect of the wall is to push the wake towards the downstream cylinder, thus promoting reattachment. For the case of $L/D = 6$ and $G/D = 0.3$ (Fig. 5.10i) the scenario is further complicated, since the pure shedding is associated with a flapping jet-like ejection from the slot created by the second cylinder and the wall. This feature is not observed in the cases of $L/D = 1.5$ and $L/D = 3$ since in both cases the wake of the upstream cylinder does not have enough stream-wise length to spread and merge with the wall boundary layer, producing blockage in the lower wall gap. However, even for the case of $L/D = 6$ and $G/D = 0.3$ (Fig. 5.10i) the intermittent release of vorticity of shedding wakes is still observable at $y/D = 1.5 - 2$, even though more diffused. This shedding is likely to be originating from the upstream cylinder, thus providing a picture of a shedding-attached regime, in which the wake of the downstream cylinder is strongly asymmetric, with an intermittent oscillating jet on the wall side and a shedding of vortices on the outer side.

The analysis of higher order modes is performed following the procedure described in §2.3 to identify the harmonic relation with the 1st mode. Following Eq. 2.33, the harmonic relation with the first mode is found in the form:

$$b^{(i)} = \sqrt{2\lambda^{(i)}} sin(2\pi m^{(i)} f^{(1)} + \varphi^{(i)}) \tag{5.3}$$

in which the parameters $m^{(i)}$ and $\varphi^{(i)}$ are found through the minimization problem in Eq. 2.35. The harmonic relation is considered successful when the correlation coefficient between the normalized time coefficient vector and the harmonic relation is above 0.7. For ease of notation, in the following the frequency of higher order modes will be indicated as $f^{(m)} = mf^{(1)}$.

Higher order modes present a more various set of behaviours for changing longitudinal pitch and wall gap ratios: same order modes can strongly differ from one case to the other, mostly because of the energy redistribution that characterizes these modes. In the cases where a pure vortex shedding is clearly the dominant behaviour (namely for *bluff-body regime* at high wall gap ratios), higher order modes are prevalently characterized by intermittent release of vorticity at a spatial and temporal frequency that is an integer multiple of the principal shedding frequency. The vorticity distribution is in some cases symmetric with respect to the stream-wise direction (see, for instance, for the 4th POD mode, the case of Fig. 5.12a and 5.12e), in some others asymmetric (see for example Fig. 5.12b and 5.12d). Symmetric modes tune the intensity and size of the

(a) L/D=1.5, G/D=3 4TH MODE

(b) L/D=1.5, G/D=1 4TH MODE

(c) L/D=1.5, G/D=0.3 4TH MODE

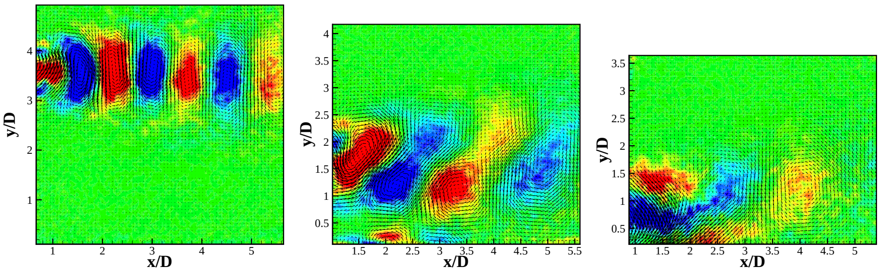

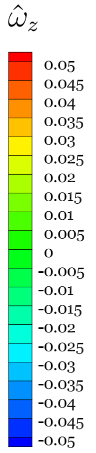

(d) L/D=3, G/D=3 4TH MODE

(e) L/D=1.5, G/D=1 6TH MODE

(f) L/D=6, G/D=3 4TH MODE

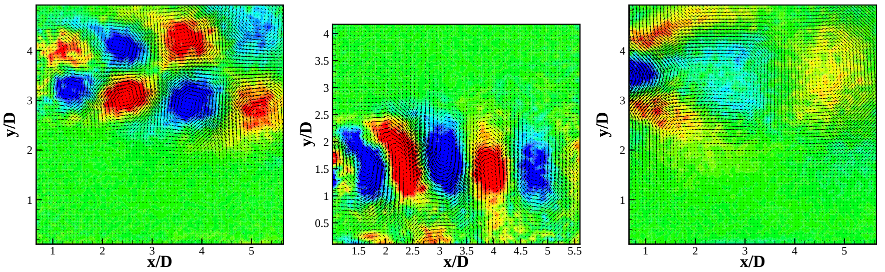

Fig. 5.12 Contour maps of non-dimensional vorticity $\hat{\omega}_z = D\left(\frac{\partial \phi_y}{\partial x} - \frac{\partial \phi_x}{\partial y}\right)$ of POD modes.

vortices shed in the wake, and are related to odd multiples of the shedding frequency (see, for instance, Fig.5.13a and 5.13e). Asymmetric modes, on the other side, model the cross-wise oscillation of the shedding wake, and are related to even multiples of the shedding frequency (see, for instance, Fig.5.13b and 5.13d). For cases not characterized by a pure shedding (such as for *reattachment* and *co-shedding regimes*), oscillations not correlated with the shedding (Fig. 5.12c and 5.12f and Fig. 5.13c and 5.13f) can account for higher energy content than the higher order harmonics of the shedding.

5.4 Discussion and conclusions

An extensive investigation has been carried out to study the effect of the ground on the wake produced by two cylinders in tandem configuration at $Re = 4.9 \times 10^3$. A number of interesting cases have been selected on the basis of the existing literature about the topic: 3 different longitudinal pitch ratios ($L/D = 1.5, 3, 6$) to span the typical regimes found for cylinders in tandem configuration with no wall effect; 3 different wall gap

(a) L/D=1.5, G/D=3 4TH MODE

(b) L/D=1.5, G/D=1 4TH MODE

(c) L/D=1.5, G/D=0.3 4TH MODE

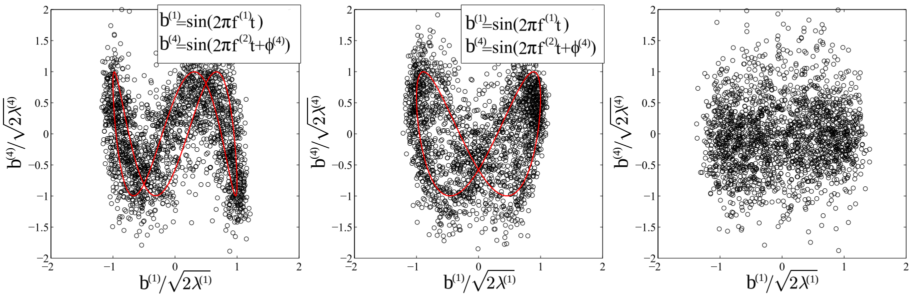

(d) L/D=3, G/D=3 4TH MODE

(e) L/D=1.5, G/D=1 6TH MODE

(f) L/D=6, G/D=3 4TH MODE

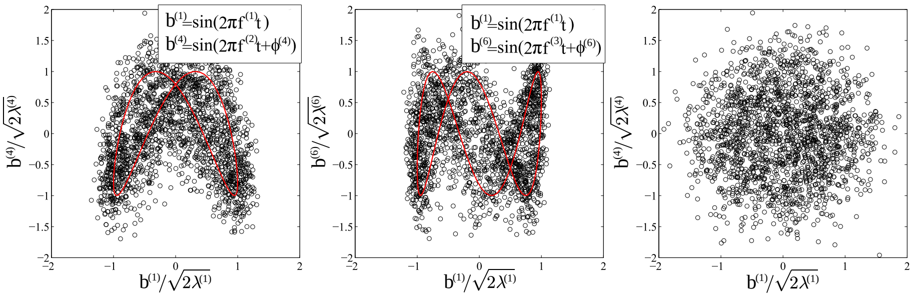

Fig. 5.13 Scatter plot of time coefficients of POD modes with respect to the time coefficients of the 1st mode.

ratios ($G/D = 3, 1, 0.3$) to study the effect of the ground. As a reference, the cases of a single cylinder at the same wall gap ratios have been studied. The study has been performed by means of PIV measurements in the wake of the downstream cylinder. The non-time-resolved measurements have been used to retrieve information about the first and second order statistics of the flow fields. The wake characteristics have been identified, finding in almost all the cases a good agreement with the self-similar wake model proposed by Schlichting and Gersten (2003). A modal decomposition of the fluctuating flow field has been performed to identify the dominant oscillations of the wake. This analysis has been performed by means of Proper Orthogonal Decomposition.

In all the cases, decreasing the wall gap ratio, asymmetry is introduced in the average flow, resulting in a bent wake: the very near wake is tilted upwards due to the effect of a wall jet released from the wall gap; the wake is then pulled towards the wall, most likely due to the presence of a wall-low-pressure region. This effect is strengthened for the cases in which a strong and localized blockage occurs, such as in the *reattachment regime.*

For moderate wall gap ratios, a still strong average flow is present through the gap. This results in the formation of a wall jet whose maximum velocity point can be considered as a boundary for the wall boundary layer. The wall jet appears to be strongly related to the width of the wake, resulting in a thickening of the boundary layer for thicker wakes, and thus in the merging of wake and boundary layer closer to the cylinders. Downstream of the merging, no more resemblance of the lower part of the former wake with the Schlichting model is found, suggesting that the low velocity region that is formed develops its own characteristics. Fluctuations in the wake of the cylinders are generally strengthened closer to the wall. For small wall gap ratios the average flow through the gap tends to be suppressed, due to the merging of wake and boundary layer close to the cylinder. Fluctuations tend to be further strengthened close to the wall gap, while they tend to disappear in the low velocity region which forms close to the wall downstream the merging point. This behaviour suggests the formation of a pulsating-jet-like flow in the gap and the periodical separation of the flow from the wall downstream with respect to the second cylinder.

The two most energetic modes from the decomposition revealed the presence in all the cases of study the presence of an underlying shedding-like mode. For high and moderate wall gap ratios ($G/D = 3, 1$) these modes model the von Kármán vortex shedding. Different characteristics in the shedding have been noticed at $G/D = 3$, depending on the L/D regime: in the *bluff-body regime* a simple and well localized shedding is observed; in the *reattachment regime* vortices are stretched in the streamwise direction and mix up with the shear layer deployed from the cylinders; in the *co-shedding regime* the vortices are stretched along the cross-wise direction and seem to be characterized by a double core. A reduction of the wall gap ratio to moderate values ($G/D = 1$) seems not to deeply influence the shedding, but a vorticity paired with it appears at the wall. The only exception appears to be the case $L/D = 6$, $G/D = 1$ in which the regime seems to change from the *co-shedding regime* to the *reattachment regime* as the wall gap is reduced. This behaviour may be explained by a bending of the shear layer released by the upstream cylinder due to the proximity of the wall and its reattachment on the surface of the downstream cylinder. For small wall gap ratio ($G/D = 0.3$) this vortex shedding appears to be at a significantly higher frequency and strong interaction with the wall is highlighted by strong asymmetry in the vorticity map. This behaviour suggests that this mode does not model anymore a von Kármán vortex shedding. The authors suggest that this vorticity release may be related with pulsating jet instabilities coupled with shedding from the outer side of the cylinders. Also for $G/D = 0.3$ the case $L/D = 6$ appears to be an exception: in this case it is possible to recognize a flapping jet that pairs with the shedding from the upstream cylinder.

The energy content of the first two POD modes is strongly reduced both for an increase of the longitudinal pitch ratio L/D and for a decrease of the wall gap ratio G/D. At the same time, higher order modes are generally interested by an energy redistribution. This suggests a shift of the flow towards less coherent behaviours and a reduction of the relevance of vortex shedding with respect to pure von Kármán shedding cases. It must also be remarked herein that the introduction of the downstream cylinder in the *bluff-body regime* results in a strengthening of the shedding modes with respect to the single cylinder case, suppressing shear layers oscillations.

The analysis of higher order POD modes and of their time coefficients revealed the presence, in most of the cases, of POD modes harmonically related to the first 2. These modes can be simply accounted as higher order harmonics of the vortex shedding and model vortex oscillations in both stream-wise and cross-wise directions. Due to the energy redistribution, for increasing L/D or for decreasing G/D these modes appear to be less energetically relevant and are often replaced by non harmonically related modes.

Chapter 6

Unsteady force and flow structures over flapping airfoil

In Chapter 5 it has been shown that POD can be used to describe the dynamics of the flow field with a compact subset of modes. In this chapter, the modal analysis is carried out on both the flow field and the aerodynamic force acting on a flapping airfoil in forward flight. The main interest is focused on the formation of vortical structures during the pitching/plunging motion of a 2D wing. These structures determine high unsteady loads on the wing, which cannot be captured by classical steady aerodynamics theories. The modal decomposition proposed in this chapter is aimed at determining a reduced-order model describing the mechanism of production of the force associated with these unsteady vortical features. The POD is applied on the fluctuating part of the phase-averaged flow field. Due to the presence of a moving boundary, the approach has been modified in order to obtain the modal description of the flow in the non-inertial body-fixed reference frame. The use of the Extended POD, which exploits the statistical correlation between two different set of signals (velocity fields and forces), allows for the estimation of the contribution to the fluctuating aerodynamic force of the flow structures extracted from POD. Finally, by comparing the different modal content for different kinematic parameters, a parametric model of the aerodynamic force is obtained.

6.1 Introduction

Several engineering problems deal with the unsteady aerodynamics of streamlined bodies in flapping motion, thus attracting a transversal interest on the topic. Some relevant examples are wing flutter instability (Bisplinghoff et al., 2013), dynamic stall of rotor blades both in helicopters (Harris et al., 1970, Tarzanin, 1972, Young Jr, 1981) and wind turbines (Hansen and Butterfield, 1993, Shipley et al., 1995). A recently growing interest on flapping wings is due to the development of the concept of Micro Air Vehicles (MAVs), i.e. vehicles with a wing span and weight lower than $15cm$ and $200g$ (Pines and Bohorquez, 2006), respectively.

Due to their small size and flight speed, MAVs operate in a low Reynolds number regime, ($Re \leqslant O(10^4)$, Shyy et al., 2007). In this regime the performances of traditional fixed wings are seriously compromised due to the earlier occurrence of stall with respect to higher Reynolds number airfoils (Lian and Shyy, 2007). On the other side, rotary wings, when scaled to the small size of a MAV, generate induced drag which reduces the aerodynamic efficiency.

These considerations led to aim towards bio-inspired paradigms to improve MAVs aerodynamic performances. Birds, insects, fishes and any other natural flyer (or swimmer) make use of flapping wings (or fins) to efficiently produce high lift and thrust coefficients despite operating at low Reynolds numbers (Lighthill, 1969, Ellington, 1984). The superior performances of flapping wings with respect to their fixed counterparts are ascribed to the formation of vortical structures on both the leading and the trailing edge of the wing during the unsteady separation of the flow. The high lift coefficient experienced in flapping flight is ascribed to the formation of a Leading Edge Vortex (LEV) and to the *delayed stall* effect which it induces. As long as the LEV is attached to the wing, complete separation of the flow is delayed; consequently, the maximum lift coefficient attained before stall is greater than the maximum lift coefficient of a conventional fixed wing (McCroskey, 1982). Thrust generation in natural flyers and swimmers has instead been connected to the spatial organization of the vortical structures shed in the wake (Platzer et al., 2008): thrust-producing wakes are characterized by an inverse von Kármán street, which produces an increase of momentum in the wake, oppositely to a classic von Kármán street, which produces a momentum deficit. This is, however, a simplified picture, since in some cases an inverse von Kármán street might not be thrust-generating (Mackowski and Williamson, 2015, Andersen et al., 2017).

A commonly investigated simplified version of the 3D flapping wing consists in a 2D airfoil with a two degrees of freedom motion, namely a sinusoidal vertical plunging motion $h(t)$ and a sinusoidal pitching motion $\alpha(t)$. The parametric space of the involved physical quantities includes the airfoil chord $c\,[\mathrm{m}]$, the free-stream velocity $V_\infty\,[\mathrm{m/s}]$, the fluid kinematic viscosity $\nu\,[\mathrm{m/s^2}]$, the flapping frequency $f\,[\mathrm{Hz}]$ or the flapping period $\tau = 1/f\,[\mathrm{s}]$ and the plunging amplitude $h_0\,[\mathrm{m}]$. According to the Buckingham π

theorem (Buckingham, 1914), the scaling of 2D flapping airfoils performances is based on three non-dimensional numbers: the chord-based Reynolds number, $Re = cV_\infty/\nu$; the Strouhal number, $St = 2h_0 f/V_\infty$; the reduced frequency, $k = \pi c f/V_\infty$. The airfoil geometry should be added to the set (even though it has been shown to have minor effects, except for the leading edge shape, see e.g. Rival et al., 2014), as well as the effective angle of attack history

$$\alpha_{eff}(t) = \alpha(t) - \tan^{-1}\left(\dot{h}(t)/V_\infty\right) \tag{6.1}$$

where $\dot{h}(t)$ is the time-derivative of $h(t)$. The effective angle of attack history, as reported in Eq. 6.1, is implicitly including also the information about the pitching motion history (which, in case of sinusoidal motion would be determined by the pitching amplitude and by the phase delay).

6.1.1 Potential flow models for force generation in flapping airfoils

The first models of lift generation in plunging and pitching airfoils date back to the works of Theodorsen (1935) and von Kármán and Sears (1938). The models were derived within the framework of the linear potential flow theory, which implies inviscid fluid, small oscillations and planar wake. While these hypotheses are suitable for the study of wing flutter instability, the wing kinematics of natural flyers determine effects far beyond the limits of linear theory. Nevertheless, these linear models still provide a useful framework for the understanding of flapping wing aerodynamics (Baik et al., 2012). In the work by von Kármán and Sears (1938) it is assumed that the flow is two-dimensional and that the wake produced by the airfoil is located on its chord-wise direction (planar wake). In this framework the theory of thin airfoils is used for the calculation of the lift. In unsteady flows the total circulation around the airfoil is time-variable, producing a wake of distributed vortex lines. For the computation of the lift, it is considered that the vorticity γ along the chord-wise direction is composed of two parts:

1. the quasi-steady vorticity distribution γ_0, which is the vorticity that would be produced according to the thin airfoil theory without accounting for the wake effect;

2. the vorticity distribution induced by the wake γ_1.

It can be shown that the lift per unit area $\mathscr{L}/S$ is composed of three contributions:

$$\mathscr{L}/S = \underbrace{-\rho\frac{d}{dt}\int_0^1 \gamma_0(\xi)\xi d\xi}_{\text{non-circulatory lift}} + \underbrace{\rho V_\infty \Gamma_0}_{\text{quasi-steady lift}} + \underbrace{\rho V_\infty \int_1^\infty \frac{\gamma_1(\xi)d\xi}{\sqrt{\xi^2-1}}}_{\text{wake-induced vorticity}} \tag{6.2}$$

where ξ is the non-dimensional chord-wise coordinate (which coincides with the stream-wise coordinate under the small angles assumption) using the wing chord as reference length. The non-circulatory term that appears in Eq. 6.2 accounts for the effect of the added mass, i.e. the mass of fluid moved by the wing acceleration, and depends on the change of circulation over the wing.

Wagner (1925) calculated the lift response of a flat plate to a step input, i.e. the lift generated on an impulsively started airfoil. The circulatory lift from Wagner (1925) results in:

$$C_l = 2\pi \sin(\alpha) W(s) \tag{6.3}$$

where $W(s)$ is the Wagner's "indicial" function depending on $s = 2V_\infty t/c$. The Wagner's function can be approximated (within a 2% error) as:

$$W(s) \approx 1 - \frac{2}{4+s} \tag{6.4}$$

In the formulation by Theodorsen (1935), the vorticity is modelled according to the velocity potential of an airfoil in sinusoidal pitching/plunging motion. Theodorsen (1935) expresses the sinusoidal motion using the complex exponentials notation:

$$\begin{aligned} h(t) &= h_0\, e^{\iota(2\pi f t)} \\ \alpha(t) &= \alpha_m + \alpha_0\, e^{\iota(2\pi f t + \varphi)} \end{aligned} \tag{6.5}$$

with h_0 being the plunging amplitude, α_0 the pitching amplitude, α_m the mean angle of attack and φ the phase delay between plunging and pitching motion.

Following the notation reported by Baik et al. (2012), the lift coefficient can be expressed as in Eq. 6.6:

$$\begin{aligned} C_l(t) &= \underbrace{\frac{\pi c}{2V_\infty}\left(\dot{\alpha}_{eff}(t) - \frac{c}{2V_\infty}\ddot{\alpha}(t)(2\xi_p - 1)\right)}_{\text{non-circulatory lift}} + \underbrace{2\pi\alpha_m + 2\pi C(k)Q(t)}_{\text{circulatory lift}} \\ Q(t) &= \alpha_{eff}(t) - \alpha_m + \frac{c}{2V_\infty}\dot{\alpha}(t)(1.5 - 2\xi_p) \end{aligned} \tag{6.6}$$

where ξ_p is the position of the pivot point with respect to the leading-edge expressed as a fraction of the chord and the dot notation $\dot{g}$ indicates the time derivative of the generic quantity g. The complex-valued function $C(k)$ is the Theodorsen's function defined according to Eq. 6.7 (Jones, 1945):

$$C(k) = \frac{H_1^{(2)}(k)}{H_1^{(2)}(k) + \iota\, H_0^{(2)}(k)} \tag{6.7}$$

where $H_n^{(2)}(k)$ is the Hankel function of the second kind of order n of the reduced frequency k. This function accounts for the wake vorticity contribution and it is equal to 1 for $k = 0$. The only physically meaningful part in Eq. 6.6 is the real part. Garrick (1938) showed that the Wagner's function $W(s)$ and the Theodorsen's function $C(k)$ are related through the Fourier transform.

Concerning drag/thrust generation in flapping airfoils with sinusoidal motion, in a pioneering study, Garrick (1937) identified 2 contributions to the unsteady drag: the projection in the flight direction of the pressure force on the airfoil (roughly corresponding to the lift in the Theodorsen's model) and a leading-edge (LE) suction produced by the accelerated flow about the leading edge.

Following the notation by Baik et al. (2012), the drag coefficient can be expressed according to Eq. 6.8:

$$C_d(t) = \underbrace{-C_l(t)\,\alpha}_{\text{lift projection}} \underbrace{-\,\pi\left(\frac{\sqrt{2}}{2}\left(2C(k)Q(t) - \frac{c}{2V_\infty}\dot{\alpha}\right)\right)^2}_{\text{LE suction term}} \tag{6.8}$$

where the suction term is calculated from the energy balance necessary to generate the wake vorticity. It should be remarked that the model by Garrick is based on potential flow theory, thus disregards the effects of friction drag (for reference, see DeLaurier, 1993). At low Reynolds number this assumption is severely challenged. Also, in Eq. 6.8 small angles of attack have been assumed.

The models by Wagner (1925), Theodorsen (1935) and Garrick (1937) rely on the hypothesis of small amplitude oscillations, thus they are not accurate in describing the forces for the high angles of attack which typically characterize flapping flight. Several other models have been proposed in literature to overcome this limitation. Aerodynamic force models which are of interest for flight control applications in MAVs have been recently reviewed by Sun (2014). In the following a few examples are reported.

Sane and Dickinson (2002) developed a quasi-steady model which has been largely employed for flight dynamics. The total instantaneous force F_{inst} on the wing is decomposed in four components, all acting perpendicularly to the chord:

$$F_{inst} = F_a + F_{trans} + F_{rot} + F_{wc} \tag{6.9}$$

where F_a is the added-mass force, F_{trans} is the circulatory force which is induced by the wing translation, F_{rot} is the force depending on the wing rotation and F_{wc} is the force due to the wake capture. The quasi-steady circulatory force due to translation is obtained by Sane and Dickinson (2002) by fitting measurements of mutually orthogonal lift and drag forces for the wing to model to account also for the dynamic stall effects.

The added-mass force for a flat plate is obtained theoretically by Sedov (1965) through the method of the complex coordinates. For a plunging/pitching flat plate, the added-mass force has 2 components, $F_{a,y'}$, normal to the plate and $F_{a,x'}$, tangent to the plate:

$$\begin{aligned} F_{a,y'} &= -\frac{\rho\pi c^2}{4}\dot{V}_{y'} - \frac{\rho\pi c^3}{8}\ddot{\alpha} \\ F_{a,x'} &= \frac{\rho\pi c^2}{4}\dot{\alpha}V_{y'} + \frac{\rho\pi c^3}{8}\dot{\alpha}^2 \end{aligned} \tag{6.10}$$

with $V_{y'}$ and $V_{x'}$ being respectively the velocity of the flow in the normal and in the tangential direction with respect to the plate. The circulatory force due to wing rotation is derived by Fung (2002) and corresponds to:

$$F_{rot} = \rho V_\infty \pi c^2 \left(\frac{3}{4} - \xi_p\right)\dot{\alpha} \tag{6.11}$$

The model by Sane and Dickinson (2002) has been further refined by Pesavento and Wang (2004) and by Berman and Wang (2007), removing the wake-capture term and adding a term for the viscous force. Pesavento and Wang (2004) estimate the circulatory forces by fitting the pressure force obtained from the Navier-Stokes solution with the force obtained by a circulation over the airfoil which includes both the part due to translation and the part due to rotation. A similar approach has been also employed by Taha et al. (2014), who accounted for the effect of the wake in a generic motion by extending the Wagner's indicial function by means of a superposition principle. An attempt to develop a semi-analytical model with no semi-empirical adjustements has been proposed by Ansari et al. (2006). The model by Ansari et al. (2006) is based on the unsteady vortex lattice method, modified to account for LEVs and TEVs. The effect of added-mass, wing-rotation and wake-capture forces are included in the model. Despite the model by Ansari et al. (2006) does not require empirical adjustments, its solution is computationally expensive for a MAVs microprocessor, an thus cannot be employed for flight control applications.

The recent work by Floryan et al. (2017) proposes a novel scaling for propulsive forces in pure pitching and pure plunging airfoils. The scaling is based on the results of potential flow theory. The time-averaged thrust is found to depend mainly on the Strouhal number (based on the trailing edge displacement amplitude) and on the reduced frequency. For pure pitching motion, the thrust is entirely ascribed to the added mass effects. For pure plunging motion, the thrust is entirely due to lift-based (circulatory) forces. The thrust estimated from potential flow theory has to be corrected by subtracting a viscous drag term which is shown to be almost independent on the amplitude and frequency of the motion. Consequently, since the lift projection term of the thrust decreases for slower flapping motions, viscous drag is dominant with respect to thrust at low Strouhal numbers.

6.1.2 Force generation and flow organization

The flow topology of flapping airfoils and its effects on force generation have been object of a long debate. For instance Polhamus (1966), differently from Garrick (1937), considered the LEV as a source of lift in delta-wings rather than a thrust source. According to the so called Polhamus's leading-edge-suction analogy, the LEV produces a low-pressure region on the upper surface of the wing which generates a *vortex lift*. More recently, an assessment of models for forces generation and their relation with the vortex dynamics has been proposed by Baik et al. (2012). The lift and drag measurements were compared with the estimations provided according to Theodorsen (1935) and Garrick (1937) theories. The measured lift was found to be in acceptable agreement with the Theodorsen's theory if adding to Eq. 6.6 the suction term from Eq. 6.8, thus proving the validity of the Polhamus's analogy in flapping wings. On the other side, the measured drag presented a poor agreement with Garrick's theory (both with and without the LE suction term). The results by Baik et al. (2012) confirm that the LEV produces lift, as suggested by Polhamus (1966), and identify the force component normal to the chord as the main contributor to the total aerodynamic force. The importance of the LEVs and Trailing Edge Vortices (TEVs) on force generation in flapping wing aerodynamics has been further studied by Pitt Ford and Babinsky (2013) for an impulsively started wing. The LEV and the TEV are modelled as additional circulation sources in a potential flow model, thus confirming the importance of these vortical structures in determining the aerodynamic forces over the wing.

It is clear that both the correct prediction of the temporal variation of the aerodynamic forces and the consequent development of control strategies require a deeper understanding of the mechanisms behind the evolution of the vortical structures (LEVs and TEVs) on the wing. During the plunging and pitching motion the vorticity flux in the boundary layer feeds the growth of the LEV. The LEV increases in size providing additional suction until it detaches from the airfoil, eventually resulting in a drop of the lift coefficient. Dabiri (2009) related the optimal Strouhal number of bio-inspired propulsive systems to the optimal vortex formation time. This concept was first introduced by Gharib et al. (1998) for ring vortices generated as the result of the amplification of the instability of a shear layer between two flows moving with a difference in velocity equal to ΔV. Dabiri (2009) extended the concept of non-dimensional vortex formation time ($\widehat{T}$) to flapping wings:

$$\widehat{T} = \frac{K\Gamma}{c\Delta V} \tag{6.12}$$

where Γ is the instantaneous vortex intensity, c is the airfoil chord, ΔV is the boundary layer strength (i.e. the total velocity difference through the boundary layer between the wing wall and the outer flow) and K is a non-dimensional constant related to the inverse of the dimensionless vorticity flux $d\widehat{\Gamma}/d\widehat{T}$. An optimum vortex formation leads to maximize the circulation of the vortex and consequently its contribution to the aerodynamic force. Past the optimal vortex formation time, the vortex growth cannot be sustained anymore and the vortex pinch-off occurs. The optimal vortex formation time is found to be approximately equal to $\widehat{T} \approx 4$. The relationship of $\widehat{T}$ with the Strouhal number can be expressed as:

$$\widehat{T} = \frac{\Gamma_{max}}{V_\infty c} \frac{2}{2\pi St} \tag{6.13}$$

with Γ_{max} being the maximum vortex intensity.

It follows that the typical Strouhal numbers characterizing the mechanics of animal locomotion (in the range $0.2 < St < 0.4$) correspond to the optimal vortex formation. The concept of $\widehat{T} \approx 4$ as the limiting point for the LEV growth has been experimentally proven by Rival et al. (2009) and Baik et al. (2012) for low reduced frequencies and kinematic parameters compatible with efficient flight. For higher reduced frequencies Baik et al. (2012) found much lower formation times. A possible explanation is provided by Widmann and Tropea (2015) who identified two different mechanisms for the LEV pinch-off in flapping wings: the *boundary layer eruption* and the *bluff-body detachment* mechanism. The *boundary layer eruption* (Doligalski et al., 1994) occurs when the LEV is expelled from the boundary layer due to the impossibility to sustain its growth. This phenomenon is mainly related to the characteristics of the boundary layer at the leading edge. The *bluff-body detachment* mechanism (Gerrard, 1966) is obtained when the LEV reaches the size of chord of the airfoil. Widmann and Tropea (2015) show that, while the LEV is attached to the airfoil, it is bounded between the stagnation point and a reattachment point on the airfoil, which, according to singularity-based topology analysis (Foss, 2004), represent two half-saddle points in the flow field. As the LEV grows, the reattachment point moves towards the trailing edge. If the reattachment point moves beyond the trailing edge, it merges with the half-saddle point of the rear stagnation point, forming a full-saddle point in the free-stream. This full-saddle point results in a flow reversal on the airfoil and in the consequent detachment of the LEV. This phenomenon is more likely to occur for moderate reduced frequencies.

6.1.3 Bridging the gap between flow topology and reduced-order models

Although the topology of the flow around a flapping airfoil has been well characterized for a wide portfolio of kinematics in the literature, a simple model describing the influence of the kinematics on the vortex growth and pinch-off is still lacking. More importantly, the effect of the kinematic parameters on the aerodynamic force (i.e. lift and drag/thrust components) needs to be further understood. Simplified models such as those by Theodorsen (1935) for the lift and Garrick (1937) for the drag/thrust have shown to be a powerful starting point for control strategies (see, e.g. Brunton et al., 2013). Nevertheless, classical theories have shown some limits in predicting aerodynamic loads, especially in the low Reynolds number range (as shown by Baik et al., 2012), thus an improvement is needed for the optimization of flapping wings performances and control.

The objective of the work included in this chapter is to identify a simplified model of the evolution of the vortical features (LEV and TEV) and of the generation of lift and drag/thrust in flapping airfoils, depending on motion kinematics. The final aim is to derive corrections to the models by Theodorsen (1935) and Garrick (1937), accounting for the vortex organization during the motion. The approach to relate force generation and vortex organization is based on measuring simultaneously velocity fields and forces, and then decomposing both on the same temporal basis. The basis is obtained through POD to extract low-order reconstructions based on the most energetically relevant flow features. To this purpose a set of airfoil kinematics have been investigated in a water tunnel. The Reynolds number based on the chord and on the free-stream velocity is set equal to 3600 (thus in the region of interest of MAVs). The Strouhal number is fixed to 0.2, which has shown to be a typical value for natural flyers over a wide range of size and flight speed (Shyy et al., 2007). Setting a plunging half-amplitude of one chord, the reduced frequency results equal to 0.31. This shrinks down the non-dimensional parametric space to the effective angle of attack history. The experimental arrangement is described in §6.2.

The projection onto the same temporal basis to correlate force and velocity field features grounds in the extended POD approach (Borée, 2003) which has been successfully used in the past to correlate with flow coherent structures several synchronized measurements such as wall pressures (Picard and Delville, 2000) and concentrations in reactive flows (Duwig and Iudiciani, 2010). Measured forces are projected onto the POD temporal basis in order to estimate the force contribution over time of each mode. The flow fields are priorly reported in the wing-fixed non-inertial reference frame to compensate the wing motion and mantain fixed the grid on which the POD analysis is carried out. A discussion on the effect of rotation on the vorticity is reported in §6.3.1. Phase and time average flow fields and forces are reported in §6.4, while modal decompositions of the flow fields and of the forces are discussed in §6.5. The modal analysis performed through POD and EPOD gives a deeper insight both on flow features and on their effect of the force than what is possible to get from phase-averaged quantities, eventually setting the pathway to the construction of a reduced model for the force. In §6.6 the contributions of the modes on the forces are contrasted against the force terms of the models by Theodorsen and Garrick, suggesting a new interpretation and paving the way for their modification.

6.2 Experimental setup

The experimental measurements have been performed on a two-dimensional flapping wing in the water tunnel of the Aerospace Engineering Group at the *Universidad Carlos III de Madrid*. The water tunnel has a 2.5 m long rectangular test section of $0.5 \times 0.55\,\mathrm{m}^2$ with full optical access. The tunnel is capable of reaching a maximum speed of 2 m/s with a stream-wise turbulence intensity lower than 1% of the free-stream velocity at a 0.12 m/s.

The model tested is an aluminium wing with rectangular plan-form and aspect ratio equal to 16.3. The wing section is a NACA 0012 airfoil with chord c equal to

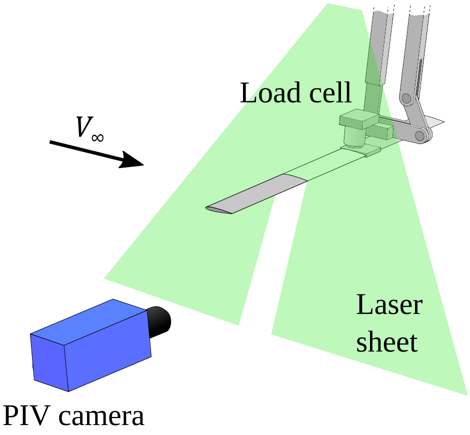

Fig. 6.1 Sketch of the experimental setup.

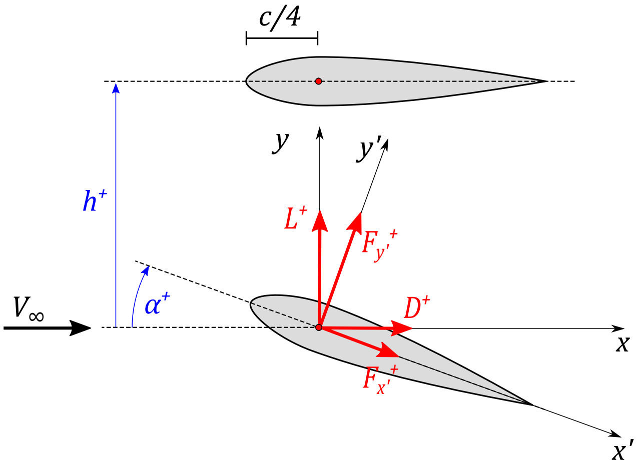

Fig. 6.2 Pitching/plunging airfoil motion and forces. The + superscript indicates positive direction.

0.03 m. The wing span is 0.49 m, thus fitting almost from side-to-side the test chamber. This ensures minimal finite wing effects while still providing sufficient clearance to avoid contact with the tunnel walls during the movement. The experimental setup is sketched in Fig. 6.1. In the following details on the movement system and on the measurement systems (load cell and PIV system) will be given.

6.2.1 Wing kinematics and motion system

The wing kinematics is a combination of sinusoidal pitching and plunging motion described in Eq. 6.14:

$$\begin{aligned} h(t) &= h_0 \sin(2\pi f t) \\ \alpha(t) &= \alpha_m + \alpha_0 \sin(2\pi f t + \varphi) \end{aligned} \tag{6.14}$$

which is equivalent to Eq. 6.5. The positive direction of the movements is sketched in Fig. 6.2, which also reports the wind reference frame (x, y) and the airfoil reference frame (x', y').

$L_{12} = 600.0\,\text{mm}$	$L_{23} = 60.0\,\text{mm}$	$L_w = 12.0\,\text{mm}$
$L_{45} = 565.0\,\text{mm}$	$L_{34} = 40.0\,\text{mm}$	$x_5 - x_1 = 40.0\,\text{mm}$

Table 6.1 Lengths of the bars of the linkage mechanism.

The wing movement is achieved by means of a home-built four-bar linkage (sketched in Fig. 6.3a) which converts the displacements of two independent linear actuators into a pitching/heaving motion. The linear movement of the actuators is obtained from the kinematic inversion of the mechanism. According to the mechanism diagram given in Fig. 6.3b, the position of the hinges of the linkage and of the wing aerodynamic center is described by the equation system:

$$\begin{cases} x_2 = x_1 \\ y_2(t) = y_1(t) - L_{12} \\ x_4 = x_5 \\ y_4(t) = y_5(t) - L_{45} \\ x_3(t) = x_2 + L_{23}\cos(\alpha(t)) = x_4 + L_{34}\sin(\beta(t)) \\ y_3(t) = y_2(t) - L_{23}\sin(\alpha(t)) = y_4(t) - L_{34}\cos(\beta(t)) \\ x_w(t) = x_2 - L_w\sin(\alpha(t)) \\ y_w(t) = y_2(t) - L_w\cos(\alpha(t)) \end{cases} \tag{6.15}$$

where the length of each bar is give in Table 6.1.

By solving the system for $y_1(t)$ and $y_5(t)$ as a function of $y_w(t)$ and $\alpha(t)$, it is possible to get the inverse kinematic relations of the mechanism. It is worth noticing that the mechanism only allows for two inputs (corresponding to $y_1(t)$ and $y_5(t)$) and two independent outputs ($y_w(t)$ and $\alpha(t)$). The output $x_w(t)$ is a slowly varying function on $\alpha(t)$ and cannot be compensated due to the lack of a third degree-of-freedom in the system. This dependence can be reduced by reducing L_w, i.e. setting the aerodynamic center as close as possible to the linkage rotation center. However, since the linkage is connected close to the middle-span of the wing, a minimum distance is required in order to avoid contact between the wing and the linkage mechanism.

The vertical positions $y_1(t)$ and $y_5(t)$ are controlled by means of two independent linear drives Festo EGSK-26-50-6P (maximum span 100 mm, maximum acceleration 3 m/s^2, 0.01 mm positioning precision). The uncertainty in the position of the wing is equal to 0.01 mm in the vertical direction and lower than 0.03° for the angle of attack.

Due to the limited acceleration, the system can work in a parametric space which is limited in terms of k, St and h_0 as sketched in Fig. 6.4, where the shaded area contains the parametric space of allowed motions. The span of the linear actuator, along with the limitation imposed by the angles of the linkage, limits the range in the parametric space including φ, α_m, α_0 and h_0.

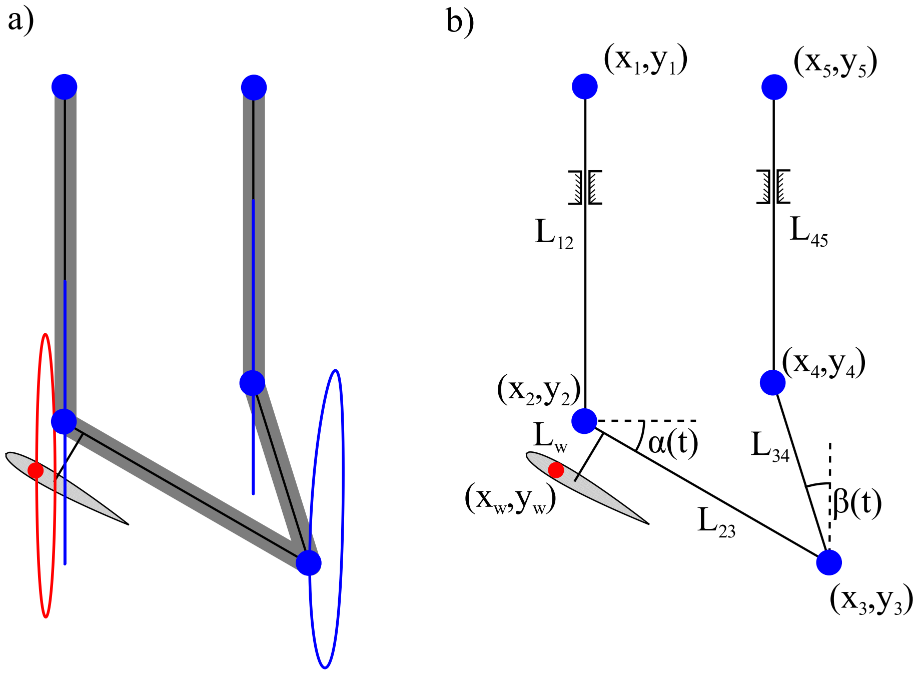
a)
b)
(x1,y1)
(x5,y5)
L12
L45
(x4,y4)
(x2,y2)
Lw
α(t)
L34
β(t)
(xw,yw)
L23
(x3,y3)

Fig. 6.3 Four-bar mechanical linkage: a) example of the wing aerodynamic center (red) and linkage hinges (blue) pattern; b) diagram of the mechanism.

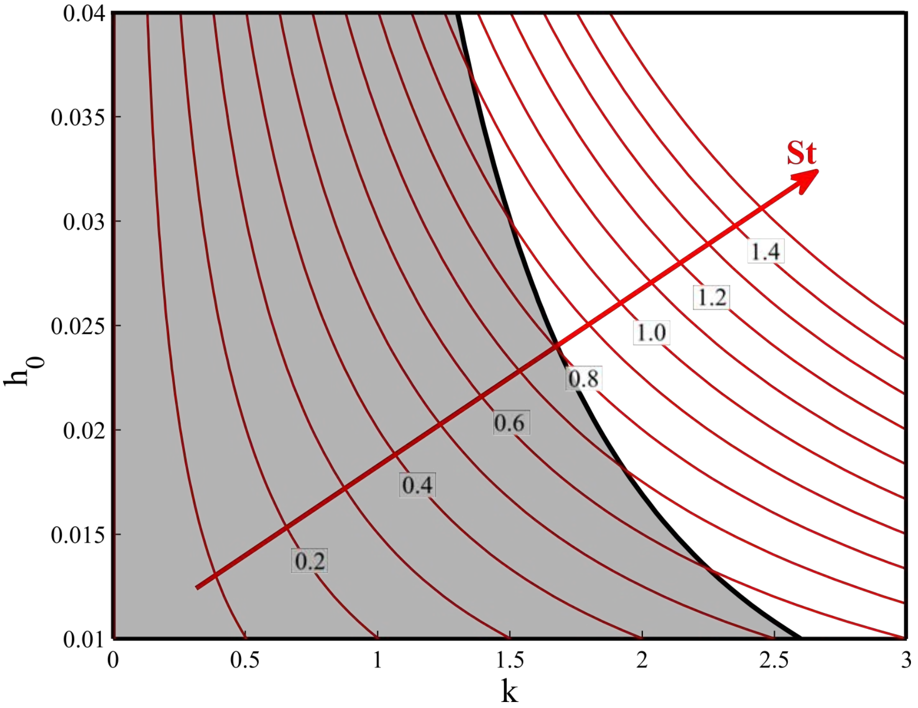

Fig. 6.4 Parametric space spanned by the motion system. The shaded area contains the parametric space allowed.

Test Name	h_0 [mm]	α_0	α_m	φ	St
Case A	30	0°	0°	90°	0.2
Case B	30	10°	0°	90°	0.2
Case C	30	20°	0°	90°	0.2
Case D	30	0°	10°	90°	0.2
Case E	30	10°	10°	90°	0.2
Case F	30	20°	10°	90°	0.2

Table 6.2 Summary of the wing kinematics parameters.

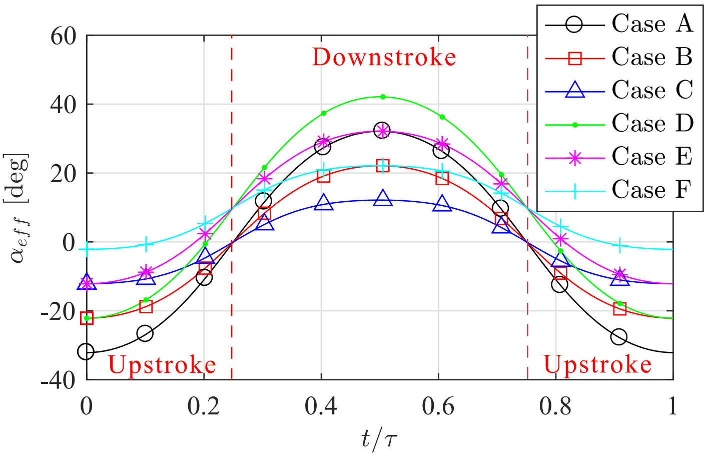

Fig. 6.5 Effective angle of attack history for all the cases.

As mentioned in §6.1.3, the experiments described in this chapter are performed at $St = 2h_0 f/V_\infty = 0.2$ and $k = \pi c f/V_\infty = 0.31$ (corresponding to a flapping frequency $f = 0.4\,\text{Hz}$), with a free-stream velocity of $V_\infty = 0.12\,\text{m/s}$ corresponding to a chord-based Reynolds number $Re = cV_\infty/\nu = 3600$ (with ν the kinematic viscosity of water). Six different kinematics have been explored (see Table 6.2).

The six cases result in different time-histories of the effective angle of attack of the airfoil (see Fig. 6.5). This angle can be calculated from the kinematic parameters by reworking Eq. 6.1 and 6.14 as

$$\alpha_{eff}(t) = \alpha_m + \alpha_0 \cos(2\pi f t) - \tan^{-1}\left(\pi\, St \cos(2\pi f t)\right) \tag{6.16}$$

6.2.2 Aerodynamic forces measurements

The aerodynamic force components in the airfoil reference frame ($F_{x'}$ and $F_{y'}$, with positive directions indicated in Fig. 6.2) are measured with an ATI Industrial Automations Nano-17 IP68 load cell with IP68 waterproofing. The load cell connects the wing to the mechanical linkage as sketched in Fig. 6.1. The force components are reduced to non-dimensional force coefficients using the dynamic pressure $q = \frac{1}{2}\rho V_\infty^2$ and the wing area S as reference force:

$$C_{F_{y'}} = F_{y'}/\left(qS\right) = F_{y'}/\left(\frac{1}{2}\rho V_\infty^2 S\right) \qquad \text{chord-normal force coefficient}$$

$$C_{F_{x'}} = F_{x'}/\left(qS\right) = F_{x'}/\left(\frac{1}{2}\rho V_\infty^2 S\right) \qquad \text{chord-wise force coefficient}$$

$$C_L = \mathscr{L}/\left(qS\right) = \mathscr{L}/\left(\frac{1}{2}\rho V_\infty^2 S\right) \qquad \text{lift coefficient}$$

$$C_D = \mathscr{D}/\left(qS\right) = \mathscr{D}/\left(\frac{1}{2}\rho V_\infty^2 S\right) \qquad \text{drag coefficient}$$

According to the load cell manufacturer specifications, within the adopted calibration range the force measurement resolution is of 1/341 N. For a tunnel speed of about 0.12 m/s, a density of 1000 kg/m^3 and a wing surface of 0.015 m^2 the typical resolution of force coefficients measurements is about 0.03. The sensor response is also affected by a long-period thermal drift. While this effect is easily removed from the fluctuating part of the force by signal detrending, a bias error on the average force is still present. Consequently the uncertainty on the average force components has been experimentally estimated accordingly to the typical thermal drift and measurement duration. The uncertainty on the force coefficients is estimated to be lower than 0.1 and 0.05 respectively for the chord-wise and chord-normal components. This results in an experimental uncertainty of about 1% and 6% of the maximum force-fluctuation amplitude respectively for the chord-wise and chord-normal components. The analogue signal from the load cell is digitalized by a National Instruments Data Acquisition device (NI USB-6210) at a sample rate of 1000 Hz. A low pass filter with threshold at 10 Hz is applied to the force data to remove spurious noise content (mostly due to electromagnetic noise from the water tunnel pumps running at 13 Hz). While this cutoff frequency may look fairly low, it must be specified that it still results in a 25 times bigger frequency than the flapping one for the present experiments. Also, the main interest in the following will be towards the lower order modes obtained through the EPOD of the force, which are not affected by the filtering. The phase averages of the force components are obtained after correction of the inertial forces of the wing and of the height-dependent bias induced by the waterproofing, which have been both determined experimentally. The inertial forces have been measured in a *dry experiment*, i.e. with empty tunnel. The height-dependent bias has been determined with a static wet experiment, i.e. with filled test section, no free-stream flow and very slow wing motion (actuation frequency of $0.04Hz$).

6.2.3 Flow field measurements

The flow field measurements are carried out with planar Particle Image Velocimetry in a x-y plane. The flow is seeded with neutrally-buoyant polyamide particles with 56 μm diameter. The illumination is provided by a dual cavity Nd:Yag Quantel Evergreen laser (200 mJ/pulse at 15 Hz); the laser beam is shaped into a light sheet with a thickness of approximately 1 mm and a width of about 10 chords in the stream-wise direction. A 5.5 Mpixels Andor sCMOS camera is used to capture images with a resolution of about 8.5 pix/mm. The PIV system is synchronized with the movement system in order to provide phase-averaged measurements. Measurements are performed for 80 different phases, acquiring for each of them a set of 55 phase-locked flow field snapshots. The images are pre-processed to remove the background intensity via an eigenbackground removal procedure (applied separately for each phase-locked snapshot set) outlined in Chapter 4 and in Mendez et al. (2017). A multi-pass image deformation algorithm implemented in the software SPIV (Astarita, 2006) is used to extract the velocity fields. The velocity fields are computed using a custom-made multipass image deformation algorithm (Scarano, 2001). The final interrogation region size is 32×32 pixels with 75% overlap, thus corresponding to about 32 independent vectors per chord. The typical displacement error is equal to 0.1 pixels (Westerweel, 1997), thus corresponding to an error of 0.8% of the free-stream velocity at the present image resolution. Due to the presence of the shadow of the wing in the PIV images, after phase averaging, the velocity vectors in the flow field regions which are not illuminated by the laser light are replaced on the basis of symmetry arguments with data from a specular experiment.

6.3 Data Processing

6.3.1 Change of reference frame

In case of problems with moving boundaries (such as a flapping wing), the fluid domain changes with time, thus the decomposition approach needs to be modified. The POD with the snapshot method operates with indices corresponding to the measurement grid points and does not directly account for the relative position with respect to the wing. In a problem with a time-varying domain, the location of the grid points has to be adapted for each snapshot outside of the fluid domain (for instance inside of the moving wing). Based on these arguments, in the following, velocity values are estimated over a grid with points fixed with respect to the airfoil (i.e. the grid is heaving and pitching together with the airfoil). A similar POD approach over a moving grid was proposed by Anttonen et al. (2003).

To pass from the inertial reference frame $\underline{x} = (x, y)$ in which the wing is moving to the non-inertial one $\underline{x}' = (x', y')$ in which the wing is steady, a rotation and a translation, according to the pitching angle $\alpha(t)$ and heaving $h(t)$ history are needed. Given $\underline{i}$ and $\underline{j}$ the unit vectors in the x and y directions and $\underline{i}'$ and $\underline{j}'$ the unit vectors in the x' and y' directions, the space transformation is expressed by:

$$\begin{aligned} \underline{x}' &= \underline{\underline{M}}(\alpha)\left(\underline{x} - h(t)\underline{j}\right) \\ \underline{x} &= \underline{\underline{M}}^{-1}(\alpha)\underline{x}' + h(t)\underline{j} \end{aligned} \tag{6.17}$$

where the rotation matrix $\underline{\underline{M}}(\alpha)$ is given by:

$$\underline{\underline{M}}(\alpha) = \begin{bmatrix} \cos(\alpha) & -\sin(\alpha) \\ \sin(\alpha) & \cos(\alpha) \end{bmatrix} \tag{6.18}$$

The transformation of the velocity field $\underline{\dot{x}} \equiv (u, v)$ in the inertial reference frame to the velocity field $\underline{\dot{x}}' \equiv (u', v')$ in the wing-fixed reference frame is obtained through derivation of the Eq. 6.17. The transformation of the velocity field is then given by:

$$\begin{aligned} \underline{\dot{x}}' &= \underline{\underline{\dot{M}}}(\alpha)\left(\underline{x} - h(t)\underline{j}\right) + \underline{\underline{M}}(\alpha)\left(\underline{\dot{x}} - \dot{h}(t)\underline{j}\right) \\ \underline{\dot{x}} &= \underline{\underline{M}}^{-1}(\alpha)\left(\underline{\dot{x}}' - \underline{\underline{\dot{M}}}(\alpha)\underline{\underline{M}}^{-1}(\alpha)\underline{x}'\right) + \dot{h}(t)\underline{j} \end{aligned} \tag{6.19}$$

in which the temporal derivative of the rotation matrix is expressed as a function of the angle of attack and of its derivative:

$$\underline{\underline{\dot{M}}}(\alpha) = -\dot{\alpha}(t) \begin{bmatrix} \sin(\alpha) & \cos(\alpha) \\ -\cos(\alpha) & \sin(\alpha) \end{bmatrix} \tag{6.20}$$

The definition of the vorticity field $\underline{\omega}'$ in the wing-fixed reference frame requires the derivation of the gradient operator in the new reference frame. The vorticity in the frame $\underline{x} = (x, y)$ is thus given by:

$$\underline{\omega}' = \underline{\nabla}' \times \underline{\dot{x}} = \underline{\underline{J}}^T \underline{\nabla} \times \underline{\dot{x}} \tag{6.21}$$

where $\underline{\underline{J}} = \underline{\underline{M}}^T$ is the Jacobian matrix of the rotation. For two-dimensional flows, the out-of-plane (z) component of the vorticity is the only non-zero component of the vorticity field. From Eq. 6.21, it can be shown that the transformation of the z-component of the vorticity field is simply given by:

$$\omega_z' = \omega_z + 2\dot{\alpha}(t) \tag{6.22}$$

6.3.2 Estimation of the extended POD modes

The POD is performed on the phase-averaged fluctuating velocity fields rotated in the wing-fixed reference frame. This approach is analogous to the phase-averaged POD reported by Fogleman et al. (2004) to study the flow inside the cylinder of an internal combustion engine. The POD is then extended to phase-averaged fluctuating forces. In the following, the subscript $\|V\|$ will be employed to indicate all the quantities which are calculated from the velocity field. Similarly, the subscripts ω, F_y and F_x will indicate the quantities related to vorticity, chord-normal force component and chord-parallel force component, respectively.

The POD *chronoi* $\underline{\psi}^{(i)}_{\|V\|}$ are calculated as the eigenvectors of the two-points temporal correlation matrix $\underline{\underline{R}}$ of the fluctuating velocity snapshot matrix, according to Eq. 6.23:

$$\underline{\underline{R}} = \underline{\underline{U}}'\,\underline{\underline{U}}'^T + \underline{\underline{V}}'\,\underline{\underline{V}}'^T = \underline{\underline{\Psi}}_{\|V\|}\,\underline{\underline{\Sigma}}^2_{\|V\|}\,\underline{\underline{\Psi}}^T_{\|V\|} \tag{6.23}$$

where $\underline{\underline{U}}'$ and $\underline{\underline{V}}'$ are the snapshot matrices of the fluctuating chord-wise and chord-normal velocity components, respectively and $\underline{\underline{\Sigma}}_{\|V\|}$ are the singular values obtained from the economy-size SVD of $\underline{\underline{R}}$. In Eq. 6.23 and in the following, for the ease of notation all the extended POD matrices do not show the apex $'$ in the subscripts although all the quantities are referred to the wing-fixed reference frame.

Accordingly with Eq. 2.36, the components in the wing-fixed frame of the POD *topoi* of the velocity are calculated through projection of the fluctuating velocity components on the temporal basis $\underline{\underline{\Psi}}_{\|V\|}$:

$$\begin{aligned} \underline{\underline{\Sigma}}_{\|V\|}\underline{\underline{\Phi}}_u &= \underline{\underline{\Psi}}^T_{\|V\|}\underline{\underline{U}}' \\ \underline{\underline{\Sigma}}_{\|V\|}\underline{\underline{\Phi}}_v &= \underline{\underline{\Psi}}^T_{\|V\|}\underline{\underline{V}}' \end{aligned} \tag{6.24}$$

with $\underline{\underline{\Phi}}_u$ and $\underline{\underline{\Phi}}_v$ being the *topoi* of $\underline{\underline{U}}'$ and $\underline{\underline{V}}'$ respectively.

Similarly, the projection of the rotated vorticity field $\underline{\underline{\omega}}_z'$ is obtained by:

$$\underline{\underline{\Sigma}}_{\omega}\underline{\underline{\Phi}}_{\omega} = \underline{\underline{\Psi}}_{\|V\|}^{T}\underline{\underline{\omega}}_{z}' \tag{6.25}$$

where $\underline{\underline{\Sigma}}_{\omega}$ is a diagonal matrix containing the norm $\sigma_{\omega}^{(i)}$ of the projection of the vorticity on each *chronos* of the velocity, and each row of $\underline{\underline{\Phi}}_{\omega}$ is the ith *topos* $\underline{\phi}_{\omega}^{(i)}$ (with unitary norm) of the projection of the vorticity. It must be remarked that the vorticity *topoi* found through Eq. 6.25 are equivalent to the vorticity of the velocity *topoi* (apart from a scaling) since curl is a linear operator. In fact:

$$\underline{\underline{\Psi}}_{\|V\|}^{T}\underline{\underline{\omega}}_{z}' = \underline{\underline{\Psi}}_{\|V\|}^{T}\left[\underline{\underline{U}} \quad \underline{\underline{V}}\right]\underline{\underline{C}} = \underline{\underline{\Sigma}}_{\|V\|}\left[\underline{\underline{\Phi}}_{u} \quad \underline{\underline{\Phi}}_{v}\right]\underline{\underline{C}} \tag{6.26}$$

with $\underline{\underline{C}}$ being the matrix representation of the curl operator.

Following Eq. 2.37, the temporal basis $\underline{\underline{\Psi}}_{\|V\|}$ is used to project the fluctuating part of the force components in the airfoil reference frame $\underline{F}_{x'}$, $\underline{F}_{y'}$. For the force, the projection is:

$$\begin{aligned} \underline{\Sigma}_{F_x} &= \underline{\underline{\Psi}}_{\|V\|}^{T}\underline{F}_{x'} \\ \underline{\Sigma}_{F_y} &= \underline{\underline{\Psi}}_{\|V\|}^{T}\underline{F}_{y'} \end{aligned} \tag{6.27}$$

where $\underline{\Sigma}_{F_x}$ and $\underline{\Sigma}_{F_y}$ are vectors containing the projection coefficients $\sigma_{F_x}^{(i)}$ and $\sigma_{F_y}^{(i)}$ of the force components.

It has to be remarked that the *chronoi* obtained from Eq. 6.25 and Eq. 6.27 have zero mean since they are estimated from zero-mean signals, thus it is not needed to remove the time average value from $\underline{\underline{\omega}}_z'$, $\underline{F}_{x'}$ and $\underline{F}_{y'}$ in order to estimate the corresponding projections.

Also, it has to be remarked that $\sigma_{F_x}^{(i)}$ and $\sigma_{F_y}^{(i)}$ are not necessarily positive since they are not singular values but are instead obtained as the projections on the POD velocity *chronoi*. This implies that the extended POD modes can be either in-phase (positive diagonal value) or in phase opposition (negative diagonal value) with respect to the velocity POD modes. The absolute values of the projection coefficients $\sigma_{\omega}^{(i)}$, $\sigma_{F_x}^{(i)}$ and $\sigma_{F_y}^{(i)}$ can be considered as *pseudo singular values* accounting for the mean square of the projection of force/vorticity on each POD *chronos*.

Following Eq. 2.38 the truncated reconstruction of both vorticity and forces is defined as:

$$
\begin{aligned}
\underline{\underline{\omega'}}_{n_m} &\approx \langle \underline{\underline{\omega'}} \rangle + \underline{\underline{\Psi}}_{\|V\|} \begin{pmatrix} \underline{\underline{I}}_{n_m} & 0 \\ 0 & 0 \end{pmatrix} \underline{\underline{\Sigma}}_{\omega} \, \underline{\underline{\Phi}}_{\omega} \\
\underline{F}_{x',n_m} &\approx \langle \underline{F}_{x'} \rangle + \underline{\underline{\Psi}}_{\|V\|} \begin{pmatrix} \underline{\underline{I}}_{n_m} & 0 \\ 0 & 0 \end{pmatrix} \underline{\underline{\Sigma}}_{F_x} \\
\underline{F}_{y',n_m} &\approx \langle \underline{F}_{y'} \rangle + \underline{\underline{\Psi}}_{\|V\|} \begin{pmatrix} \underline{\underline{I}}_{n_m} & 0 \\ 0 & 0 \end{pmatrix} \underline{\underline{\Sigma}}_{F_y}
\end{aligned}
\tag{6.28}
$$

6.4 Flow topology and forces

6.4.1 Phase-averaged flow fields and forces

Before discussing the phase-averaged velocity fields and forces, an important feature of the tested cases is underlined. For cases A, B and C, characterized by mean angle of attack $\alpha_m = 0°$, realizations in phase opposition are antisymmetric with respect to the chord as the motion of the wing is perfectly specular. In the following, these cases will be simply referred as *antisymmetric* cases. Instead, cases D, E and F, which are characterized by $\alpha_m = 10°$, do not present symmetry of the wing motion and thus of the flow behaviour. These cases will be referred to as *asymmetric* cases. During the periodic motion the suction side switches its position from the upper side to the lower side of the airfoil due to the large oscillations in α_{eff} (with amplitude higher than 20°, as shown in Fig. 6.5). While for antisymmetric cases the upper side acts as pressure and suction side during the same amount of time, in asymmetric cases the upper side acts prevalently as suction side. The phase-averaged velocity fields and force components are reported for the antisymmetric cases in Fig. 6.6 (cases A, B and C) and for the asymmetric cases in Fig. 6.7 (cases D, E and F).

Almost all the cases, with exception of case C, are characterized by the formation of a LEV on the suction side. The LEV, when attached to the airfoil, is characterized by a vorticity blob surrounded by streamlines ending on the airfoil surface in a reattachment point (Widmann and Tropea, 2015). For antisymmetric cases A and B, the LEV forms on the lower and upper sides during the upstroke and downstroke, respectively. For asymmetric cases the LEV forms only on the upper side during the downstroke, with the exception of case D for which a weak LEV forms also on the lower side during the upstroke. By comparing these observations with respect to the instantaneous effective angle of attack reported in Fig. 6.5 it is reasonable to assume that the formation of the LEV is subjected to the condition of reaching a minimum α_{eff} sightly higher than the static stall angle of attack ($\approx 12°$ for $Re = 3600$), in agreement with what reported by Prouty (1995). Given the phase shift of $\pi/2$ between pitching and plunging motion for the present study, increasing the pitching amplitude α_0 results in a decrease of the maximum α_{eff} (see Fig. 6.5), thus generating a smaller and more stretched LEV.

During the downstroke the LEV grows in size and the reattachment point on the airfoil moves progressively towards the trailing edge. The growth of the LEV produces an increase of the chord-normal component of the force, which reaches values far beyond the static stall values (for the present airfoil and Re the static stall lift coefficient has been measured to be about 0.7). Accordingly with Widmann and Tropea (2015), as the reattachment point reaches the trailing edge, the LEV starts detaching from the airfoil surface. A reverse-flow forms on the suction side during the detachment process of the LEV, leading to the failure of the Kutta condition at the trailing edge. The LEV detachment approximately coincides with a peak in the chord-normal component of the force. After this instant the airfoil undergoes a part of the cycle characterized by the aerodynamic stall, for which the chord-normal component of the force rapidly decreases.

While the LEV forms on the suction side, the pressure side sheds in the wake a continuous trail of vorticity of opposite sign, accordingly to the vorticity balance imposed by the Kelvin theorem. When the LEV detaches, this trail of vorticity, before being shed in the wake, concentrates in a Trailing Edge Vortex due to the reverse-flow on the suction side. Both the LEV and the TEV are then convected downstream in the wake, forming typical mushroom-like structures (see, e.g. the experimental visualizations by Andersen et al., 2017 and the DNS simulations by Moriche et al., 2016).

The LEV and TEV formation and dynamics are strongly affected by the kinematics parameters. In particular, since the LEV intensity depends on the maximum effective angle of attack, an increase of α_0 produces a less intense LEV, up to its inhibition as in case C; instead, an increase of α_m enhances the LEV intensity on the upper side, while, on the lower side, the LEV is weakened till disappearing (see cases E and F).

In all the tested cases the fluctuating part of the chord-normal component of the force $F_{y'}$ has periodicity equal to the flapping period. The peak-to-peak amplitude of the chord-normal force component is reduced for increasing α_0, due to the decreasing intensity of the LEV.

The chord-wise force component $F_{x'}$ shows a more diverse behaviour. The pitching amplitude α_0 has the dominant influence. For $\alpha_0 = 0°$ and $\alpha_m = 0°$ (case A), $F_{x'}$

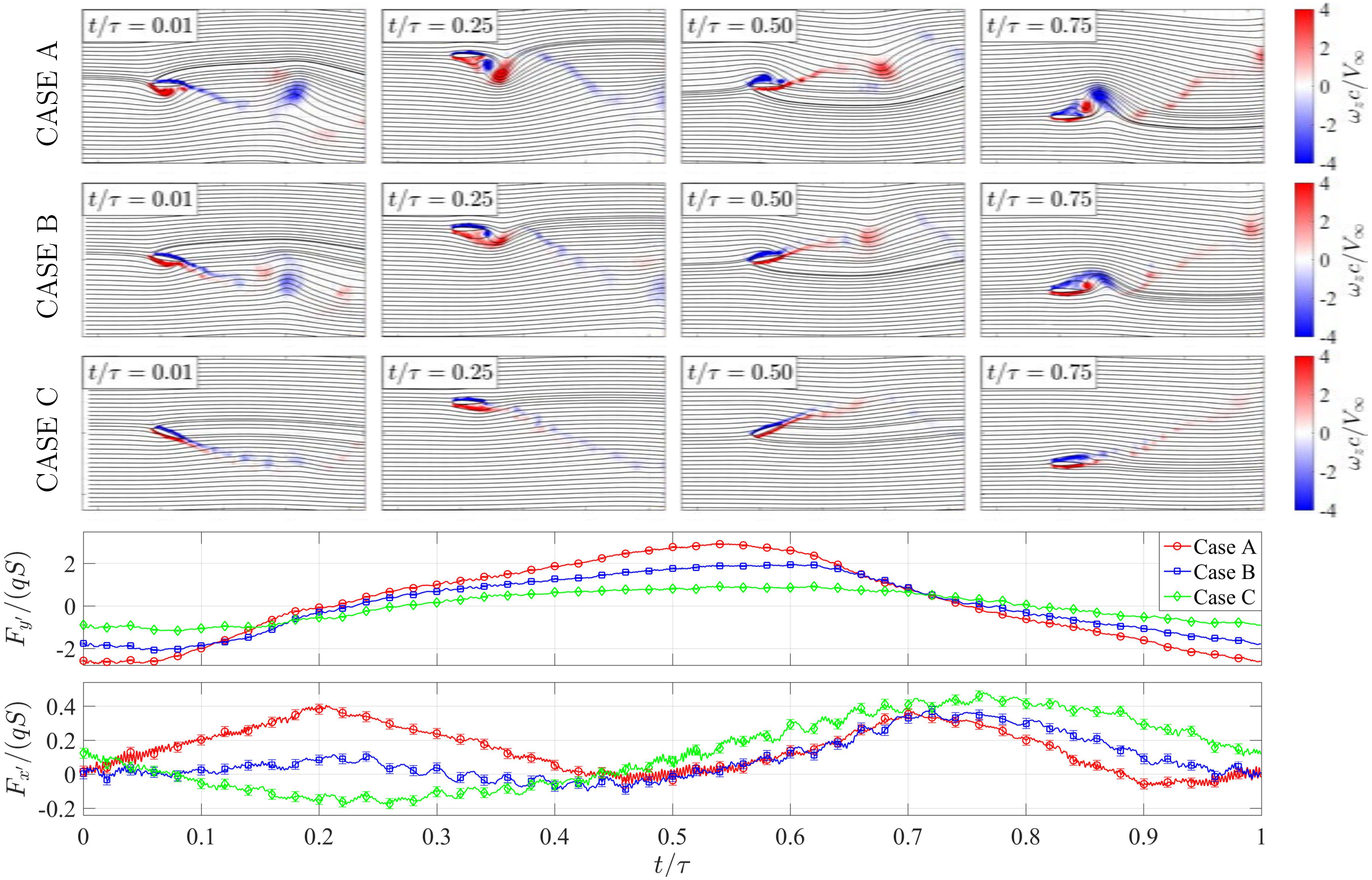

Fig. 6.6 Phase-averaged flow field and force components evolution during the flapping cycle: case A, B and C. Contour indicates the normalized vorticity field, streamlines the velocity field.

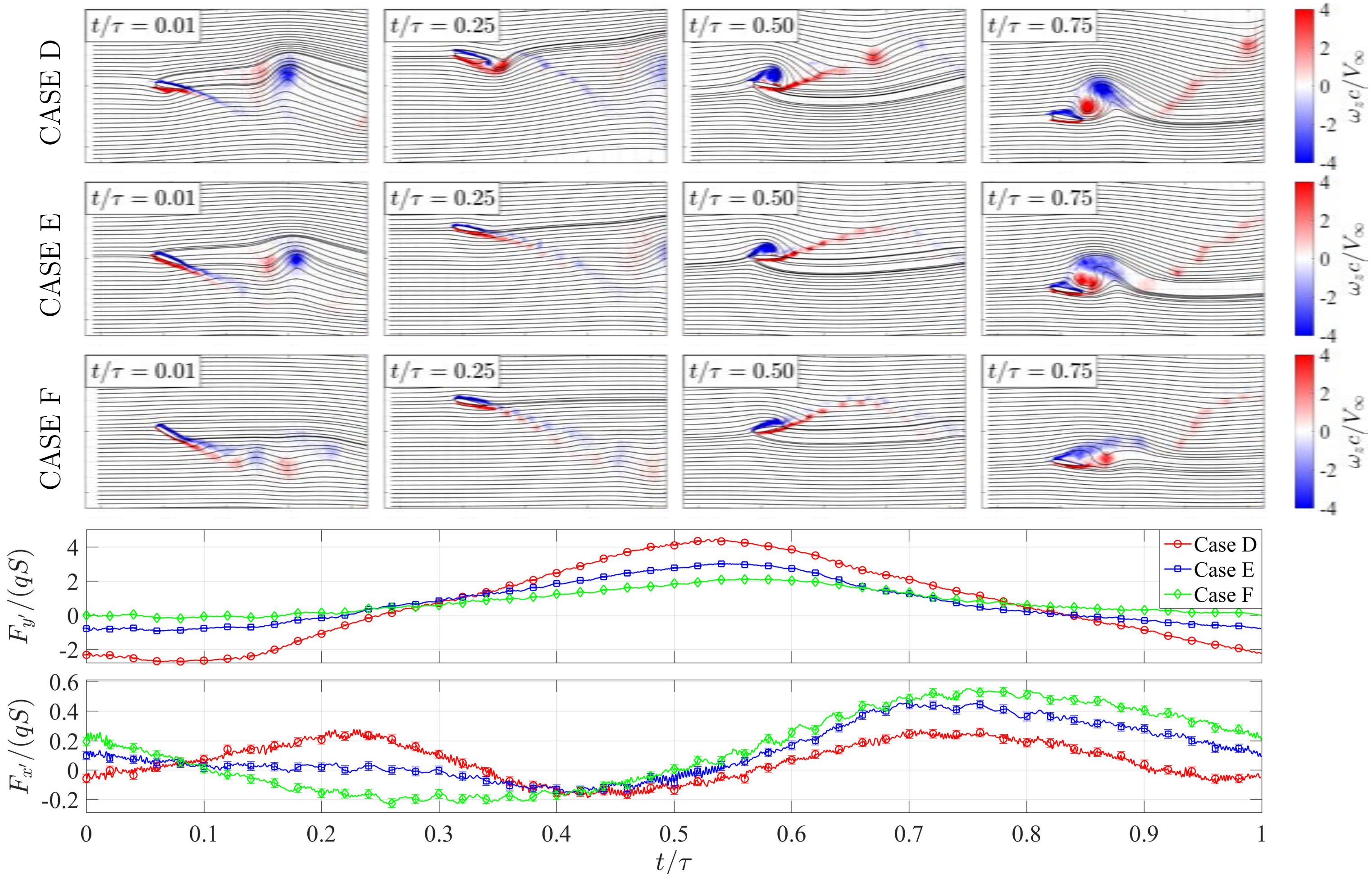

Fig. 6.7 Phase-averaged flow field and force components evolution during the flapping cycle: case D, E and F. Contour indicates the normalized vorticity field, streamlines the velocity field.

shows 2 peaks (at about $t/\tau \approx 0.2$ and $t/\tau \approx 0.7$) with almost the same strength for each complete stroke of the flapping wing. A similar double-peak behaviour is present for case D ($\alpha_0 = 0°$ and $\alpha_m = 10°$). Increasing the pitching amplitude to $\alpha_0 = 10°$ (cases B and E), the double peak is still present, but the first one is significantly lower with respect to that observed in case A. For case E the difference between the peak at $t/\tau \approx 0.2$ and that at $t/\tau \approx 0.75$ results amplified with respect to case B. Finally, for $\alpha_0 = 20°$ (cases C and F), the first peak completely disappears and the fluctuating part of the chord-wise force component has s single maximum at $t/\tau \approx 0.75$. Thus, for what concerns chord-wise forces, an analogy between antisymmetric and asymmetric cases A-D, B-E and C-F, is obtained at fixed α_0, regardless of the α_m value.

Despite the problem under study is symmetric in time (with respect to $t/\tau = 0.5$) for cases B and C, the force measurements show an asymmetric time-history of the chord-wise component of the force. This asymmetry is not consistent with the picture of a symmetric vorticity time-history which results from the phase-averaged flow fields. It can be deduced, therefore, that the asymmetry must be related to non-circulatory forces acting on the wing. In §6.5 it will be shown that a force mode inducing this asymmetry can be extracted by means of the EPOD. In §6.6.2 this force mode will be ascribed to an added-mass force induced by the airfoil rotation which closely resembles the contribution calculated by Sedov (1965).

6.4.2 Time average flow fields and forces in the wing-fixed reference frame

Time averaged flow fields are estimated after applying the transformation to the wing-fixed reference frame (Fig. 6.8). For the asymmetric cases (D, E and F) a downward deflection of the flow past the wing is recognizable, accompanied by on-average positive lift and chord-normal force component (see Table 6.3). Antisymmetric cases (A, B and C) are instead symmetric with respect to the chord as, on average, each side of the airfoil undergoes the same flow conditions during a complete period. As a consequence, nearly no streamline deflection is detected (apart from small asymmetries which may arise from not completely converged time-averaging), and the average lift coefficient is approximately zero within experimental uncertainty.

It is worth highlighting that the average lift force generated in the asymmetric cases is significantly lower than the expected $C_L = 2\pi\alpha_m$ (valid for a steady airfoil at high Reynolds number). The values of $\langle C_L \rangle$ for case D are in good agreement both with steady measurements performed at the same Reynolds number ($C_L \approx 0.56$)

Test Name	$\langle C_L \rangle$	$\langle C_D \rangle$	$\langle C_{F_{y'}} \rangle$	$\langle C_{F_{x'}} \rangle$
Case A	0.071	0.193	0.071	0.193
Case B	0.071	−0.121	0.073	0.035
Case C	−0.073	−0.004	−0.068	0.138
Case D	0.592	0.171	0.613	0.066
Case E	0.727	0.109	0.749	0.126
Case F	0.761	0.163	0.824	0.175

Table 6.3 Summary of time-averaged force coefficients for all the cases analysed.

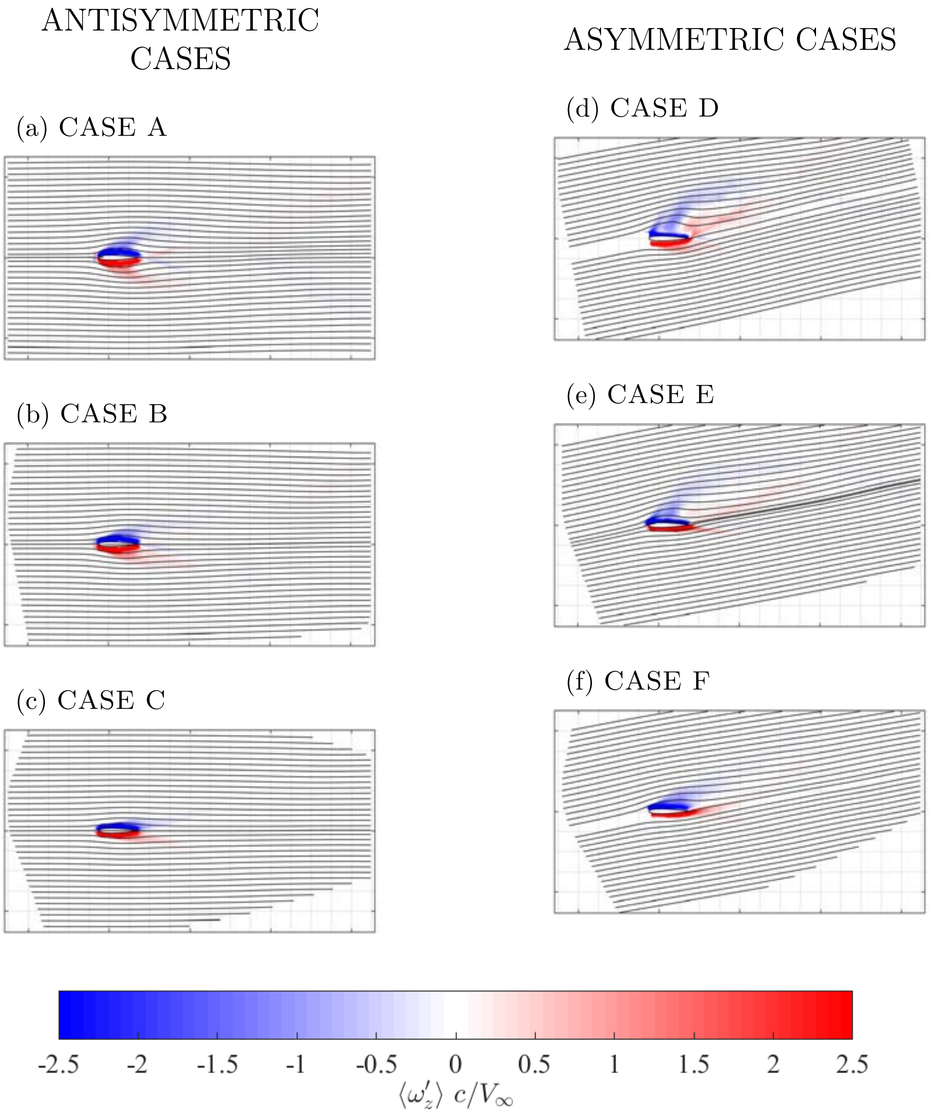
ANTISYMMETRIC CASES

ASYMMETRIC CASES

(a) CASE A

(d) CASE D

(b) CASE B

(e) CASE E

(c) CASE C

(f) CASE F

Fig. 6.8 Average flow field in wing-fixed reference frame for all the cases. Contour indicates the normalized vorticity field, streamlines the velocity field.

and with the results reported by Sunada et al. (2002), thus suggesting that viscosity plays a major role in the determination of the average forces. An increase of the mean lift is observed when the pitching is introduced (cases E and F). This effect has been already observed by Dawson et al. (2016) for purely pitching airfoils. Dawson et al. (2016) ascribe this effect to the forcing imposed by the pitching motion on the wake instabilities. It is possible to suppose that a similar effect may be present also for combined pitching/plunging motions, such the cases here studied, even if the present experimental campaign does not provide sufficient data to support this claim. This observation highlights that there is a clear mismatch between the mean lift at low Reynolds numbers and the mean values used in the Theodorsen's theory. This mismatch may be caused either by the viscosity, which has been neglected in the Theodorsen's model, either by effects of forcing on the wake instabilities due to the pitching.

While α_m introduces an asymmetry in the field, a secondary effect on $\langle C_L \rangle$ is played by α_0. Increasing α_0 avoids the formation of the LEV on the lower side, resulting in a greater time average lift for the cases with $\alpha_m \neq 0$. For the case with $\alpha_m = 0$, as discussed in the previous section, the LEV is suppressed symmetrically on both sides of the airfoil. The effect of α_0 on the LEV is made clear in the average vorticity distribution: non-zero vorticity regions spread farther away from the airfoil as α_0 decreases, indicating that the rotation of the flow occurs farther from the body. These non-zero vorticity regions follow the trace of the LEV which evolves (growing and detaching) in time (see Fig. 6.7). As already commented in §6.4.1, the size of the LEV is strictly connected to the pitching angle spanned, reducing as the pitching increases. It can be argued that, as the LEV grows in size, the airfoil appears to the flow, on average, thicker. As will it be shown in the following this same effect occurs also for the fluctuating part of the flow field. The increase of the effective thickness of the airfoil may be also in agreement with the reduction of $\langle C_L \rangle$: Sunada et al. (2002) have shown that the lift at low Reynolds number is reduced as the airfoil becomes thicker.

For what concerns the chord-wise force coefficient it has to be remarked that, in agreement with what reported by Floryan et al. (2017), aerodynamic forces for airfoil kinematics at the considered low Reynolds and Strouhal numbers might be dominated by a viscous term. For the experimental setup used in this study, the viscous term was found to be approximately equal to 0.15 from steady measurements and to be practically constant with the angle of attack. The steady viscous force value matches with the time-average chord-wise force coefficients for most of the cases reported.

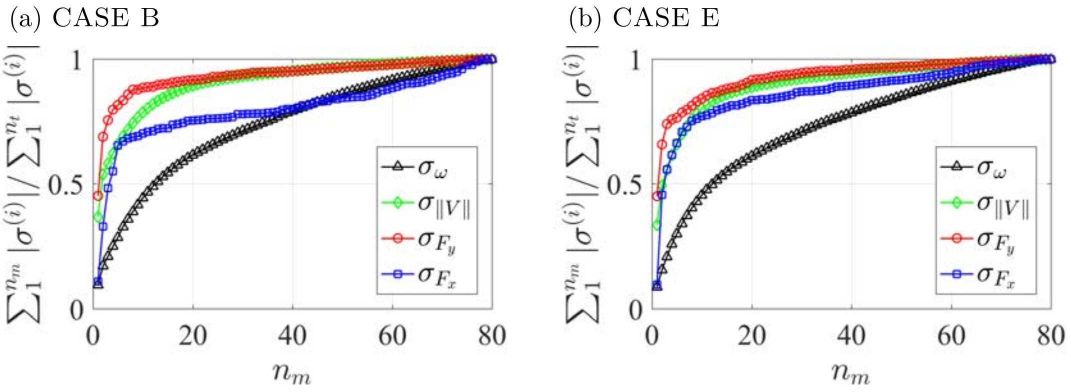
(a) CASE B

(b) CASE E

Fig. 6.9 Cumulative spectral density of the Extended POD modes.

6.5 Modal decomposition

It has been observed in §6.4.1 that a modification in the flapping-motion parameters strongly influences the dynamics of both the flow field and of the aerodynamic force acting on the wing. Phase-averaged data, however, do not permit to clearly draw a picture of how different motion parameters affect the flow field. Neither it is possible to spot a clear correlation between the change in the flow field and the change in the aerodynamic force history. To fill this gap, in the following a modal analysis will be performed on both phase-averaged flow fields (using POD) and phase-averaged force measurements (using EPOD). The analysis will be devoted to the comparison of different cases in the basis spanned by the flow-field POD modes, highlighting similarities between different cases and shedding light on the role of different motion parameters on both flow organization and aerodynamic force generation. The final aim of this analysis is the low-order modelling of the flow features involved in flapping flight and of their influence on the aerodynamic force history, both included in §6.6.

6.5.1 Spectral distribution of extended POD modes

The *pseudo singular values* $|\sigma_{F_x}|$, $|\sigma_{F_y}|$ and $|\sigma_\omega|$ represent the mean squares associated to each *chronos* and can be assimilated to a spectral density in the POD temporal basis (§6.3.2). In Fig. 6.9 the *extended* cumulative spectral densities of chord-wise and chord-normal force components, velocity and vorticity are reported for two representative cases, namely case B and case E.

The velocity spectrum $\sigma_{\|V\|}$ has been optimized through the POD algorithm, i.e. has been mathematically constrained to achieve the most compact spectral distribution in terms of number of modes between all the possible spectra. The optimality of the POD modes according to the L^2 norm leads to spectral coefficients of the signal decaying faster than in any other basis. Measurement noise instead spreads uniformly over the entire spectrum, thus leading to nearly constant singular values (and thus linearly growing cumulative spectrum) for higher order modes. The same behaviour is observed for the vorticity spectrum since vorticity is linearly related to the velocity.

The spectral distributions of force components shown in Fig. 6.9 have instead been obtained by means of a projection, meaning that the basis has not been chosen to optimize these spectra. Consequently, a more or less compact representation using extended POD modes is to be ascribed only to a higher correlation between the projection basis and the quantity to be projected, i.e. only on physical grounds of relation between flow features and force generation. Differently from standard POD, in the Extended POD approach the uncorrelated component contains both measurement noise and the uncorrelated part between the quantity to be projected (e.g the force in the present application) and the quantity originally used to generate the POD temporal basis.

Assuming the beginning of the linear part in the cumulative spectrum as a threshold following the scree plot test (see Chapter 3 and Raiola et al., 2015), the velocity field results to be very well described with about 25 modes. The same statement can be made for the vorticity spectrum, which indeed has a lower signal-to-noise ratio, i.e. a higher noise contribution, resulting in a steeper slope of the linear part for case B and E.

It has been checked for all the tested cases (not included for brevity) that the force components spectra are more compact than both the velocity and the vorticity spectrum, i.e. can be described with a lower number of modes, typically below 10. This reveals that force generation has to be ascribed prevalently to the most energetic features of the velocity fields. This should not be surprising since the aerodynamic forces applied by the airfoil to the fluid are largely contributing to the kinetic energy of the flow, thus the POD is expected to capture them in the very first modes.

The most energetic features correspond to the large scale structures close to the airfoil as it will be shown in §6.5.3 and §6.5.4. As a consequence, the break-up of the mid-far wake is not relevant from the viewpoint of the force generation (as shown by Moriche, 2017). Followng this argument, the configuration of the vortices in the wake plays a secondary role; the force generation (expecially for what concerns the chord-wise component) is mostly affected by the relative position of the LEV and the TEV at the pinch-off. This is the reason behind the observation by Andersen et al.

(2017), which report non-thrust-generating kinematics despite the presence of a reverse Kármán wake.

The spectral distribution of the force components reveals a slight but consistent difference between antisymmetric cases (case B in Fig. 6.9) and asymmetric cases (case E in Fig. 6.9). For the antisymmetric cases the contribution of the first modes is higher, as testified by steeper trend of the cumulative spectrum. This behaviour is indicative of a higher importance gained from higher order modes in the force reconstruction when $\alpha_m \neq 0°$ (especially for the chord-wise component), and thus of a *richer* spectral content of these cases. An explanation of this behaviour will be given in the following sections.

6.5.2 Low-order reconstruction of the force

The spectral distribution observed in §6.5.1 ensures that the bulk of the force is contained in the first few modes ($n_m \leqslant 10$). Following Eq. 6.28, the low-order reconstruction with the first n_m modes of the chord-normal and chord-wise force components is calculated. This section is a prelude to §6.5.3 and §6.5.4, where a description of the modes will be provided and the physical meaning of the LOR will be discussed.

The LOR of the chord-normal force component with the first n_m modes is reported in Fig. 6.10 along with the original measurement of the force. For the sake of brevity the reconstruction is presented only for test cases B (antisymmetric) and E (asymmetric).

The periodic behaviour of the fluctuating chord-normal force component (discussed in §6.4.1) is almost entirely reproduced by the first 2 extended POD modes (check Table 6.4 for the coefficient of determination R^2). Although the reconstruction with $n_m = 2$ represents the bulk of $F_{y'}$, it is not able to recover the smaller oscillations in the measured force which define the peaks positions. This is especially evident for the asymmetric case (case E). For the antisymmetric case (case B) a reconstruction with the first 6 modes is capable of following almost perfectly the measured force. For the asymmetric case (case E), instead, the first six modes are able to provide an excellent reconstruction of the chord-normal force component (for $n_m = 6$, $R^2 = 0.994$), but the force peak is not completely recovered. This can be a consequence of the higher spectral *richness* of force modes in asymmetric cases, as discussed in §6.5.1.

The LOR of the chord-wise force component with the first n_m modes is reported in Fig. 6.11. Owing to the variety of different behaviours discussed in §6.4.1, only 4 cases are included in the discussion (case E and F show trends similar to cases B and C and are excluded for brevity). For case A, the first two modes play a secondary role on

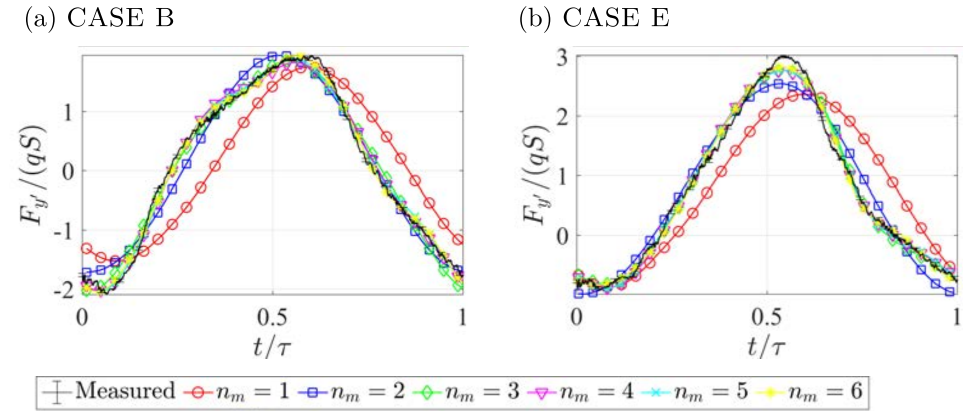

Fig. 6.10 Low-order reconstruction of the chord-normal force component ($F_{y'}$) with extended POD modes. Each curve represents the reconstruction with the firsts n_m modes.

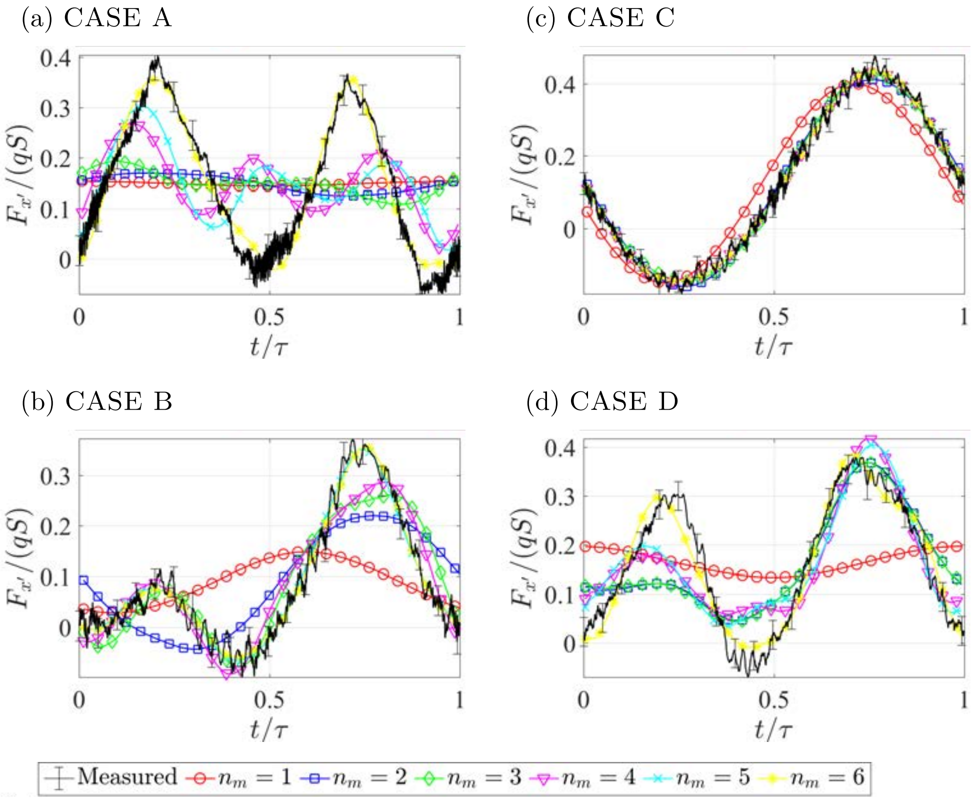

Fig. 6.11 Low-order reconstruction of chord-wise force component ($F_{x'}$) with extended POD modes. Each curve represents the reconstruction with the first n_m modes.

n_m	CASE B		CASE E	
	$F_{y'}$	$F_{x'}$	$F_{y'}$	$F_{x'}$
1	0.760	0.116	0.796	0.058
2	0.969	0.594	0.964	0.874
3	0.986	0.822	0.991	0.937
4	0.992	0.868	0.992	0.958
5	0.994	0.972	0.992	0.973
6	0.995	0.975	0.994	0.986

Table 6.4 Coefficient of determination R^2 of the force LOR.

$F_{x'}$, while the modes from 3rd to 6th reconstruct together almost entirely the measured force and are responsible for the double peak formation. For case B the modes from 3rd to 6th are responsible for the double peak in $F_{x'}$. The 1st and 2nd modes introduce a sinusoidal behaviour, determining a difference in the amplitude of the force peaks. For case C, modes 1st and 2nd represent almost completely $F_{x'}$, while modes from 3rd to 6th seem to play a minor role.

The similitude of the chord-wise force behaviour for corresponding antisymmetric and asymmetric cases affects also the associated extended POD modes. The LOR for case D is the one that most differs from its corresponding antisymmetric case, i.e. case A. The first 2 extended POD modes are responsible for recovering completely the peak of $F_{x'}$ at $t/\tau = 0.75$, while the modes 3rd to 6th are responsible for recovering the peak at $t/\tau \approx 0.2$. This difference depends on the particular organization of the POD modes of the velocity, and in particular of its 2nd *chronos*, as it will be shown in §6.5.3.

As a final remark, it must be specified that the force modes here presented are the result of the extended POD, thus represent solely the part of the force which is linearly correlated to the velocity field modes. However, the LOR obtained is shown to follow with high fidelity the measurements, thus suggesting that the effects of non-linearities are negligible.

6.5.3 Description of the 1st and 2nd extended POD modes

A compact overview of the 1st POD mode of the velocity with its associated extended POD modes of vorticity and force is reported in Fig. 6.12 for all the analysed cases.

The *topoi* of the velocity ($\underline{\phi}_x$ and $\underline{\phi}_y$) and of the vorticity ($\underline{\phi}_\omega$) of the 1st mode present common features for all the cases. The 1st mode describes two counter-rotating vorticity regions bounded to the airfoil. The negative vorticity region which concentrates at the

(a) CASE A

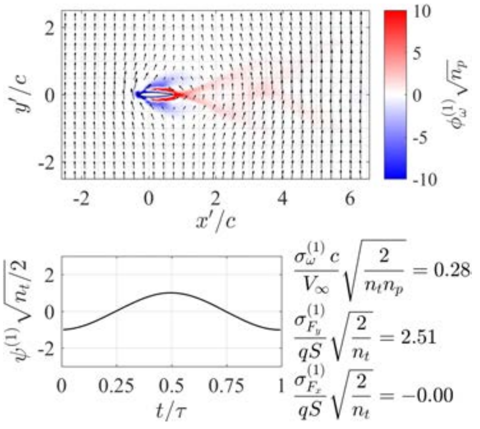

(b) CASE B

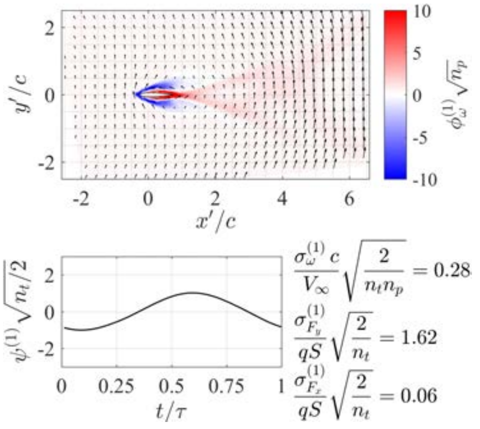

(c) CASE C

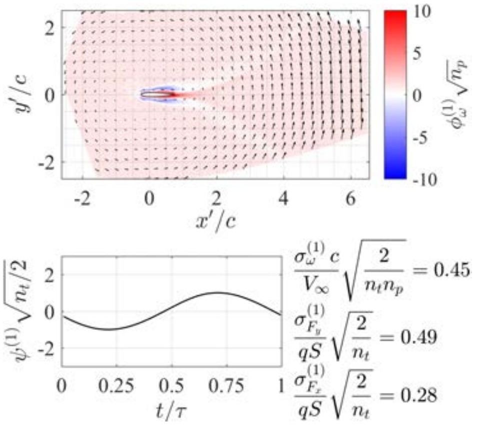

(d) CASE D

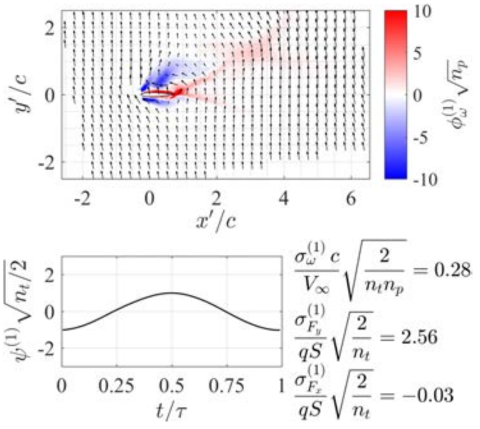

(e) CASE E

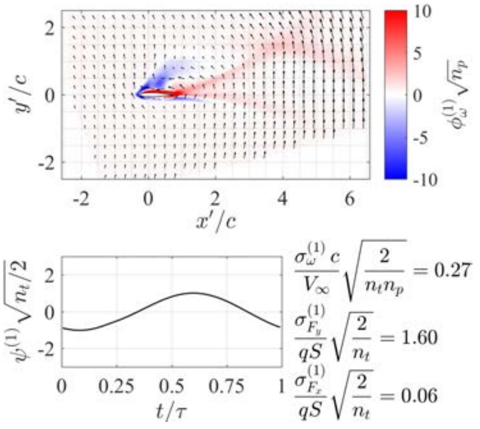

(f) CASE F

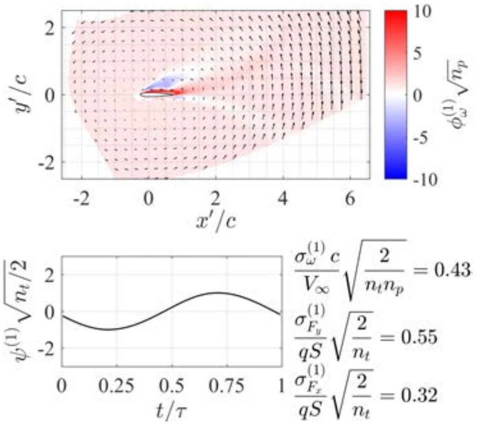

Fig. 6.12 Compact overview of the 1st POD modes of velocity and extended POD modes of vorticity and force for all the cases. The *topos* of the velocity ($\underline{\phi}_x$ and $\underline{\phi}_y$) is reported as a quiver plot. The *topos* of the vorticity ($\underline{\phi}_\omega$) is reported as a contour plot. The *chronos* ($\underline{\psi}_{\|V\|}$) of the mode is reported below along with the norm of the vorticity projection (σ_ω) and the projection coefficient of the force components ($\sigma_{F,x}$ and $\sigma_{F,y}$).

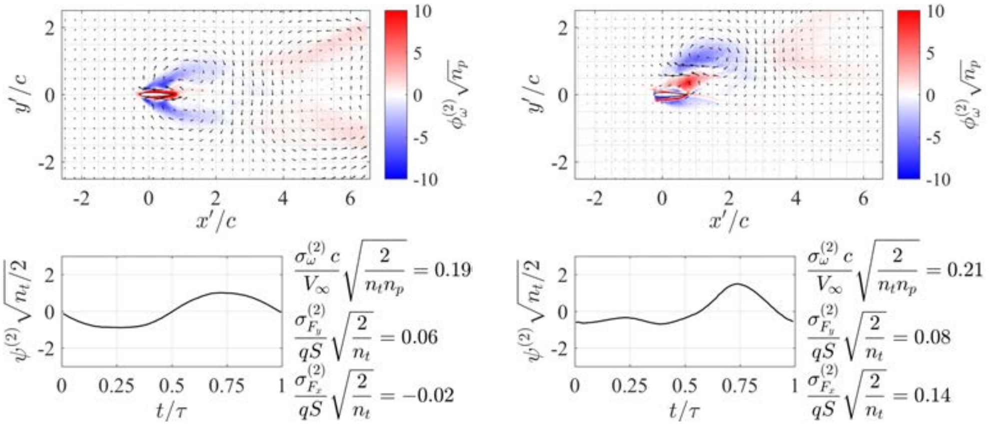
(a) CASE A

(d) CASE D

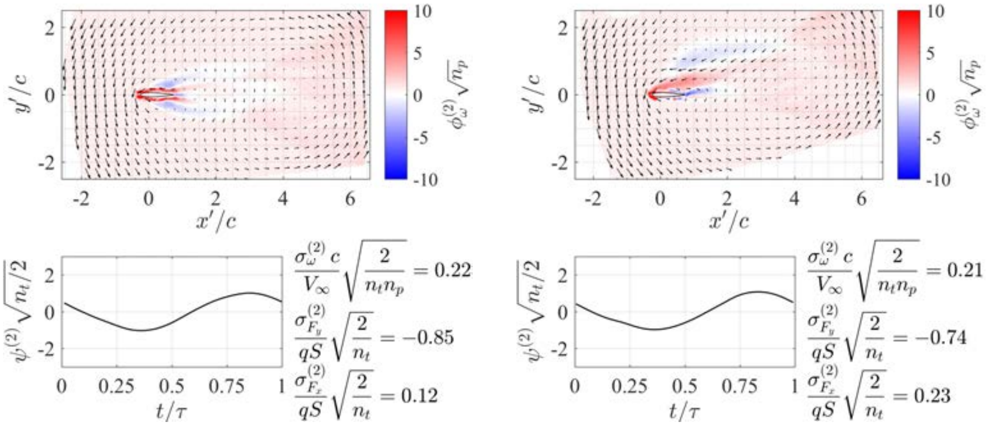
(b) CASE B

(e) CASE E

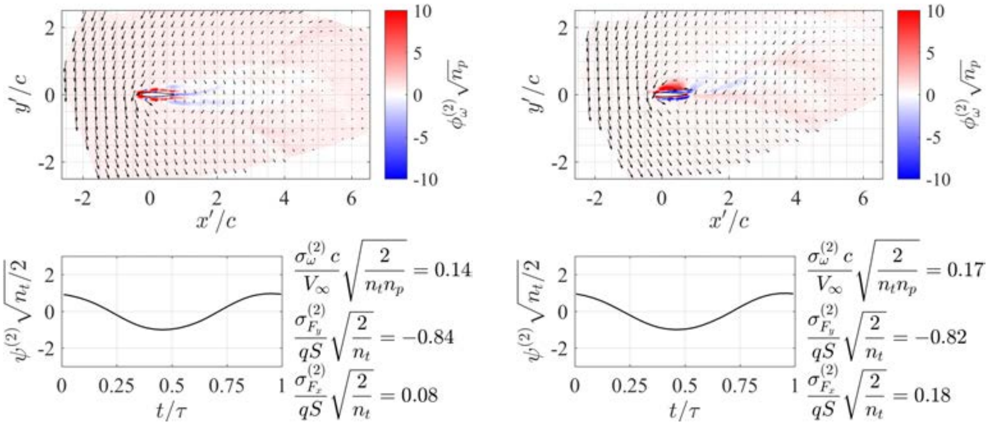
(c) CASE C

(f) CASE F

Fig. 6.13 Compact overview of the 2nd POD modes of velocity and extended POD modes of vorticity and force for all the cases. The *topos* of the velocity ($\underline{\phi}_x$ and $\underline{\phi}_y$) is reported as a quiver plot. The *topos* of the vorticity ($\underline{\phi}_\omega$) is reported as a contour plot. The *chronos* ($\underline{\psi}_{\|V\|}$) of the mode is reported below along with the norm of the vorticity projection (σ_ω) and the projection coefficient of the force components ($\sigma_{F,x}$ and $\sigma_{F,y}$).

leading edge is connected to the formation of the LEV and to its growth over the wing. The positive vorticity region at the trailing edge, instead, is connected to the release of vorticity which has to compensate the vorticity of the LEV according to the Kelvin theorem.

For antisymmetric cases (cases A, B and C) the vorticity distributes symmetrically with respect to the chord. For asymmetric cases (see cases D, E and F) the vorticity regions are more extended on the upper side of the airfoil. This difference is induced by the asymmetrical flow conditions between the two sides of the airfoil for the latter cases, which has been shown to affect in a similar way the average flow field (see §6.4.2).

The 1st mode also captures an upward motion of the flow, especially recognizable for case A, which appears to be connected to the plunging motion of the airfoil. A complete correspondence between the 1st mode and the plunging motion is however present only for the pure plunging cases. When the pitching motion is introduced, the 1st mode does not entirely capture the plunging motion (as clarified by the discrepancy of the *chronoi* from a cosine), which is partially contained in the 2nd mode. The pitching motion adds a rigid vortex to the flow in the wing-fixed frame whose intensity is proportional to the angular velocity of the airfoil (see Minotti, 2002). Similarly to the plunging motion, also the pitching motion is captured in the 1st and 2nd modes, while none of the two is completely aligned with it.

For both antisymmetric and asymmetric cases, α_0 controls the relative strength of the counter-rotating vorticity regions. For pure plunging airfoils ($\alpha_0 = 0°$, cases A and D) the vorticity regions are balanced to fulfil the Kelvin theorem, and their induction results in a flow oriented in the chord-normal direction. Introducing the pitching motion (cases B and E), the relative strength of the vortices is modified due to the change of reference, as shown in Eq. 6.22.

The rationale behind the effect of α_0 on the vorticity distribution of the extended POD modes can be extracted by observation of the *chronoi* $\psi^{(1)}_{\|V\|}$. The *chronoi* of the 1st POD mode are for all the cases sinusoidal functions with periodicity equal to the flapping period of the wing. The overall effect of α_0 is to produce a phase shift of the *chronoi*. The mean angle of attack α_m, instead, does not affect the *chronoi*, which are similar for corresponding antisymmetric and asymmetric cases. The phase shift observed for varying α_0 is related to the introduction of the rigid rotation. This rotation can be considered as a rigid vortex with intensity varying sinusoidally in time according to the angular velocity (thus with maximum at $t/\tau = 0.75$, see Eq. 6.22). As this rigid rotation grows in importance, the modes tend to temporally align with it. It must be specified that this phase shift phenomenon is not simply a mathematical artefact but it has a physical explanation. It is reasonable to assume that the kinetic energy entering the fluid system is connected to the growth rate of the LEV circulation. The first POD modes, therefore, should be aligned with the direction of maximum circulation growth rate. According to Roshko (1954) the circulation growth rate of the LEV can be approximated as the integral over the boundary layer thickness δ_{BL} of the vorticity flux, e.g. on the upper side during the downstroke:

$$\dot{\Gamma}_{LEV}(t) = \int_0^{\delta_{BL}} \omega'_z(y',t)u'(y',t)dy' \tag{6.29}$$

Defining with $V_{eff}(t) = \|V_\infty \underline{i} + \dot{h}(t)\underline{j}\|$ as the magnitude of the effective velocity "seen" by the airfoil, and considering that it is possible to approximate (assuming triangular velocity distribution inside the boundary layer):

$$\begin{aligned} \omega_z(y',t) &\approx \frac{V_{eff}(t)}{\delta_{BL}(t)} \\ \int_0^{\delta_{BL}(t)} u'(y',t)dy' &\approx \frac{1}{2}V_\infty \delta_{BL}(t) \end{aligned} \tag{6.30}$$

and recalling Eq. 6.22, the growth rate of the LEV is:

$$\dot{\Gamma}_{LEV} \approx \frac{1}{2}V_\infty \delta_{BL}(t)\left(\frac{V_{eff}(t)}{\delta_{BL}(t)} + 2\dot{\alpha}(t)\right) \tag{6.31}$$

Eq. 6.31 (which would have opposite sign when referring to the lower side during the upstroke) expresses the simple concept that the angular velocity of the wing influences the growth rate of the LEV in the wing-fixed frame. For the present cases, due to the phase shift between the plunging and the pitching motion, as α_0 grows the modes shaping the circulation growth are temporally delayed with respect to the cosine function which shapes $\dot{h}(t)$.

The change in pitching amplitude also strongly affects the projection coefficients of the forces. The projection coefficient of the normal force component σ_{F_y} decreases with α_0 increasing. Oppositely, the projection coefficient σ_{F_x} slowly increases with α_0 increasing.

The parallelism between antisymmetric and asymmetric cases extends also to the projection coefficients of the force σ_{F_x} and σ_{F_y} and to the norm of the projection of the vorticity σ_ω, which result almost identical for corresponding cases. The variation of both the vorticity spatial integral and of the force which is modelled by the 1st mode is then uncorrelated with the mean angle of attack α_m, which only affects the spatial distribution of vorticity.

A compact overview of the 2nd POD mode of the velocity with its associated extended POD modes of vorticity and force components is reported in Fig. 6.13. Similarly to the 1st mode, the differences between *chronoi* of cases with the same α_0 are not relevant. Also, similarly to the 1st mode, a quite strong similarity can be observed for the norm of the vorticity projection (σ_ω) and for the force projection coefficients (σ_{F_x} and σ_{F_y}) for cases with the same α_0. The *chronoi* $\underline{\psi}^{(2)}_{\|V\|}$ of the 2nd mode are sinusoidal functions in phase quadrature with respect to the 1st mode for all the cases except for case D. This exception is responsible for the difference in the force reconstruction of the first 2 modes which have been observed for case D in §6.5.2 with respect to the rest of the cases. The reason behind this difference could be ascribed to the larger maximum α_{eff} achieved in this case (Fig. 6.5), thus determining stronger spectral contamination due to deep stall conditions reached at mid-cycle.

The *topoi* of the 2nd mode are strictly related to those of the 1st mode, as evident from visual inspection. For the antisymmetric cases, the negative vorticity region associated to the LEV is completely detached from the airfoil. The positive vorticity region extends over the entire airfoil, occupying also the leading edge. For cases E and F, both the positive and negative vorticity regions appear only on the upper side of the airfoil, while their presence on the lower side is negligible due to the absence of the LEV on the lower side in these cases. Similarly to what observed for the 1st mode, the relative strength of the counter-rotating vorticity regions is influenced by α_0, with the negative vorticity region decreasing in importance as α_0 increases.

The interconnection between the 1st and the 2nd mode suggests that they are the in-phase and quadrature components of the formation and release of a bound vortex over the airfoil, to which both quasi-steady, LEVs and TEVs circulations contribute. These modes also contain the acceleration of the flow induced by the wing motion. A more detailed discussion of this group of modes and of its effect on the force will be given in §6.6.

6.5.4 Description of higher order extended POD modes

Fig. 6.14 shows the modes from the 3rd to the 6th for case B. Differently from the 1st and 2nd modes, these modes are characterized by more complex (non-sinusoidal) *chronoi* featuring several peaks per flapping period. Despite being characterized by different shapes, the *chronoi* of these four modes are closely interconnected. The position of the peaks is phase-shifted of about $\pi/4$ from one mode to the other, thus suggesting that they are half-quadrature components of the same phenomenon.

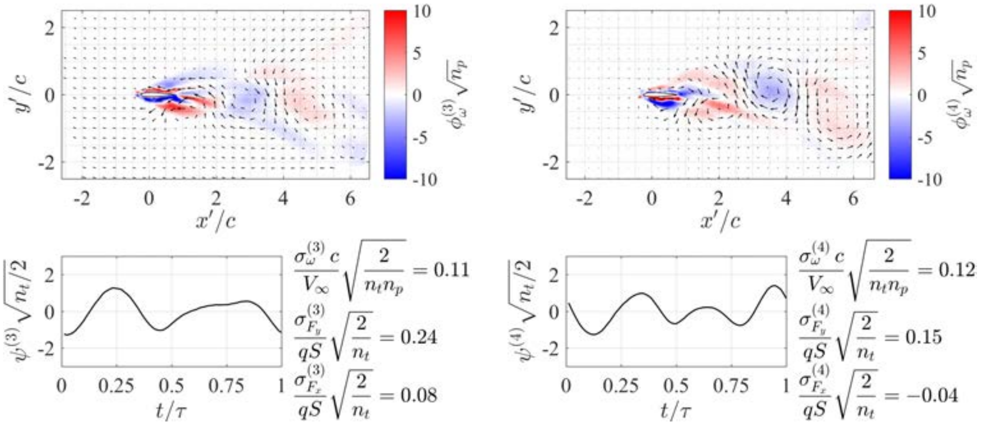

(a) POD mode 3

(c) POD mode 4

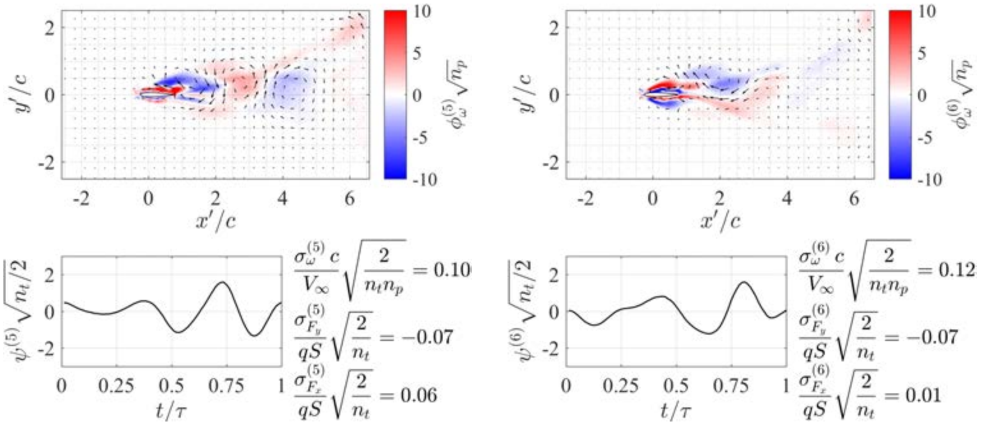

(b) POD mode 5

(d) POD mode 6

Fig. 6.14 Compact overview of the 3rd, 4th, 5th and 6th POD modes of velocity and extended POD modes of vorticity and force for case B. The *topos* of the velocity ($\underline{\phi}_x$ and $\underline{\phi}_y$) is reported as a quiver plot. The *topos* of the vorticity ($\underline{\phi}_\omega$) is reported as a contour plot. The *chronos* ($\underline{\psi}_{\|V\|}$) of the mode is reported below along with the norm of the vorticity projection (σ_ω) and the projection coefficient of the force components ($\sigma_{F,x}$ and $\sigma_{F,y}$).

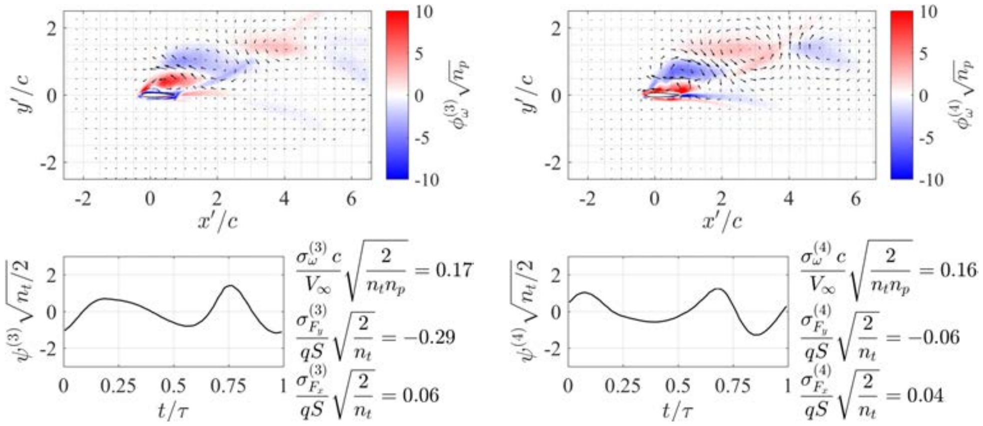
(a) POD mode 3 (c) POD mode 4

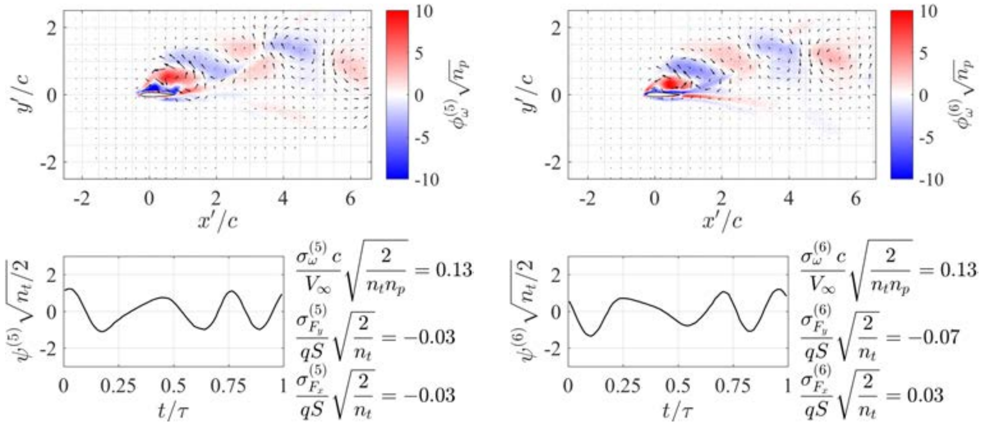
(b) POD mode 5 (d) POD mode 6

Fig. 6.15 Compact overview of the 3rd, 4th, 5th and 6th POD modes of velocity and extended POD modes of vorticity and force for case E. The *topos* of the velocity ($\underline{\phi}_x$ and $\underline{\phi}_y$) is reported as a quiver plot. The *topos* of the vorticity ($\underline{\phi}_\omega$) is reported as a contour plot. The *chronos* ($\underline{\psi}_{\|V\|}$) of the mode is reported below along with the norm of the vorticity projection (σ_ω) and the projection coefficient of the force components ($\sigma_{F,x}$ and $\sigma_{F,y}$).

This is indeed testified by the vorticity organization of the corresponding *topoi*. In all the presented modes a double-vorticity shedding which alternatively interests both sides of the airfoil is present. For each vorticity blob shed in the wake, a wall-bounded counter-rotating vorticity region forms on the corresponding side of the airfoil. These modes clearly model the LEV shedding in the wake and the modulation of the bound vorticity which they produce on the airfoil. These considerations similarly apply for cases A and C (not reported here for brevity).

Fig. 6.15 shows the modes from the 3rd to the 6th for case E (cases D and F are here omitted for brevity). The 3rd and 4th modes are temporally described by a double peak function. The peaks positions are phase-shifted by $\pi/4$, thus suggesting again that they are two half-quadrature components of a single phenomenon. From the *topoi* it appears clear that these modes describe a shedding generated from the upper side of the airfoil. The presence of the double peak in each *chronos* shows that two couples of counter-rotating vortices are shed per each cycle, even if this phenomenon is not periodical with half of the flapping period. The shedding of the vorticity blobs is contrasted by the formation of a bound vorticity region on the airfoil with opposite sign with respect to the detaching vortex. Similarly to the antisymmetric cases, these modes model the pinch-off and shedding of the LEV. However, the lack of two more half-quadrature components in case E has to be ascribed to the asymmetry in the flow topology and to the absence of the LEV on the lower side of the airfoil.

The 5th and the 6th mode of case E describe a shedding from the upper side characterized by three-peaked *chronoi*. The peaks of the *chronoi* are displaced of about $\pi/8$, thus suggesting that these modes are quarter-quadrature components of a single shedding phenomenon mainly located in the second half of the period.

6.6 Low-order model of the flow field features and their contribution to the force

6.6.1 Low-order reconstruction of flow features

As outlined in §6.5, some groups of POD modes are in-quadrature components of time-varying flow features. For a better understanding of these features, the composition of these modes is proposed in Fig. 6.16 and in Fig. 6.17 respectively for case B and E. The LORs are obtained without including the time-average flow field. The corresponding fluctuating flow field is added for comparison (Fig. 6.16a and Fig. 6.17a). According to the analysis carried out in §6.5, for case B two groups of interrelated modes can be

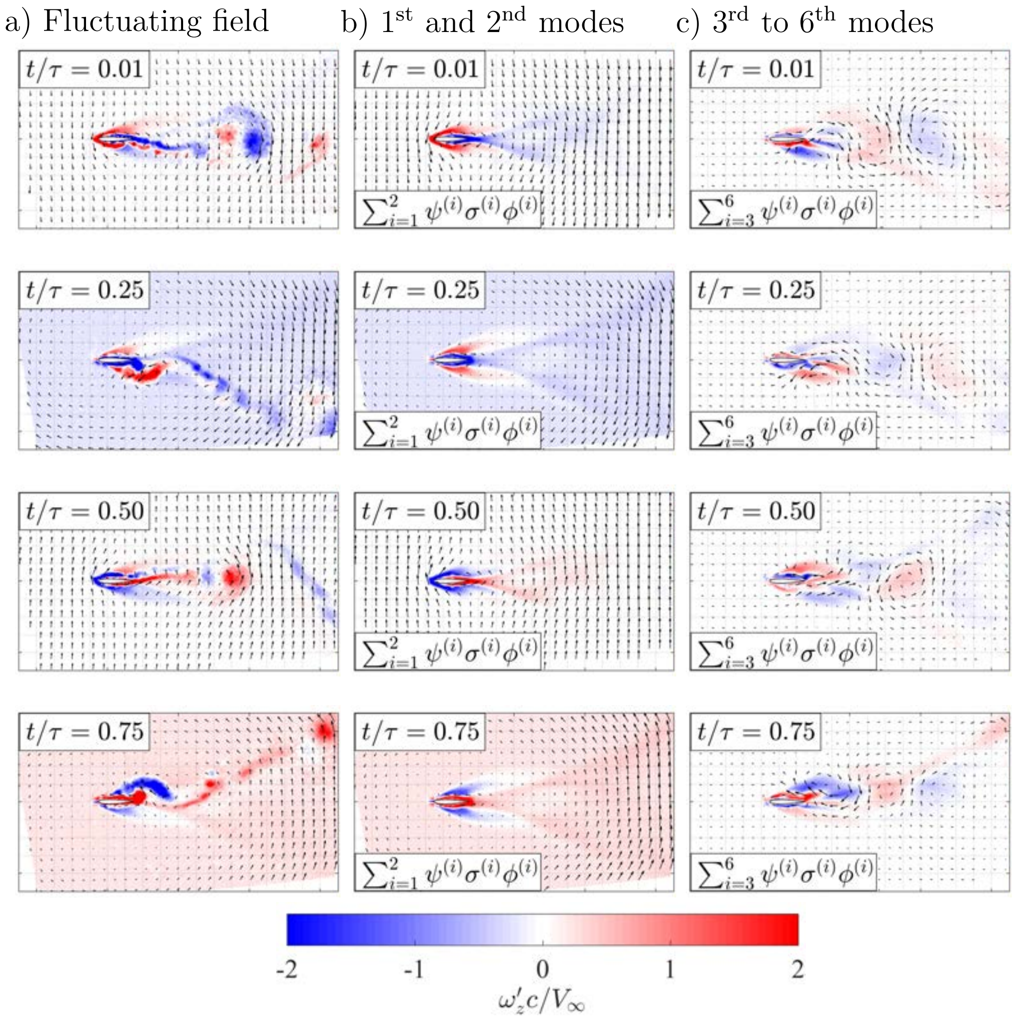
a) Fluctuating field b) 1st and 2nd modes c) 3rd to 6th modes

Fig. 6.16 Case B. Snapshot of the flow field: left) fluctuating flow field; center) LOR with 1st and 2nd modes; right) LOR with 3rd to 6th modes.

identified, i.e 1st-2nd modes and modes from the 3rd to the 6th. For the case E, instead, higher order modes have highlighted different in-quadrature arrangement, thus the 5th and the 6th have to be isolated from the 3rd and the 4th.

As already anticipated in §6.5.3, the 1st and 2nd modes are strongly connected with a bound vortex over the wing. The vorticity which is contributing to this mode (and thus to the bound vortex) corresponds to the region in which the LEV develops and to the region occupied by the counter rotating vorticity which is continuously shed from the TE. These features can be identified in Fig. 6.16b and Fig. 6.17b. The LEV coincides with the vorticity region which starts from the leading edge and grows up to its detachment. The counter rotating vorticity corresponds to the aft-region of the airfoil and to the trail which is shed from the TE. As commented in §6.5.3, these

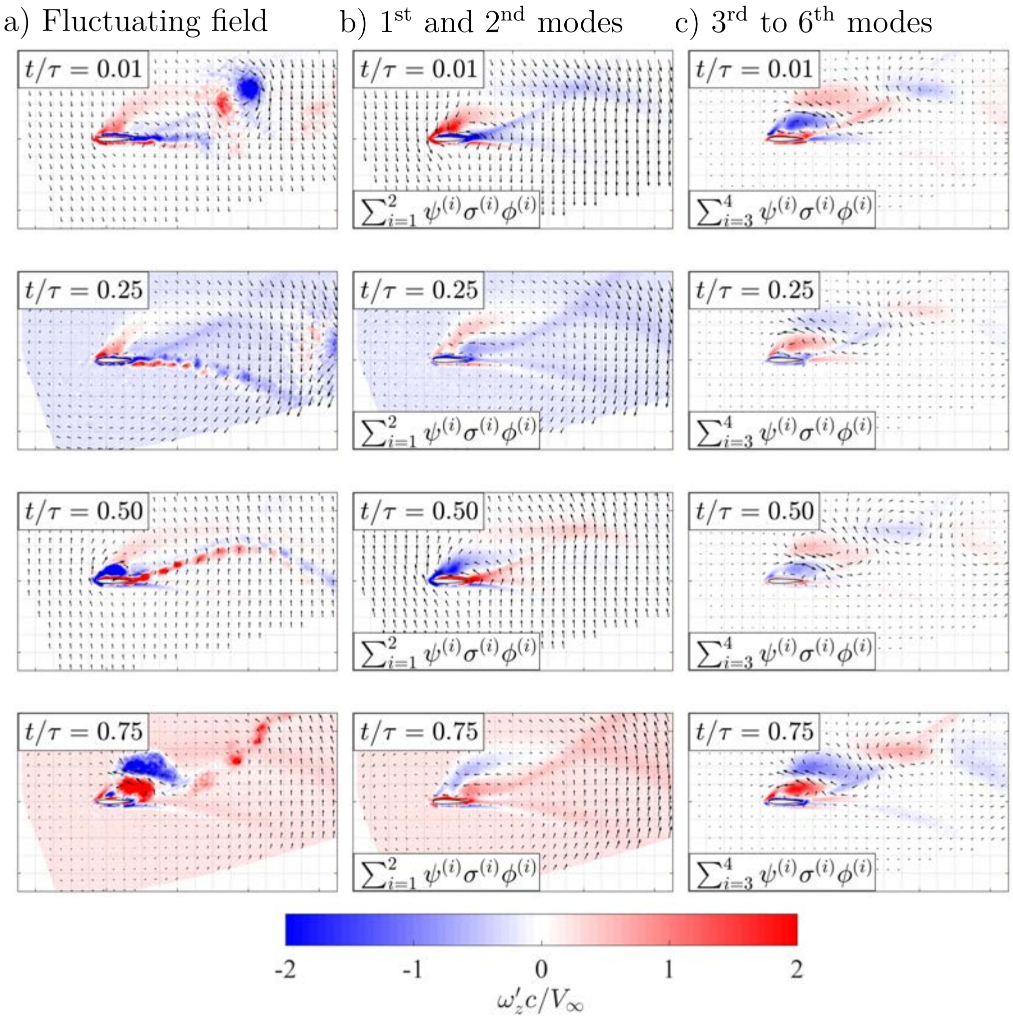
a) Fluctuating field b) 1st and 2nd modes c) 3rd to 6th modes

Fig. 6.17 Case E. Snapshot of the flow field: left) fluctuating flow field; center) LOR with 1st and 2nd modes; right) LOR with 3rd and 4th modes.

modes are strongly affected by the pitching rotation, which is included in the form of a rigid vortex. This rigid rotation is responsible of the modification of the vorticity distribution of both the attached LEV (decreasing it according to the pitching/plunging phase shift) and the bound vortex (enhancing it) and thus produce an asymmetry in the vorticity distribution between the leading edge and the trailing edge.

The group of modes from the 3rd to the 6th in case B (Fig. 6.16c) represent a vortex shedding that interests alternatively the upper and the lower side of the airfoil. It must be highlighted that the vortex blobs which are modeled by these modes only partially coincide with the LEVs. For each LEV shed in the measured field, three vorticity blobs are actually shed in these modes: one of them coincides with the LEV of the measured flow field, while the other two respectively precede and follow the LEV in time. The vorticity blob that temporally precedes the LEV clearly represents the counter-rotating vorticity blob which balances out the LEV formation according to the Kelvin theorem. The vorticity blob which follows the LEV in time cancels out the detached vorticity region of the 1st and 2nd mode, thus likely modelling the reattachment of the flow on the suction side after the pinch-off of the LEV.

Similarly to the 3rd to 6th modes of the antisymmetric cases, the 3rd and 4th modes in case E represent a vortex shedding associated with the LEV. Also in this case the vortex shedding in these modes only in part coincides with the actual vortices configuration. The spurious vortices contribute to cluster the vorticity which is continuously released from the trailing edge. Further components of the shedding are contained in the higher order modes, e.g. the couple formed by the 5th and the 6th modes which model a shedding at the double of the frequency than the 3rd and 4th modes. It is worth remarking that differently with respect to the antisymmetric cases, in the asymmetric cases these modes are quite important for the modelling of the forces (§6.5.2), thus suggesting a non negligible role played by the near-wake vorticity in forces generation.

6.6.2 Reduced-order model of the force

In §6.5.2 it has been observed that there is a clear pattern in the contribution of the extended POD modes to the fluctuating force depending on wing kinematics. The light shed on the nature of these modes from the analysis of both *topoi* and *chronoi* helps clarifying the role played by these modes in the force reconstruction. The behaviour of the time-average forces is not taken into account in this analysis, as the extended POD modes are intended to model solely the fluctuating part of the force linearly correlated with the velocity field.

According to the analysis performed previously in §6.6.1, the contribution of the 1st and 2nd mode is connected to the bound vortex. The bound vortex observed in these modes is strictly correlated to the trail of vorticity released by the pressure side and thus it may account for the fluctuating part of both the quasi-steady circulation and the wake-induced circulation, expressed in the Theodorsen's model by Eq. 6.32:

$$C_{L,c}(t) = 2\pi C(k) Q(t) \tag{6.32}$$

with $Q(t)$ defined in Eq. 6.6. It can be stated then that these first two modes account completely for the contributions of the Theodorsen's circulatory force. To prove this statement, the results of the circulatory force exposed in Eq. 6.32 are plotted against the LOR of the forces in Fig. 6.18 for all the tested cases. In the following, the

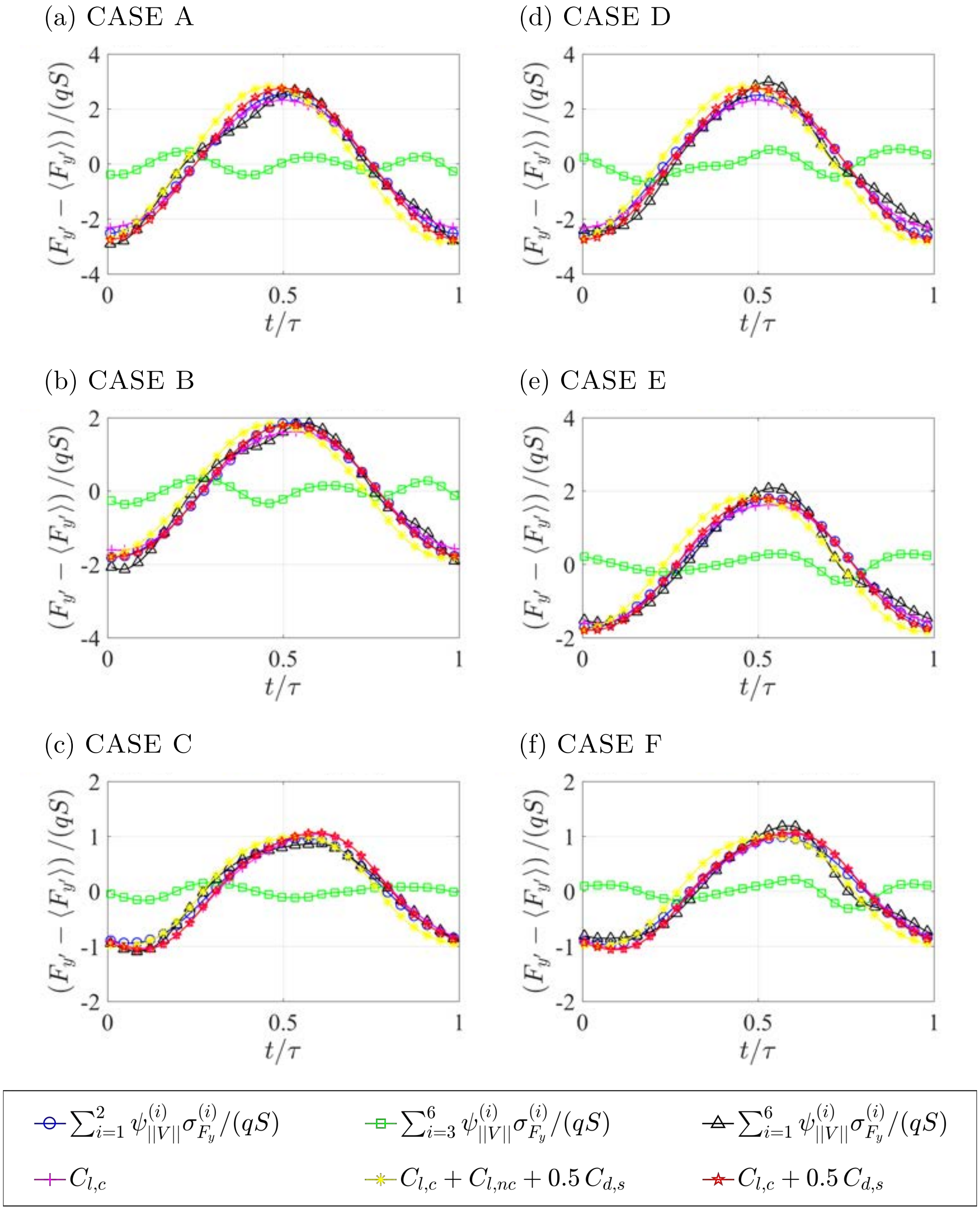

(a) CASE A

(b) CASE B

(c) CASE C

(d) CASE D

(e) CASE E

(f) CASE F

Fig. 6.18 Chord-normal component of the fluctuating force: comparison of LOR and theoretical force models.

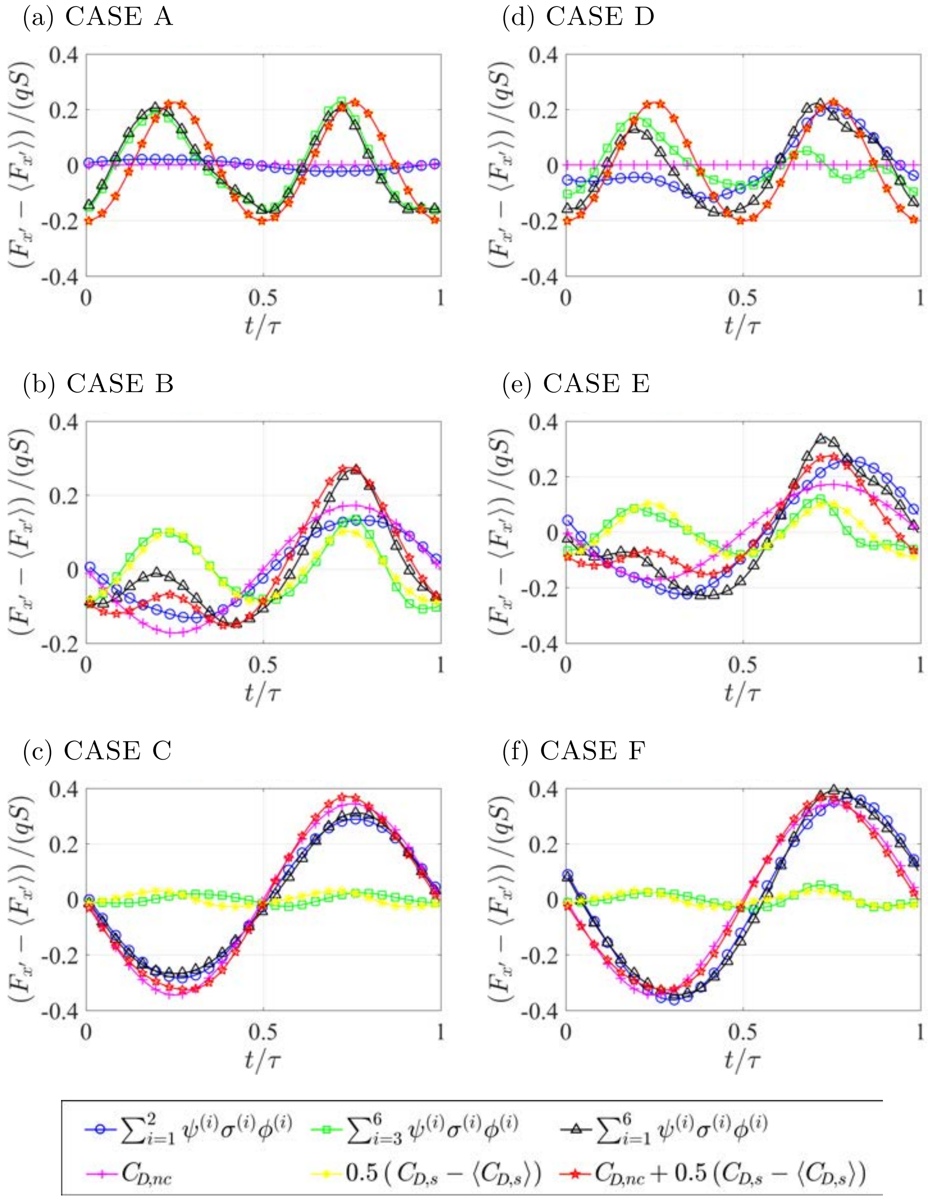

Fig. 6.19 Chord-wise component of the fluctuating force: comparison of LOR and theoretical force models.

circulatory force from the Theodorsen's model has been considered normal to the chord, despite it has been originally developed as a lift force. Also, in Eq. 6.32 only the fluctuating part of the force is considered to compare with the LOR of the fluctuating force. A discussion about the mean force is included in §6.4.2. From Fig. 6.18, few considerations can be extracted:

1. the 1st and 2nd extended POD modes model the circulatory force which arises to fulfil the Kutta condition at the Trailing Edge. For sinusoidal motion, this term can be described through the Theodorsen function (see Eq. 6.32);
2. there is no relevant non-circulatory force on the chord-normal direction;
3. the circulatory force accounted through the Theodorsen's function is orthogonal to the chord.

The last statement is in agreement with the finding of Dickinson et al. (1999) for a flat plate and with the more recent findings of Moriche (2017) for a thick airfoil. The second statement can be further reinforced by considering in the force model also the non-circulatory force contribution obtained from Theodorsen (1935) and reported in Eq. 6.33:

$$C_{L,nc}(t) = \frac{\pi c}{2V_\infty}\left(\dot{\alpha}(t) - \frac{\ddot{h}(t)}{V_\infty} - \frac{c}{2V_\infty}\ddot{\alpha}(t)(2\xi_p - 1)\right) \tag{6.33}$$

Despite the 1st and 2nd modes are strongly affected by the rigid rotation of the wing and its plunging motion (as discussed in §6.5.3), non-circulatory forces accounted through Eq. 6.33 does not fit the LOR in Fig. 6.18.

It has been observed in §6.6.1 that the rigid rotation introduced by the pitching motion introduces an asymmetry in the vorticity distribution between the leading edge and the trailing edge. Also, in §6.5.2 it has been observed that the 1st and 2nd modes introduce a sinusoidal force component on the chord-parallel direction. It is possible to assume that this force is connected with a non-circulatory force depending on $\dot{\alpha}(t)$. In the following, we model this contribution on the chord-wise axis by means of the rotational added-mass force term included originally by Theodorsen (1935) in the lift expression and given by Eq. 6.34:

$$C_{D,nc}(t) = \frac{\pi c}{2V_\infty}\dot{\alpha}(t) \tag{6.34}$$

The comparison in Fig. 6.19 proves that this non-circulatory term captures the contribution to the chord-wise force of the 1st and 2nd modes. Despite Theodorsen

(1935) considers this term on the lift (and thus orthogonally to the chord due to the small angles hypothesis), a similar term is given in Sedov (1965) on the chord-wise direction for a flat plate (as reported in Eq. 6.10). It must be remarked, however, that the term given by Sedov (1965) would is significantly different from that in Eq. 6.34, which is not including any dependence on chord-normal wing velocity V_y. To stress out the difference between the two expressions, it is possible to rewrite the corresponding term from Eq. 6.10 as:

$$C_{D,Sedov} = \frac{\pi c}{2V_\infty}\frac{V_y}{V_\infty}\dot{\alpha}(t) = C_{D,nc}(t)\frac{V_y}{V_\infty} \tag{6.35}$$

Higher order modes account for the shedding of vortices and for the modulation that they produce on the vorticity around the airfoil. It has been observed in §6.5.2 that their most relevant contribution to the force is directed chord-wise. As a further evidence, the modes both in Fig. 6.16c and Fig. 6.17c clearly show that the pairing between shed and induced vorticity on the airfoil surface generate a jet-like flow along the chord-wise direction. In line with the sign of $F_{x'}$, this jet is directed downstream for $t/\tau \approx 0$ and $t/\tau \approx 0.5$, thus producing negative $F_{x'}$, while it is directed upstream for $t/\tau \approx 0.25$ and $t/\tau \approx 0.75$.

These modes can be associated to the suction term of the Garrick's model. Garrick (1937) calculates this term from an energy balance in the wake of the airfoil. This model can be therefore associated with the energy required to form the concetrated vortices in the wake. The suction contribution is given by Eq. 6.36:

$$C_{D,s}(t) = -\pi\left(\frac{\sqrt{2}}{2}\left(2C(k)Q(t) - \frac{c}{2V_\infty}\dot{\alpha}\right)\right)^2 \tag{6.36}$$

It must be remarked that the model by Garrick was intended to be applied on the free-stream direction rather than in the chord-wise direction, i.e. for small angles of attack. Nevertheless the reference frame transformation applied in this work allows to apply it also for flapping wings in the chord-wise direction. According to the results from Baik et al. (2012), this model did not prove to be effective in describing the thrust/drag of the airfoil for the entire flapping cycle.

In Fig. 6.19 the force contribution of the modes from the 3rd to the 6th is compared with half the suction term included in the model by Garrick (see Eq. 6.36) after removing its average value. A good agreement with all the cases is found, thus suggesting that the application of the Garrick's model should be preferably done in the chord-wise direction. Consequently, the oscillation of bound vorticity observed in

Fig. 6.16c and Fig. 6.17c may be at least partially explained through the Garrick's model for the leading-edge suction. It is worth noting that $\langle C_{F_{x'}} \rangle \neq \langle C_{D,s} \rangle$: this is a consequence of the Garrick's model being based on the potential flow assumption. At low Reynolds numbers the skin friction contribution is relevant, thus discrepancies in the average forces are expectable.

Following the Leading Edge suction analogy of Polhamus (1966), it is possible to account half of the suction term by Garrick (1937) in the chord-normal direction. Fig. 6.18 shows that the discrepancies between the Theodorsen's model and the LOR are slightly reduced if half of the suction contribution from the Garrick's model is included to the normal force. The direction of the suction is chosen accordingly with the position of the LEV on either the upper or the lower side of the airfoil. The split of the Garrick's suction term between chord-wise and chord-normal force components might be ascribed to the airfoil leading edge shape. Ashraf et al. (2011) and Yu et al. (2012b) report that the propulsive force is strongly depending on the airfoil shape, increasing for thicker airfoils. This suggest that the bulk of the LEV suction might be contributing more in the chord-wise direction more than in the chord-normal direction for thicker LEs.

The higher order modes are also responsible for the introduction of oscillations in the normal force which are not captured neither by the 1st and 2nd modes, neither by the Theodorsen's model. These oscillation can be explained either as a modulation of the bound vorticity operated by the shed vorticity, either as a change in the chord-normal component of the momentum in the wake.

6.7 Conclusions

This chapter describes an experimental study over an airfoil in both plunging and pitching motion. Measurements of the phase-averaged flow fields and of the phase-averaged force are reported. A novel approach to decompose the unsteady aerodynamic forces acting on an airfoil in flapping motion is employed. The approach is based on the statistical decomposition of the flow field through the Proper Orthogonal Decomposition and to its extension to decompose the force in a common temporal basis following the extended POD (Borée, 2003). The approach is applied to phase-averaged velocity fields, measured by means of PIV, and to phase-averaged force components in the chord-wise and chord-normal direction, measured by means of a high-resolution load cell. The measured velocity and vorticity fields are transformed into the corresponding fields in the non-inertial wing-fixed reference frame in order to remove the influence of the moving boundary, i.e. the airfoil, from the decomposition. Subsequently, velocity/vorticity fields in the wing-fixed reference frame are decomposed via POD. The *chronoi* obtained from the POD of the velocity are used as a basis to project the force and to extract the force contribution of each mode. The proposed approach draws a statistical interconnection between the force generation and the flow organization described through the POD modes.

From the analysis of the different cases, it results that the force components can be modelled using a very compact subset of modes of the velocity field. The compactness of the correlation ensures that a simple link can be found between flow field and force, paving the way to simple data-driven models for the fluctuating force. Independently on the case, this subset of modes accounts for very specific and well-organized flow features: the first two modes are the in-quadrature components describing the temporal evolution of the bound vortex (including the LEV while still attached on the airfoil); higher order modes model the near-wake generated by the flapping wing, thus including the shedding of free LEVs and TEVs and their induction both on the airfoil and in the wake. Thanks to this link with the actual flow features in the field, both the *topoi* and the *chronoi* of these modes present similar characteristics. Very localized and consistent changes are operated spanning the parameters of the motion. A change in α_m introduces an asymmetry in the *topoi* of the modes, modifying the relative strength between features on the upper side (which are enhanced) and the lower side (which are weakened) of the airfoil. The temporal evolution of these features, which is contained in the *chronoi*, remains substantially unaffected by the introduction of an asymmetry in the motion. The pitching amplitude α_0 is found to influence both the size of the vortical structures attached to the wing or shed in the wake (according to the observation of the *topoi*) and their temporal evolution (*chronoi*). Specifically, the size of the vortical structures is reduced as the pitching amplitude increases, while their growth in time is delayed. These changes can be connected to the reduction of the vorticity flux feeding the LEV due to the angular velocity of the wing, which weakens the vortical structures for the phase delay that has been chosen in the wing motion ($\varphi = \pi/2$ between plunging and pitching).

Finally, the contribution of each mode to the force has been assessed, finding a correspondence between the modelled flow features and their contribution to the force. The 1st and the 2nd mode, which include the contribution of the bound circulation, are the main source of the normal component of the force. Their contribution on the chord-wise component is strongly dependent on the pitching motion amplitude. Higher order modes, which include the contribution of free vortices in the wake, are mainly responsible for the chord-wise component of the force. Similarly to *topoi* and *chronoi*, also the contribution to the force ascribed to each mode is found to depend on the parameters of the wing motion. This relation can be accounted for through a modification of the models by Theodorsen and Garrick. The normal force component due to the first two modes coincides with the superposition of the circulatory component of the lift of Theodorsen model and (part of) the Garrick suction term, while its chord-wise component is essentially ascribed to the non-circulatory forces from the Theodorsen model. The chord-wise force component ascribed to high order modes can be associated to part of the suction term in the Garrick's model.

In summary it has been found that the force components in the wing-fixed reference frame can be successfully modelled by correctly rearranging the terms included in the models by Theodorsen and Garrick. The model found is given by Eq. 6.37:

$$\begin{aligned} C_{F_{y'}} &= \langle C_{F_{y'}} \rangle + C_{L,c} + 0.5\, C_{D,s} \\ C_{F_{x'}} &= C_{D,nc} + 0.5\, C_{D,s} + C_{D,f} \end{aligned} \tag{6.37}$$

where $C_{L,c}$, $C_{D,nc}$ and $C_{D,s}$ are respectively the circulatory lift (from Eq. 6.32), the non-circulatory drag (from Eq. 6.34) and the suction term (from Eq. 6.36). The term $C_{D,f}$ represents an average drag term which accounts for friction forces and which has not been considered in the analysis, which is focused on potential flow theories.

The presented analytical model provides an excellent estimation of the experimental data. However, further studies are needed to prove that it can be directly extended to other configurations. In particular, further studies are needed to estimate the share of the Garrick suction term between chord-wise and chord-normal force components which has probably to be ascribed to the airfoil leading edge shape.

Part IV

Other applications

Chapter 7

Estimation of time-resolved turbulent fields

In §2.4 it has been introduced the *extended* POD, which allows estimating the modes of a certain flow *quantity* that are linearly correlated to the POD modes of another flow *quantity*. The term *quantity* is here expressing a very generic concept: it can either refer to two different physical quantities (such as velocity, pressure, temperature, etc.), or the same physical quantities evaluated on different domains. When the linear stochastic relation between these *quantities* is statistically well-converged, the extended POD modes can be successfully exploited to obtain the estimation of one of the two *quantities* from the knowledge of the other one.

In this chapter, the extended POD will be exploited to estimate a time-resolved turbulent field from the combination of non-time-resolved field measurements and time-resolved point measurements. The proposed method poses its fundaments on a stochastic estimation based on the Proper Orthogonal Decomposition of the field measurements and of the time-resolved point measurements. The statistical correlation between the field measurements and the point measurements at synchronized instants can be evaluated by means of the *extended* POD. In order to improve the correlation, field snapshots are correlated to *probe snapshots* obtained by considering point measurements over a finite timespan. This procedure, therefore, implicitly accounts for multiple time delays for different extended POD modes. The correlation between field measurements and point measurements is then extended to the "out-of-sample" time instants for the field measurements, i.e. those in which field data are not available. Through the estimation of the POD time coefficients in the out-of-sample instants it is possible to obtain the reconstruction of the corresponding flow fields.

The method here reported extends the work by Hosseini et al. (2015) by proposing a truncation criterion which allows to remove the uncorrelated part of the signal from the reconstruction of flow fields. The truncation is fundamental in case of turbulent flow fields, in which a great wealth of scales is involved, thus reducing the correlation between the probes signal and the field measurements. The threshold selection poses its basis on the random distribution of the uncorrelated signal.

The mathematical details of the method and of the truncation are given in §7.2. The method is validated with a synthetic test case and an experimental one in §7.3. A Direct Numerical Simulation database of a channel flow is selected since its spectral richness is expected to represent a significant challenge for this method. This dataset allows isolating the effects of correlation between field measurements and point measurements, removing issues connected to noise contamination or to the finite spatial resolution which would inevitably affect experimental data. The experimental test case is the wake flow behind a high-angle-of attack airfoil with a relatively small number of samples, affected by significant noise. The quality of the dynamic estimation is found to be affected by the noise contamination of the data and by poor convergence of the POD modes, which add on the effect of the probes location, i.e. on the correlation between probes events and flow features. The selection of the probes timespan to perform the POD analysis on the probes signal is also discussed. The determination coefficient between reconstructed data and in-sample data is proposed as an assessment of the flow fields estimation quality. The use of the determination coefficient directly on the in-sample data is allowed by the truncation itself, while it would not be possible for extended POD modes without truncation.

7.1 Dynamic estimation of turbulent flow fields

In the last decades Experimental Fluid Mechanics has experienced the flourishing of field measurement techniques, disclosing the access to the instantaneous distribution of field quantities such as velocities, concentrations, temperatures or pressures as in Particle Image Velocimetry (Westerweel et al., 2013), thermographic phosphors (Abram et al., 2015), Infrared thermography (Raiola et al., 2017) or pressure sensitive paints (Pastuhoff et al., 2013). Unfortunately due to limitations related to data rate or sensor technology, it often occurs that such measurement techniques are unable to provide information on the flow dynamics, such as for instance in moderate to high Reynolds number turbulent flows. For example, for the case of Particle Image Velocimetry, although the most recent technological developments have led in the last decades to powerful high speed light sources and fast high-resolution scientific cameras, which have triggered the development of novel approaches exploiting time resolution (see, e.g. the reviews in van Oudheusden, 2013, and Kähler et al., 2016), time-resolved PIV remains of real practical use prevalently for low Reynolds numbers flows.

When the real-flow dynamics are not accessible due to hardware limitations, dynamic estimation of coherent structures is an extremely appealing option. Some promising attempt of dynamic estimation relies on physics-driven methods such as the vortex-in-cell (VIC, Schneiders et al., 2014) method. While VIC can provide high-quality estimation of the time-resolved flow, it is inherently a three-dimensional method. This limits the use of VIC in turbulent flows to 3D flow field measurements. Its extension to planar flow field measurements its only possible for purely two-dimensional flows.

Dynamic estimation based on low order models has proven to be a prominent candidate to elaborate flow control strategies (see, e.g. Noack et al., 2011, Holmes et al., 2012). Low order models often truncate small scales and aim to model prevalently the dynamics of large scale structures, thus losing detail of description in high Reynolds number flows. Nonetheless, large scale structures are widely recognized to be the main actors in momentum transport in turbulent flows. For example in wall-bounded flows large scale structures carry the bulk of the kinetic energy and contribute largely to the production of Reynolds stresses (see for instance the very large scale structures in pipe flows (Balakumar and Adrian, 2007), or the interaction between large scale structures in the outer layer and near wall features in adverse-pressure-gradient boundary layers Harun et al. (2013), Sanmiguel et al. (2017)).

Among the possible solutions, one relevant candidate is based on modal analysis. Coherent structures are often detected through Proper Orthogonal Decomposition (POD, Berkooz et al., 1993) and then, through further analysis, their dynamics is identified. In case of shedding-dominated phenomena, POD has been widely used to extract phase coherent information for the first and higher order harmonics, both in 2D (see, e.g. Chapter 5 of this thesis, van Oudheusden et al., 2005, Legrand et al., 2011, Raiola et al., 2016) and 3D (Ceglia et al., 2014, Cafiero et al., 2014). This is however only possible when a dominant phase relation between POD modes can be identified from the scatter plots of the time coefficients and does not allow to extract any absolute frequency information. Through some physical assumptions on convection velocities it is however possible to identify also modes temporal information as done by Jaunet et al. (2016).

The modes frequency information can be retrieved with the help of additional time-resolved data by making use of Linear Stochastic Estimation (LSE). Originally developed to provide an approximation of a conditional average (see Adrian, 1994), LSE allows to estimate the most probable value of a certain quantity (e.g. a POD time coefficient), given another measured quantity. By using a time-resolved probe, LSE allows thus to estimate the most probable instantaneous flow field given a certain value measured by the probe. This flow-field estimation capability can be especially exploited in flow control applications in which real-time flow diagnostics are required. The first attempts of dynamic estimations of the flow fields were based on the information from only one time instant and are referred to as single-time-delay techniques (see, e.g. Guezennec, 1989). The word *delay* refers to the fact that a time shift, typically corresponding to a given convective time, was imposed between the value to be estimated and the value used to perform the estimation.

The temporal coherence of time-resolved probes was later exploited more intensively by means of multi-time-delay LSE. Of course, multi-time delays are beneficial since they allow to reduce the effect of noise contamination on the probe measurements and are able to deal with several convective time scales. Depending on the application of interest, multi-time-delay LSE has been preferred in the spectral (e.g. for aeroacoustics applications Tinney et al., 2006) or temporal domain (for flow field reconstruction from PIV data or flow control applications, Durgesh and Naughton, 2010). An assessment of stochastic estimation methods performances and on the effect of the sensor location is reported in Arnault et al. (2016).

Most recent developments for LSE-based dynamic estimations of flow fields include the method proposed by Tu et al. (2013), who defined a linear model of the flow field and incorporated a Kalman smoother to improve the estimation and minimize the effects of noise contamination. Baars and Tinney (2014) proposed a significant improvement of spectral LSE providing a POD-based method exploiting higher order coherences and thus able to identify mutual interaction between coherent structures. This aspect is especially interesting when dealing with turbulent flows in which more energetic coherent structures affect the convective velocity of less energetic ones; a higher order representation thus appears necessary to account for the multiple interaction of coherent structures.

An interesting alternative approach is based on the Extended POD (EPOD). Borée (2003) has shown that, when dealing with multiple synchronized measurements, the correlation between them can be ascertained through the evaluation of the *extended POD modes* which are estimated through the projection of the snapshot matrix of a given quantity on the temporal basis corresponding to another one. This technique reduces to the LSE if all POD modes of the probes data are retained in the reconstruction.

A recent improvement of this technique for shedding wake flows has been proposed by Hosseini et al. (2015), which proposed to perform the EPOD projection using the correlation between temporal coefficients of the POD of both velocity fields and probes data. The advantage is that the spatio-temporal correlations of the EPOD approach are replaced by solely temporal correlations. Additionally, history effects are taken into account by adding "virtual" probes using time-shifted probes data (with the support of the Taylor's hypothesis of uniform convection). A similar probes data organization was previously proposed in Sicot et al. (2012) to extract the conditional flow structure downstream of a reattaching flow region. Hosseini et al. (2015) argued that only the modes for which the correlation with the velocity is non-vanishing are considered, i.e. the method is self-tuning. It has to be underlined that Hosseini et al. (2015) applied their method to three kind of modes: symmetric, antisymmetric and non-periodic low-frequency modes in the wake of a wall-mounted pyramid at $Re = 28000$. It will be shown later that, for turbulent flows with a richer variety of scales, the self-adjustment to only non-vanishing modes is not straightforward and uncorrelated modes might introduce spurious effects. In this case the method converges to a Linear Stochastic Estimation, losing the advantage of the Extended POD which allows to minimize the noise contamination of the reconstructed signal due to uncorrelated signal which results in random noise.

Additionally, it has to be noted that in all the aforementioned cases both LSE and EPOD have been extensively applied to shedding-dominated phenomena. The scenario of a turbulent flow with full rank of frequencies appears intuitively more complex. For instance Kerhervé et al. (2017) report the dynamic description of very-large-scale motions in high Reynolds number turbulent boundary layers, based on synchronized low-repetition-rate two-dimensional stereo-PIV measurements and hotwires. The experiments by Kerhervé et al. (2017) made use of a two-dimensional rake of 143 single probes sampled at 30 kHz to obtain a satisfactory reconstruction of the flow dynamics using LSE. The large number of probes needed might possibly be due to the inability of LSE to deal with optimal truncation of the uncorrelated part of the signal.

In the following a modified EPOD procedure to deal with the dynamic estimation of field quantities in turbulent flows is demonstrated. The modification of the procedure consists in an automated simple truncation criterion which allows to remove the noise and the uncorrelated part of the signal. Additionally, while for shedding-dominated fields the selection of the optimum time span for multi-time delay approaches is straightforward (for instance Hosseini et al., 2015, use the shedding period, and tune the number of virtual sensors to describe a clearly periodic phenomenon), this choice is not trivial for turbulent flows and will be discussed in the following.

7.2 Mathematical foundations

7.2.1 An extended POD approach for turbulent fields estimation

Suppose that a set of n_t field snapshots, each containing n_p points, is acquired. Suppose also that the signal of m synchronized fast probes is sampled with a rate s times faster than the sampling rate of the field measurements. Therefore, data from the synchronized fast probes is available such that $m \times s$ independent probe samples are recorded for each field snapshot and $n_{pr} = m \times s \times n_t$ probe samples are recorded in total. For example, a low repetition rate PIV system capturing flow fields at 10 Hz for 10 s would provide $n_t = 100$ PIV samples, and three hotwires capturing at 1 kHz for the same time period would lead to $n_{pr} = m \times s \times n_t = 30000$ total samples and $n_{pr}/n_t = 300$ independent samples per snapshot.

The snapshots of the fluctuating flow field can be rearranged in vectors and then in the data matrix $\underline{\underline{U}}$ with size $n_t \times n_p$ and decomposed by means of the *snapshots* POD as described in §2.1:

$$\underline{\underline{U}} = \underline{\underline{\Psi}}\ \underline{\underline{\Sigma}}\ \underline{\underline{\Phi}} \tag{7.1}$$

Also the probes data can be rearranged in a matrix $\underline{\underline{U}}_{pr}$, with the rows being formed by n_{tt} "virtual" probes data pertaining to each corresponding snapshot (thus having n_t rows as the snapshot data matrix, and n_{tt} columns). Without leading the generality of the problem, we will assume that the probe snapshot matrix is built considering $n_{tt} = n_{pr}/n_t$, i.e. assigning to each field snapshot a number of virtual probes equal to the captured probe data in the time interval between the field snapshots. In general for turbulent flows the choice of the time span depends on the average convection velocity, as it will be shown in §7.3.

The proposed approach for virtual probe construction is analogous to that proposed by Sicot et al. (2012) and Hosseini et al. (2015) which generated virtual probes under the Taylor hypothesis assumption. This probes snapshot matrix can be decomposed with a POD snapshot approach (Sirovich, 1987) as:

$$\underline{\underline{U}}_{pr} = \underline{\underline{\Psi}}_{pr}\ \underline{\underline{\Sigma}}_{pr}\ \underline{\underline{\Phi}}_{pr} \tag{7.2}$$

The modes included in the rows of $\underline{\underline{\Phi}}_{pr}$ constitute a pseudo-spatial basis of the probe *snapshot* vectors. $\underline{\underline{\Psi}}_{pr}$, as for the field data, represents the corresponding temporal basis and $\underline{\underline{\Sigma}}_{pr}$ is again a diagonal matrix containing the singular values. The probes snapshot vectors can thus be reconstructed using n_m modes as:

$$\underline{u}_{pr}\,(t) \approx \sum_{i=1}^{n_m} \psi_{pr}^{(i)}\,(t)\,\sigma_{pr}^{(i)}\;\underline{\phi}_{pr}^{(i)} \tag{7.3}$$

Although the rows of $\underline{\underline{\Phi}}_{pr}$ would be a basis for the n_{tt}-vector space only for $n_t = n_{tt}$, if the experiment is ergodic and the decomposition of the $\underline{\underline{U}}_{pr}$ matrix contains a dataset sufficiently large and rich (i.e. it contains enough snapshots which are taken over a sufficiently long sampling time) to reach statistical convergence, the modes $\underline{\underline{\Sigma}}_{pr}\ \underline{\underline{\Phi}}_{pr}$ are a basis sufficiently large and well converged to reconstruct any $\underline{u}_{pr}$ vector with a minimal residual error. For a square snapshot matrix ($n_t = n_{tt}$) the rows of $\underline{\underline{\Phi}}_{pr}^{T}$ form a basis in the n_{tt} vector space and the reconstruction in Eq. (7.3) is exact for any $\underline{u}_{pr}(t)$ if $n_m = n_t$. A generic probe acquisition $\underline{u}_{pr}^{+}$ at a generic time instant t^{+} can be used to estimate the vector of time coefficients $\underline{\psi}_{pr}^{+}$ which allows approximating the probe acquisition as a linear combination of the probe snapshot modes $\sigma_{pr}^{(i)}\underline{\phi}_{pr}^{(i)}$

$$\underline{\psi}_{pr}^{+}\ \left(t^{+}\right) = \underline{u}_{pr}^{+}\left(t^{+}\right)\underline{\underline{\Phi}}_{pr}^{T}\ \underline{\underline{\Sigma}}_{pr}^{-1} \tag{7.4}$$

where the superscript T refer to a transpose. It has to be noted that if the experiment is ergodic whatever probe sequence $\underline{u}_{pr}^{+}(t^{+})$ can also be acquired outside (either before or after) of the acquisition from which the modes were estimated, and used for the flow field estimation.

For the problem under investigation, the *extended POD modes* (Borée, 2003) corresponding to the field measurements can be estimated as:

$$\underline{\underline{\Psi}}_{pr}^{T}\ \underline{\underline{U}} = \underline{\underline{\Sigma}}_{e}\ \underline{\underline{\Phi}}_{e} = \underline{\underline{\Psi}}_{pr}^{T}\ \underline{\underline{\Psi}}\ \underline{\underline{\Sigma}}\ \underline{\underline{\Phi}}\ = \ \underline{\underline{\Xi}}\ \underline{\underline{\Sigma}}\ \underline{\underline{\Phi}} \tag{7.5}$$

where the subscript e refers to extended POD modes and the matrix $\underline{\underline{\Xi}} = \underline{\underline{\Psi}}_{pr}^{T}\underline{\underline{\Psi}}$ is a matrix containing information about the temporal correlation between fields and probes modes.

Given Eq. (7.5), the probes time coefficient $\underline{\psi}_{pr}^{+}\ (t^{+})$ can be used to reconstruct the part of the field snapshots which is correlated with the probes signal through the extended POD modes. For computational efficiency, it is preferable to operate in the space of POD modes (Hosseini et al., 2015). If the dataset is sufficiently large to reach statistical convergence, it is possible to assume that the matrix $\underline{\underline{\Psi}}_{pr}^{T}\underline{\underline{\Psi}}$ represents a good estimate of the dyadic product $\underline{\psi}_{pr}^{+T}$ $\underline{\psi}_{DYN}^{+}$ which embeds the relation between the time coefficient of the probe snapshot at t^{+} and the time coefficient $\underline{\psi}_{DYN}^{+}$ of the out-of-sample estimate of the field measurement. Through a linear transformation between the probes time coefficients and the flow fields time coefficients, the dynamic estimation of the latter starting from $\underline{\psi}_{pr}^{+}(t^{+})$ is obtained as:

$$\underline{\psi}_{DYN}^{+}\left(t^{+}\right) \approx \underline{\psi}_{pr}^{+}\left(t^{+}\right) \underline{\underline{\Psi}}_{pr}^{T} \underline{\underline{\Psi}} \tag{7.6}$$

The time coefficients can then be used to reconstruct the flow field snapshot at the time instant t^{+}.

This procedure can be carried out for any time instant t^{+} at which probes data are available, allowing to provide an estimation of the field measurements at the same sampling frequency of the probes.

$$\underline{u}_{DYN}^{+}(t^{+}) \approx \sum_{i=1}^{n_m} \psi_{DYN}^{+(i)}(t^{+})\sigma^{(i)}\underline{\phi}^{(i)} \tag{7.7}$$

Following the previous example of n_t field snapshots synchronized with m probes sampling s times faster than the field measurements, this would lead to obtain up to sn_t fields, increasing the sampling rate by a factor s.

7.2.2 Truncation of the time coefficients correlation matrix

The ith extended POD mode $\underline{\underline{\Sigma}}_e$ $\underline{\underline{\Phi}}_e$ in Eq. (7.5) contains solely and entirely the part of $\underline{\underline{U}}$ which is correlated to the ith probe mode (Borée, 2003). A proof of this statement is provided in §2.4.1. Consequently extended POD has been used in the past to correlate flow field modes with other measured quantities, e.g. OH concentrations in flames (Duwig and Iudiciani, 2010) and wall pressures (Sicot et al., 2012). As shown on the right hand side of Eq. (7.5), an extended POD mode is the combination of all the POD modes of the snapshot field. Consequently, the estimation of the time coefficients of a certain mode (Eq. 7) depends on all the probes time coefficients, accounting also for modes interaction through the matrix $\underline{\underline{\Xi}} = \underline{\underline{\Psi}}_{pr}^{T}\underline{\underline{\Psi}}$. This estimation method removes the need of multiple-time delays and accounts for the variation of the modes time delays due to modal interaction.

Nevertheless, this modes interaction might result in the noise contamination of the highly energetic POD modes. In fact, although in PIV measurements noise has typically a spectrally white content and has a greater impact on low-energy modes (see, e.g., Chapter 3 of this thesis and Raiola et al., 2015, which report the noise distribution through the POD modes in turbulent flows) the contamination from higher order modes can produce spurious effect also in the first extended POD modes.

The larger (in term of number of samples) and richer (in term of statistical convergence) is the dataset with which the fields and probes times coefficients and modes are estimated, the greater will be the accuracy of the estimation of the modes mutual interaction. Nevertheless, both the columns of $\underline{\underline{\Psi}}_{pr}$ and $\underline{\underline{\Psi}}$ are orthonormal vectors and form 2 bases in the n_t-dimension vector space; consequently also $\underline{\underline{\Xi}}$ is composed by columns forming a basis. This implies that higher order modes which might be mutually uncorrelated are taken into account for the dynamic estimation in Eq. (7.6) which coincides with a LSE for $n_m = n_t$.

The error in the estimation of a generic snapshot $\underline{u}^+_{DYN}(t^+)$ is dependent on the correlation between probes and field modes, on the convergence in the estimation of the modes and on the noise content of the measurements. In particular, the noise content requires to be taken into account carefully. According to Hosseini et al. (2015), the vanishing elements of $\underline{\underline{\Xi}}$ will not contribute in building the dynamic estimated field, thus this approach is, in this sense, self-adjusting. However, while for a spatially persistent shedding the correlation between the velocity and probe data is dominating, in case of a richer range of scales this correlation might become weaker, giving rise to significant noise contamination. Reminding that all rows/columns of $\underline{\underline{\Xi}}$ have unitary norm and supposing that at a certain i^{th} probe mode (j^{th} field mode) is uncorrelated with the field modes (the snapshot modes) the ith row (j^{th} column) of $\underline{\underline{\Xi}}$ will be composed of randomly distributed elements, with unitary norm and zero mean, thus standard deviation equal to $\sigma_{std} = 1/\sqrt{n_t}$.

This consideration can be easily exploited to reduce the spurious contamination due to uncorrelated residual components, thus enabling a powerful truncation. In fact, for a normal distribution (such as that of the rows and columns corresponding to uncorrelated POD modes) 99.7% of the data is within three standard deviations of the mean (Pukelsheim, 1994). Consequently it is possible to remove practically all the uncorrelated and noisy contribution from $\underline{u}^+_{DYN}$ by truncating all the elements of $\underline{\underline{\Xi}}$ with the $3\sigma_{std}$ rule, i.e:

$$-\frac{3}{\sqrt{n_t}} \leq \Xi_{ij} \leq +\frac{3}{\sqrt{n_t}} \Rightarrow \; \Xi_{ij} = 0 \quad , \quad i,j = 1,\ldots,n_t \tag{7.8}$$

It will be shown that the proposed truncation allows to obtain higher quality data with a smaller number of probes, as well as to provide a useful strategy to obtain a reconstruction accuracy estimate for real experimental data.

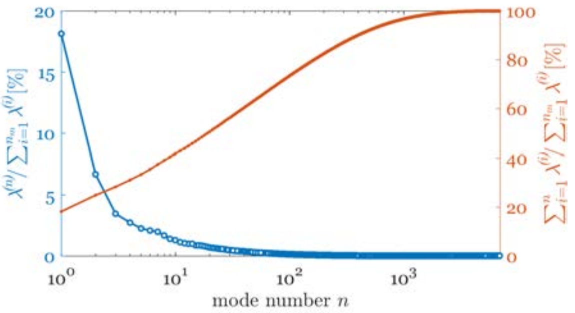

Fig. 7.1 Energy spectrum and cumulative energy contribution of the flow field modes of the channel simulation.

7.3 Method validation

The method is applied to synthetic and experimental data using a Direct Numerical Simulation (DNS) dataset and an experimental PIV test case. The DNS dataset includes fields from numerical simulations in a channel at friction Reynolds number $Re_\tau \sim 1000$ (centerline Reynolds number $Re_c = 2.2625 \times 10^4$, Li et al., 2008, Yu et al., 2012a). This dataset has been chosen since the spectrum of a fully turbulent wall bounded flow without any dominant shedding frequency poses an extremely challenging environment for the present technique. Moreover, the absence of noise contamination and the high spatial resolution of the DNS database allows assessing the sole effect of the correlation between field measurements and point measurements. The assessment on experimental data is carried out using data of a time-resolved PIV experiment. Time-resolved probes are extracted considering localized grid points as pseudo-probes, while a non-time resolved PIV sequence is obtained via down-sampling (as done by Tu et al., 2013). The PIV snapshots are collected in the wake of a NACA0012 2D wing at angle of attack equal to 15° and chord based Reynolds number equal to 1800. This dataset is characterized by a clear vortex shedding (even though still involving a range of scales after the break-up of the wake vortices), which is well resolved with the PIV, thus allowing for a strong correlation between the field measurements and the probe measurements. The limited number of snapshots supposes a further challenge due to the poorer statistical convergence of the dataset and the noise contamination of the modes.

7.3.1 DNS test case

A virtual stereo PIV experiment has been simulated using the velocity field of the Channel Flow DNS database contained in the John Hopkins Turbulence Databases (`http://turbulence.pha.jhu.edu/`). For more details about the Channel Flow DNS, see §3.4.1. The three components of the velocity field were extracted over a square $h \times h$

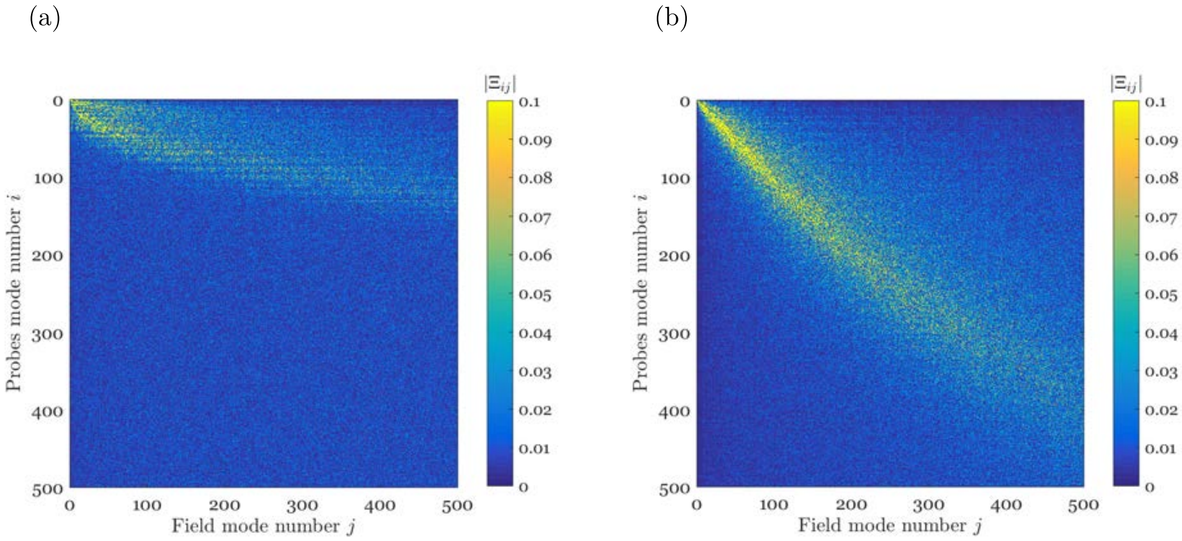

Fig. 7.2 North-West corner of the time coefficients correlation matrix $\underline{\underline{\Xi}}$ for a probe acquisition time of 1 convective time h/U_b: (a) 3 probes and (b) 11 probes. The symbol i indicates the number of POD mode of the probes, while j indicates the number of POD mode of the field measurements.

domain (going from the wall to the centerline) in the $x - y$ plane to simulate a PIV snapshot. The methodology applied for the extraction of the sub-domains is similar to that of the synthetic test case reported in Chapter 3. Snapshots were extracted one each convective time h/U_b in order to reduce the temporal correlation between them. Due to the limited temporal duration of the simulation, a maximum of 24 uncorrelated snapshots at different temporal position and in the same spatial position can be extracted, which is not enough to reach the statistical convergence of the dataset. In order to obtain a well-converged dataset, sequences of temporally-separated flow field snapshots were extracted at different spatial positions, exploiting problem symmetry, spatial homogeneity and statistically stationary state. In particular, slices were extracted in 80 span-wise locations both at the beginning and at half channel stream-wise length, both at the bottom and upper side of the channel over 24 instants. The spacing in both space and time between snapshots has been chosen to minimize their correlation. A sketch of the DNS domain slicing is given in Fig. 3.1. A total of 7680 snapshots with 88 × 88 points (along the channel height and in the stream-wise direction) were used. The slices size, from the wall up to half channel height, allows to identify adequately the main flow structures present in the flow field under study.

The probes data were obtained probing the three velocity components at 11 points equally spaced from the wall up to the channel centerline between 0.05 h and 0.95 h.

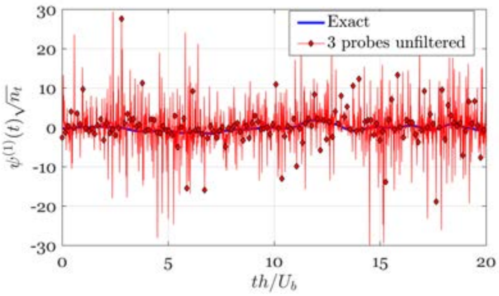

Fig. 7.3 Temporal evolution of the time coefficients of the first mode estimated with three probes, using a sampling length of one convective time. No truncation is performed on the time-coefficients correlation matrix.

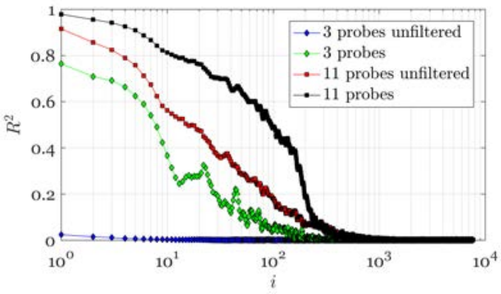

Fig. 7.4 Squared correlation coefficient of the reconstructed time coefficient series with the ground truth solution for the case of sampling length equal to h/U_b and for different number of probes.

For each snapshot the corresponding probes were placed at the same span-wise locations as the corresponding slice and at a stream-wise location immediately downstream of the slice domain. For each flow field snapshot, each probe sequence included 880 time samples during the 1.25 convective times h/U_b starting after the time instant corresponding to the flow field snapshot. Consequently the probes frequency was arbitrarily set in order to obtain 704 time instants for each turnover time, i.e. with time spacing approximately equal to the DNS time step.

This well statistically converged dataset was used to estimate the snapshot modes $\underline{\underline{\Sigma}}\ \underline{\underline{\Phi}}$. Figure 7.1 reports both the modes energy distribution ($\lambda^{(i)} = \sigma^{(i)\,2}$) and the cumulative energy content for the flow field snapshots. High energy contribution is due to the first modes corresponding to the large scale motions (Liu et al., 2001) while following modes have a lower energy contribution. Owing to the wide range of spatial scales, a high number of modes (about 400) is needed to reach 90% of the cumulative energy spectrum.

The probes signal was used to estimate the probes modes $\underline{\underline{\Sigma}}_{pr}\ \underline{\underline{\Phi}}_{pr}$ and the time-coefficients correlation matrix $\underline{\underline{\Xi}}$. The effect of the number of probes and of the temporal length of the sequence was analysed using all 11 probes and a restricted set of 3 probes (using the probes located closer to the wall, closer to the channel centerline and in the center of the domain) over 1 convective time h/U_b. The effect of the probes snapshot length is further addressed using 11 probes over 0.75, 1 and 1.25 convective times h/U_b.

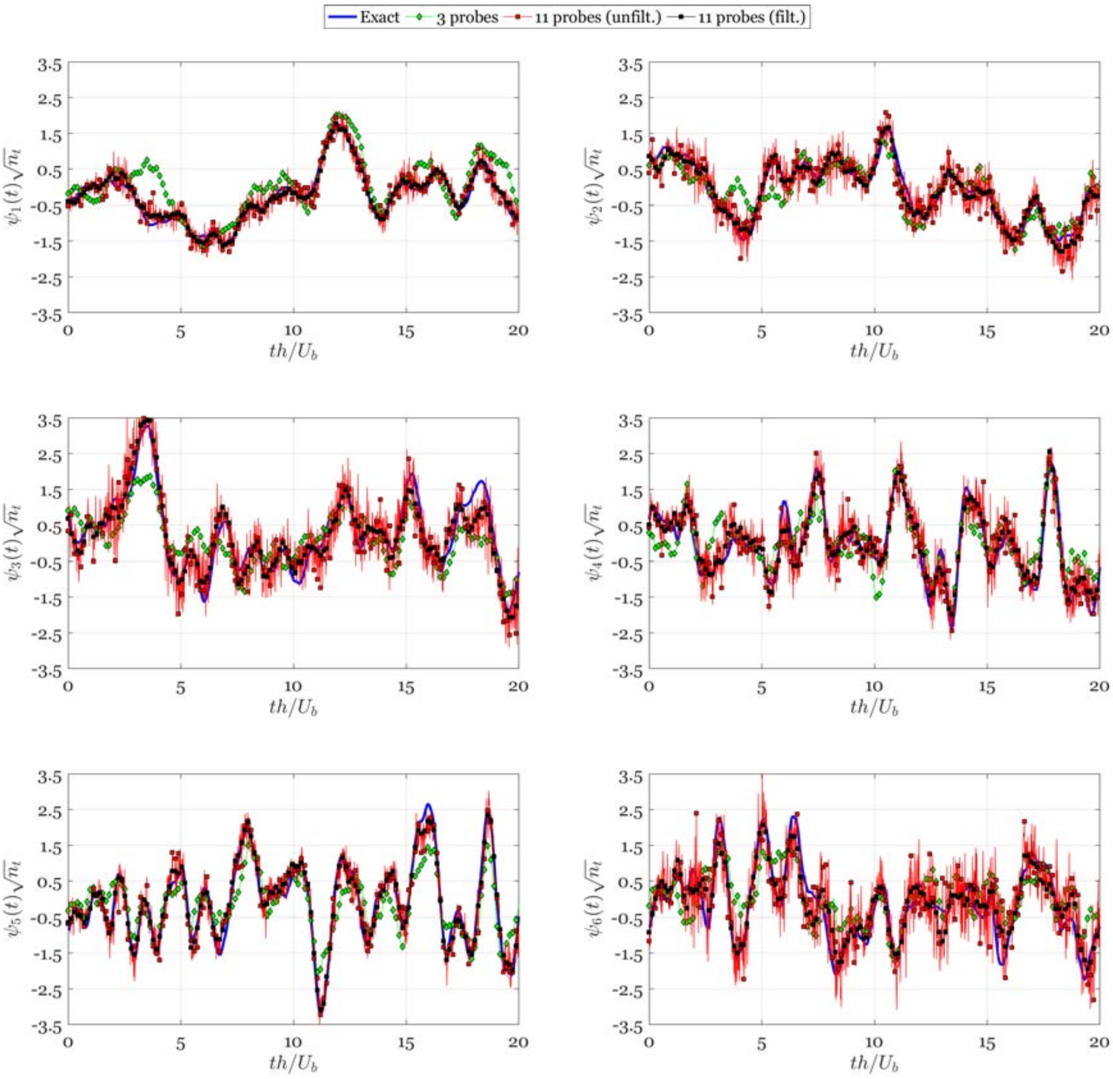

Fig. 7.5 Temporal evolution of the time coefficients of the first 6 modes obtained with sampling time equal to h/U_b for different number of probes.

Figure 7.2 reports the contour plot of the north-west corner of the matrix $\underline{\underline{\Xi}}$ estimated with probes signal from 3 (Figure 7.2a) and 11 probes (Figure 7.2b). The flow field estimation task would be straightforward and noise-free if the matrix $\underline{\underline{\Xi}}$ would be diagonal, i.e. if the problem would be characterized by a biunivocal correspondence between probes and field modes. The matrix, however, exhibits a diagonal dominance in the north-west corner, corresponding to high energy probes and field modes; moving along the diagonal towards the matrix center (for increasing number of modes) this dominance disappears. Using only 3 probes the diagonal dominance of the $\underline{\underline{\Xi}}$ matrix is lost beyond the 100th probe mode while a wider range of diagonal dominance is

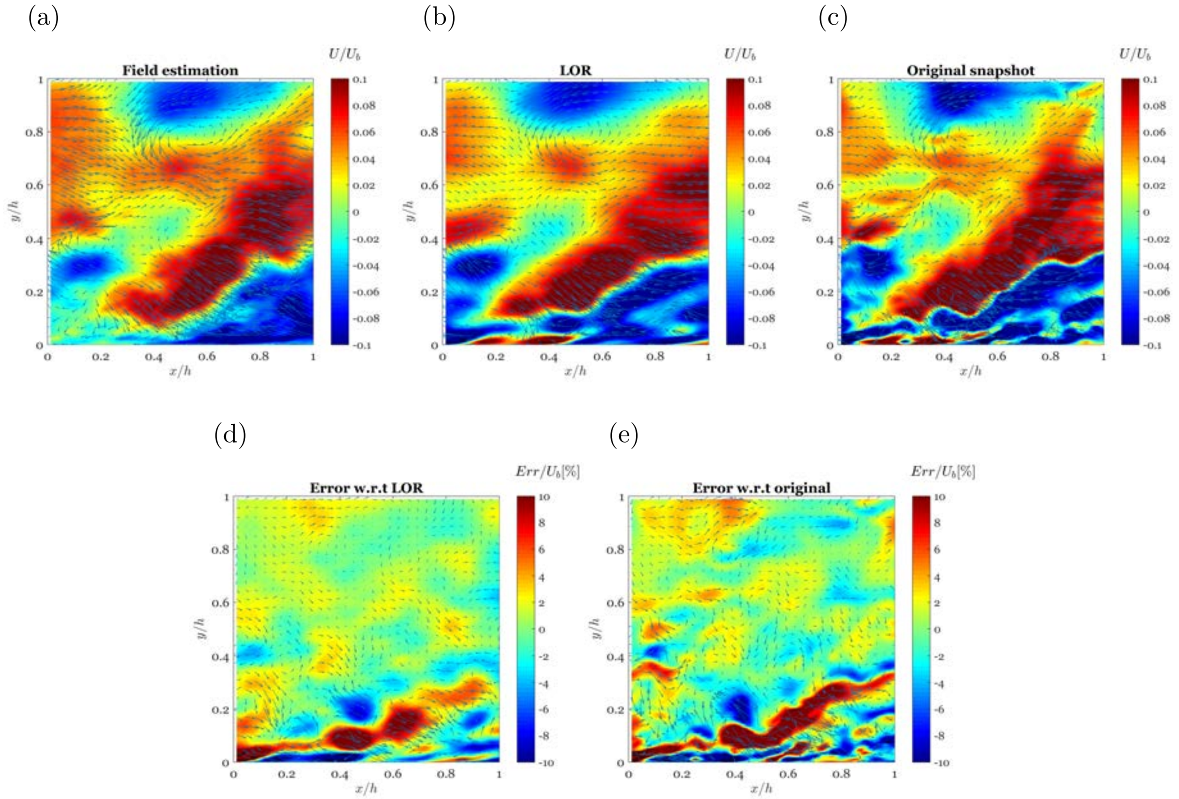

Fig. 7.6 Contour plot of fluctuating stream-wise velocity component with superimposed (down-sampled) vector arrows. Top: comparison of the dynamic reconstruction of the flow field (a) against the exact flow field (c) and the exact low-order reconstruction with the same mode truncation (200 modes) as the dynamically estimated flow field (b). Bottom: reconstruction error distributions in percentage with respect to the LOR (e) and to the original field (e).

attained for the case with 11 probes. This has to be ascribed to the better spatial sampling of the 11 probes case which captures modes with smaller wavelengths.

A time sequence with a length of 25 convective times h/U_b was acquired at a fixed location for both the probes and the slices. The chosen region is different from any of the ones used to estimate the modes. It is located at a stream-wise coordinate $x/h = 0$ and at a span-wise location equal to $z/h = 0.1$. Therefore all fields have to be considered as "out-of-sample". Time resolved probes were used to perform the flow field estimation at each instant of the time sequence and the available exact velocity fields were used as ground truth for comparison. The effects of the poor diagonal behaviour shown by the matrix $\underline{\underline{\Xi}}$ for the 3 probes case are evident from Figure 7.3 which reports the time coefficients of the first mode $\psi^{(1)}_{DYN}(t)$ estimated without any truncation on the matrix $\underline{\underline{\Xi}}$. The dynamically-estimated time coefficients are compared with the true time coefficients, computed by projection as $\psi^{(i)}_{true}(t) = \underline{u}(t)\underline{\phi}^{(i)\,T}\sigma^{(i)\,-1}$ with $\underline{u}(t)$ being the true velocity field at the time t (and represented as a vector with size $1 \times n_p$). The estimation of the time coefficients appears to be noise-dominated. The flow field estimation, in fact, here converges to a LSE which is not able to capture the flow evolution since spurious effects due to the contamination of uncorrelated higher-order modes affects even the most energetic mode.

This phenomenon can be synthesized through the representation of the squared correlation coefficient R^2 of the modes time coefficients, defined as:

$$R^2(i) = \frac{\langle(\psi_{i,DYN}(t)\psi_{i,true}(t))\rangle^2}{\left\langle(\psi_{i,DYN}(t))^2\right\rangle\left\langle(\psi_{i,true}(t))^2\right\rangle} \tag{7.9}$$

where angular brackets indicate ensemble averaging. The squared correlation coefficient is reported in Figure 7.4 against the mode number for 3 and 11 probes both with and without truncation on the uncorrelated elements of $\underline{\underline{\Xi}}$. Here, again, the true time coefficients are estimated as done for the first mode. Increasing the number of probes significantly improves the squared correlation coefficient and thus the quality of the flow field estimation, thus justifying the choice by Kerhervé et al. (2017) of using more than 100 probes. However, it is remarkable that, by means of the truncation on $\underline{\underline{\Xi}}$, acceptable results are recovered also for the set with only 3 probes.

When using 11 probes the already satisfactory estimation is significantly improved by the truncation, allowing for a squared correlation coefficient greater than 0.5 for the 100th mode. A visual representation of the estimation quality is assessed in Figure 7.5 which reports the time coefficients estimated with 3 and 11 probes against the true solution. Data is reported for 3 probes only for the truncated version of $\underline{\underline{\Xi}}$ while for 11 probes both the time coefficient for truncated and non-truncated $\underline{\underline{\Xi}}$ are reported. Both with 3 and 11 probes the signal reconstruction is quite satisfactory, however the non-truncated estimation with 11 probes exhibits spurious high frequency content, probably ascribed to contamination from uncorrelated modes; the truncated case with 3 probes, instead presents a smoother time-coefficient history with only minor errors.

Fig. 7.6 provides a visual representation of the flow field reconstruction quality attained with 11 probes and truncating $\underline{\underline{\Xi}}$. The contour of the reconstruction of the fluctuating stream-wise velocity component with superimposed vector arrows is reported for one single snapshot (Fig. 7.6a). The true flow field is reported for comparison (Fig. 7.6c), as well as the exact reconstruction of the flow field truncated at 200 modes (Fig. 7.6b). The LOR truncation at 200 modes can be assumed to be comparable to the

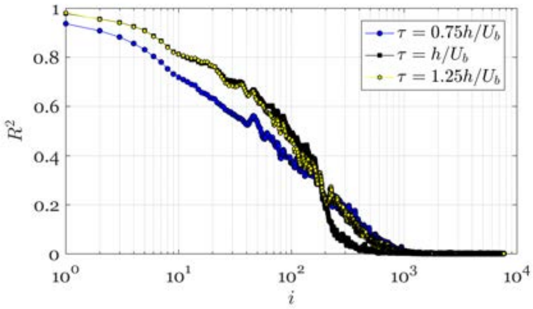

Fig. 7.7 Squared correlation coefficient of the reconstructed time coefficient series with the ground truth solution for the case with 11 probes and different probes sampling time equal to 0.75, 1 and 1.25 h/U_b.

filtering on Ξ, since the squared correlation coefficient falls below 0.3 after the 200th temporal mode (as shown in Fig. 7.4).

The error maps reported in Figure 7.6d and Figure 7.6e show that the method correctly estimates the large scale features located sufficiently far from the wall (for $y/h > 0.4$ the error is about ±2% of the bulk velocity). Small scales located nearby the wall are instead estimated with a larger error (for $y/h < 0.4$ the errors reach peaks of the order of ±10%). The higher error for small wall-near scales is only marginally affecting the quality of the proposed reconstruction, which is mainly focused to the estimation of large-scale structures in the flow. The poorer estimation nearby the wall might be ascribed to three reasons:

1. the lower convective velocity of near wall flow structures which might not reach the probes location during the probes sampling time;
2. the highly three-dimensional flow field nearby the wall which might cause these flow features to never be convected towards the probe location since they leave the flow field slice.
3. smaller structures are characterized by smaller turnover times and their convective velocities are affected by the larger scales, thus reducing the correlation between field measurements and point measurements. In this sense recent works have shown that the Taylor's hypothesis is not applicable for near-wall structures (Geng et al., 2015).

While the issue of three-dimensionality can be solved as done by Kerhervé et al. (2017) by placing the probes in multiple spanwise planes, the fact that different eddies have different convective velocities poses a question on the most suitable choice for the probe sampling time. This issue was solved by Hosseini et al. (2015) for cases in which a clear shedding is identified by choosing for the virtual probes a timespan equal to the vortex shedding period. For turbulent flows in which no dominating frequencies are present a more suitable choice appears to be connected with the convection time through the field measurement domain. In particular Figure 7.7 reports the squared correlation coefficient of estimated modes time coefficients against the mode number for varying probe sampling time equal to 0.75, 1 and 1.25 h/U_b. The results show that it is fundamental to select a probe time span equal to at least the time needed for all the information in the field to pass through the probe location. It has to be underlined that a time span slightly larger than one simple convective time might be partly beneficial since it might improve the correlation between field data and probes close to the wall, where the local convective velocity is lower. Adaptive approaches might be suggested using different time series lengths according to the local value of the time-average velocity.

Finally, it should be highlighted that in the present validation the probe signal is constituted of velocity point measurements, which simulate hot-wire probes inside the flow. The use of velocity probes is not the most common configuration for both flow sensing/control, preferring a more suitable (from a purely experimental point of view) configuration with wall-mounted pressure probes. The estimation of the flow field dynamics through wall-mounted pressure probes is possible for flows with a significant imprint of large-scale structures on the wall. Few examples are the test cases proposed by Sicot et al. (2012), investigating the separating/reattaching flow on a thick plate with sharp leading edge, and by Hosseini et al. (2015) with the shedding wake of a wall-mounted pyramid obstacle. For large scale motion estimation in wall-bounded flows (such as the channel flow here reported) a similar setup is not optimal since the correlation of the wall pressure fluctuations with the large scale structures in the outer boundary layer is expected to be rather weak. As a matter of fact, in wall-bounded flows, near-wall features are mostly characterized by an amplitude modulation of high frequency events rather than by a linear relation between large wavelength events (see e.g. the seminal works by Marusic et al., 2010, and Mathis et al., 2013). This suggests that, perhaps, in this case the extended POD should be performed between the spatial modes of the velocity fields and modes of the near wall fluctuations expressed in the Fourier space (analogously to what done for instance by Baars and Tinney, 2014).

7.3.2 Experimental test case

The experimental database is generated using time-resolved PIV data collected in the wake of a NACA0012 2D wing in stall conditions. The experiment is carried out in the recirculating water tunnel of the *Universidad Carlos III de Madrid*. For details about this facility the reader should refer to §6.2. The wing chord is $c = 30\,\mathrm{mm}$ and spans the test section from side-to-side in order to minimize 3D flow effects. The free-stream velocity has been tuned to 0.06 m/s, which results in a Reynolds number, based on the wing chord, of 1800. The wing is set to an angle of attack of 15° to promote the formation of a complex separated flow in the wake including a dominant vortex shedding with additional smaller scales turbulence. The observation region extends from approximately 1.5 to 5.5 chords in the stream-wise direction (measured from the wing leading edge) and from -1.2 to 2 chords in the cross-wise direction.

A schematic of the PIV experimental setup is reported in Fig. 7.8. The particles used for seeding the flow are neutrally-buoyant polyamide particles with 56 µm diameter. A dual cavity pulsed Nd:Yag Quantel Evergreen laser (200 mJ=pulse at 15 Hz), reshaped in a sheet with 1 mm thickness, illuminates the observation region. The recording device is a 5.5 Mpixels Andor sCMOS camera, with 6.5 µm pixel pitch. The camera is equipped with a 100 mm Tokina objective set at f/#=11. The magnification is approximately 0.06, thus leading to a resolution of about 9.1 pix/mm. A set of 27000 PIV snapshots has been collected at a frequency of 30 Hz by setting the time separation of the two laser heads at 1/30 s (which represent the limit sampling frequency for the PIV system employed). With the adopted imaging, flow speed and sampling rate, the particle displacement in the images is of almost 20 pixels and allows for time resolved estimation of the velocity in the airfoil wake. The maximum displacement of 20 pixels results in strong particles displacement gradients, thus reducing the correlation quality and resulting in velocity fields with significant noise contamination (Westerweel, 1997). The relatively large displacement is due to repetition rate limitations of the used laser source. Nonetheless the consequent signal degradation is exploited to isolate the effects of the noise contamination and poor convergence in a test case in which there is a less reach wealth of scales with respect to the synthetic validation (being the wake dominated by vortex shedding), and thus the correlation between probe signal and velocity fields is much stronger (provided that the probes are located within the shedding wake).

PIV processing was performed after background removal (see Chapter 4 or Mendez et al., 2017) with the PIV code developed at the University of Naples (Astarita, 2006, 2007) with final interrogation window size equal to 64 x 64 pixels at 75% overlap, resulting in a resolution of 17 vectors/chord.

From the full set of 27000 PIV snapshots, 334 velocity field snapshots are extracted, equally spaced in time, down-sampled by a factor of 80 with respect to the original time-resolved data. The set of 334 velocity field snapshots is assumed to be a virtual non-time-resolved field measurement employed for the dynamic estimation of the

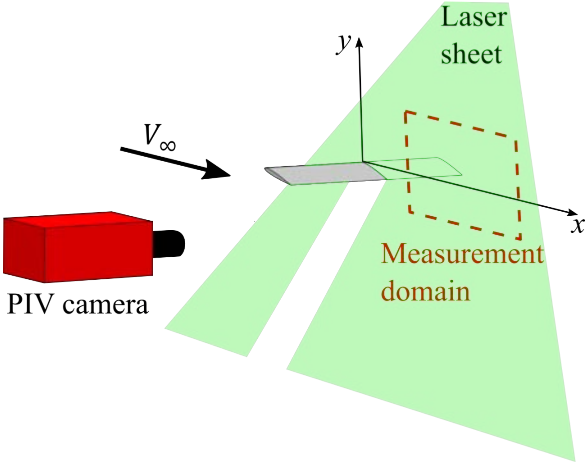

Fig. 7.8 Sketch of the PIV experimental setup.

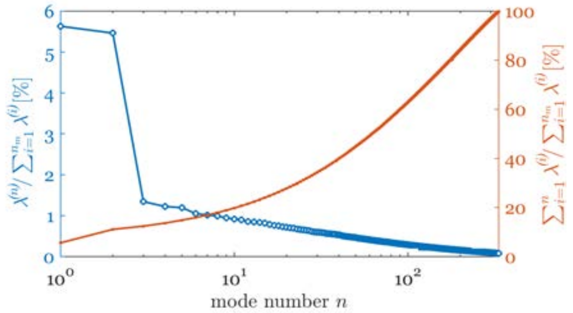

Fig. 7.9 Energy spectrum and cumulative energy contribution of the flow field modes of the experimental test case.

turbulent field. Pseudo-probes are located in the wake of the wing and generated by extracting velocity vectors with the original time resolution (i.e. $s = 80$ and $n_{tt} = m \times 80$) while the original PIV snapshots are used as a ground truth to assess the quality of the dynamic estimation of the flow fields. Two pseudo-probes have been used, located at $y/c = -0.3$ and $y/c = -0.7$, at the same stream-wise position $x/c = 5.25$. The choice of the downsampling rate and of a time span for the probes snapshot matrix equal to 80 PIV snapshots is ascribed to the convective velocity in the wake. Assuming a displacement in the wake of approximately 15 pixels between each PIV snapshot, a time span of 80 snapshots leads to a displacement of 1200 pixels in the stream-wise direction, which is the stream-wise length of the observed region. The selected timespan allows to include in the rows of the probes snapshot matrix all the information included in the corresponding PIV snapshots. This choice is following the guidelines obtained in §7.3.1. The resulting probe snapshot matrix U_{pr} contains $334 \times (m \times s)$ elements, being $m = 2$ and $s = 80$.

The spectral distribution of the energy of the POD modes is shown in Fig. 7.9. The first two modes, corresponding to the vortex shedding, are energetically dominant. The

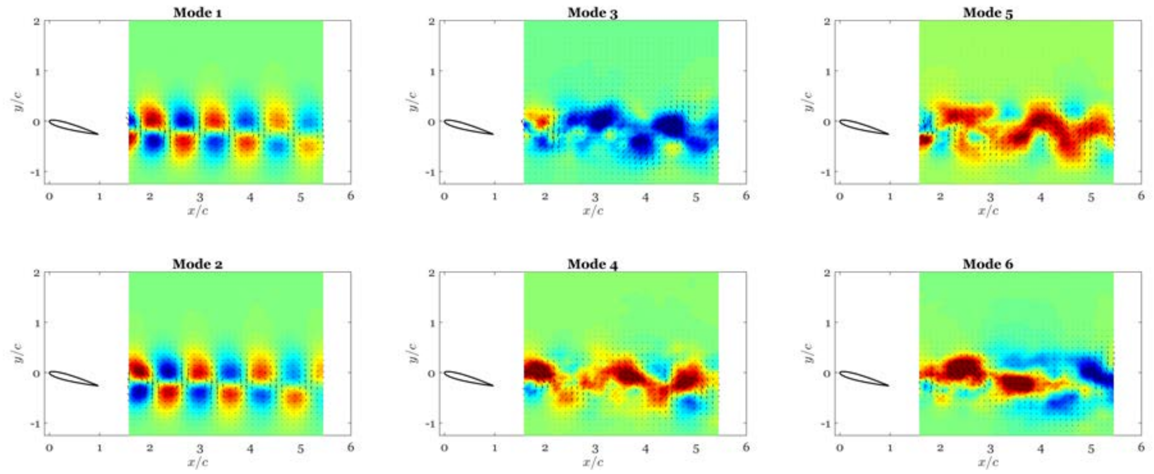

Fig. 7.10 Contour plot of the stream-wise velocity component of the first 6 flow fields modes with superimposed (down-sampled) vector arrows.

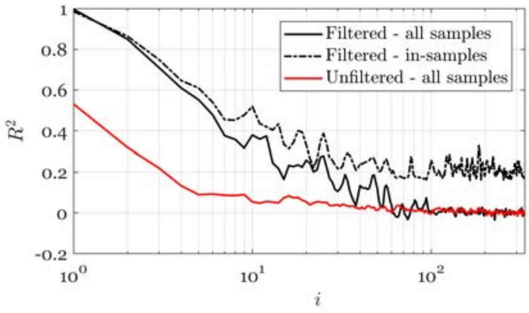

Fig. 7.11 Squared correlation coefficient between dynamically estimated time coefficient and original time coefficients of the PIV sequence. The squared correlation coefficient is calculated in the time instants of the used PIV samples.

modes spectrum falls rapidly in intensity, until reaching nearly constant eigenvalues due to the strong noise contamination (see e.g. Chapter 3 or Raiola et al., 2015).

The first 6 flow field spatial modes (evaluated over only 334 snapshots in order to simulate a real non-time-resolved experiment) are reported in Fig. 7.10. While the first two modes describe the shedding in the wake of the stalled airfoil, higher order modes have not yet reached a full statistical convergence. In particular modes 4 and 5 are poorly converged as they seem to represent a higher frequency component of the shedding phenomenon (i.e. higher order harmonics, similarly to what observed in the wake of a cylinder in Chapter 5 and by Raiola et al., 2016) although partially contaminated by cross-talk with higher order modes.

Fig. 7.11 reports the squared correlation coefficient of the estimated POD time coefficients with respect to the true temporal variation of the POD time coefficients. The squared correlation coefficient is evaluated using the reconstructed time coefficients of the entire sequence, including both in-sample (i.e. used for the POD calculation)

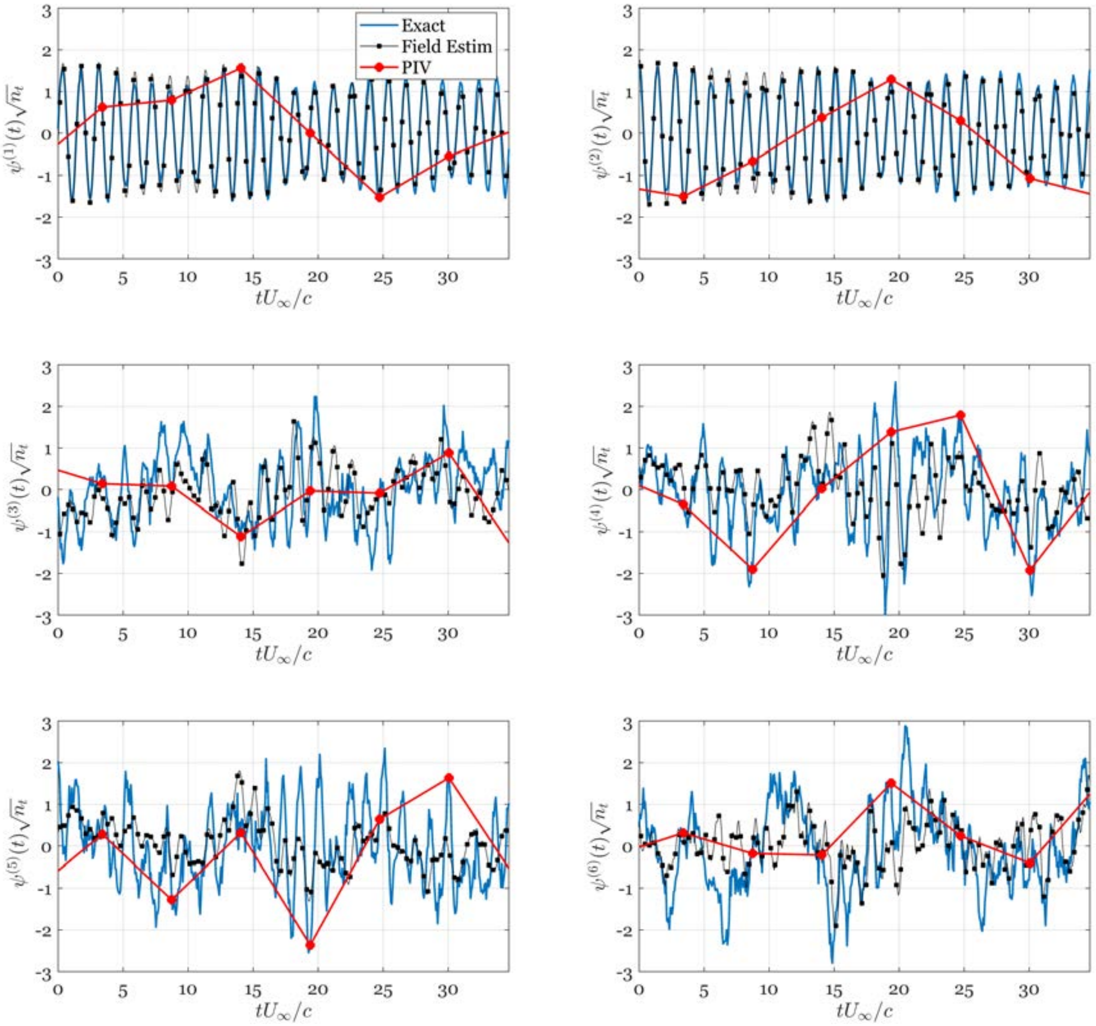

Fig. 7.12 Time coefficients of the true measured signal, of the dynamic estimation and of the subsampled PIV sequence.

and out-of-sample (i.e. not used for the POD calculation) snapshots. The improvement using the $3\sigma_{std}$ approach is remarkable, allowing to use up to 25 modes if a threshold of 0.2 is set on the squared correlation coefficient (while for the unfiltered approach only 3 modes should be included under the same criteria).

It is important to underline that in a real experiment a ground truth is not available for out-of-sample snapshots. In-sample snapshots do not allow a direct application of the squared correlation coefficient as a metric for reconstruction accuracy quantification, since indeed using all modes would provides a perfect reconstruction for the in-sample snapshots, i.e. $R^2 = 1$. The available alternative with experimental data is to eliminate from the sequence part of the samples, and use them as fictitious out-of-sample

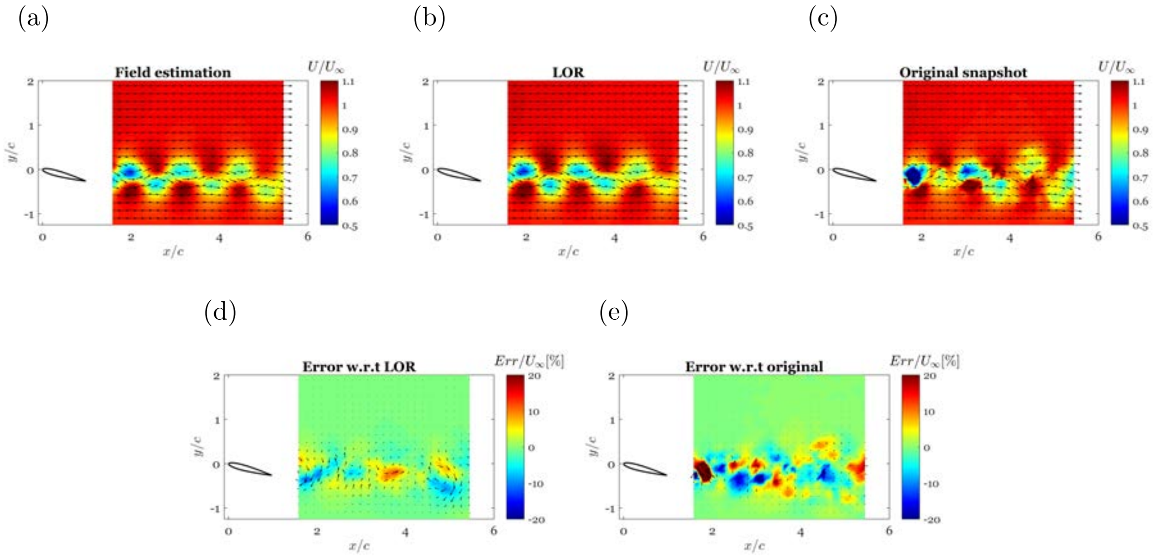

Fig. 7.13 Contour plot of stream-wise velocity component with superimposed (down-sampled) vector arrows. Top: comparison of the dynamic reconstruction of the flow field (a) against the exact flow field (c) and the exact low-order reconstruction with the same mode truncation (20 modes) as the dynamically estimated flow field (b). Bottom: reconstruction error distributions in percentage with respect to the LOR (e) and to the original field (e).

snapshots for comparison. In some cases this approach might pose convergence issues (consider for instance short duration experiments due to facilities limitations). The results of Fig. 7.11 show that the squared correlation coefficient applied on in-sample snapshots using the $3\sigma_{std}$ filtering is still an indicative figure of merit, thus providing a useful assessment instrument also for short sequences. Nonetheless, it has to be underlined that the squared correlation coefficient obtained with in-sample data is still slightly larger than the real one, thus requiring a stricter cutoff on the number of modes to reduce noise contamination of the reconstructed time coefficients history.

The reconstruction quality can be assessed through the observation of Fig. 7.12 and Fig. 7.13. Fig. 7.12 reports the POD modes time coefficients estimated (with black markers and black line) against the original values (in blue line) and the samples used to build the original snapshot dataset (in red markers connected through red lines). The proposed methodology is able to reconstruct events with a frequency far beyond the Nyquist limit and results are satisfactory both for time-periodic modes (modes 1 and 2) and non-periodic modes (modes 3-6). As expected, the estimation quality drops with respect to the channel DNS database due both to the decrease of the number of snapshots (and consequent increase of $1/\sqrt{n_t}$), which imposes a stronger truncation on the matrix $\underline{\underline{\Xi}}$, and to the increase of measurement noise which causes a poorer statistical convergence of the POD modes. It is possible to argue that a longer time-sequence would increase the estimation quality. In fact, as discussed in Chapter 3 (see also Raiola et al., 2015) noise contamination can be reduced by increasing the number of snapshots used, here limited by memory storage restriction when working with time-resolved sequences.

A visual representation of the reconstruction quality can be seen in Fig. 7.13 which reports the reconstruction of one single snapshot (Fig. 7.13a) against the true flow field (Fig. 7.13c) and the exact reconstruction of the flow field truncated at 20 modes (Fig. 7.13b). The errors with respect to the truncated LOR and the original field reported in Fig. 7.13d,e, respectively, shows that the discrepancy is mostly due to the truncation of the smaller scales of the shedding. Indeed the error with respect to the original field which contains the small scales is significantly higher that the error with respect to the LOR. The poor convergence of the modes 4 and 5 and consequently their poor dynamic estimation is the cause of the errors in the quantification of the velocity fluctuations in the wake. Although the shedding frequency is perfectly identified, the lack of convergence of higher order modes causes a modulation in the estimation of the wake deformation.

7.4 Conclusions

A robust and easy-to-implement method for the estimation of flow fields using synchronized acquisition with fast probes (such as hotwires) and non-time-resolved field measurement techniques (such as PIV) for turbulent flows has been assessed. The method poses its foundations on the work by Hosseini et al. (2015), which is improved here by truncating the time correlation matrix between temporal modes of the flow field measurements and of the probes measurements. The rationale behind the truncation is in the random distribution of noise and uncorrelated field-probes measurements. Using a standardized $3\sigma_{std}$ criterion, a robust approach is proposed, which is applicable for flows involving a significative spectral richness.

The method has been validated with a synthetic test case, based on DNS data of a turbulent channel flow, and with an experimental test case of the wake of an airfoil in stall conditions. The proposed dynamic estimation method has proved to be able to properly capture the dynamics of the large-scale structures via estimating the time coefficients of the most energetic POD modes. Two aspects arose from the validation of the filtering approach:

1. When building the probes snapshot matrix, the choice of the timespan of the probes data corresponding to each field snapshot has to be similar to the time needed to convect all the information contained in the field snapshots to the probe location. This depends on the probe location (either past the field or embedded in it). In case of a preferential direction of the mean flow this timespan might be trivially equal to the length of the domain divided by the mean convection velocity. In case of strong mean velocity gradients or in absence of a preferential direction of the mean flow, an adaptive-probe timespan might be a suitable solution. This aspect might be object of future studies;

2. When dealing with turbulent flows, thus without any dominant shedding frequency, truncation of the time correlation matrix allows to reduce significantly the time-jittering in the rebuilt history of the time coefficients, and to remarkably improve the reconstruction quality also for a small number of probes. This filtering is fundamental for turbulent flows, where uncorrelated small scale features contribute in contaminating the time correlation matrix, and consequently, the field estimation. While this filter is of simple implementation for the extended POD case, it is not trivial to include it in the LSE, which is instead strongly dependent on a proper statistical convergence of the correlation between the quantities to be measured.

This second point reflects directly in the experimental test case, where a small set of snapshots is used for the dynamics reconstruction in the separated wake of a stalled airfoil. Considering the poor convergence of the POD modes, the time correlation matrix filtering with the $3\sigma_{std}$ criterion has shown to significantly improve the quality of the reconstructed time coefficients history. Additionally the filtered data can be used to evaluate the squared correlation coefficient of the modes time coefficients directly on the in-sample data. This is potentially useful in case of short time sequences, in which in-sample snapshots can not be extracted to benchmark the reconstruction without affecting the convergence itself.

Part V

Final remarks

Chapter 8

Conclusions

8.1 Summary

In this dissertation a showcase of applications of the Proper Orthogonal Decomposition developed by the author and coworkers has been reported. On the author judgement, these applications have a potential impact in the field of Experimental Aerodynamics, both for data conditioning and reduction.

Some of the applications reported in this manuscript can be used to improve data quality. The applications reported herein focus prevalently on Particle Image Velocimetry (PIV), an optical velocity measurement technique. PIV is a well-assessed instrument for turbulent flows investigation thanks to its capability to measure velocity at multiple spatial positions with a relatively high spatial resolution. The uncertainty of this technique is usually classified in random and bias errors, both of which may be hard to suppress in case of non-time-resolved measurements.

In Chapter 3, which reports the work published by Raiola et al. (2015), the POD is employed to reduce random errors in PIV velocity fields. The method exploits the spectral separation of coherent features in the flow -which represent the valuable part of the measured signal- from the random noise. Due to the properties of the POD eigenspectrum, the coherent part of the signal is contained in the lower-order modes, while the noise, being spectrally white, spreads all over the POD eigenspectrum. It has been demonstrated theoretically, for a sample flow field, that it is possible to set an optimal trade-off between signal recovery and noise contamination when performing a low-order reconstruction. The method described can be assimilated, for simplicity, to a low-pass filter in the POD basis. The main advantage with respect to standard filters is the compactness of the POD-basis. Since the analytical determination of the optimal number of modes depends on the knowledge of the flow field, an empirical criterion has been assessed to deduce this threshold from the eigenspectrum of the measured (and thus corrupted by random error) flow fields. The results show a significant reduction of the random error (with consequent improvement of the dynamic velocity range) if compared to standard filters.

In Chapter 4, reporting the work published by Mendez et al. (2017), the spectral separation properties of the POD are applied over a PIV image ensemble to remove background and reflections which are a source of uncertainty. The method is conceptually similar to the filter described in Chapter 3: the background and the reflections are identified as low-order features in the eigenspectrum, and thus eliminated from the images by means of a "high-pass" filter. The Proper Orthogonal Decomposition of PIV images is analysed theoretically to build a robust mathematical background of the method. The POD-based background removal method have been tested extensively. At present state, its capabilities outclass all the other background removal methods in literature.

The applications described in Chapter 3 and 4 leverage the spectral optimality of the POD to obtain more effective filtering capabilities than the ones achievable in other spectral descriptions. While this property is extremely useful for signal treatment applications, in Fluid Mechanics POD is best known for extracting coherent structures. In the non-homogeneous directions of a flow field, the description with *empirical eigenfunctions*, due to the POD optimality property, is more compact than in any other basis. In the second part of this dissertation, POD has been used in its most "traditional" framework, i.e. for modal decomposition of turbulent flows.

In Chapter 5 POD is applied to PIV measurements in the wake behind a couple of circular cylinders in tandem configuration with the additional interference of a wall. This application has been published by Raiola et al. (2016). This flow shows several modal behaviours which are related to the geometrical arrangement of the cylinders with respect to each other and with respect to the wall. In particular, the modes which describe the von Kármán shedding and the Kelvin-Helmholtz instabilities are temporally quasi-periodic. Due to the properties of the correlation matrix, the temporal modes of the POD corresponding to these features can be effectively approximated by Fourier modes. This temporal description holds also for non-time-resolved data, since POD retrieves the modes by means of a statistical approach. Therefore it is possible to recover the harmonical relation between modes by looking for Lissajous figures in the scatter plot of the temporal coefficients of different modes. As an example, it can be observed that the shedding typically found in bluff-body wakes can be represented as a travelling wave by means of two modes with the same temporal frequency but phase-shifted of $\pi/2$.

In Chapter 6, the modal analysis has been performed on the flow around an airfoil in plunging/pitching motion. This flow is characterized by a periodical separation of the boundary layer from the airfoil surface, which results in the formation of vortical structures, normally grouped under the names of Leading Edge Vortices (LEVs) and Trailing Edge Vortices (TEVs). According to the literature, these structures strongly influence the aerodynamic loads on the airfoil, leading to forces which cannot be predicted by classical aerodynamics theory. In order to deal with the moving domain (due to the airfoil motion), the velocity fields have been transformed to the non-inertial wing-fixed reference frame. The modal decomposition of the velocity field over a single phase-averaged period has been obtained through POD. This decomposition has been extended to the force measurements by means of the EPOD in order to determine the contribution of the different modes to the fluctuating part of the force. This extension is equivalent to approximate linearly the relation between the fluctuating aerodynamic force and the kinetic energy in the flow. It is shown that the majority of the force can be ascribed to only two flow features (accounting each one for several POD modes) of the flow field: a bound vortex over the wing, which accounts for the circulation of the vortical structures on the airfoil (while they are attached to its surface) and which is intimately connected to the flow acceleration imposed by the added-mass forces; a shedding-like instability which describes the roll-up in concentrated vortices of the boundary layer, thus determining the formation of the vortical features in the wake. The contribution to the force of the bound vortex feature is mainly directed orthogonally to the chord and can be effectively described by quasi-steady circulatory force models from the literature. The added-mass forces, depending on the pitching, are pointing in the chord-parallel direction. The contribution of the roll-up of vortices is mostly directed parallel to the chord and it accounts for the energy which is extracted to form the vortices in the wake of the airfoil.

Chapter 6 reports an extensive use of the EPOD, which allows to express the linear relation underlying two different sets of measurements in a POD basis. Chapter 7 deals with the identification of the correlation between two different datasets and its exploitation to estimate a flow quantity in points on the (either temporal or spatial) domain in which the measurements have not been performed. More specifically, the correlation is determined between a set of non-time-resolved field measurements (for example obtained by means of PIV) and a set of time-resolved point measurements (obtained by one or more point probes such as hotwires). The correlation of the two datasets is obtained through a modified EPOD approach, from which spurious correlation between physically uncorrelated events is removed on statistical grounds. The estimation of the velocity field has been obtained by extending the EPOD to unmeasured time instants thanks to the information of the time-resolved probe. The method has been tested over both a synthetic and a real experiment to assess its performances. It has been observed that the length of the point probes time-series used for the correlation has to be long enough to allow the convection of the information from the location of the field measurements to that of the point probes. Additionally, it has been observed that the filtering included in the modified EPOD allows to extend the estimation to turbulent flows even in absence of easily recognizable features such as, for instance, a vortex shedding.

8.2 Future work

This manuscript would not be complete without some considerations about the remaining ideas whose development has not been completed due essentially to lack of time. While these ideas are not included in this thesis, they might be research topics of the author in the near future.

In Chapter 6 it has been described a non-conventional decomposition for the unsteady aerodynamic force over a flapping wing. Rather than being based on an analytical model, this decomposition has been derived with a data-driven approach. While this decomposition is quite powerful in describing the forces, it does not provide automatically a phenomenological model. This gap has been partially filled by the author, modifying the potential models of Theodorsen and Garrick to match with the force modes extracted. The modification imposed to the potential models is based, however, on heuristic considerations and does not follow a rigorous mathematical formulation. This aspect would require further studies to set solid theoretical foundations for the proposed model and to understand minor effects, such as the ones linked to the leading edge shape. On the author opinion, a possible way to accomplish this task would be to exploit the velocity information contained in the POD modes to directly compute forces. Such approach can be carried out by applying the impulse equation (Noca et al., 1999) to the velocity POD modes to verify which are the sources of the forces in each mode. Nevertheless, this approach presents some drawbacks which should be previously fixed. The impulse equation is based on the Navier-Stokes equation formulated in an inertial reference frame. To extract useful information from the modes, the impulse equation has to be expressed in the non-inertial body-fixed frame. Also, this equation, while not requiring the pressure field in input, strongly relies on the calculation of both temporal and spatial derivatives. In order to have a sufficiently accurate estimate of the derivatives, a higher resolution of the velocity measurements should be achieved.

In both Chapter 5 and Chapter 6, the POD has been mainly employed as a mean to explore data. While this technique proved to be extremely useful to compare different experimental runs, the POD is quite limited when it comes to parametric studies. The POD can only be employed to decompose a flow field in two directions, i.e. space (without distinctions between components of the Cartesian space) and time, since it is essentially based on a 2D matrix decomposition (the SVD). The retrieved modes are therefore strictly modes of the single data sequence employed in the decomposition and cannot contain any information about the effect of additional parameters. To overcome similar limitations, a tensor decomposition might be employed, with additional parameters forming the additional dimensions of the tensor. An extension of SVD to tensors is already present in the literature (multilinear SVD, De Lathauwer et al., 2000), even if, to the author knowledge, it has not been employed in the study of fluid flows. A similar decomposition might be especially interesting for flow control applications. However, the effectiveness of a similar technique in the study of flows requires an extensive testing before it could be applied, both to verify that it can retrieve useful informations and to give a proper interpretation to tensor modes.

Chapter 9

Conclusiones

9.1 Síntesis

En esta tesis doctoral ha sido presentado un muestrario de aplicaciones de la POD desarrolladas por el propio autor y sus colaboradores. En la opinión del autor, estas aplicaciones tienen un elevado potencial de impacto en el campo de la Aerodinámica Experimental, tanto para el tratamiento de datos como para su reducción. Algunas de las aplicaciones descritas en esta tesis pueden ser usadas para mejorar la calidad de los datos. Estás aplicaciones descritas aquí están centradas principalmente en la PIV, una técnica de medida de velocidad óptica. PIV es un muy buen instrumento para el estudio de flujos turbulentos, gracias a su capacidad para medir velocidad en múltiples posiciones con una relativa alta resolución espacial. La incertidumbre de esta técnica es normalmente clasificada en errores aleatorios y sistemáticos, ambos tipos de error pueden llegar a ser difíciles de suprimir en el caso de medidas que no sean resultas en el tiempo. En el Capítulo 3, en donde es descrito el trabajo publicado por Raiola et al. (2015), la POD es empleada en reducir errores de carácter aleatorio en medidas de campos de velocidad de PIV. El método explota la separación espectral de fenómenos coherentes en el flujo –que representan el componente útil de la señal medida- con respecto al ruido aleatorio que también está incluido en la señal. Gracias a las propiedades del autoespectro de la POD, la parte coherente de la señal está contenida en los modos de orden bajo, mientas que el ruido, siendo posible considerarlo espectralmente ruido blanco, se propaga a lo largo de todo el autoespectro de la POD. En relación con ello, se ha demostrado de manera teórica que para una muestra de un campo fluido es posible alcanzar un compromiso óptimo entre el grado de reconstrucción de una señal y la cantidad de ruido presente en ella, a la hora de realizar una reconstrucción de orden bajo. El método descrito puede asemejarse por simplicidad a un filtro pasa bajos en una base POD. La principal ventaja con respecto al filtro estándar es la compacidad de la base de la POD. Como la determinación analítica del numero óptimo de modos depende del grado de conocimiento del campo fluido, un criterio empírico ha sido proporcionado para poder estimar este número límite con la información proporcionado por el autoespectro del campo fluido medido (siendo este afectado por errores aleatorios). Los resultados muestran una importante reducción de los errores aleatorios (con la consecuente mejora del rango dinámico de los campos de velocidad) cuando estos son comparados con los filtros estándar. En el Capítulo 4, se detalla el trabajo publicado por Mendez et al. (2017), donde las propiedades de separación espectrales de la POD son aplicadas sobre un conjunto de imágenes de PIV para quitar el fondo y las reflexiones, las cuales son una gran fuente de incertidumbre. El método es conceptualmente muy simular al filtro descrito en el Capítulo 3 el fondo de la imagen y sus reflexiones son identificadas como fenómenos de bajo orden en el autoespectro, y por tanto pudiendo ser eliminados de las imágenes filtrando como un "filtro pasa altos". La POD de las imágenes de PIV es analizada de manera teórica para desarrollar un modelo matemático robusto del método. Este filtro POD ha sido testado extensivamente en numerosas pruebas demostrando que actualmente, sus capacidades sobrepasan las de cualquier otro método descrito en la literatura. Las aplicaciones descritas en los Capítulos 3 y 4 se aprovechan de la optimización espectral de la POD para obtener filtros muchos más efectivos que otros filtros también basados en descripciones espectrales. Mientras que esta propiedad de la POD es extremadamente útil para aplicaciones relacionadas con el tratamiento de señales, en Mecánica de Fluidos la POD es más conocida por su capacidad de extraer estructuras coherentes. En las direcciones no homogéneas de un campo fluido, la descripción realizada usando autofunciones empíricas, gracias a las propiedades de la base optima de la POD, es mucho más compacta que en cualquier otra base. En la segunda parte de esta tesis, la POD ha sido usada en su contexto más "habitual", i.e. para la descomposición modal de flujos turbulentos. En el Capítulo 5 la POD es aplicada en medidas de PIV en la estela detrás de una pareja de cilindros circulares en configuración de tándem con la perturbación adicional de una pared. Esta aplicación ha sido publicada en Raiola et al. (2016). Este tipo de flujos muestran diversos comportamientos modales, los cuales están relacionados con las diferentes configuraciones geométricas de los cilindros entre ellos mismos y con respecto a la pared. Concretamente, los modos que describen la estela de von Kármán y las inestabilidades de Kelvin-Helmholtz son temporalmente cuasi-estacionarios. Como consecuencia de las propiedades de la matriz de correlación, los modos POD asociados a estos fenómenos pueden ser aproximados de manera precisa por modos de Fourier. Esta descripción temporal también es válida para datos que no sean resueltos en el tiempo, ya que la POD extrae los modos mediante una aproximación estadística. Por ello, es posible recuperar la relación armónica entre los diferentes modos buscando las figuras de Lissajous en las gráficas donde los coeficientes de tiempo de los diferentes modos son representados. Como muestra de ello, se puede observar que el desprendimiento de vórtices que se encuentra típicamente en la estela de un cuerpo no fuselado puede ser representada por una onda que viaja mediante el uso de dos modos con la misma frecuencia temporal pero desfasados $\pi/2$. En el Capítulo 6, el análisis modal ha sido realizado en el flujo alrededor de un perfil aerodinámico en movimiento de rotación y traslación vertical. Este tipo de flujo esta caracterizado por una separación periódica de la capa límite de la superficie del perfil alar, que resulta en la formación de estructuras vorticosas, normalmente agrupadas bajo el nombre de vortices del borde ataque (Leading Edge Vortices, LEVs) y vortices del borde de salida (Trailing Edge Vortices, TEVs). Acorde a la literatura, estas estructuras afectan de manera crucial a las fuerzas aerodinámicas que se producen en el perfil alar, dando como resultado fuerzas que no pueden ser predichas usando las teorías clásicas de la aerodinámica. Para poder lidiar con un dominio que está en movimiento (debido al propio movimiento del perfil alar), los campos de velocidad han sido cambiados de ejes al sistema de referencia no inercial fijo al ala. La descomposición modal de los campos de velocidad ha sido realizada sobre un periodo promediado en fase donde se ha aplicado la POD. Esta descomposición ha sido extendida a las medidas de fuerza utilizando la EPOD para poder determinar la contribución de los diferentes modos a la parte fluctuante de las fuerzas. Esta extensión es equivalente a aproximar linealmente la relación entre la parte fluctuante de las fuerzas aerodinámicas y la energía cinética del flujo. Se muestra como la mayoría de las fuerzas pueden ser adscritas a tan solo dos fenómenos del campo fluido (cada uno de ellos con varios modos POD): un vórtice ligado al ala, que explica la circulación de las estructuras vorticosas en el perfil alar (mientras que estén adheridas a la superficie del ala) y que además está conectado de manera muy cercana con la aceleración que experimenta el flujo impulsado por las fuerzas de inercia; el otro fenómeno puede ser visto como una inestabilidad que recuerda a un desprendimiento de vórtices el cual describe como se enrolla en vórtices concentrados la capa limite, determinando de esta manera la formación de estructuras vorticosas en la estela. La contribución a la fuerza del vórtice ligado al ala es principalmente dirigida de manera ortogonal a la cuerda y puede ser descrita de manera efectiva mediante modelos cuasi-estacionarios de circulación existentes en la literatura. Las fuerzas de inercia, dependiendo del movimiento de rotación, son orientadas en la dirección paralela a la cuerda. La contribución de los vórtices que se enrollan es principalmente dirigida paralela a la cuerda y tiene en cuenta la energía que se extrae para formar los vórtices en la estela del perfil alar. El Capítulo 6 describe un uso extensivo de la EPOD, que permite expresar la relación lineal subyacente entre dos conjuntos diferentes de medidas en una base POD. El Capítulo 7 trata sobre la identificación de la correlación entre dos conjuntos de datos y como aprovechar esto para poder estimar una propiedad del flujo en puntos del dominio (tanto temporales como espaciales) en donde no se han realizado las medidas. Más concretamente, la correlación es determinada entre un conjunto de medidas no resueltas en el tiempo de un campo fluido (como podrían ser medidas de PIV) y un conjunto de medidas resueltas en el tiempo puntuales (obtenidas por uno o más sensores como podrían ser sondas de anemometría caliente). La correlación de los dos conjuntos de datos es obtenida mediante una EPOD modificada, mediante la cual la correlación espuria entre eventos no correlacionados físicamente es eliminada en términos estadísticos. La estimación del campo de velocidad ha sido obtenida extendiendo la EPOD para instantes de tiempo no medidos gracias a la información resuelta en el tiempo provista por el sensor. El método ha sido probado tanto con casos sintéticos como con un experimento real para verificar su rendimiento. Se ha observado que la longitud de las series temporales del sensor que provee la información resuelta en el tiempo debe ser suficientemente grande como para permitir la convección de la información desde el lugar donde se realizan las medidas de campo fluido hasta la localización donde se sitúen los sensores. Adicionalmente, se ha observado también que el filtrado incluido en la EPOD modificada permite extender la estimación para el caso de flujos turbulentos incluso en casos donde no existan fenómenos reconocibles como podrían ser una estela de vórtices.

9.2 Perspectivas futuras

Esta tesis doctoral no podría estar completa sin realizar algunas consideraciones sobre ideas pendientes, cuyo desarrollo no ha podido ser completado debido principalmente a la falta de tiempo. Aunque esas ideas no estén incluidas en la tesis doctoral, estas quizás podrían ser futuros temas de investigación del autor en un futuro cercano. En el Capítulo 6 se ha descrito una descomposición no convencional para las fuerzas aerodinámicas no estacionarias sobre un perfil aerodinámico oscilante. Esta descomposición, más que estar basada en un modelo analítico, ha sido obtenida usando un enfoque basado en datos. A pesar de que esta descomposición es bastante potente cuando describe las fuerzas, no es capaz de proporcionar automáticamente un modelo fenomenológico.

Este vacío ha sido parcialmente llenado por el autor realizando una modificación de los modelos potenciales de Theodorsen y Garrick para hacerlos coincidir con el modelo de fuerzas extraído. La modificación impuesta a los modelos potenciales está basada en consideraciones heurísticas, las cuales no siguen una formulación matemática rigorosa. Este aspecto requeriría un estudio más detallado para poder realizar un fundamento teórico solido que permita entender pequeñas modificaciones, como podrían ser aquellas conectadas a la forma del borde de ataque. En la opinión del autor, una manera posible para lograr este objetivo podría ser utilizar el uso de la información contenida en los modos POD para directamente calcular las fuerzas. Esta aproximación puede ser llevada a cabo utilizando la ecuación del impulso (Noca et al., 1999) en los modos POD de la velocidad para verificar cuales son la causa de las fuerzas en cada modo. Sin embargo, esta aproximación presenta algunas desventajas que deberían ser arregladas previamente. La ecuación de impulso está basada en las ecuaciones de Navier-Stokes cuando son formuladas en un sistema de referencia inercial. Para extraer información útil de los modos, la ecuación de impulso debe de ser expresada en un sistema de ejes no inercial. Además, esta ecuación, aunque no requiere el campo de presiones como variable de entrada, esta influenciada de manera importante por el cálculo de derivadas tanto espaciales como temporales. Para poder estimar de una manera suficientemente precisa el cálculo de las derivadas es necesario obtener una mayor resolución en las medidas del campo de velocidad. Tanto en el Capítulo 5 como en el 6, la POD ha sido principalmente empleada como un medio para explorar los datos. A pesar de que esta técnica ha demostrado ser extremadamente útil a la hora de comparar diferentes ensayos experimentales, la POD está bastante limitada cuando se enfrenta a estudios paramétricos. LA POD solo puede ser empleada para descomponer un campo fluido en dos direcciones, p. ej. espacio (sin distinciones entre las diferentes componentes del espacio cartesiano) y tiempo, ya que esta esencialmente basado en una descomposición 2D de matrices (la SVD). Los modos obtenidos, por tanto, son modos estrictamente de la secuencia de datos empleada en la descomposición y no puede contener ningún tipo de información sobre el efecto de ningún parámetro adicional. Para poder superar este tipo de limitaciones se debería utilizar una descomposición tensorial donde los parámetros adicionales son empleados para formar las dimensiones adicionales del tensor. Una extensión de la SVD para tensores ya existe en la literatura (SVD multilineal, De Lathauwer et al., 2000), aunque hasta donde llega el conocimiento del autor, este tipo de técnica no ha sido empleada para el análisis de flujos. Una descomposición de este estilo seria especialmente interesante para aplicaciones de control de flujo. Sin embargo, para comprobar la efectividad de un método con estas características sería necesario hacer una evaluación exhaustiva antes de poder ser aplicado, tanto para verificar si su posible uso es capaz de dar información útil como para ser capaces de dar una correcta interpretación de los modos tensoriales.

References

Abram, C., Fond, B., and Beyrau, F. (2015). High-precision flow temperature imaging using ZnO thermographic phosphor tracer particles. *Optics Express*, 23(15):19453–19468.

Adrian, R. J. (1977). On the role of conditional averages in turbulence theory. *Turbulence in Liquids*, 1:323–332.

Adrian, R. J. (1991). Particle-image techniques for experimental fluid mechanics. *Annual Review of Fluid Mechanics*, 23:261–304.

Adrian, R. J. (1994). Stochastic estimation of conditional structure: a review. *Applied Scientific Research*, 53(3):291–303.

Adrian, R. J. (1997). Dynamic ranges of velocity and spatial resolution of particle image velocimetry. *Measurement Science and Technology*, 8(12):1393.

Adrian, R. J., Christensen, K. T., and Liu, Z.-C. (2000). Analysis and interpretation of instantaneous turbulent velocity fields. *Experiments in Fluids*, 29:275–290.

Adrian, R. J., Jones, B. G., Chung, M. K., Hassan, Y., Nithianandan, C. K., and Tung, A.-C. (1989). Approximation of turbulent conditional averages by stochastic estimation. *Physics of Fluids A: Fluid Dynamics*, 1(6):992–998.

Adrian, R. J. and Westerweel, J. (2011). *Particle image velocimetry*. Cambridge University Press.

Alam, M. M., Moriya, M., Takai, K., and Sakamoto, H. (2003). Fluctuating fluid forces acting on two circular cylinders in a tandem arrangement at a subcritical reynolds number. *Journal of Wind Engineering and Industrial Aerodynamics*, 91(1):139–154.

Alam, M. M. and Zhou, Y. (2007). Phase lag between vortex shedding from two tandem bluff bodies. *Journal of Fluids and Structures*, 23(2):339–347.

Algazi, V. and Sakrison, D. (1969). On the optimality of the Karhunen-Loéve expansion (corresp.). *IEEE Transactions on Information Theory*, 15(2):319–321.

Andersen, A., Bohr, T., Schnipper, T., and Walther, J. H. (2017). Wake structure and thrust generation of a flapping foil in two-dimensional flow. *Journal of Fluid Mechanics*, 812.

Andrews, C. A., Davies, J. M., and Schwarz, G. R. (1967). Adaptive data compression. *Proceedings of the IEEE*, 55(3):267–277.

Ansari, S. A., Żbikowski, R., and Knowles, K. (2006). Aerodynamic modelling of insect-like flapping flight for micro air vehicles. *Progress in Aerospace Sciences*, 42(2):129–172.

Anttonen, J. S. R., King, P. I., and Beran, P. S. (2003). POD-based reduced-order models with deforming grids. *Mathematical and Computer Modelling*, 38(1):41–62.

Arnault, A., Dandois, J., and Foucaut, J.-M. (2016). Comparison of stochastic estimation methods with conditional events optimization for the reconstruction of the flow around a supercritical airfoil in transonic conditions. *Computers & Fluids*, 136:436–455.

Ashraf, M. A., Young, J., and Lai, J. C. S. (2011). Reynolds number, thickness and camber effects on flapping airfoil propulsion. *Journal of Fluids and Structures*, 27(2):145–160.

Astarita, T. (2006). Analysis of interpolation schemes for image deformation methods in PIV: Effect of noise on the accuracy and spatial resolution. *Experiments in Fluids*, 40:977–987.

Astarita, T. (2007). Analysis of weighting windows for image deformation methods in PIV. *Experiments in Fluids*, 43:859–71.

Astarita, T. and Cardone, G. (2005). Analysis of interpolation schemes for image deformation methods in PIV. *Experiments in Fluids*, 38:233–243.

Aubry, N. (1991). On the hidden beauty of the proper orthogonal decomposition. *Theoretical and Computational Fluid Dynamics*, 2(5):339–352.

Aubry, N., Guyonnet, R., and Lima, R. (1991). Spatiotemporal analysis of complex signals: theory and applications. *Journal of Statistical Physics*, 64(3):683–739.

Aubry, N., Holmes, P., Lumley, J. L., and Stone, E. (1988). The dynamics of coherent structures in the wall region of a turbulent boundary layer. *Journal of Fluid Mechanics*, 192:115–173.

Azar, Y., Fiat, A., Karlin, A., McSherry, F., and Saia, J. (2001). Spectral analysis of data. In *Proceedings of the thirty-third annual ACM symposium on Theory of computing*, pages 619–626. ACM.

Baars, W. J. and Tinney, C. E. (2014). Proper orthogonal decomposition-based spectral higher-order stochastic estimation. *Physics of Fluids*, 26(5):055112.

Baik, Y. S., Bernal, L. P., Granlund, K., and Ol, M. V. (2012). Unsteady force generation and vortex dynamics of pitching and plunging aerofoils. *Journal of Fluid Mechanics*, 709:37–68.

Bakewell, H. P. J. and Lumley, J. L. (1967). Viscous sublayer and adjacent wall region in turbulent pipe flow. *The Physics of Fluids*, 10(9):1880–1889.

Balakumar, B. J. and Adrian, R. J. (2007). Large-and very-large-scale motions in channel and boundary-layer flows. *Philosophical Transactions of the Royal Society of London A: Mathematical, Physical and Engineering Sciences*, 365(1852):665–681.

Ben Chiekh, M., Michard, M., Grosjean, N., and Bera, J. C. (2004). Reconstruction temporelle d'un champ aérodynamique instationnaire à partir de mesures PIV non résolues dans le temps. *9ème Congrès Français de Vélocimétrie Laser, Brussels, Belgium, paper D*, 8.

Bergmann, M., Cordier, L., and Brancher, J.-P. (2005). Optimal rotary control of the cylinder wake using proper orthogonal decomposition reduced-order model. *Physics of Fluids*, 17.

Berkooz, G., Holmes, P., and Lumley, J. L. (1993). The proper orthogonal decomposition in the analysis of turbulent flows. *Annual Review of Fluid Mechanics*, 25(1):539–575.

Berman, G. J. and Wang, Z. J. (2007). Energy-minimizing kinematics in hovering insect flight. *Journal of Fluid Mechanics*, 582:153–168.

Berry, M. W., Dumais, S. T., and O'Brien, G. W. (1995). Using linear algebra for intelligent information retrieval. *SIAM review*, 37(4):573–595.

Bhattacharyya, S. and Dhinakaran, S. (2008). Vortex shedding in shear flow past tandem square cylinders in the vicinity of a plane wall. *Journal of Fluids and Structures*, 24(3):400–417.

Bishop, C. M. (2006). *Pattern recognition and machine learning.* Springer.

Bisplinghoff, R. L., Ashley, H., and Halfman, R. L. (2013). *Aeroelasticity.* Courier Corporation.

Borée, J. (2003). Extended proper orthogonal decomposition: a tool to analyse correlated events in turbulent flows. *Experiments in Fluids*, 35(2):188–192.

Boussinesq, J. (1877). *Essai sur la théorie des eaux courantes.* Imprimerie nationale.

Bouwmans, T., Sobral, A., Javed, S., Ki Jung, S., and Zahzah, E.-H. (2016). *Handbook of Robust Low-Rank and Sparse Matrix Decomposition: Applications in Image and Video Processing*, chapter Robust Principal Component Analysis via Decomposition into Low-Rank and Sparse Matrices: An Overview, page Chapter 1. CRC Press, Taylor and Francis Group.

Brunton, S. L., Rowley, C. W., and Williams, D. R. (2013). Reduced-order unsteady aerodynamic models at low Reynolds numbers. *Journal of Fluid Mechanics*, 724:203–233.

Buckingham, E. (1914). On physically similar systems; illustrations of the use of dimensional equations. *Physical Review*, 4(4):345.

Cafiero, G., Ceglia, G., Discetti, S., Ianiro, A., Astarita, T., and Cardone, G. (2014). On the three-dimensional precessing jet flow past a sudden expansion. *Experiments in Fluids*, 55(2):1677.

Cattell, R. (1966). The scree test for the number of factors. *Multivariate Behavioral Research*, 1:245–276.

Ceglia, G., Discetti, S., Ianiro, A., Michaelis, D., Astarita, T., and Cardone, G. (2014). Three-dimensional organization of the flow structure in a non-reactive model aero engine lean burn injection system. *Experimental Thermal and Fluid Science*, 52:164–173.

Chambers, D. H., Adrian, R. J., Moin, P., Stewart, D. S., and Sung, H. J. (1988). Karhunen-Loéve expansion of Burgers' model of turbulence. *Physics of Fluids*, 31(9):2573–2582.

Cierpka, C., Lütke, B., and Kähler, C. J. (2013). Higher order multi-frame particle tracking velocimetry. *Experiments in Fluids*, 54:1–12.

Da Vinci, L. (1500). *Codex Atlanticus, folio 74v.* Biblioteca Ambrosiana di Milano.

Dabiri, J. O. (2009). Optimal vortex formation as a unifying principle in biological propulsion. *Annual Review of Fluid Mechanics*, 41:17–33.

Dawson, S. T. M., Floryan, D. C., Rowley, C. W., and Hemati, M. S. (2016). Lift enhancement of high angle of attack airfoils using periodic pitching. In *54th AIAA Aerospace Sciences Meeting*, page 2069.

De Lathauwer, L., De Moor, B., and Vandewalle, J. (2000). A multilinear singular value decomposition. *SIAM journal on Matrix Analysis and Applications*, 21(4):1253–1278.

Deane, A. E., Kevrekidis, I. G., Karniadakis, G. E., and Orszag, S. A. (1991). Low-dimensional models for complex geometry flows: Application to grooved channels and circular cylinders. *Physics of Fluids A: Fluid Dynamics*, 3(10):2337–2354.

Deardorff, J. W. (1970). A numerical study of three-dimensional turbulent channel flow at large reynolds numbers. *Journal of Fluid Mechanics*, 41(2):453–480.

Deen, N. G., Willems, P., van Sint Annaland, M., Kuipers, J. A. M., Lammertink, R. G. H., Kemperman, A. J. B., Wessling, M., and van der Meer, W. G. J. (2010). On image pre-processing for PIV of single- and two-phase flows over reflecting objects. *Experiments in Fluids*, 49(2):525–530.

DeLaurier, J. D. (1993). An aerodynamic model for flapping-wing flight. *The Aeronautical Journal (1968)*, 97(964):125–130.

Dellenback, P. A., Macharivilakathu, J., and Pierce, S. R. (2000). Contrast-enhancement techniques for particle-image velocimetry. *Applied Optics*, 39(32):5978–5990.

Dickinson, M. H., Lehmann, F.-O., and Sane, S. P. (1999). Wing rotation and the aerodynamic basis of insect flight. *Science*, 284(5422):1954–1960.

Doligalski, T. L., Smith, C. R., and Walker, J. D. A. (1994). Vortex interactions with walls. *Annual Review of Fluid Mechanics*, 26(1):573–616.

Durgesh, V. and Naughton, J. W. (2010). Multi-time-delay LSE-POD complementary approach applied to unsteady high-reynolds-number near wake flow. *Experiments in Fluids*, 49(3):571–583.

Duwig, C. and Iudiciani, P. (2010). Extended proper orthogonal decomposition for analysis of unsteady flames. *Flow, Turbulence and Combustion*, 84(1):25–47.

Eckart, G. and Young, G. (1936). The approximation of one matrix by another of lower rank. *Psychometrika*, 1:211–218.

Ellington, C. P. (1984). The aerodynamics of hovering insect flight. iv. aeorodynamic mechanisms. *Philosophical Transactions of the Royal Society of London B: Biological Sciences*, 305(1122):79–113.

Everson, R. and Sirovich, L. (1995). Karhunen–Loéve procedure for gappy data. *Journal of the Optical Society of America*, 12:1657–64.

Fahl, M. (2000). *Trust-Region methods for flow control based on reduced order modeling.* PhD thesis, Trier University, Trier, Germany.

Feng, L.-H., Wang, J.-J., and Pan, C. (2011). Proper orthogonal decomposition analysis of vortex dynamics of a circular cylinder under synthetic jet control. *Physics of Fluids*, 23(1):014106.

Fey, U., König, M., and Eckelmann, H. (1998). A new Strouhal-Reynolds-number relationship for the circular cylinder in the range $47 < Re < 2 \times 10^5$. *Physics of Fluids*, 10:1547–1549.

Feynman, R., Leighton, R. B., and Sands, M. (1964). *The Feynman lectures on physics.* Addison-Wesley, Boston, MA.

Fincham, A. and Delerce, G. (2000). Advanced optimization of correlation imaging velocimetry algorithms. *Experiments in Fluids*, 29(1):S013–S022.

Fincham, A. M. and Spedding, G. R. (1997). Low cost, high resolution DPIV for measurement of turbulent fluid flow. *Experiments in Fluids*, 23:449–462.

Floryan, D., Van Buren, T., Rowley, C. W., and Smits, A. J. (2017). Scaling the propulsive performance of heaving and pitching foils. *Journal of Fluid Mechanics*, 822:386–397.

Fogleman, M., Lumley, J., Rempfer, D., and Haworth, D. (2004). Application of the proper orthogonal decomposition to datasets of internal combustion engine flows. *Journal of Turbulence*, 5(23):1–3.

Foss, J. F. (2004). Surface selections and topological constraint evaluations for flow field analyses. *Experiments in Fluids*, 37(6):883–898.

Fung, Y. C. (2002). *An introduction to the theory of aeroelasticity.* Courier Corporation.

Garrick, I. E. (1937). Propulsion of a flapping and oscillating airfoil. *NACA Report 567.*

Garrick, I. E. (1938). On some reciprocal relations in the theory of nonstationary flows. *NACA Report 629.*

Geng, C., He, G., Wang, Y., Xu, C., Lozano-Durán, A., and Wallace, J. M. (2015). Taylor's hypothesis in turbulent channel flow considered using a transport equation analysis. *Physics of Fluids*, 27(2):025111.

Gerrard, J. H. (1966). The mechanics of the formation region of vortices behind bluff bodies. *Journal of Fluid Mechanics*, 25(02):401–413.

Gharib, M., Rambod, E., and Shariff, K. (1998). A universal time scale for vortex ring formation. *Journal of Fluid Mechanics*, 360:121–140.

Giordano, R., Ianiro, A., Astarita, T., and Carlomagno, G. M. (2012). Flow field and heat transfer on the base surface of a finite circular cylinder in crossflow. *Applied Thermal Engineering*, 49:79–88.

Glauser, M. N., Zheng, X., and Doering, C. R. (1989). The dynamics of organized structures in the axisymmetric jet mixing layer. *Turbulence and Coherent Structures*, pages 253–265.

Graham, J., Lee, M., Malaya, N., Moser, R., Eyink, G., Meneveau, C., Kanov, K., Burns, R., and Szalay, A. (2013). Turbulent channel flow data set. available at http://turbulence.pha.jhu.edu/docs/README-CHANNEL.pdf.

Guezennec, Y. G. (1989). Stochastic estimation of coherent structures in turbulent boundary layers. *Physics of Fluids A: Fluid Dynamics*, 1(6):1054–1060.

Gui, L., Merzkirch, W., and Shu, J. Z. (1997). Evaluation of low image density recordings with the MQD method and application to the flow in a liquid bridge. *Journal of Flow Visualization and Image Processing*, 4:333–43.

Guo, S., Wu, X., and Li, Y. (2006). On the lower bound of reconstruction error for spectral filtering based privacy preserving data mining. *Knowledge Discovery in Databases: PKDD 2006*, pages 520–527.

Hansen, A. C. and Butterfield, C. P. (1993). Aerodynamics of horizontal-axis wind turbines. *Annual Review of Fluid Mechanics*, 25(1):115–149.

Harichandan, A. B. and Roy, A. (2012). Numerical investigation of flow past single and tandem cylindrical bodies in the vicinity of a plane wall. *Journal of Fluids and Structures*, 33:19–43.

Harris, F. D., Tarzanin, F. J., and Fisher, R. K. (1970). Rotor high speed performance, theory vs. test. *Journal of the American Helicopter Society*, 15(3):35–44.

Hart, D. P. (1996). Sparse array image correlation. In *Proceedings of 8th International Symposia on Applications of Laser Techniques to Fluid Mechanics*, Lisbon.

Harun, Z., Monty, J. P., Mathis, R., and Marusic, I. (2013). Pressure gradient effects on the large-scale structure of turbulent boundary layers. *Journal of Fluid Mechanics*, 715:477–498.

Heikkila, J. (2000). Geometric camera calibration using circular control points. *Pattern Analysis and Machine Intelligence, IEEE Transactions on*, 22(10):1066–1077.

Hey, T., Tansley, S., and Tolle, K. M. (2009). *The fourth paradigm: data-intensive scientific discovery*, volume 1. Microsoft Research, Redmond, WA.

Holmes, P., Lumley, J. L., Berkooz, G., and Rowley, C. (2012). *Turbulence, coherent structures, dynamical systems and symmetry.* Cambridge university press.

Holmes, P. J., Lumley, J. L., Berkooz, G., Mattingly, J. C., and Wittenberg, R. W. (1997). Low-dimensional models of coherent structures in turbulence. *Physics Reports*, 287(4):337–384.

Hong, J., Katz, J., Meneveau, C., and Schultz, M. (2012). Coherent structures and associated subgrid-scale energy transfer in a rough-wall turbulent channel flow. *Journal of Fluid Mechanics*, 712:92–128.

Honkanem, M. and Nobach, H. (2005). Background extraction from double-frame PIV images. *Experiments in Fluids*, 38:348–362.

Hopf, E. (1948). A mathematical example displaying features of turbulence. *Communications on Pure and Applied Mathematics*, 1(4):303–322.

Hosseini, Z., Martinuzzi, R. J., and Noack, B. R. (2015). Sensor-based estimation of the velocity in the wake of a low-aspect-ratio pyramid. *Experiments in Fluids*, 56(1):13.

Hotelling, H. (1933). Analysis of a complex of statistical variables into principal components. *Journal of Educational Psychology*, 24(6):417–441.

Huang, H. T., Dabiri, D., and Gharib, M. (1997). On errors of digital particle image velocimetry. *Measurement Science and Technology*, 8:1427–40.

Huang, Z., Du, W., and Chen, B. (2005). Deriving private information from randomized data. In *In Proceeding of the ACM SIGMOD Conference of Management of Data*, Baltimore, BA.

Igarashi, T. (1981). Characteristics of the flow around two circular cylinders arranged in tandem: 1st report. *Bulletin of JSME*, 24(188):323–331.

Jalaleddine, S. M. S., Hutchens, C. G., Strattan, R. D., and Coberly, W. A. (1990). ECG data compression techniques-a unified approach. *IEEE transactions on Biomedical Engineering*, 37(4):329–343.

Jaunet, V., Collin, E., and Delville, J. (2016). POD-Galerkin advection model for convective flow: application to a flapping rectangular supersonic jet. *Experiments in Fluids*, 57(5):1–13.

Jolliffe, I. (2002). *Principal Component Analysis.* Springer Series in Statistic. Springer-Verlag New York.

Jones, W. P. (1945). *Aerodynamic forces on wings in non-uniform motion.* HM Stationery Office.

Jovanović, M. R., Schmid, P. J., and Nichols, J. W. (2014). Sparsity-promoting dynamic mode decomposition. *Physics of Fluids*, 26(2):024103.

Kähler, C., Astarita, T., Vlachos, P. P., Sakakibara, J., Hain, R., Discetti, S., La Foy, R., and Cierpka, C. (2016). Main results of the 4th international PIV challenge. *Experiments in Fluids*, 57(6):1–71.

Kargupta, H., Datta, S., Wang, Q., and Sivakumar, K. (2003). On the privacy preserving properties of random data perturbation techniques. In *Proceedings of the Third IEEE International Conference on Data Mining*, pages 99–106. IEEE.

Kerhervé, F., Roux, S., and Mathis, R. (2017). Combining time-resolved multi-point and spatially-resolved measurements for the recovering of very-large-scale motions in high reynolds number turbulent boundary layer. *Experimental Thermal and Fluid Science*, 82:102–115.

Kirby, M. and Sirovich, L. (1990). Application of the Karhunen-Loéve procedure for the characterization of human faces. *IEEE Transactions on Pattern analysis and Machine intelligence*, 12(1):103–108.

Kleinberg, J. M. (1999). Authoritative sources in a hyperlinked environment. *Journal of the ACM (JACM)*, 46(5):604–632.

Kolmogoroff, A. (1933). *Grundbegriffe der Wahrscheinlichkeitsrechnung.* Springer, Berlin. [2nd English trans.: A.N. Kolmogorov. Foundations of the Theory of Probability, Chelsea. New York (1956).].

Kolmogoroff, A. (1941a). Energy dissipation in locally isotropic turbulence. *Doklady Akademii Nauk SSSR*, (32):19–21.

Kolmogoroff, A. (1941b). Local structure of turbulence in an incompressible fluid at very high reynolds numbers. *Doklady Akademii Nauk SSSR*, (30):299–303.

Korn, F., Labrinidis, A., Kotidis, Y., and Faloutsos, C. (1998). Ratio rules: A new paradigm for fast, quantifiable data mining. In *Proceedings of the 24rd International Conference on Very Large Data Bases*, VLDB '98, pages 582–593, San Francisco, CA, USA. Morgan Kaufmann Publishers Inc.

Landau, L. D. and Lifshitz, E. M. (1959). *Fluid Mechanics.* Pergamon Press, Oxford. (translated by J. B. Sykes and W. H. Reid from original Russian published in 1944).

Lecordier, B. and Westerweel, J. (2004). *Particle Image Velocimetry: Recent Improvements: Proceedings of the EUROPIV 2 Workshop held in Zaragoza, Spain, March 31 – April 1, 2003*, chapter The EUROPIV Synthetic Image Generator (S.I.G.), pages 145–161. Springer Berlin Heidelberg, Berlin, Heidelberg.

Legrand, M., Nogueira, J., and Lecuona, A. (2011). Flow temporal reconstruction from non-time-resolved data part I: mathematic fundamentals. *Experiments in Fluids*, 51(4):1047–1055.

Lei, C., Cheng, L., and Kavanagh, K. (1999). Re-examination of the effect of a plane boundary on force and vortex shedding of a circular cylinder. *Journal of Wind Engineering and Industrial Aerodynamics*, 80(3):263–286.

Li, L., Huang, W., Gu, I. Y.-H., and Tian, Q. (2004). Statistical modeling of complex backgrounds for foreground object detection. *IEEE Transactions on Image Processing*, 13(11):1459–1472.

Li, Y., Perlman, E., Wan, M., Yang, Y., Meneveau, C., Burns, R., Chen, S., Szalay, A., and Eyink, G. (2008). A public turbulence database cluster and applications to study Lagrangian evolution of velocity increments in turbulence. *Journal of Turbulence*, 9:N31.

Lian, Y. and Shyy, W. (2007). Laminar-turbulent transition of a low Reynolds number rigid or flexible airfoil. *AIAA journal*, 45(7):1501–1513.

Liang, Y. C., Lee, H. P., Lim, S. P., Lin, W. Z., Lee, K. H., and Wu, C. G. (2002). Proper orthogonal decomposition and its applications—Part I: Theory. *Journal of Sound and Vibration*, 252(3):527–544.

Lighthill, M. J. (1969). Hydromechanics of aquatic animal propulsion. *Annual Review of Fluid Mechanics*, 1(1):413–446.

Lin, J. H.and Perlin, M. (1998). Improved methods for thin, surface boundary layer investigations. *Experiments in Fluids*, 25(5):431–444.

Lin, W.-J., Lin, C., Hsieh, S.-C., and Dey, S. (2009). Flow characteristics around a circular cylinder placed horizontally above a plane boundary. *Journal of Engineering Mechanics*, 135(7):697–716.

Liu, Z., Adrian, R. J., and Hanratty, T. J. (2001). Large-scale modes of turbulent channel flow: transport and structure. *Journal of Fluid Mechanics*, 448:53–80.

Lumley, J. (1970). *Stocastic Tools in Turbulence.* Academic Press.

Lumley, J. L. (1967). The structure of inhomogeneous turbulent flows. In *Atmospheric turbulence and radio wave propagation*, pages 166–178.

Lumley, J. L. (1981). Coherent structures in turbulence. In *Transition and turbulence*, pages 215–242.

Mackowski, A. W. and Williamson, C. H. K. (2015). Direct measurement of thrust and efficiency of an airfoil undergoing pure pitching. *Journal of Fluid Mechanics*, 765:524–543.

Mahir, N. (2009). Three-dimensional flow around a square cylinder near a wall. *Ocean Engineering*, 36(5):357–367.

Marchenko, V. A. and Pastur, L. A. (1967). Distribution of eigenvalues for some sets of random matrices. *Matematicheskii Sbornik*, 114(4):507–536.

Martinuzzi, R. J., Bailey, S. C. C., and Kopp, G. A. (2003). Influence of wall proximity on vortex shedding from a square cylinder. *Experiments in fluids*, 34(5):585–596.

Marusic, I., Chauhan, K. A., Kulandaivelu, V., and Hutchins, N. (2015). Evolution of zero-pressure-gradient boundary layers from different tripping conditions. *Journal of Fluid Mechanics*, 783:379–411.

Marusic, I., Mathis, R., and Hutchins, N. (2010). Predictive model for wall-bounded turbulent flow. *Science*, 329(5988):193–196.

Mathis, R., Marusic, I., Chernyshenko, S. I., and Hutchins, N. (2013). Estimating wall-shear-stress fluctuations given an outer region input. *Journal of Fluid Mechanics*, 715:163–180.

Maurel, S., Borée, J., and Lumley, J. L. (2001). Extended proper orthogonal decomposition: application to jet/vortex interaction. *Flow, Turbulence and Combustion*, 67(2):125–136.

McCroskey, W. J. (1982). Unsteady airfoils. *Annual Review of Fluid Mechanics*, 14(1):285–311.

Mejia-Alvarez, R. and Christensen, K. T. (2013). Robust suppression of background reflections in PIV images. *Measurement Science and Technology*, 24:027003.

Mendez, M. A., Raiola, M., Masullo, A., Discetti, S., Ianiro, A., Theunissen, R., and Buchlin, J.-M. (2017). POD-based background removal for particle image velocimetry. *Experimental Thermal and Fluid Science*, 80:181–192.

Meneghini, J. R., Saltara, F., Siqueira, C. L. R., and Ferrari, J. A. (2001). Numerical simulation of flow interference between two circular cylinders in tandem and side-by-side arrangements. *Journal of Fluids and Structures*, 15(2):327–350.

Meyer, K. E. and Westerweel, J. (2000). Advection velocities of flow structures estimated from particle image velocimetry measurements in a pipe. *Experiments in Fluids*, Suppl.:237–247.

Mezić, I. (2013). Analysis of fluid flows via spectral properties of the Koopman operator. *Annual Review of Fluid Mechanics*, 45:357–378.

Michelis, T. and Kotsonis, M. (2015). Interaction of an off-surface cylinder with separated flow from a bluff body leading edge. *Experimental Thermal and Fluid Science*, 63:91–105.

Minotti, F. O. (2002). Unsteady two-dimensional theory of a flapping wing. *Physical Review E*, 66(5):051907.

Miranda, A. A., Le Borgne, Y.-A., and Bontempi, G. (2008). New routes from minimal approximation error to principal components. *Neural Process Lett*, 27:197–207.

Moin, P. and Moser, R. D. (1989). Characteristic-eddy decomposition of turbulence in a channel. *Journal of Fluid Mechanics*, 200:471–509.

Moriche, M. (2017). *A numerical study on the aerodynamic forces and the wake stability of flapping flight at low Reynolds number*. PhD thesis, Universidad Carlos III de Madrid.

Moriche, M., Flores, O., and García-Villalba, M. (2016). Three-dimensional instabilities in the wake of a flapping wing at low reynolds number. *International Journal of Heat and Fluid Flow*, 62:44–55.

Neal, D. R., Sciacchitano, A., Smith, B. L., and Scarano, F. (2015). Collaborative framework for PIV uncertainty quantification: the experimental database. *Measurement Science and Technology*, 26(7):074003.

Noack, B. R., Morzynski, M., and Tadmor, G. (2011). *Reduced-order modelling for flow control*, volume 528. Springer Science & Business Media.

Noca, F., Shiels, D., and Jeon, D. (1999). A comparison of methods for evaluating time-dependent fluid dynamic forces on bodies, using only velocity fields and their derivatives. *Journal of Fluids and Structures*, 13(5):551–578.

Noy-Meir, I. (1973). Trasformations in Ecological Ordination: I. Some advantages of Non-Centering. *Journal of Ecology*, 61(2):329–341.

Okamoto, K., Nishio, S., Saga, T., and Kobayashi, T. (2000). Standard images for particle-image velocimetry. *Measurement Science and Technology*, 11(6):685.

Oliver, N. M., Rosario, B., and Pentland, A. P. (2000). A bayesian computer vision system for modeling human interactions. *IEEE Transactions on Pattern Analysis and Machine Intelligence*, 22(8):831–843.

Olmos, S., Millan, M., Garcia, J., and Laguna, P. (1996). ECG data compression with the Karhunen-Loéve transform. In *Computers in Cardiology, 1996*, pages 253–256. IEEE.

Orszag, S. A. and Patterson, Jr., G. S. (1972). Numerical simulation of three-dimensional homogeneous isotropic turbulence. *Physical Review Letters*, 28(2):76.

Papoulis, A. (1965). *Probability, random variables, and stochastic processes.* McGraw-Hill.

Pastuhoff, M., Yorita, D., Asai, K., and Alfredsson, P. H. (2013). Enhancing the signal-to-noise ratio of pressure sensitive paint data by singular value decomposition. *Measurement Science and Technology*, 24(7):075301.

Paterna, E., Moonen, P., Dorer, V., and Carmeliet, J. (2013). Mitigation of surface reflection in PIV measurement. *Measurement Science and Technology*, 24(5):057003.

Payne, F. R. and Lumley, J. L. (1967). Large eddy structure of the turbulent wake behind a circular cylinder. *The Physics of Fluids*, 10(9):S194–S196.

Pearson, K. (1901). On lines and planes of closest fit to systems of points in space. *Philosophical Magazine*, 2(11):559–572.

Perrin, R., Braza, M., Cid, E., Cazin, S., Barthet, A., Sevrain, A., Mockett, C., and Thiele, F. (2007). Obtaining phase averaged turbulence properties in the near wake of a circular cylinder at high Reynolds number using POD. *Experiments in Fluids*, 43(2-3):341–355.

Pesavento, U. and Wang, Z. J. (2004). Falling paper: Navier-Stokes solutions, model of fluid forces, and center of mass elevation. *Physical Review Letters*, 93(14):144501.

Picard, C. and Delville, J. (2000). Pressure velocity coupling in a subsonic round jet. *International Journal of Heat and Fluid Flow*, 21(3):359–364.

Pines, D. J. and Bohorquez, F. (2006). Challenges facing future micro-air-vehicle development. *Journal of Aircraft*, 43(2):290–305.

Pitt Ford, C. W. and Babinsky, H. (2013). Lift and the leading-edge vortex. *Journal of Fluid Mechanics*, 720:280–313.

Platzer, M. F., Jones, K. D., Young, J., and Lai, J. C. S. (2008). Flapping wing aerodynamics: progress and challenges. *AIAA Journal*, 46(9):2136–2149.

Polhamus, E. C. (1966). A concept of the vortex lift of sharp-edge delta wings based on a leading-edge-suction analogy.

Prandtl, L. (1925). Bericht uber untersuchungen zur ausgebildeten turbulenz. *Zeitschrift für Angewandte Mathematik und Mechanik*, 5(2):136–139.

Price, S. J., Sumner, D., Smith, J. G., Leong, K., and Paidoussis, M. P. (2002). Flow visualization around a circular cylinder near to a plane wall. *Journal of Fluids and Structures*, 16(2):175–191.

Prouty, R. W. (1995). *Helicopter performance, stability, and control*, chapter 6, pages 397–407.

Pukelsheim, F. (1994). The three sigma rule. *The American Statistician*, 48(2):88–91.

Raben, S. G., Charonko, J., and Vlachos, P. P. (2012). Adaptive gappy proper ortogonal decomposition for particle image velocimetry data reconstruction. *Measurement Science and Technology*, 23:025303.

Raffel, M., Willert, C., Werely, S., and Kompenhans, J. (2007). *Particle Image Velocimetry: A Practical Guide.* Springer.

Raiola, M., Discetti, S., and Ianiro, A. (2015). On PIV random error minimization with optimal POD-based low-order reconstruction. *Experiments in Fluids*, 56(4):1–15.

Raiola, M., Greco, C. S., Contino, M., Discetti, S., and Ianiro, A. (2017). Towards enabling time-resolved measurements of turbulent convective heat transfer maps with IR thermography and a heated thin foil. *International Journal of Heat and Mass Transfer*, 108:199–209.

Raiola, M., Ianiro, A., and Discetti, S. (2016). Wake of tandem cylinders near a wall. *Experimental Thermal and Fluid Science*, 78:354–369.

Ravindran, S. (2000). Reduced-order adaptive controllers for fluid flows using POD. *Journal of Scientific Computing*, 15:457–478.

Reynolds, O. (1894). On the dynamical theory of incompressible viscous fluids and the determination of the criterion. *Proceedings of the Royal Society of London*, 56(336-339):40–45.

Reynolds, W. C. (1976). Computation of turbulent flows. *Annual Review of Fluid Mechanics*, 8(1):183–208.

Rival, D., Prangemeier, T., and Tropea, C. (2009). The influence of airfoil kinematics on the formation of leading-edge vortices in bio-inspired flight. *Experiments in fluids*, 46(5):823–833.

Rival, D. E., Kriegseis, J., Schaub, P., Widmann, A., and Tropea, C. (2014). Characteristic length scales for vortex detachment on plunging profiles with varying leading-edge geometry. *Experiments in fluids*, 55(1):1660.

Rodriguez, J. D. and Sirovich, L. (1990). Low-dimensional dynamics for the complex Ginzburg-Landau equation. *Physica D: Nonlinear Phenomena*, 43(1):77–86.

Roshko, A. (1954). On the drag and shedding frequency of two-dimensional bluff bodies. 1954. *National Advisory Committee on Aeronautics.*

Roth, G. I. and Katz, J. (2001). Five techniques for increasing the speed and accuracy of PIV interrogation. *Measurement Science and Technology*, 12:238–245.

Rowley, C. W. (2005). Model reduction for fluids, using balanced proper orthogonal decomposition. *International Journal of Bifurcation and Chaos*, 15(03):997–1013.

Rowley, C. W., Colonius, T., and Murray, R. M. (2004). Model reduction for compressible flows using POD and Galerkin projection. *Physica D: Nonlinear Phenomena*, 189(1):115–129.

Rowley, C. W., Mezić, I., Bagheri, S., Schlatter, P., and Henningson, D. S. (2009). Spectral analysis of nonlinear flows. *Journal of Fluid Mechanics*, 641:115–127.

Sane, S. P. and Dickinson, M. H. (2002). The aerodynamic effects of wing rotation and a revised quasi-steady model of flapping flight. *Journal of Experimental Biology*, 205(8):1087–1096.

Sanmiguel, C., Örlü, R., Vinuesa, R., Schlatter, P., Ianiro, A., and Discetti, A. (2017). Adverse-pressure-gradient effects on turbulent boundary layers: statistics and flow-field organization. *In press on Flow Turbulence and Combustion.* , doi: 10.1007/s10494-017-9869-z.

Sarkar, S. and Sarkar, S. (2010). Vortex dynamics of a cylinder wake in proximity to a wall. *Journal of Fluids and Structures*, 26(1):19–40.

Scarano, F. (2001). Iterative image deformation methods in PIV. *Measurement Science and Technology*, 13(1):R1.

Scarano, F. (2003). Theory of non-isotropic spatial resolution in PIV. *Experiments in Fluids*, 35:268–77.

Schiavazzi, D., Coletti, F., Iaccarino, G., and Eaton, J. K. (2014). A matching pursuit approach to solenoidal filtering of three-dimensional velocity measurements . *Journal of Computational Physics*, 263:206 – 221.

Schlichting, H. and Gersten, K. (2003). *Boundary-layer theory.* Springer Science & Business Media.

Schmid, P. J. (2010). Dynamic mode decomposition of numerical and experimental data. *Journal of Fluid Mechanics*, 656:5–28.

Schneiders, J. F. G., Dwight, R. P., and Scarano, F. (2014). Time-supersampling of 3d-piv measurements with vortex-in-cell simulation. *Experiments in Fluids*, 55(3):1692.

Sciacchitano, A. and Scarano, F. (2014). Elimination of PIV light reflections via a temporal high pass filter. *Measurement Science and Technology*, 25(8):0S84009.

Sciacchitano, A., Scarano, F., and Wieneke, B. (2012). Multi-frame pyramid correlation for time-resolved PIV. *Experiments in Fluids*, 53:1087–105.

Sedov, L. I. (1965). *Two-dimensional problems of hydrodynamics and aerodynamics.* Interscience Publishers.

Shavit, U., Lowe, R. J., and Steinbuck, J. V. (2007). Intensity Capping: a simple method to improve cross-correlation PIV results. *Experiments in Fluids*, 42:225–440.

Shi, L. L., Liu, Y. Z., and Wan, J. J. (2010). Influence of wall proximity on characteristics of wake behind a square cylinder: PIV measurements and POD analysis. *Experimental Thermal and Fluid Science*, 34(1):28–36.

Shipley, D. E., Miller, M. S., and Robinson, M. C. (1995). Dynamic stall occurrence on a horizontal axis wind turbine blade. Technical report, National Renewable Energy Lab., Golden, CO (United States).

Shyy, W., Lian, Y., Tang, J., Viieru, D., and Liu, H. (2007). *Aerodynamics of low Reynolds number flyers*, volume 22. Cambridge University Press.

Sicot, C., Perrin, R., Tran, T. T., and Boree, J. (2012). Wall pressure and conditional flow structures downstream of a reattaching flow region. *International Journal of Heat and Fluid Flow*, 35:119–129.

Sieber, M., Paschereit, C. O., and Oberleithner, K. (2016). Spectral proper orthogonal decomposition. *Journal of Fluid Mechanics*, 792:798–828.

Sirovich, L. (1987). Turbulence and the dynamics of coherent structures: I, II, III. *Quarterly of Applied Mathematics*, 45:561–590.

Stewart, G. W. (2001). *Matrix Algorithms Volume 2: Eigensystems*, volume 2. Siam.

Stitou, A. and Riethmuller, M. (2001). Extension of PIV to super resolution using PTV. *Measurement Science and Technology*, 12(9):1398.

Sumner, D. (2010). Two circular cylinders in cross-flow: a review. *Journal of Fluids and Structures*, 26(6):849–899.

Sun, M. (2014). Insect flight dynamics: stability and control. *Reviews of Modern Physics*, 86(2):615.

Sunada, S., Yasuda, T., Yasuda, K., and Kawachi, K. (2002). Comparison of wing characteristics at an ultralow reynolds number. *Journal of Aircraft*, 39(2):331–338.

Taha, H. E., Hajj, M. R., and Beran, P. S. (2014). State-space representation of the unsteady aerodynamics of flapping flight. *Aerospace Science and Technology*, 34:1–11.

Taira, K., Brunton, S. L., Dawson, S., Rowley, C. W., Colonius, T., McKeon, B. J., Schmidt, O. T., Gordeyev, S., Theofilis, V., and Ukeiley, L. S. (2017). Modal analysis of fluid flows: An overview. *arXiv preprint arXiv:1702.01453*.

Tarzanin, F. J. (1972). Prediction of control loads due to blade stall. *Journal of the American Helicopter Society*, 17(2):33–46.

Taylor, G. I. (1915). Eddy motion in the atmosphere. *Philosophical Transactions of the Royal Society of London. Series A, Containing Papers of a Mathematical or Physical Character*, 215:1–26.

Taylor, J. A. and Glauser, M. N. (2004). Towards practical flow sensing and control via POD and LSE based low-dimensional tools. *Journal of Fluids Engineering*, 126(3):337–345.

Theodorsen, T. (1935). General theory of aerodynamic instability and the mechanism of flutter. *NACA Report 496*.

Theofilis, V. (2011). Global linear instability. *Annual Review of Fluid Mechanics*, 43:319–352.

Theunissen, R., Scarano, F., and Riethmuller, M. (2008). On improvement of PIV image interrogation near stationary interfaces. *Experiments in Fluids*, 45:557–572.

Thielicke, W. and Stamhuis, E. J. (2014). Towards user-friendly, affordable and accurate digital particle image velocimetry in matlab. *JORS*, 2(1):e30.

Tinney, C. E., Coiffet, F., Delville, J., Hall, A. M., Jordan, P., and Glauser, M. N. (2006). On spectral linear stochastic estimation. *Experiments in Fluids*, 41(5):763–775.

Tipping, M. E. and Bishop, C. M. (1999). Probabilistic principal component analysis. *Journal of the Royal Statistical Society: Series B (Statistical Methodology)*, 61(3):611–622.

Towne, A., Schmidt, O. T., and Colonius, T. (2017). Spectral proper orthogonal decomposition and its relationship to dynamic mode decomposition and resolvent analysis. *Journal of Fluid Mechanics*, 825:1113–1152.

Tu, J. H., Griffin, J., Hart, A., Rowley, C. W., Cattafesta, L. N., and Ukeiley, L. S. (2013). Integration of non-time-resolved PIV and time-resolved velocity point sensors for dynamic estimation of velocity fields. *Experiments in Fluids*, 54(2):1429.

Tu, J. H., Rowley, C. W., Luchtenburg, D. M., Brunton, S. L., and Kutz, J. N. (2014). On dynamic mode decomposition: theory and applications. *Journal of Computational Dynamics*, 1(2):391–421.

Turk, M. and Pentland, A. (1991). Eigenfaces for recognition. *Journal of Cognitive Neuroscience*, 3(1):71–86.

van Oudheusden, B. W. (2013). PIV-based pressure measurement. *Measurement Science and Technology*, 24(3):032001.

van Oudheusden, B. W., Scarano, F., van Hinsberg, N. P., and Watt, D. W. (2005). Phase-resolved characterization of vortex shedding in the near wake of a square-section cylinder at incidence. *Experiments in Fluids*, 39(1):86–98.

Venturi, D. (2006). On proper orthogonal decomposition of randomly perturbed fields with applications to flow past a cylinder and natural convection over a horizontal plate. *Journal of Fluid Mechanics*, 559:215–254.

Venturi, D. and Karniadakis, G. E. (2004). Gappy data and reconstruction procedures for flow past a cylinder. *Journal of Fluid Mechanics*, 519:315–336.

Violato, D., Ianiro, A., Cardone, G., and Scarano, F. (2012). Three-dimensional vortex dynamics and convective heat transfer in circular and chevron impinging jets. *International Journal of Heat and Fluid Flow*, 37:22–36.

von Kármán, T. (1935). Some aspects of the turbulence problem. In *Proceedings of the 4th Internationañ Congress for Applied Mechanics, Cambridge*, pages 54–91.

von Kármán, T. and Sears, W. R. (1938). Airfoil theory for non-uniform motion. *Journal of the Aeronautical Sciences*, 5(10):379–390.

Wagner, H. (1925). Über die entstehung des dynamischen auftriebes von tragflügeln. *Zeitschrift für Angewandte Mathematik und Mechanik*, 5(1):17–35.

Wang, X. K., Hao, Z., and Tan, S. K. (2013). Vortex-induced vibrations of a neutrally buoyant circular cylinder near a plane wall. *Journal of Fluids and Structures*, 39:188–204.

Wang, X. K., Hao, Z., Zhang, J.-X., and Tan, S. K. (2014). Flow around two tandem square cylinders near a plane wall. *Experiments in Fluids*, 55(10):1–14.

Wang, X. K. and Tan, S. K. (2008). Comparison of flow patterns in the near wake of a circular cylinder and a square cylinder placed near a plane wall. *Ocean Engineering*, 35(5):458–472.

Wax, M. and Kailath, T. (1985). Detection of signals by information theoretic criteria. *IEEE Transactions on Acoustics, Speech, and Signal Processing*, 33(2):387–392.

Werely, S. T. and Gui, L. (2002). Advanced algorithm for microscale particle image velocimetry. *AIAA Journal*, 40:1047–55.

Westerweel, J. (1993). *Digital Particle Image Velocimetry. Theory and Practice.* PhD thesis, Delft University of Technology.

Westerweel, J. (1994). Efficient detection of spurious vectors in particle image velocimetry data sets. *Experiments in Fluids*, 16:236–47.

Westerweel, J. (1997). Fundamentals of digital particle image velocimetry. *Measurement Science and Technology*, 8:1379–92.

Westerweel, J. (2000). Theoretical analysis of the measurement precision in particle image velocimetry. *Experiments in Fluids*, 29:S3–12.

Westerweel, J., Elsinga, G. E., and Adrian, R. J. (2013). Particle image velocimetry for complex and turbulent flows. *Annual Review of Fluid Mechanics*, 45:409–436.

Westerweel, J. and Scarano, F. (2005). Universal outlier detection for PIV data. *Experiments in Fluids*, 39:1096–100.

Widmann, A. and Tropea, C. (2015). Parameters influencing vortex growth and detachment on unsteady aerodynamic profiles. *Journal of Fluid Mechanics*, 773:432–459.

Willert, C. (1997). Stereoscopic digital particle image velocimetry for application in wind tunnel flow. *Measurement Science and Technology*, 8:1465–79.

Williamson, C. H. K. (1996). Vortex dynamics in the cylinder wake. *Annual Review of Fluid Mechanics*, 28(1):477–539.

Wu, Y. and Christensen, K. T. (2010). Spatial structure of a turbulent boundary layer with irregular surface roughness. *Journal of Fluid Mechanics*, 655:380–418.

Xu, G. and Zhou, Y. (2004). Strouhal numbers in the wake of two inline cylinders. *Experiments in Fluids*, 37(2):248–256.

Young Jr, W. H. (1981). Fluid mechanics mechanisms in the stall process of helicopters. *NASA Technical Memorandum 81956*.

Yu, H., Kanov, K., Perlman, E., Graham, J., Frederix, E., Burns, R., Szalay, A., Eyink, G., and Meneveau, C. (2012a). Studying Lagrangian dynamics of turbulence using on-demand fluid particle tracking in a public turbulence database. *Journal of Turbulence*, 13:N12.

Yu, M., Wang, Z. J., and Hu, H. (2012b). Airfoil thickness effects on the thrust generation of plunging airfoils. *Journal of Aircraft*, 49(5):1434–1439.

Zdravkovich, M. M. (1987). The effects of interference between circular cylinders in cross flow. *Journal of Fluids and Structures*, 1(2):239–261.

Zhou, Y. and Yiu, M. W. (2006). Flow structure, momentum and heat transport in a two-tandem-cylinder wake. *Journal of Fluid Mechanics*, 548:17–48.

Zovatto, L. and Pedrizzetti, G. (2001). Flow about a circular cylinder between parallel walls. *Journal of Fluid Mechanics*, 440:1–25.

Zuiderveld, K. (1994). Contrast limited adaptive histogram equalization. In *Graphics Gems IV*. Academic Press Professional, Inc.

Papers and author contributions

Published journal papers

- Raiola, M., Discetti, S., and Ianiro, A. (2015). On PIV random error minimization with optimal POD-based low-order reconstruction. *Experiments in Fluids*, 56(4):1–15.
- Raiola, M., Ianiro, A., and Discetti, S. (2016). Wake of tandem cylinders near a wall. *Experimental Thermal and Fluid Science*, 78:354–369.
- Mendez, M. A., Raiola, M., Masullo, A., Discetti, S., Ianiro, A., Theunissen, R., and Buchlin, J.-M. (2017). POD-based background removal for particle image velocimetry. *Experimental Thermal and Fluid Science*, 80:181–192.
- Raiola, M., Greco, C. S., Contino, M., Discetti, S., and Ianiro, A. (2017). Towards enabling time-resolved measurements of turbulent convective heat transfer maps with IR thermography and a heated thin foil. *International Journal of Heat and Mass Transfer*, 108:199–209.
- Discetti, S., Raiola, M., and Ianiro, A. (2018). Estimation of time resolved turbulent fields through correlation of non-time resolved field measurements and time-resolved point measurements. *Experimental Thermal and Fluid Science*, 93: 119-130.
- Raiola, M., Discetti, S., Ianiro, A., Samara, F., Avallone, F., and Ragni, D. (2018). Smart rotors: a strategy for dynamic stall control by means of an actuated flap. *AIAA Journal*, Article in Advance, DOI: 10.2514/1.J056342.

Conference papers

- Raiola, M., Discetti, S., and Ianiro, A. (2014). On the suppression of piv measurement noise with a pod based filter. In *17th International Symposium on Applications of Laser Techniques to Fluid Mechanics*, 07-10 July, Lisbon, Portugal.
- Raiola, M., Discetti, S., and Ianiro, A. (2015). PIV measurements in the wake of two circular cylinders in tandem configuration with ground effect. In *10th Pacific Symposium on Flow Visualization and Image Processing*, 15-18 June, Naples, Italy.
- Raiola, M., Discetti, S., and Ianiro, A. (2016). Low order modelling of flow features and aerodynamic forces in flapping airfoils. In *34th AIAA Applied Aerodynamics Conference, AIAA AVIATION*, 13-17 June, Washington, D.C.
- Raiola, M., Ianiro, A., Discetti, S., Gillebaart, T., Ragni, D., van Kuik, G., and van Wingerden, J.-W. (2016). Smart rotor: controlling dynamic stall by means of an actuated flap. In *8th AIAA Flow Control Conference, AIAA AVIATION*, 13-17 June, Washington, D.C.
- Raiola, M., Ianiro, A., Discetti, S., Gillebaart, T., Ragni, D., Navalkar, S., van Kuik, G., and van Wingerden, J.-W. (2016). Smart rotor: control of dynamic loads on a rotor blade. In *11th European Fluid Mechanics Conference*, 12-16 September, Seville, Spain.
- Raiola, M., Moral, P., Discetti, S., and Ianiro, A. (2016). Modal decomposition of flow features in flapping wings and modes contribution to forces. In *11th European Fluid Mechanics Conference*, 12-16 September, Seville, Spain.
- Raiola, M., Ianiro, A., Discetti, S., Moriche, M., Flores, O. and García-Villalba (2016). Flow over flapping airfoils: qualitative and quantitative comparison between experiments and simulations. In *11th European Fluid Mechanics Conference*, 12-16 September, Seville, Spain.
- Raiola, M., Discetti, S., and Ianiro, A. (2016). Modelling forces and flow features in flapping wings: a POD based approach. In *69th Annual Meeting of the APS Division of Fluid Dynamics*, 20-22 November, Portland, Oregon.
- Discetti, S., Raiola, M., and Ianiro, A. (2017). Dynamic estimation of flow fields through correlation of non-time-resolved field measurements and time-resolved

point measurements. In *9th World Conference on Experimental Heat Transfer, Fluid Mechanics and Thermodynamics*, 12-15 June, Iguazu Falls, Brazil.

- Discetti, S., Sanmiguel Vila, C., Raiola, M., Serpieri, J., Örlü, R., Mascotelli, L., Fiorini, T., Bellani, G., Talamelli, A. and Ianiro, A. (2017). Very-large-scale motion measurements in pipe flows at high Reynolds numbers. In *16th EUROMECH European Turbulence Conference*, 21–24 August, Stockholm, Sweden.
- Raiola, M., Discetti, S., and Ianiro, A. (2017) A data-driven decomposition approach to model aerodynamic forces on flapping airfoils. In *70th Annual Meeting of the APS Division of Fluid Dynamics*, 19-21 November, Denver, Colorado.